Theoretical studies of underscreened Kondo physics in quantum dots

Christopher James Wright
Balliol College, Oxford

A thesis submitted for the degree of
Doctor of Philosophy
at the University of Oxford, Trinity 2011

Theoretical studies of underscreened Kondo physics in quantum dots

Christopher James Wright
Balliol College, Oxford

A thesis submitted for the degree of
Doctor of Philosophy
at the University of Oxford, Trinity 2011

Abstract

We study correlated two-level quantum impurity models coupled to a metallic conduction band in the hope of gaining insight into the physics of nanoscale quantum dot systems. We focus on the possibility of formation of a spin-1 impurity local moment which, on coupling to the band, generates an underscreened (USC) singular Fermi liquid state. By employing physical arguments and the numerical renormalization group (NRG) technique, we analyse such systems in detail examining in particular both the thermodynamic and dynamic properties, including the differential conductance.

The quantum phase transitions occurring between the USC phase and a more ordinary Fermi liquid (FL) phase are analysed in detail. They are generically found to be of Kosterlitz-Thouless type; exceptions occur along lines of high symmetry where first-order transitions are found. A 'Friedel-Luttinger sum rule' is derived and, together with a generalization of Luttinger's theorem to the USC phase, is used to obtain general results for the $T = 0$ zero-bias conductance — it is expressed solely in terms of the number of electrons present on the impurity and applicable in both the USC and FL phases. Relatedly, dynamical signatures of the quantum phase transition show two broad classes of behaviour corresponding to the collapse of either a resonance or antiresonance in the single-particle density of states. Evidence of both of these behaviours is seen in experimental devices.

We study also the effect of a local magnetic field on both single- and two-level quantum impurities. In the former case we attempt to resolve some points of contention that remain in the literature. Specifically we show that the position of the maximum in the spin resolved density of states (and related peaks in the differential conductance) is not linear in the applied field, showing a more complicated form than a simple 'Zeeman splitting'. The analytic result for the low-field asymptote is recovered. For two-level impurities we illustrate the manner in which the USC state is destroyed: due to two cancelling effects an abrupt change in the zero-bias conductance does not occur as one might expect. Comparison with experiment is made in both cases and used to interpret experimental findings in a manner contrary to previous suggestions. We find that experiments are very rarely in the limit of strong impurity-host coupling. Further, features in the differential conductance as a function of bias voltage should not be simply interpreted in terms of isolated quantum dot states. The many-body nature of such systems is crucially important to their observed properties.

Acknowledgements

First I would like to thank my supervisor Professor David Logan, who has been an outstanding undergraduate tutor and passionate, if impatient, mentor.

I would also like to thank Dr Martin Galpin, whose help and advice has been more than invaluable. It has been a great pleasure also to work with other members of the Logan group including Fred, who perhaps will one day escape being asked questions about India, and Adam who has brought a more relaxed atmosphere (and Sky Sports) to the office.

Finally and most importantly, I would like to thank my fianceé, Elsa, for her endless love and support, particularly whilst writing this thesis.

Contents

CHAPTER 1

Introduction

Recent experimental advances have led to a diverse range of mesoscopic electronic devices including so-called quantum dots [1]. These devices typically contain an 'island' of localised electrons coupled to a larger bath such as the conduction band of a metal. Their small size results in quantization of the electronic energy levels, whilst their relative isolation means that in general the number of resident electrons is a well-defined quantity [1, 2]. The island may take various forms, the smallest of which might be a transition metal ion deposited on a metallic surface [3, 4]. A larger island can be constructed from a single small organic molecule such as a fullerene [5–7], or a more extended molecule such as a carbon nanotube or graphene sheet [8, 9].

In all of the above examples the inherent properties of the island such as its classical charging energy (or capacitance), electronic level spacings, spin, and vibrational modes, are all predetermined and cannot, to a large extent, be controlled by the experimentalist. Rather more tunable devices are semiconductor quantum dots formed, for example, in GaAs heterostructures [1]. A schematic illustration of such a device is shown in fig. 1.1. The device consists of a modulation doped layer of $Ga_xAl_{1-x}As$ sandwiched between two layers of undoped GaAs. The resulting structure of the conduction band, as drawn in fig. 1.1c), permits the formation of a so-called two-dimensional electron gas (2DEG) underneath the $Ga_xAl_{1-x}As$ layer [10]. Within the 2DEG electrons are strongly confined in the perpendicular direction due to extreme quantization — electrons are thereby restricted to movement parallel to the interface of the two semiconductor layers and do so as free particles. The second crucial feature of the device is the electrodes placed on top of the heterostructure. A voltage applied to these electrodes electrostatically depletes the 2DEG in the region directly beneath, thus sculpting the 2DEG into any desired form. Positioning the electrodes as shown in the fig. 1.1a) leads to an arrangement of the 2DEG as depicted in fig. 1.1b). Two extended regions of the 2DEG, the

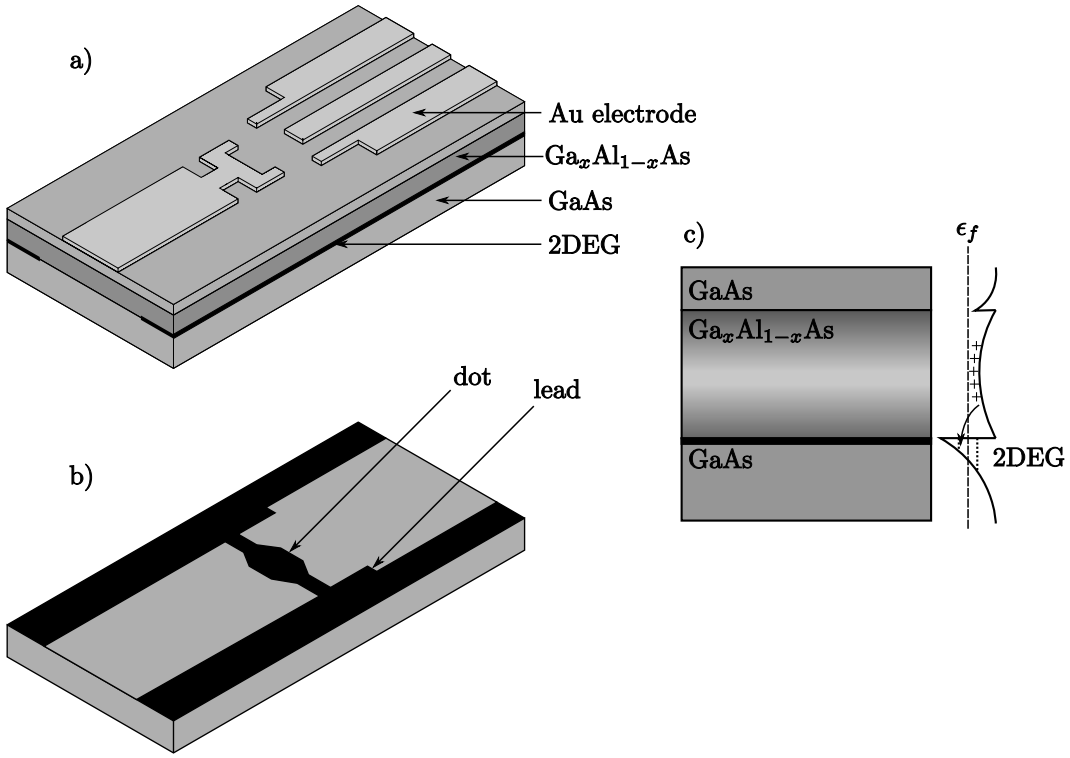

Figure 1.1: Schematic diagram of the basic quantum dot device. a) The complete device with Au electrodes on a semiconductor heterostructure. b) The 2DEG formed at the interface between the $Ga_xAl_{1-x}As$ and GaAs layers. c) Formation of a 2DEG. Donors in the $Ga_xAl_{1-x}As$ layer are ionized when their electrons fall into the triangular potential below the Fermi level, ϵ_f.

'leads', are connected via narrow channels to a smaller region, the quantum dot. This is precisely analogous to the systems outlined above. However the size of the tunneling channels and of the dot itself can be controlled with exquisite precision by varying the voltages applied to the surface electrodes. The most significant of these electrodes is the gate electrode supplying the voltage V_g. In the simplest models the effect of V_g is to shift the energy levels of the dot to higher or lower energy. When an energy level moves below the Fermi level of the leads, an electron can in principle move from the lead to the dot. The gate thereby controls the number of electrons present on the quantum dot.

Once the 2DEG is prepared the transport properties of the dot, *i.e.* its electrical conductance, can be measured by connecting an external circuit and applying a voltage across the two leads [11]. Adding an electron with charge e costs a classical Coulomb charging energy $E_C = e^2/2C$, where C is capacitance of the dot to the rest of the system. Due to the small size of the devices, the capacitance is often very small indeed leading to charging energies well above the thermal energy k_BT. The resulting Coulomb blockade effect, whereby the charge on the dot increases in

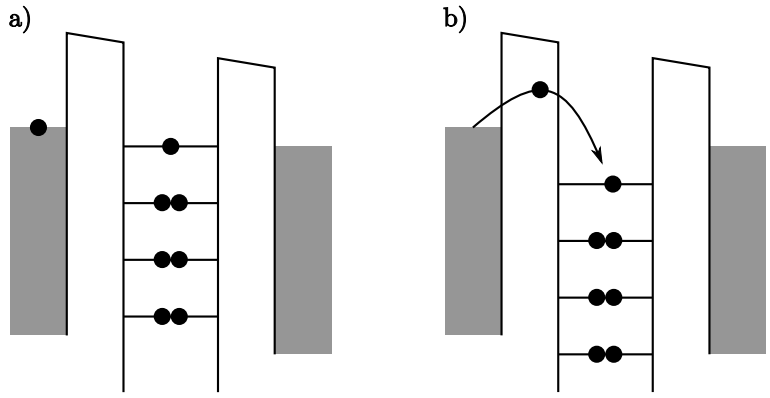

Figure 1.2: Schematic energy level diagram of a quantum dot illustrating the Coulomb blockade effect. Current flows by electrons tunneling from the left electrode through the barrier to the dot and subsequently to the right electrode. a) A low conductance configuration: Coulombic repulsion with the electron already present on the dot hinders the electron on the left electrode from tunneling to the dot. b) Application of a gate voltage lowers the energy levels of the dot, overcoming the Coulombic repulsion allowing the electron to tunnel to the dot.

essentially integer steps, is a well-studied phenomenon [12–18]. The essential physics is illustrated in fig. 1.2 where we show a set of quantum dot levels between a left and a right conduction band filled to their respective Fermi levels $\epsilon_{f,L}$ and $\epsilon_{f,R}$. We denote the energy of the highest dot level ϵ. In a blocking state [fig. 1.2a)], the electron residing at the Fermi level of the left lead cannot move onto the dot due to the additional Coulomb repulsion U that would result. This is despite the dot level lying below the Fermi level of the left lead, that is to say $\epsilon < \epsilon_{f,L}$ but $2\epsilon + U > \epsilon_{f,L}$. Movement of electrons from the left to the right lead is therefore hampered and the dot will display a low conductance. On altering the gate voltage V_g the dot energy levels are lowered in energy, fig. 1.2b). In this transmitting state $2\epsilon + U$ is now lower in energy than the left Fermi level such that the electron may tunnel to the dot. If in addition $2\epsilon + U > \epsilon_{f,R}$ the electron will subsequently move through the dot to the right lead — the conductance of the quantum dot will be high.

Measurements of the conductance of a graphene quantum dot [19] are shown in fig. 1.3 as a function of both the gate voltage V_g and the source-drain bias $V_{\rm sd}$ (the bias placed across the quantum dot), which has the effect of shifting the Fermi levels of the leads. Along the line of zero source-drain bias ($\epsilon_{f,L} = \epsilon_{f,R} \equiv \epsilon_f$) the conductance is low, and essentially constant except for at discrete points. In our simple model above these points correspond to the situation in which $\epsilon = 2\epsilon + U = \epsilon_f$ (or $\epsilon = \epsilon_f$)[1] such that on crossing one of these points of high conductance the dot charge increases by one. Away from $V_{\rm sd}$ the peaks in conductance shift essentially

[1] As we will see in the next section the interactions between electrons on the impurity are more complicated. However the simple model used here suffices to illustrate the point.

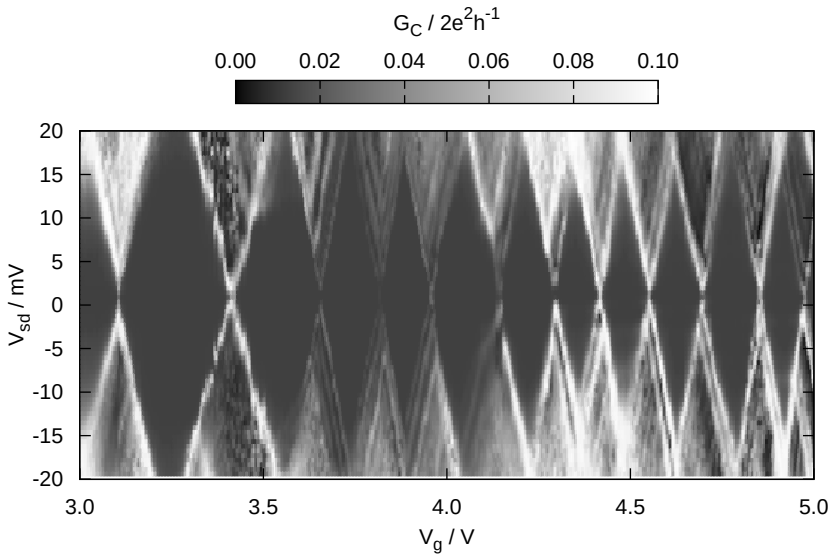

Figure 1.3: Coulomb blockade diamonds in a graphene quantum dot [19]. White areas are those of high conductance. Strong electron repulsion, quantified by the Coulomb integral U, hinders conductance of electrons from the source to drain electrodes when an electron is already present on the dot. When the gate voltage V_g is swept, and the quantum dot level energies are altered, a doubly occupied state may become degenerate with a singly occupied state thereby increasing the conductance.

linearly in V_g reflecting the second point alluded to above: not only do the energy levels of the dot have to be such to allow an electron to tunnel from the source to the dot, but also that the Fermi levels of the leads must be such as to allow subsequent tunneling to the drain. Characteristic Coulomb blockade diamonds are thereby observed.

The Coulomb blockade effect and sequential tunneling transport are therefore, in a sense, quite trivial. Of more interest theoretically are situations in which the conductance of quantum dots is enhanced by other means. One such mechanism is the Kondo effect [20], long known in the context of the electrical properties of bulk metals but now well established in quantum dots being first observed in a GaAs quantum dot [1]. The Kondo effect will be central to this thesis and so a little historical overview of the effect and its physical explanation is appropriate.

In the middle of the twentieth century physicists struggled to explain two observations regarding the physical properties of dilute magnetic alloys (*e.g.* samples of very pure gold with trace amounts of a magnetic impurity such as copper) at low temperatures. Firstly, experiments indicated the existence of magnetic moments within the alloys. It was not immediately obvious how such moments could survive within an itinerant electron host. Further, the alloys displayed a curious resistance minimum at low temperatures. This observation directly contradicted contemporary theories of resistive scattering involving static impurities.

It was suggested by Anderson [21] that these two observations might be related and that the local magnetic moments might arise due to local correlations at the impurity sites. Anderson proposed a model — now known as the Anderson impurity model (AIM) — which describes a single impurity with an on-site Coulomb interaction U and which is coupled to a metallic host, via a matrix element V, such that electrons may 'hop' from the host to the impurity and back. We will discuss the AIM more fully in section 2.1 and here consider only the difficulties that arise in considering how to calculate relevant physical properties of the simple model.

In essence it is the combination of the local Coulombic interaction U and the large number of conduction band electrons which renders the AIM difficult to manage. Such a large number of particles obviously means that *ab initio* methods of the sort employed in electronic structure calculations of molecules are inapplicable. Mean-field approaches are also unable to describe the detailed electron-electron correlations — Anderson originally took this approach with his analysis suggesting a phase transition in the AIM between a magnetic and a non-magnetic state as a function of the interaction strength U. In fact, this conclusion is now known to be incorrect [22–24] and the ground state of the AIM is always non-magnetic.

A second method to tackle the AIM might be to use finite-order perturbation theory in the interaction U [25–27]. Such an approach is naturally limited to the regime of small U; otherwise the perturbative series is meaningless. However it turns out that it is precisely the strongly-correlated regime of large U which leads to the most interesting physics, notably the Kondo effect. Perturbation theory in the hopping V is also troublesome as the initial Hamiltonian then contains the Coulomb interaction and thereby has a correlated ground state. Wick's theorem cannot be employed therefore and standard diagrammatic techniques are inappropriate. More elaborate perturbative techniques have been tried including the $1/N$ expansion (which replaces the impurity level with a spin-N variable) the non-crossing approximation (NCA), and slave-boson mean-field (SBMF) theories [20]. All of these techniques ultimately fail to capture the behaviour of the AIM and the properties of dilute magnetic alloys across the full temperature range of interest.

The first successes in describing magnetic alloys came from the study of a second model Hamiltonian, the spin-$\frac{1}{2}$ Kondo Hamiltonian which can be derived as a limit of the AIM.[2] (Again, we will illustrate this Hamiltonian more fully in the following chapter). Kondo was able to explain [28] the resistance minimum by considering the coupling of the spin-$\frac{1}{2}$ impurity to the free conduction band Hamiltonian as a perturbation. To third order in the coupling host-impurity coupling J, Kondo

[2] The converse is not true as the AIM encompasses a larger array of physical behaviours than the Kondo model.

obtained

$$R(T) = a + bT^5 + c\ln\left(\frac{k_B T}{D}\right), \tag{1.1}$$

for the resistance of the host. The first term here, a constant, arises from simple scattering processes occurring at the impurity sites whilst the second term is the phonon contribution, it naturally decays rapidly as the temperature is lowered. The final term is that arising from the exchange coupling of the impurity to the conduction band and increases as T approaches zero. The form of (1.1) was found to agree very well with the available experimental data and hence Kondo had essentially explained the resistance minimum. However, in solving one issue Kondo had created another. This third-order result for the resistance does not explain the behaviour of the Kondo model as $T \to 0$, the logarithmic term diverging in this limit. This problem became known as the 'Kondo Problem'. A full solution of the Kondo model on all temperature scales remained elusive throughout the 1960s. Whilst it was clear that magnetic impurities had a crucial role in determining the resistance of dilute magnetic alloys, their full effect could not be explained rigorously.

A key breakthrough came in the 1970s with the advent of renormalization group (RG) approaches. These techniques access the properties of a system at a given energy (or length) scale from knowledge of the properties of the system at a larger scale. By successive application of such a RG transform the full evolution of physical properties can be found. Anderson developed an approximate RG scheme for the Kondo model which he called a 'poor man's scaling' approach [29]. We will see this approach in action in section 2.2.1. This technique highlighted the so-called 'scaling' physics of quantum impurity models and indicated the existence of an exponentially-small energy scale (the Kondo scale). However, as poor man's scaling remained inherently perturbative, it still failed to obtain the correct $T \to 0$ limit.

Only when Wilson proposed the non-perturbative numerical renormalization group (NRG) was a full solution of the Kondo model found [22]. The NRG discretizes the host conduction band into logarithmic intervals thereby including all energy scales whilst also reducing the complexity of the problem. A full account will be given in chapter 3. Wilson showed conclusively that as $T \to 0$, the impurity spin becomes locked into a macroscopic many-body singlet state with the electrons of the conduction band. This solution of the Kondo Problem did not kill research work on the Kondo effect. Soon after Wilson's work, Nozières [30] showed that the NRG results were entirely consistent with Landau's Fermi liquid theory — the ground state of the Kondo model being a classic Fermi liquid state. Later Krishnamurthy [23, 24] extended the NRG to the AIM, obtaining results which solidified the relationship between the two models. Subsequently analytic solutions for both the Kondo [31] and AIM [32] were found by using the Bethe ansatz technique. However the NRG remains an important tool for it is applicable to a wider range of impurity models

than the Bethe ansatz and can be used to calculate accurately dynamic properties.[3]

Both the AIM and Kondo model receive considerable theoretical attention even today, particularly since the advent of quantum dot devices displaying the Kondo effect. Exotic quantum impurity models have now been proposed and studied with the NRG including: the gapped [34] and pseudogapped [35] Anderson impurity models, multichannel [36, 37] variants, and systems with bosonic rather than fermionic baths [38, 39]. The focus is now naturally on the enhanced conductance of the impurity (quantum dot) rather than the increased resistance of the host.

A classic variant on the ordinary spin-$\frac{1}{2}$ Kondo model is formed by taking spin-N impurities. Such systems were studied via the NRG first by Cragg [40] who showed that, contrary to prevailing opinion, these systems possessed a magnetic 'underscreened' ground state — on coupling to the lead the spin-1 impurity is only partially screened, leaving a state with a residual spin $\frac{1}{2}$ and a ground state which is not a Fermi liquid. High spin states may be generated in a quantum dot device if multiple dot energy levels are 'active', *i.e.* the levels do not fill sequentially. For example a two-electron triplet state might be stabilized by an interlevel Hund's rule exchange coupling [41, 42]. This state has been observed experimentally in quantum dots containing an even number of electrons in a variety of semiconductor devices [43–47] as well as in a single-molecule quantum dots [5, 7, 48]. The spin-1 Kondo effect leads, as does the spin-$\frac{1}{2}$ effect, to an enhancement of the zero-bias conductance of the device [49, 50] — the 'zero-bias anomaly'.

Much important theoretical work on multilevel Anderson models and spin-1 Kondo models has ensued, both in the one-channel case [49, 51–58] where only a single conduction band channel couples to the impurity leading to an underscreened (USC) state as described above, and the two-channel case [49, 50, 55, 59–62] where the spin-1 moment is screened successively by the two channels leading to a non-magnetic state. In a two-level Anderson model both the spin-1 and spin-$\frac{1}{2}$ Kondo effects can be observed. In the single-channel case therefore, a phase transition naturally occurs between the USC state and the Fermi liquid state associated with the spin-$\frac{1}{2}$ Kondo effect, as a function of the level energies. This too has been studied quite extensively [51–54, 56, 57, 59–62]. However the large majority of previous work on this 'singlet-triplet' transition has focused on a somewhat particular case — the middle of the two-electron Coulomb-blockade valley, where throughout both phases the impurity charge remains close to two. This is not a generic condition under which experiments on quantum dots are performed. Several efforts [56, 61, 63] have been made to understand systems with two impurity levels away from this limit but a complete understanding is still missing. Similarly, ambiguities in the explanation of experimental results are apparent; experiments have been explained in terms of

[3] The spinon approximation [33] allows only approximate correlation functions to be calculated within the Bethe ansatz.

simple models entirely inappropriate to the many-body nature of the systems in question.

Our aim in this thesis is to develop a deeper understanding of experimental results regarding the properties of quantum dots which appear to have more than a single active dot energy level. In chapter 2 we review more thoroughly both the AIM and Kondo models; examining the relationship between the two models and Anderson's poor man's scaling approach. Strong on-site Coulomb repulsion is seen to be key to observing the Kondo effect. This background material is important to understanding our later work. We then move to create realistic quantum impurity models appropriate to both single-molecule and semiconductor quantum dot devices, uncovering the most relevant, most important, interactions required in such models. We define the model used throughout this thesis: a simple two-level model (2LM).

In chapter 3 we outline in some detail Wilson's numerical renormalization group. We explain the single approximation made within the approach and the logarithmic discretization upon which the technique is founded. We expound the NRG in terms of both a numerical technique for diagonalizing large Hamiltonians and as a framework for explaining the underlying physics of impurity models. As the NRG essentially obtains a solution to the eigenvalue problem, both the thermodynamic and dynamic properties of the systems of interest can be calculated by application of basic results in statistical physics and thermodynamics. Towards the end of the chapter we present in some detail the necessary machinery for the accurate calculation of dynamic properties and how results from the NRG may be further used to calculate the zero-bias conductance of quantum dot devices. We introduce also a simple, pragmatic approximation for calculating the non-equilibrium conductance.

Chapter 4 surveys the thermodynamic properties of the 2LM for arbitrary impurity occupation. We start by examining the so-called renormalization group fixed points of the AIM and the 2LM. We go on to derive an effective low-energy model for the 2LM in order to rationalise intuitively the physics observed. Our focus is naturally on the spin-1 Kondo effect arising in the model and, the associated USC phase and transition to it from the normal FL phase. We examine how various on-site interactions affect the stability of the USC phase, elucidating under what conditions it is expected to arise in experimental setups.

In chapter 5 we go on to study the dynamic properties of the 2LM through the impurity Green functions and associated spectral densities. The aim is not only to reach an understanding of the observed electrical conductivity of quantum dot devices but also to examine theoretically various aspects of the impurity dynamics when a transition to the USC state is made. We introduce a 'Friedel-Luttinger sum rule' relating the static impurity phase shift to the impurity occupation and the so-called Luttinger integral. Some interesting insights and hypotheses are made in this area.

Finally in chapter 6 we present and examine critically a number of results falling under the umbrella of magnetic field effects in both single and two-level quantum dots. In the latter, the magnetic USC phase is naturally destroyed on application of a field and no phase transition is observed; the ground state becomes a Fermi liquid regardless of the interaction parameters or level energies. To illustrate the improved numerical techniques used in this thesis, we show that in both models the NRG recovers exact Bethe Ansatz results for the impurity magnetization as a function of field. Following this we focus primarily on the magnitude of the Kondo peak splitting in the equilibrium spectra density, which has been studied previously by a number of techniques, yielding contradictory results. We try to address this issue with very accurate NRG calculations.

We finish with a short summary in chapter 7. We mention that much of the work of chapters 4 and 5 has appeared in ref. [64], whilst the work of chapter 6 has been submitted for publication [65].

CHAPTER 2

Quantum Impurity Models

In this chapter we introduce briefly the models used to describe simple quantum impurities, for a review see ref. [20]. We illustrate their low-energy behaviour and introduce the ideas of scaling and universality in such systems. We then work towards more realistic models for describing more complex systems such as molecular junctions and semiconductor devices with more than one 'active' level, ultimately arriving at the model we use throughout the rest of this thesis: the two-level model (2LM).

Simple metals, *i.e.* those with broad conduction bands derived from atomic s and p states, contain electrons which move in a periodic potential and can be assumed to behave essentially independently. The long-range Coulomb interaction is screened such that the electrons can be replaced by non-interacting quasi-particles: electrons 'dressed' by their screening cloud. This can of course be shown formally by the hugely successful Fermi liquid theory of Landau [20, 66]. The resulting one-particle Hamiltonian used to describe such a system is simply:

$$\hat{H} = \sum_{\mathbf{k}\sigma} \epsilon_{\mathbf{k}} c^{\dagger}_{\mathbf{k}\sigma} c_{\mathbf{k}\sigma}, \tag{2.1}$$

where the operators $c^{\dagger}_{\mathbf{k}\sigma}$ and $c_{\mathbf{k}\sigma}$ create and destroy particles in Bloch states with wavevector $\mathbf{k}$, energy $\epsilon_{\mathbf{k}}$, and spin σ. These fermion operators obey the standard anticommutation relations:

$$[c^{\dagger}_{\mathbf{k}\sigma}, c_{\mathbf{k}'\sigma'}]_+ = \delta_{\mathbf{k}\mathbf{k}'}\delta_{\sigma\sigma'} \qquad [c_{\mathbf{k}\sigma}, c_{\mathbf{k}'\sigma'}]_+ = 0. \tag{2.2}$$

The conduction band can be characterised solely by a density of states $\rho(\epsilon) = \sum_{\mathbf{k}} \delta(\epsilon - \epsilon_{\mathbf{k}})$. A free conduction band is then, on its own, a rather simple object. When an impurity is placed in the bulk, such as a heteroatom in a silicon lattice, the situation can quickly become rather more complex, as we now show.

2.1 The Anderson impurity model

Introducing an impurity into the bulk metal has the effect of introducing an effective potential $V_{\text{imp}}(\mathbf{r})$ from which the conduction electrons will scatter. The correct Hamiltonian will then be [20]

$$\hat{H} = \sum_{\mathbf{k}\sigma} \epsilon_{\mathbf{k}} c^{\dagger}_{\mathbf{k}\sigma} c_{\mathbf{k}\sigma} + \sum_{\mathbf{k}\mathbf{k}'\sigma} V_{\mathbf{k}\mathbf{k}'} c^{\dagger}_{\mathbf{k}\sigma} c_{\mathbf{k}'\sigma}, \tag{2.3}$$

with $V_{\mathbf{k}\mathbf{k}'} = \langle \mathbf{k} | V_{\text{imp}} | \mathbf{k}' \rangle$. Such a potential, if relatively weak, has only the simple consequence of leading to characteristic Friedel oscillations [67] in the conduction band density of states. However if the potential is rather more strong it will lead to the formation of virtual bound states: states where conduction electrons tend to localize around the impurity for an extended period of time.

In his seminal work [21], Anderson outlined the case for considering a solute atom in a bulk metal as an isolated local impurity. He gave a rather simple rationale for this claim. The conduction band states of the bulk metal are largely of s and p symmetry whilst for a transition metal impurity atom the valence electrons will be in the d-shell. These valence electrons therefore have little overlap with conduction band states and do not mix with them.

With these insights, one can write down a Hamiltonian for the full system. The Anderson impurity model (AIM) is given by [21]:

$$\begin{aligned} \hat{H}^{\text{AIM}} &= \hat{H}_{\text{L}} + \hat{H}_{\text{D}} + \hat{H}_{\text{T}} \\ &= \sum_{\mathbf{k}\sigma} \epsilon_{\mathbf{k}} c^{\dagger}_{\mathbf{k}\sigma} c_{\mathbf{k}\sigma} + \sum_{\sigma} \left[\epsilon_{i\sigma} \hat{n}_{i\sigma} + \tfrac{1}{2} U \hat{n}_{i\uparrow} \hat{n}_{i\downarrow} \right] + \sum_{\mathbf{k}\sigma} V_{i\mathbf{k}} \left[d^{\dagger}_{i\sigma} c_{\mathbf{k}\sigma} + c^{\dagger}_{\mathbf{k}\sigma} d_{i\sigma} \right]. \end{aligned} \tag{2.4}$$

Here the operators $d^{\dagger}_{i\sigma}$ and $d_{i\sigma}$ create and destroy σ-spin electrons on the impurity level i; $\hat{n}_{i\sigma} = d^{\dagger}_{i\sigma} d_{i\sigma}$ is the electron counting operator. The first term $\hat{H}_{\text{L}}$ is the same free electron (or lead) Hamiltonian as before. It is often assumed that the conduction band has a constant density of states ρ and is symmetric about the Fermi level ϵ_f with sharp cutoffs at $\epsilon = \pm D$, see fig. 2.1. $\hat{H}_{\text{D}}$ describes the impurity (or dot) with a single level i. Electrons occupying this level gain a spin-dependent energy ϵ_i. At most two electrons can occupy the impurity, with a Coulomb repulsion energy U associated with double occupancy. The final term $\hat{H}_{\text{T}}$ describes the coupling of the impurity to the host with matrix element $V_{i\mathbf{k}}$, and renders the Hamiltonian rather difficult to solve.

We can make some progress in solving the AIM by considering the case $V_{i\mathbf{k}} = 0$, the 'atomic limit'. The impurity is now isolated from the conduction band. There are a total of four impurity states as depicted in fig. 2.1b)–d). The first state is the empty state and has no electrons present on the impurity. It has an energy $E_0 = 0$.

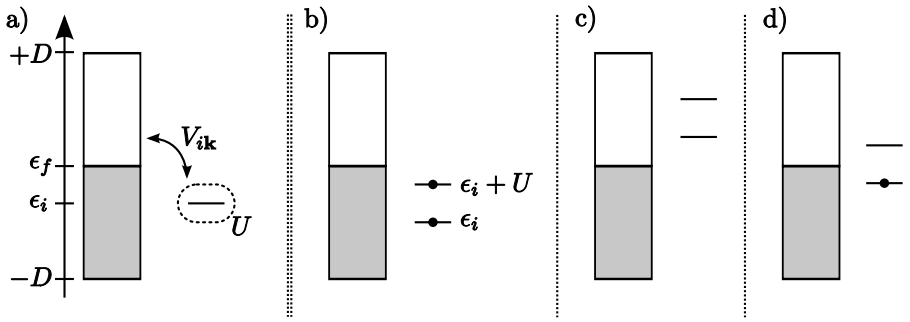

Figure 2.1: a) The Anderson impurity model (AIM). A local impurity level couples to a free electron conduction band via matrix elements $V_{i\mathbf{k}}$. b)–d) The atomic limit states of the impurity are represented by two levels at energy ϵ_i and $\epsilon_i + U$, each of which can hold a single electron. Circles show the filling of the levels in the three possible cases. Case d) indicates the possibility of local moment formation.

The impurity can be singly occupied with either a $\sigma =\uparrow$ or $\sigma =\downarrow$ electron. These states are degenerate for $\epsilon_{i\uparrow} = \epsilon_{i\downarrow} = \epsilon_i$ and have energy $E_1 = \epsilon_i$. Finally the doubly occupied state with both a $\sigma =\uparrow$ and a $\sigma =\downarrow$ electron has energy $E_2 = 2\epsilon_i + U$.

It is clear that if ϵ_i and U are such that the singly-occupied states form a doubly-degenerate ground state, corresponding to a spin $\frac{1}{2}$, the impurity will behave as a local magnetic moment giving rise to a Curie Law susceptibility. What are the conditions for this to occur? The level energy ϵ_i must be below the Fermi level ϵ_f of the conduction band (which we take to be our zero of energy) such that it is favourable to add an electron to the impurity. It must also be the case that $\epsilon_i + U$ is above the Fermi level, so that it is unfavourable to add a second electron.

This local moment will undoubtedly be affected for the case $V_{i\mathbf{k}} \neq 0$ when the impurity states are mixed. However as we now show the local moment remains provided the $V_{i\mathbf{k}}$ are 'sufficiently small'.

2.2 Schrieffer-Wolff transformation and the Kondo model

As we have seen the AIM admits the possibility of forming a local moment ground state in the atomic limit [20, 21]. The so-called Kondo model assumes the impurity to be a pure spin from the outset; coupling to the conduction band is modelled as a Heisenberg exchange interaction. The relation between the AIM and the Kondo model can be obtained by second order perturbation theory (in $V_{i\mathbf{k}}$) about the atomic limit: a Schrieffer-Wolff transformation [20, 68]. After sketching this transformation below we outline several key results for the Kondo model, which can also be ascribed to the AIM at low energies.

We suppose that the full Hamiltonian for a system can be decomposed as

$$\hat{H} = \hat{H}_0 + \lambda \hat{H}_1 \tag{2.5}$$

where the eigenvectors and eigenvalues of $\hat{H}_0$ are known. By assuming that these states can be assigned to several manifolds at different characteristic energy scales *i.e.* that

$$|E_{i\alpha} - E_{j\alpha}| \ll |E_{i\beta} - E_{i\alpha}| \qquad \text{if } \beta \neq \alpha, \tag{2.6}$$

where $E_{i\alpha}$ is the ith level of the lowest energy manifold α, one can show [69] that the effective Hamiltonian $\hat{H}_{\text{eff}}$ projected into the lowest manifold is given by:

$$\begin{aligned}\hat{H}_{\text{eff}} &= \hat{P}_\alpha \hat{H}_0 \hat{P}_\alpha + \lambda \hat{P}_\alpha \hat{H}_1 \hat{P}_\alpha \\ &+ \tfrac{1}{2}\lambda^2 \sum_{\substack{i,j,k \\ \gamma\neq\alpha}} |i,\alpha\rangle\langle i,\alpha|\hat{H}_1|k,\gamma\rangle\langle k,\gamma|\hat{H}_1|j,\alpha\rangle\langle j,\alpha| \left(\frac{1}{E_{i\alpha} - E_{k\gamma}} - \frac{1}{E_{k\gamma} - E_{j\alpha}}\right).\end{aligned} \tag{2.7}$$

The projection operator $\hat{P}_\alpha = \sum_i |i,\alpha\rangle\langle i,\alpha|$ projects to the states of manifold α. For the AIM we assign the singly-occupied impurity states (together with the disconnected conduction band) to the ground state manifold, while the empty and full states form the excited states. The unperturbed Hamiltonian is thereby

$$\hat{H}_0 = \sum_{\mathbf{k}\sigma} \epsilon_{\mathbf{k}} c^\dagger_{\mathbf{k}\sigma} c_{\mathbf{k}\sigma} + \sum_\sigma \left[\epsilon_{i\sigma}\hat{n}_{i\sigma} + \tfrac{1}{2}U\hat{n}_{i\uparrow}\hat{n}_{i\downarrow}\right], \tag{2.8}$$

whilst the peturbing Hamiltonian is $\hat{H}_{\text{T}}$ with $\lambda \equiv V_{i\mathbf{k}}$:

$$\hat{H}_1 = \sum_{\mathbf{k}\sigma} \left[d^\dagger_{i\sigma} c_{\mathbf{k}\sigma} + c^\dagger_{\mathbf{k}\sigma} d_{i\sigma}\right]. \tag{2.9}$$

We set $V_{i\mathbf{k}} = V$ and neglect the contributions to $E_{k\gamma}$ arising from the conduction band electrons. This approximation is valid provided [20] $|\epsilon_{\mathbf{k}}| \ll |\epsilon_i - \epsilon_f|$.

The zeroth-order term in (2.7) simply gives the singly-occupied ground state manifold, a constant factor which we can neglect. The first-order term is also uninteresting. The Hamiltonian $\hat{H}_1$ creates excitations from the ground state manifold to the excited states, it does not connect states within the ground state manifold: the projection operators therefore render this term zero. The second-order term however is interesting. By calculating the appropriate matrix elements, it is relatively straightforward to show that [20]:

$$\begin{aligned}\hat{H}_{\text{eff}} = V^2 &\left(\frac{1}{\epsilon_i + U} - \frac{1}{\epsilon_i}\right) \sum_{\mathbf{k},\mathbf{k}'} \hat{S}^z (c^\dagger_{\mathbf{k}\uparrow} c_{\mathbf{k}'\uparrow} - c^\dagger_{\mathbf{k}\downarrow} c_{\mathbf{k}'\downarrow}) + \hat{S}^+ c^\dagger_{\mathbf{k}\downarrow} c_{\mathbf{k}'\uparrow} + \hat{S}^- c^\dagger_{\mathbf{k}\uparrow} c_{\mathbf{k}'\downarrow} \\ &- \tfrac{1}{2}V^2 \left(\frac{1}{\epsilon_i + U} + \frac{1}{\epsilon_i}\right) \sum_{\mathbf{k},\mathbf{k}',\sigma} c^\dagger_{\mathbf{k}\sigma} c_{\mathbf{k}'\sigma} + \sum_{\mathbf{k}\sigma} \epsilon_{\mathbf{k}} c^\dagger_{\mathbf{k}\sigma} c_{\mathbf{k}\sigma},\end{aligned} \tag{2.10}$$

where $\hat{S}^z = \frac{1}{2}(|\uparrow\rangle\langle\uparrow| - |\downarrow\rangle\langle\downarrow|)$, $\hat{S}^+ = |\uparrow\rangle\langle\downarrow|$ and $\hat{S}^- = |\downarrow\rangle\langle\uparrow|$ define a spin-$\frac{1}{2}$ operator $\hat{\mathbf{S}}$ for the impurity. Thus the first term couples the impurity spin to the conduction band whilst the second term accounts for potential scattering. If

$\epsilon_i = -U/2$, then the AIM Hamiltonian is particle-hole symmetric and the potential scattering term becomes zero. Equation (2.10) can be written in a more compact way by defining the conduction band spin density at the impurity:

$$\hat{\mathbf{s}}_0 = \sum_{\sigma,\sigma'} f^\dagger_{0\sigma} \sigma_{\sigma\sigma'} f_{0\sigma'} \tag{2.11a}$$

$$f^\dagger_{0\sigma} = \frac{1}{\sqrt{N}} \sum_{\mathbf{k}} c^\dagger_{\mathbf{k}\sigma} \tag{2.11b}$$

with $\sigma_{\sigma\sigma'}$ the vector of Pauli matrices and N the total number of band states. The operator $f^\dagger_{0\sigma}$ then describes a conduction orbital which contains the total band-to-impurity coupling (this orbital will reappear in chapter 3). By further defining $J_K = 2NV^2\left(\frac{1}{\epsilon_i+U} - \frac{1}{\epsilon_i}\right)$ and $K = -\frac{1}{2}NV^2\left(\frac{1}{\epsilon_i+U} + \frac{1}{\epsilon_i}\right)$, a particularly simple recasting of (2.10) is:

$$\hat{H}_{\text{eff}} = \hat{H}_{\text{L}} + J_K \hat{\mathbf{S}} \cdot \hat{\mathbf{s}}_0 + K f^\dagger_{0\sigma} f_{0\sigma}. \tag{2.12}$$

This is the Kondo model with potential scattering [20, 28]. An important result is that the Kondo coupling J_K is antiferromagnetic such that the impurity and $f^\dagger_{0\sigma}$ orbital will tend to form a singlet at low energies. It is usual to write the parameters J_K and K in terms of the asymmetry $\eta = 1 + 2\epsilon/U$, viz:

$$J_K = \frac{8NV^2}{U}\frac{1}{1-\eta^2} \tag{2.13a}$$

$$K = \frac{2NV^2}{U}\frac{\eta}{1-\eta^2}. \tag{2.13b}$$

At the particle-hole symmetric point ($\eta = 0$) the potential scattering strength is zero. Away from particle-hole symmetry the potential scattering is non-zero but, from (2.13) it follows that $K/J_K = \eta/4$ and hence for fixed η the model is characterised by the single parameter J_K. Finally by defining the hybridization strength $\Gamma = \pi\rho_0 NV^2$, with ρ_0 the density of states *per* conduction band orbital ($\rho = \rho_0 N$ being the *total* density of states), the relationship between the AIM and Kondo model can be characterised by the dimensionless parameter U/Γ. At particle-hole symmetry it is therefore usual to write

$$\rho_0 J_K = \frac{8\Gamma}{\pi U}. \tag{2.14}$$

The Kondo model is thus a low-energy effective model of the full AIM. For large U/Γ, the empty and full impurity states can be neglected. The resulting ground state can be thought of as a spin $\frac{1}{2}$ coupled to the conduction band via antiferromagnetic Heisenberg exchange. The low-energy behaviour of the Kondo model cannot however be accessed by straightforward perturbation theory in the exchange coupling. In the next section we examine the Kondo model in more detail to obtain some fundamental results which guide the study of quantum impurities.

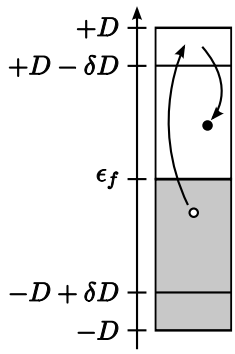

Figure 2.2: Division of the conduction band states used to perform poor man's scaling [20, 29]. Virtual excitations from the central bulk region to the band edges are treated as a perturbation. One can shrink progressively the conduction band; the Kondo Hamiltonian is self-similar under such a transformation.

2.2.1 Poor man's scaling: the scaling invariant

In the previous section we have used second-order perturbation theory to eliminate excitations from the singly occupied ground state manifold of the AIM. The result was the Kondo model where these excitations are encompassed within the exchange coupling of the impurity to the conduction band. As Anderson showed [29], this idea can be taken further by eliminating virtual excitations of particles to conduction band states far from the Fermi surface. It is this 'poor man's scaling' which we now pursue. Again our focus is to elucidate general concepts which we use in later chapters rather than fully derive the specific results. Our focus here is the emergence of a universal low-energy scale, the Kondo scale, which fully characterises seemingly distinct physical systems.

To start we assume a flat symmetric density of states in the conduction band as in fig. 2.1. Anderson's key idea was then to impose a cutoff energy on the density of states at the upper band edge of $E_c = D - \delta D$ and at the lower band edge of $-E_c = -D + \delta D$, thereby shrinking the conduction band (fig. 2.2). States near E_c are not highly occupied in the ground state and so with δD arbitrarily small it is rigorous to study states with few or no excited electrons in the regions $D > |\epsilon_{\mathbf{k}}| > E_c$.

The above division of the conduction band allows one to recast the Kondo Hamiltonian with bandwidth $2D$ by considering scattering to the band edges as a perturbation to a new Hamiltonian with a reduced bandwidth $2(D - \delta D)$. As with the Schrieffer-Wolff transformation of the previous section, (2.7) can be used to calculate the new effective Hamiltonian: H_0 and H_1 will both be Kondo Hamiltonians of the form of (2.10) but with conduction bands as described above. The second order terms are again the most interesting: they scatter electrons from the bulk to the band edges and back into the bulk. The terms which arise are illustrated diagrammatically in fig. 2.3. In each case the horizontal line represents the state

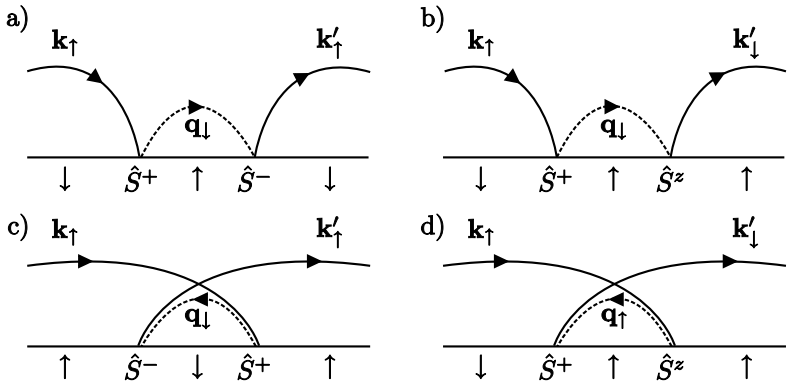

Figure 2.3: Second order diagrams for poor man's scaling. a) A particle scatters from the bulk to the band edge and back. b) Spin flip scattering of a particle. c) and d) Analogous diagrams for hole scattering.

of the impurity whilst the incoming lines illustrate band states. The dashed lines correspond to the virtual excitations which are being eliminated in the perturbative process.

Rather interestingly, evaluating these diagrams [29] one finds an effective Hamiltonian with precisely the form of the original Kondo Hamiltonian but with not only the reduced bandwidth we have imposed but also a renormalized coupling. We have achieved the transformation:

$$\hat{H}_K(J_K; 2D) \rightarrow \hat{H}_K(J_K + \delta J_K; 2(D - \delta D)), \tag{2.15}$$

with the change in the coupling given explicitly by [20, 29]:

$$\delta J_K = \rho_0 J_K^2 \frac{\delta D}{D}. \tag{2.16}$$

Clearly one can repeat the procedure: reduce the bandwidth, eliminate virtual excitations to the band edges and obtain a new effective Hamiltonian with a further reduced bandwidth and modified coupling. A differential equation can thereby be formed describing a 'scaling trajectory':

$$\frac{dJ_K}{d\ln D} = -\rho_0 J_K^2, \tag{2.17}$$

which can be integrated from an initial bandwidth D and coupling J_K to a final bandwidth $\tilde{D}$ and coupling $\tilde{J}_K$. The resulting 'scaling invariant'

$$D\exp(-1/\rho_0 J_K) = \tilde{D}\exp(-1/\rho_0 \tilde{J}_K) = T_K \tag{2.18}$$

is the Kondo scale or temperature. It is possible to extend the above calculation to

third order to obtain a better estimate of the scaling invariant. The scaling equation becomes:

$$\frac{dJ_K}{d\ln D} = -\rho_0 J_K^2 + \tfrac{1}{2}\rho_0^2 J_K^3, \tag{2.19}$$

which can again be integrated to give

$$\frac{T_K}{D} = \sqrt{\rho_0 J_K}\exp(-1/\rho_0 J_K). \tag{2.20}$$

An immediate consequence of the above is that two systems with different initial, or bare, bandwidth and couplings, D and J_K, can lie on the same scaling trajectory and therefore possess the same Kondo temperature.

There is a second, although related, consequence of the Kondo temperature [20]. Decreasing the bandwidth can be seen as decreasing the temperature: excitations of particles to the band edge are curtailed. On lowering the temperature, the effect of such processes on the low-energy physics is incorporated into a renormalized coupling. Thus all properties of a system, *e.g.* the spin susceptibility, depend universally on a single parameter, T_K, at low energies. Systems with different Kondo scales also behave identically when their temperature-dependent properties are rescaled in terms of their individual scales.

Finally, from *e.g.* (2.16) it is seen that as the (effective) bandwidth is reduced, the coupling increases. There are then only two possibilities in the $D \to 0$ limit.[1] Either, the bare coupling is precisely zero and the effective coupling remains so under scaling. Or, the bare coupling is non-zero in which case $J_K \to \infty$ under renormalization. These two possibilities constitute so-called 'fixed points' of the Kondo Hamiltonian.

The $J_K = 0$ 'local moment' fixed point describes a system where the impurity is decoupled from the conduction band. The impurity spin remains free as in the atomic limit of the AIM. By contrast the 'strong coupling' fixed point, arising for any finite bare J_K, describes a system where the impurity forms a singlet state with the lead electrons at low energies. The impurity spin is said to be screened by the itinerant electrons.

The results above have been obtained perturbatively assuming $\rho_0 J_K$ to be a small parameter. As J_K increases the analysis naturally breaks down and we cannot say anything about the properties of the system for $T < T_K$. We can only postulate that the strong coupling fixed point correctly describes system with finite J_K as $T \to 0$. Whilst this approach illustrates important results, namely that the Kondo Hamiltonian gives rise to scaling between energy scales, an inherently non-perturbative method is required to correctly access the $T = 0$ properties of the system. Such an approach is discussed in the next chapter, but first we seek to obtain a more realistic model suitable for describing quantum dot devices.

[1] We discount the possibility of $J_K < 0$ as (2.14) shows us that $J_K \geq 0$.

2.3 Kondo effects in quantum dots

Thus far we have considered only quantum impurities with a single active level. In this section we aim to develop and rationalise the model which we will study throughout the course of this thesis.

We take initially a different starting point than the previous section. Rather than considering the problem of a metal impurity ion in bulk metal, we shall consider a molecule attached to two non-interacting metallic leads — a molecular quantum dot. Not only is such a situation experimentally realisable [70–72], but a suitable model for it can be shown to be analogous to a model one might write down to describe gate-defined semi-conductor quantum dots. The interesting low-energy physics of the two systems are universal: we can study the problems simultaneously.

2.3.1 Toward a realistic model for quantum dot devices

A molecular quantum dot might conceivably be formed by 'attaching' metallic leads to two atoms or chemical groups of the molecule. We will not concern ourselves with how this attachment is made. For simplicity we will assume that a single atom couples to each lead with $\mathbf{k}$-dependent matrix elements $V_{i\mathbf{k}}^{L/R}$. Further we will assume each atom in the molecule provides one active atomic orbital (AO) to the molecular electronic structure. This assumption is not necessary, although it makes the following notationally simpler. Figure 2.4a) depicts this situation and the Hamiltonian is given explicitly by:

$$\hat{H} = \hat{H}_{\mathrm{L}} + \hat{H}_{\mathrm{M}}^{0} + \hat{H}_{\mathrm{I}} + \hat{H}_{\mathrm{T}} \tag{2.21a}$$

$$\hat{H}_{\mathrm{L}} = \sum_{\substack{\mathbf{k}\in L\\ \sigma}} \epsilon_{\mathbf{k}}^{L} c_{\mathbf{k}L\sigma}^{\dagger} c_{\mathbf{k}L\sigma} + \sum_{\substack{\mathbf{k}\in R\\ \sigma}} \epsilon_{\mathbf{k}}^{R} c_{\mathbf{k}R\sigma}^{\dagger} c_{\mathbf{k}R\sigma} \tag{2.21b}$$

$$\hat{H}_{\mathrm{M}}^{0} = \sum_{\substack{i=1\\ \sigma}}^{N} \epsilon_i d_{i\sigma}^{\dagger} d_{i\sigma} + \sum_{\substack{i\neq j\\ \sigma}} t_{ij} d_{i\sigma}^{\dagger} d_{j\sigma} \tag{2.21c}$$

$$\hat{H}_{\mathrm{I}} = \tfrac{1}{2} \sum_{\substack{i,j,k,l\\ \sigma\sigma'}} V_{ijkl}^{\sigma\sigma'\sigma\sigma'} d_{j\sigma'}^{\dagger} d_{i\sigma}^{\dagger} d_{k\sigma'} d_{l\sigma} \tag{2.21d}$$

$$\hat{H}_{\mathrm{T}} = \sum_{\substack{\mathbf{k}\in L\\ \sigma}} V_{1\mathbf{k}}^{L} \left(d_{1\sigma}^{\dagger} c_{\mathbf{k}L\sigma} + c_{\mathbf{k}L\sigma}^{\dagger} d_{1\sigma} \right) + \sum_{\substack{\mathbf{k}\in R\\ \sigma}} V_{\mathrm{N}\mathbf{k}}^{R} \left(d_{\mathrm{N}\sigma}^{\dagger} c_{\mathbf{k}R\sigma} + c_{\mathbf{k}R\sigma}^{\dagger} d_{\mathrm{N}\sigma} \right), \tag{2.21e}$$

with $\hat{H}_{\mathrm{L}}$ describing the leads coupled via $\hat{H}_{\mathrm{T}}$ to the atomic sites 1 and N. We have decomposed the molecular term into two parts. The non-interacting $\hat{H}_{\mathrm{M}}^{0}$ contains the bare level energies and a nearest-neighbour hopping t_{ij} of the orthonormal AOs, the remainder being the interaction term $\hat{H}_{\mathrm{I}}$. The complexity of the latter is hidden

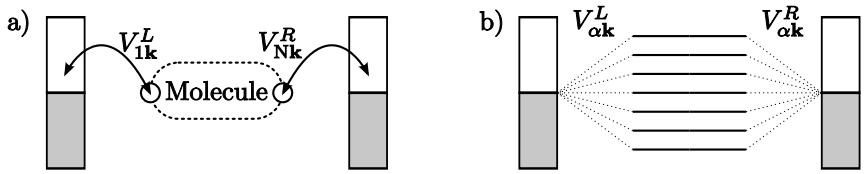

Figure 2.4: a) A molecular quantum dot. The molecule couples to a left (L) and right (R) metallic lead at two single atomic sites $i = 1$ and $i = N$ via couplings $V^L_{1\mathbf{k}}$ and $V^R_{N\mathbf{k}}$ respectively. b) an equivalent representation in a molecular orbital (MO) basis: in general all MOs couple to both leads.

in the matrix elements $V^{\sigma\sigma'\sigma\sigma'}_{ijkl}$ given in general by:

$$V^{\sigma\sigma'\sigma\sigma'}_{ijkl} = \int\int \psi^*_{i\sigma}(\mathbf{r})\psi^*_{j\sigma'}(\mathbf{r}')\frac{e^2}{4\pi\epsilon_0|\mathbf{r}-\mathbf{r}'|}\psi_{k\sigma}(\mathbf{r})\psi_{l\sigma'}(\mathbf{r}')\mathrm{d}\mathbf{r}\mathrm{d}\mathbf{r}', \tag{2.22}$$

where the $\psi_{i\sigma}(\mathbf{r})$ are the one-particle atomic wavefunctions. Naturally one might retain only some of these terms such as the on-site Hubbard interaction $U_i = V^{\sigma\sigma'\sigma\sigma'}_{iiii}$. We will later identify which of these interactions are important for successfully describing quantum dots with a minimal model *i.e.* which $V^{\sigma\sigma'\sigma\sigma'}_{ijkl}$ can be discarded without qualitatively altering the basic physics of the model.

The non-interacting molecular Hamiltonian of (2.21c) can be trivially diagonalized into a molecular orbital (MO) basis by taking appropriate linear combinations of the AOs *viz.*:

$$A^\dagger_{\alpha\sigma} = \sum_i a_{i\alpha} d^\dagger_{i\sigma} \tag{2.23a}$$

$$d^\dagger_{i\sigma} = \sum_\alpha a^*_{i\alpha} A^\dagger_{\alpha\sigma}. \tag{2.23b}$$

The non-interacting Hamiltonian (2.21c) is then:

$$\hat{H}^0_{\mathrm{M}} = \sum_{\alpha\sigma} E_\alpha A^\dagger_{\alpha\sigma} A_{\alpha\sigma}, \tag{2.24}$$

where we have set the Fermi level ϵ_f to be the zero of energy. The lead-molecule coupling becomes

$$\hat{H}_{\mathrm{T}} = \sum_{\alpha\sigma}\left[\sum_{\mathbf{k}\in L} V^L_{\alpha\mathbf{k}}\left(A^\dagger_{\alpha\sigma}c_{\mathbf{k}L\sigma} + h.c.\right) + \sum_{\mathbf{k}\in R} V^R_{\alpha\mathbf{k}}\left(A^\dagger_{\alpha\sigma}c_{\mathbf{k}R\sigma} + h.c.\right)\right] \tag{2.25}$$

with the new couplings given by:

$$\begin{aligned} V^L_{\alpha\mathbf{k}} &= a^*_{1\alpha}V^L_{1\mathbf{k}} = \langle\alpha|\hat{V}_L|\mathbf{k}_L\rangle \\ V^R_{\alpha\mathbf{k}} &= a^*_{\mathrm{N}\alpha}V^R_{\mathrm{N}\mathbf{k}} = \langle\alpha|\hat{V}_R|\mathbf{k}_R\rangle \end{aligned} \tag{2.26}$$

We have thereby achieved a transformation to the new Hamiltonian represented in fig. 2.4b): a set of MOs coupled in parallel to the two metallic leads. This is what we might naturally write down for a gate-defined semiconductor quantum dot: a spectrum of particle-in-a-box-like states all of which have some non-zero coupling to the lead states. In dealing with molecular quantum dots, the details of the molecular structure are largely irrelevant. The couplings of (2.26) depend on the expansion coefficients in (2.23), however the general calculation of these is the realm of quantum chemistry and will not concern us here; the $V_{\alpha\mathbf{k}}^{L/R}$ will enter as parameters in our final model. It is nevertheless important to determine how the interaction term $\hat{H}_{\mathrm{I}}$ transforms under the change of basis, we consider this now.

2.3.2 Interactions in the molecular basis

The aim of this section is to identify which of the interactions in (2.21d) play an important role in determining the physical behaviour of quantum dots. Having done so we will be able to construct a minimal model applicable to the study of both single molecule and semiconductor quantum dots.

By using the operators defined in (2.23) the interaction Hamiltonian of (2.21d) can be rewritten as:

$$\hat{H}_{\mathrm{I}} = \tfrac{1}{2} \sum_{\substack{\alpha\beta\gamma\delta \\ \sigma\sigma'}} U_{\alpha\beta\gamma\delta} A^{\dagger}_{\beta\sigma'} A^{\dagger}_{\alpha\sigma} A_{\gamma\sigma} A_{\delta\sigma'}, \tag{2.27}$$

with

$$U_{\alpha\beta\gamma\delta} = \sum_{ijkl} a^{*}_{i\alpha} a^{*}_{j\beta} a_{k\gamma} a_{l\delta} V^{\sigma\sigma'\sigma\sigma'}_{ijkl} \tag{2.28}$$

a pure number. There are various classes of term which arise in (2.27) depending on the choice of the labels α, β, γ and δ which can be summarised as:

- $\underline{\alpha = \beta = \gamma = \delta}$, the interaction involves only a single MO. This is the on-site Coulomb term:
$$\hat{H}_1 = \tfrac{1}{2} \sum_{\alpha\sigma} U_{\alpha\alpha\alpha\alpha} \hat{n}_{\alpha\sigma} \hat{n}_{\alpha-\sigma} \tag{2.29}$$

- $\underline{\gamma = \alpha,\ \delta = \beta}$, the interaction involves 'two pairs' of indices for two distinct levels, an intersite Coulomb term:
$$\hat{H}_{2\mathrm{a}} = \tfrac{1}{2} \sum_{\alpha\neq\beta} U_{\alpha\beta\alpha\beta} \hat{n}_{\alpha} \hat{n}_{\beta} \tag{2.30}$$

- $\underline{\gamma = \beta,\ \delta = \alpha}$, again two pairs of indices, an intersite Coulomb term with spin

exchange (particle-hole pairing):

$$\hat{H}_{2b} = \tfrac{1}{2}\sum_{\alpha\neq\beta} U_{\alpha\beta\beta\alpha}(-\tfrac{1}{2}\hat{n}_\alpha\hat{n}_\beta - 2\hat{\mathbf{s}}_\alpha\cdot\hat{\mathbf{s}}_\beta) \tag{2.31}$$

- $\underline{\beta=\alpha,\ \delta=\gamma}$, the final possibility of two pairs/two levels, a charge pairing interaction:

$$\hat{H}_{2c} = \tfrac{1}{2}\sum_{\alpha\neq\beta,\sigma} U_{\alpha\alpha\beta\beta}A^\dagger_{\alpha-\sigma}A^\dagger_{\alpha\sigma}A_{\beta-\sigma}A_{\beta\sigma} \tag{2.32}$$

- $\underline{\alpha=\gamma=\delta\neq\beta}$ *etc.*, involving 2 distinct levels, giving rise to a correlated hopping term:

$$\hat{H}_{2d} = \sum_{\alpha\neq\beta,\sigma} U_{\alpha\beta\alpha\alpha}(A^\dagger_{\beta-\sigma}A_{\alpha-\sigma} + A^\dagger_{\alpha-\sigma}A_{\beta-\sigma})\hat{n}_{\alpha\sigma} \tag{2.33}$$

- $\underline{\alpha\neq\beta\neq\gamma=\delta}$ *etc.*, involving three distinct levels:

$$\begin{aligned}\hat{H}_3 = {} & \tfrac{1}{2}{\sum_{\alpha\beta\gamma}}'\sum_\sigma U_{\alpha\alpha\beta\gamma}(A^\dagger_{\alpha-\sigma}A^\dagger_{\alpha\sigma}A_{\beta\sigma}A_{\gamma-\sigma} + h.c.)\\ & + {\sum_{\alpha\beta\gamma}}'\sum_\sigma (U_{\alpha\beta\alpha\gamma} - \tfrac{1}{2}U_{\alpha\beta\gamma\alpha})A^\dagger_{\beta\sigma}A_{\gamma\sigma}\hat{n}_\alpha\\ & - 2{\sum_{\alpha\beta\gamma}}'\sum_{\sigma\sigma'} U_{\alpha\beta\gamma\alpha}A^\dagger_{\beta\sigma}\sigma_{\sigma\sigma'}A_{\gamma\sigma'}\cdot\hat{\mathbf{s}}_\alpha\end{aligned} \tag{2.34}$$

- $\underline{\alpha\neq\beta\neq\gamma\neq\delta}$, involving four levels:

$$\hat{H}_4 = \tfrac{1}{2}{\sum_{\alpha\beta\gamma\delta}}'\sum_{\sigma\sigma'} U_{\alpha\beta\gamma\delta}A^\dagger_{\beta\sigma'}A^\dagger_{\alpha\sigma}A_{\gamma\sigma}A_{\delta\sigma'} \tag{2.35}$$

The full Hamiltonian $\hat{H}_I$ is therefore a formidable beast! We can quickly make some progress however. The coefficients $U_{\alpha\beta\gamma\delta}$ are given by (2.28) and (2.22). For the final two terms in the above we expect the integrals of (2.22) to be very small indeed, the three or four distinct AOs having little mutual overlap. We will therefore neglect these final two terms in our minimal model. The hierarchy of the remaining interactions follows from similar arguments. Of the remaining terms it is interesting to note that $U_{\alpha\beta\gamma\delta} > 0$ except in the cases of $U_{\alpha\beta\alpha\alpha}$ and $U_{\beta\alpha\alpha\alpha}$, which can be negative. The exchange interaction of (2.31) is therefore ferromagnetic: aligned spins have a lower energy than antiparallel spins, this is Hund's (first) rule of maximum multiplicity.

Even by forming a hierarchy of the interaction strengths the Hamiltonians above are not trivial, containing sums over the MOs. We now look for a way to restrict these sums in a controlled manner. A natural way to do so is to consider only the

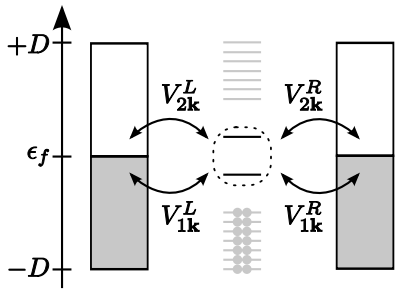

Figure 2.5: Valence shell projection of a quantum dot connected to two metallic leads. We neglect the low lying filled 'core' states and the higher lying valence states (shown in grey), retaining only two valence levels near the Fermi energy ϵ_f. Each valence level couples to both the left (L) and right (R) leads via matrix elements $V^{L/R}_{i\mathbf{k}}$. Interactions are present between electrons occupying the valence levels as indicate by the dashed oval.

'valence states' arising from considering only a few electrons populating a restricted set of orbitals $\{|\Phi_V\rangle\}$ above a closed shell $|\Phi_0\rangle$, a projection of $\hat{H}_{\rm M} = \hat{H}^0_{\rm M} + \hat{H}_{\rm I}$:

$$\hat{H}'_{\rm M} = |\Phi_0\rangle\hat{1}_V\hat{H}_{\rm M}\hat{1}_V\langle\Phi_0| \tag{2.36}$$

When α is a valence state and β a core state, (2.29)–(2.35) have very little effect: only (2.30) and (2.31) leave the core states untouched. [A change in occupation of the core is precluded by (2.36)]. A simple Hartree renormalization of the MO levels results:

$$E_\alpha \to E_\alpha + \sum_{\substack{\alpha\in\{|\Phi_V\rangle\}\\ \beta\notin\{|\Phi_V\rangle\}}} 2U_{\alpha\beta\alpha\beta} - U_{\alpha\beta\beta\alpha}. \tag{2.37}$$

An obvious question now arises: when is this valence shell projection valid? Clearly if the energy separation $\delta E = E_0 - E_M$ between the lowest valence orbital (the LUMO) and the highest core orbital (the HOMO) is larger than the interactions between the highest few core levels, then the core will be filled singlet state and excitations out of this state will be irrelevant. As an example consider the case where we have only $\hat{H}_1$, the on-level repulsion. The filled HOMO has energy $2E_M + U_M$; while by contrast the configuration with one electron in each of the HOMO and LUMO has energy $E_M + E_0$. If $2E_M + U_M \ll E_M + E_0$, (*i.e.* if $\delta E \gg U_M$), then the closed shell has a lower energy.

The physical picture is therefore as follows. We have a (small) set of 'active' interacting MOs above or near the Fermi level of two identical metallic leads. The inactive core levels are far below the Fermi level and filled. The interactions of electrons on the active levels are governed, in order of importance, by (2.29)–(2.35). We choose to retain only two impurity levels labelled $i = 1, 2$ and simply neglect the core levels. The effective model we choose to study is the two-level model (2LM):

$$\hat{H}^{\mathrm{2LM}} = \hat{H}_{\mathrm{L}} + \hat{H}_{\mathrm{D}}^{\mathrm{2LM}} + \hat{H}_{\mathrm{T}} \tag{2.38a}$$

$$\hat{H}_{\mathrm{L}} = \sum_{\substack{\alpha=L/R \\ \mathbf{k}\sigma}} \epsilon_{\mathbf{k}} c^{\dagger}_{\mathbf{k}\alpha\sigma} c_{\mathbf{k}\alpha\sigma} \tag{2.38b}$$

$$\hat{H}_{\mathrm{D}}^{\mathrm{2LM}} = \sum_{i\sigma} \left(\epsilon_{i\sigma} + \frac{U}{2} \hat{n}_{i-\sigma} \right) \hat{n}_{i\sigma} + U' \hat{n}_1 \hat{n}_2 - J_H \hat{\mathbf{s}}_1 \cdot \hat{\mathbf{s}}_2 \tag{2.38c}$$

$$\hat{H}_{\mathrm{T}} = \sum_{\substack{\alpha=L/R \\ i\mathbf{k}\sigma}} V^{\alpha}_{i\mathbf{k}} (d^{\dagger}_{i\sigma} c_{\mathbf{k}\alpha\sigma} + c^{\dagger}_{\mathbf{k}\alpha\sigma} d_{i\sigma}). \tag{2.38d}$$

We have kept the on-level Coulomb repulsion term (2.29) and in practice take the same matrix element for each of the levels 1 and 2, specifically we choose:

$$U \equiv U_{1111} = U_{2222}. \tag{2.39}$$

We have also included the intersite Coulomb repulsion and Hund's rule exchange, (2.30) and (2.31), and defined the interaction parameters

$$J_H = 2U_{1221} \tag{2.40a}$$

$$U' = U_{1212} - \tfrac{1}{4} J_H. \tag{2.40b}$$

We have discarded (2.34) and (2.35) as mentioned above, the correlated hopping term (2.32), and the charge pairing term (2.33). (The latter is in fact straightforward to retain but its inclusion does not materially alter the underlying physics as we have checked explicitely both in the case of the atomic limit and numerical calculations with the full 2LM).

2.3.3 Reduction to a single channel

Thus far we have been guided by experimental setups. Our model consists of an impurity set of levels coupled to a left and a right metallic lead. The couplings $V^{\alpha}_{i\mathbf{k}}$ in (2.38) can of course be completely independent: in fact (2.26) suggests no reason for the couplings to be equal. It will however prove to be a great utility to assume some symmetry in these couplings as we now show.

We will assume that the couplings to the left and right leads are proportional and that the same proportionality constant holds for all levels i. We choose:

$$V^{L}_{i\mathbf{k}} = V_{i\mathbf{k}} \cos\theta \quad \text{and} \quad V^{R}_{i\mathbf{k}} = V_{i\mathbf{k}} \sin\theta. \tag{2.41}$$

By performing a canonical transformation of the lead operators in (2.38) via

$$\begin{aligned} c^{\dagger}_{\mathbf{k}e\sigma} &= +\cos\theta c^{\dagger}_{\mathbf{k}L\sigma} + \sin\theta c^{\dagger}_{\mathbf{k}R\sigma} \\ c^{\dagger}_{\mathbf{k}o\sigma} &= -\sin\theta c^{\dagger}_{\mathbf{k}L\sigma} + \cos\theta c^{\dagger}_{\mathbf{k}R\sigma}, \end{aligned} \tag{2.42}$$

it is straightforward to show that the 'o' orbitals do not couple to the impurity levels and that the tunneling Hamiltonian (2.38d) is now given by:

$$\hat{H}_{\mathrm{T}} = \sum_{i\mathbf{k}\sigma} V_{i\mathbf{k}} (d^{\dagger}_{i\sigma} c_{\mathbf{k}e\sigma} + c^{\dagger}_{\mathbf{k}e\sigma} d_{i\sigma}). \tag{2.43}$$

We can therefore neglect the second lead and consider a single effective conduction band. The impurity term $\hat{H}_{\mathrm{D}}^{\mathrm{2LM}}$ is obviously not affected by this transformation while for the lead part we obtain $\hat{H}_{\mathrm{L}} = \sum_{\mathbf{k}\sigma} \epsilon_{\mathbf{k}} (c^{\dagger}_{\mathbf{k}e\sigma} c_{\mathbf{k}e\sigma} + c^{\dagger}_{\mathbf{k}o\sigma} c_{\mathbf{k}o\sigma})$.

This symmetric coupling scheme is obviously not the most general case, which would by contrast lead to an irreducibly two-lead description [49, 50]. It has moreover been argued [52, 54] that such a one-channel description is appropriate for lateral semiconductor quantum dots. The final 2LM[2] used throughout this thesis is therefore:

$$\hat{H}^{\mathrm{2LM}} = \hat{H}_{\mathrm{L}} + \hat{H}_{\mathrm{D}}^{\mathrm{2LM}} + \hat{H}_{\mathrm{T}} \tag{2.44a}$$

$$\hat{H}_{\mathrm{L}} = \sum_{\mathbf{k}\sigma} \epsilon_{\mathbf{k}} c^{\dagger}_{\mathbf{k}\sigma} c_{\mathbf{k}\sigma} \tag{2.44b}$$

$$\hat{H}_{\mathrm{D}}^{\mathrm{2LM}} = \sum_{i\sigma} \left(\epsilon_{i\sigma} + \frac{U}{2} \hat{n}_{i-\sigma} \right) \hat{n}_{i\sigma} + U' \hat{n}_1 \hat{n}_2 - J_H \hat{\mathbf{s}}_1 \cdot \hat{\mathbf{s}}_2 \tag{2.44c}$$

$$\hat{H}_{\mathrm{T}} = \sum_{i\mathbf{k}\sigma} V_{i\mathbf{k}} (d^{\dagger}_{i\sigma} c_{\mathbf{k}\sigma} + c^{\dagger}_{\mathbf{k}\sigma} d_{i\sigma}), \tag{2.44d}$$

which is identical to (2.38) except the lead index α has been dropped. In future sections we will consider the standard case [20, 23] of a symmetric, flat conduction band with $V_{i\mathbf{k}} = V_i$.

Whilst we have significantly reduced the complexity of the interactions between valence electrons the model still displays a wide variety of physical behaviour, as we shall see in chapters 4–6. The valence levels can contain 0–2 electrons each so there are 16 possible configurations (including spin). These atomic-limit configurations will be explored more fully in section 4.1.

In this chapter with have outlined perturbative approaches for solving impurity models such as the AIM and Kondo models. These could readily be extended to the 2LM. However in the next chapter we pursue a non-perturbative approach: the numerical renormalization group (NRG). This will build on the ideas of scaling introduced in this chapter via the idea of RG flows and fixed points. The NRG is essentially exact and will allow a better understanding of the low-temperature properties of quantum dot devices.

[2] In later sections references to the 2LM will invariably be to the single lead version *i.e.* (2.44) and not (2.38).

CHAPTER 3

The Numerical Renormalization Group

The Numerical Renormalization Group (NRG) [22–24, 73] is a method for calculating thermodynamic properties of impurity models. It can also yield results for the equilibrium dynamic properties of such systems. Whilst building on the scaling ideas of the late 1960s [74, 75], the inherently non-perturbative nature of the technique trades concrete analytical formulae for accurate and efficient numerical calculation.

As discussed in the previous chapter the theoretical study of quantum impurity models is hampered by the combination of many itinerant electrons in the conduction band and strong electron correlations on the impurity itself. A wide range of energies, from the bandwidth of the conduction band to small excitations near the Fermi energy, are important. We saw in the previous chapter how perturbative techniques ultimately fail to capture the complete range of behaviour of these systems.

The NRG by contrast is non-perturbative, treating all energy scales of the problem on an equal footing and is in principle essentially exact, obtaining the full eigensystem of a quantum impurity Hamiltonian to arbitrary resolution. However the numerical nature of the technique means that in practice, with finite computational resources, the Hilbert space of the Hamiltonian must be truncated. As we shall see the NRG therefore trades some knowledge of the higher energy excitations of a system to obtain the ultimate goal of capturing the correct $T \to 0$ behaviour.

In chapters 4–6 we will make extensive use of the NRG in our analysis of the 2LM, and so it is important to give some background to the original formulation of the technique and some of its recent extensions. We will focus on providing details of the technique which elucidate some of the important physics of quantum impurity models rather than giving a complete, technical description. Much of the underlying mathematics can be found in the original papers by Wilson [22] and Krishnamurthy, Wilkins, and Wilson [23, 24]. An recent review by Bulla [73] is also available. In this chapter we show specifically how the NRG can be applied to the 2LM and introduce the relevant conceptual framework necessary to understand

the results presented throughout the rest of this thesis. With regard to conductance experiments performed with real quantum dot devices, recent extensions to the NRG discussed towards the end of this chapter have put the calculation of such properties on a more mathematically sound footing.

3.1 Transformation of the Hamiltonian

The initial step of the NRG approach is to transform the 2LM Hamiltonian (2.44):

$$\begin{aligned}\hat{H}^{\mathrm{2LM}} &= \hat{H}_{\mathrm{L}} + \hat{H}_{\mathrm{D}}^{\mathrm{2LM}} + \hat{H}_{\mathrm{T}} \\ &= \sum_{\mathbf{k}\sigma} \epsilon_{\mathbf{k}} c^{\dagger}_{\mathbf{k}\sigma} c_{\mathbf{k}\sigma} \\ &+ \sum_{i\sigma} \left(\epsilon_{i\sigma} + \frac{U}{2} \hat{n}_{i-\sigma} \right) \hat{n}_{i\sigma} + U' \hat{n}_1 \hat{n}_2 - J_H \hat{\mathbf{s}}_1 \cdot \hat{\mathbf{s}}_2 \\ &+ \sum_{i\mathbf{k}\sigma} V_{i\mathbf{k}} (d^{\dagger}_{i\sigma} c_{\mathbf{k}\sigma} + c^{\dagger}_{\mathbf{k}\sigma} d_{i\sigma})\end{aligned} \tag{3.1}$$

into a one-dimensional continuum form suitable for further manipulation. The full procedure is rather simple but lengthy and is given in Appendix A of [23].

The basic transformation is achieved by assuming that the single conduction band is isotropic, extending from energy $-D$ to $+D$, and further that the $V_{i\mathbf{k}}$ depend only on $|\mathbf{k}|$. With these simplifications, when the conduction band states are expanded in terms of spherical harmonics, the impurity couples solely to the s-wave states. By further assuming the conduction band density of states to be constant $\rho(\epsilon) = \rho$ and also that $V_{i|\mathbf{k}|} = V_i$ it follows that [23] the Hamiltonian $\hat{H}^{\mathrm{2LM}}$ can be rewritten as

$$\begin{aligned}\frac{\hat{H}^{\mathrm{2LM}}}{D} &= \int_{-1}^{+1} k a^{\dagger}_{k\sigma} a_{k\sigma} \mathrm{d}k \\ &+ \sum_{i} \left(\epsilon_{i\sigma} + \frac{U}{2D} \hat{n}_{i-\sigma} \right) \hat{n}_{i\sigma} + \frac{U'}{D} \hat{n}_1 \hat{n}_2 - \frac{J_H}{D} \hat{\mathbf{s}}_1 \cdot \hat{\mathbf{s}}_2 \\ &+ \sum_{i} \sqrt{\frac{\Gamma_{ii}}{\pi D}} \int_{-1}^{+1} (d^{\dagger}_{i\sigma} a_{k\sigma} + a^{\dagger}_{k\sigma} d_{i\sigma}) \mathrm{d}k,\end{aligned} \tag{3.2}$$

with an implicit sum over the spin index σ. Here we have rescaled the Hamiltonian such that the conduction band states span an energy range $[-1, +1]$ and the remaining energies scales appear in the form of dimensionless parameters $\epsilon_{i\sigma}/D$, U/D, U'/D and J_H/D. The conduction band is now described in terms of a set of continuum operators $\{a_{k\sigma}\}$, which satisfy the usual anticommutation relations $[a^{\dagger}_{k\sigma}, a_{k'\sigma'}]_+ = \delta_{\sigma\sigma'}\delta_{kk'}$. These couple to the impurity via the hybridisation term with

$$\Gamma_{ii} = \pi \rho V_i^2. \tag{3.3}$$

3.2 Logarithmic discretization

The next step of the NRG procedure is key to its success. Equation (3.2) cannot be diagonalized directly due to the coupling of the continuum states to the local states of the impurity. The NRG reduces the complexity of the problem by forming a suitable approximation to the continuum states. The approximate states resemble Wannier states localised around the impurity [23]. As a result of the following, a clear separation of energy scales emerges making a solution of (3.1) tractable.

The Kondo physics that we wish to investigate in chapters 4–6 is dominated by exponentially low-energy excitations. Wilson's solution for the Kondo model [22] was to split the conduction band into a number of logarithmically spaced intervals centred on $k = 0$. These intervals are controlled by the parameter Λ with the nth interval for $k > 0$ lying between $\Lambda^{-(n+1)}$ and Λ^{-n} (see fig. 3.1). A complete set of orthonormal states spanning the k space can be constructed by setting up a Fourier series in each of these intervals:

$$\psi^{\pm}_{np}(k) = \begin{cases} \frac{\Lambda^{-n/2}}{(1-\Lambda^{-1})^{1/2}} e^{\pm i\omega_n pk} & \text{if } \Lambda^{-(n+1)} < \pm k < \Lambda^{-n} \\ 0 & \text{otherwise,} \end{cases} \tag{3.4}$$

where $\omega_n = 2\pi\Lambda^n/(1-\Lambda^{-1})$ is the fundamental frequency within each interval and the $p \in \mathbb{Z}$. The host destruction operators may be expanded using the $\psi^{\pm}_{np}(k)$ as

$$a_{k\sigma} = \sum_{np} [a_{np\sigma}\psi^{+}_{np}(k) + b_{np\sigma}\psi^{-}_{np}(k)]. \tag{3.5}$$

The new operators $a_{np\sigma}$ and $b_{np\sigma}$ themselves form a complete set, satisfying the usual anticommutation rules and are given explicitly by:

$$a_{np\sigma} = \int_{-1}^{+1} \left[\psi^{+}_{np}(k)\right]^* a_{k\sigma}\mathrm{d}k; \qquad b_{np\sigma} = \int_{-1}^{+1} a_{k\sigma} \left[\psi^{-}_{np}(k)\right]^* \mathrm{d}k. \tag{3.6}$$

The Hamiltonian (3.2) can now be expressed in terms of these discrete operators. For example, it is straightforward to show that

$$\int_{-1}^{+1} a_{k\sigma}\mathrm{d}k = (1-\Lambda^{-1})^{1/2} \sum_n \Lambda^{-n/2}(a_{n0\sigma} + b_{n0\sigma}), \tag{3.7}$$

and that

$$\int_{-1}^{+1} a^{\dagger}_{k\sigma}a_{k\sigma}\mathrm{d}k = \tfrac{1}{2}(1+\Lambda^{-1}) \sum_{np} \Lambda_{-n}(a^{\dagger}_{np\sigma}a_{np\sigma} - b^{\dagger}_{np\sigma}b_{np\sigma}) + \frac{1-\Lambda^{-1}}{2\pi i} \sum_{n,p\neq p'} \frac{\Lambda^{-n}}{p'-p}(a^{\dagger}_{np\sigma}a_{np'\sigma} - b^{\dagger}_{np\sigma}b_{np'\sigma}) \exp\left[\frac{2\pi i(p'-p)}{1-\Lambda^{-1}}\right]. \tag{3.8}$$

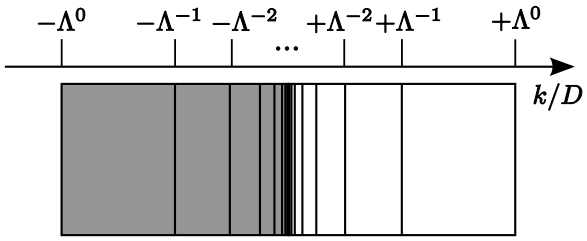

Figure 3.1: Schematic representation of the logarithmic discretization of conduction band states use in the NRG.

From (3.7) [in combination with the Hamiltonian (3.2)] it is clear that the impurity couples only to the orbitals $a_{n0\sigma}$ and $b_{n0\sigma}$. Those orbitals with $p > 0$ only enter the conduction band part of the Hamiltonian, $\hat{H}_{\rm L}$, where they appear with a prefactor $(1-\Lambda^{-1})$. Clearly if Λ is chosen to be close to 1 this coupling will be small. It is here that we make the *fundamental approximation of the NRG, to neglect those orbitals with* $p > 0$. At first, this may appear a rather crude approximation but calculations for the Kondo model [22] show that numerical results are robust for values of Λ rather larger than unity; in fact $\Lambda \simeq 3$ is a common choice [73].

The above procedure and approximation to ignore higher Fourier harmonics leads to a Hamiltonian which is certainly simpler than (3.1) but it will be expressed in term of the set of operators $\{a_{n0\sigma}, b_{n0\sigma}\}$. The operators with $p > 0$ do not enter anymore and so we drop the '0' index in the following. We can make one further transformation to simplify the interactions between these orbitals. A unitary transformation is chosen to transform the set $\{a_{n\sigma}, b_{n\sigma}\}$ into a new orthonormal set $\{f_{n\sigma}\}$. There are infinitely many such transformations but since the conduction band energy in (3.8) is already diagonal in the operators $a_{n\sigma}$ and $b_{n\sigma}$ the best that can be achieved is to choose a transformation such that the $f_{n\sigma}$ exhibit only nearest-neighbour couplings. The details of the transformation are rather lengthy [22] and we only state the following result for the 2LM:

$$\begin{aligned}\frac{\hat{H}^{\rm 2LM}}{D} &= \tfrac{1}{2}(1+\Lambda^{-1})\sum_{n=0}^{\infty}\Lambda^{-n/2}\xi_n\left(f^\dagger_{n\sigma}f_{(n+1)\sigma}+f^\dagger_{(n+1)\sigma}f_{n\sigma}\right)\\ &+\sum_i\left(\epsilon_{i\sigma}+\frac{U}{2D}\hat{n}_{i-\sigma}\right)\hat{n}_{i\sigma}+\frac{U'}{D}\hat{n}_1\hat{n}_2-\frac{J_H}{D}\hat{\mathbf{s}}_1\cdot\hat{\mathbf{s}}_2\\ &+\sum_i\sqrt{\frac{2A_\Lambda\Gamma_{ii}}{\pi D}}(f^\dagger_{0\sigma}d_{i\sigma}+d^\dagger_{i\sigma}f_{0\sigma}),\end{aligned} \tag{3.9}$$

where

$$\xi_n = (1-\Lambda^{-n-1})(1-\Lambda^{-2n-1})^{-1/2}(1-\Lambda^{-2n-3})^{-1/2} = \mathcal{O}(1) \tag{3.10}$$

$$A_\Lambda = \frac{\ln\Lambda}{2}\left(\frac{1+\Lambda^{-1}}{1-\Lambda^{-1}}\right). \tag{3.11}$$

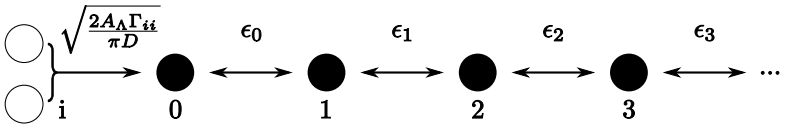

Figure 3.2: Pictorial representation of (3.9). The impurity couples solely to the 'zeroth' orbital of a one-dimensional linear chain. The chain couplings decrease exponentially, ultimately allowing solution of the Hamiltonian.

Here the factor A_Λ renormalizes the coupling to correct for the logarithmic discretization. Inclusion of this factor recovers the exact continuum limit ($\Lambda \to 1$) for non-interacting systems [23] and also seemingly achieves more accurate results for interacting systems.[1]

Equation (3.9) describes a linear chain with the impurity positioned at one end as illustrated in fig. 3.2. The impurity orbitals couple only to the 'zeroth' orbital via the matrix elements $\sqrt{2A_\Lambda\Gamma_{ii}/\pi D}$, and successive sites of the chain are coupled by $\epsilon_n \propto \Lambda^{-n/2}\xi_n$. With increasing n, the value of ξ_n approaches unity and so the chain couplings decrease exponentially. This suggests that a suitable approximation to the solution of (3.9) could be sought by truncating the chain at some suitably large n, as only states of low n couple strongly to the impurity or their neighbours. However, what is less obvious is that orbitals further along the chain are constructed from the conduction band states which, while being spatially far from the impurity, have energies close to the Fermi level [23]. It is therefore necessary to include states of rather large n in order to capture the excitations close to the Fermi level. Since each orbital may contain 0, 1 or 2 electrons the Hilbert space grows by a factor 4 for each additional site in the chain; direct diagonalization of the resulting Hilbert space for a long chain is computationally impossible. The need to include states of both high and low n is equivalent to the statement that the low-energy excitations of the system are influenced by conduction band states of both high and low energies.

3.3 Iterative diagonalization

The previous section has outlined how quantum impurity Hamiltonians such as (3.1) can be recast in terms of a linear chain Hamiltonian (3.9). Naturally one cannot obtain the full eigensystem of an infinite chain by direct diagonalization. Wilson's ingenious solution [22] was to realise that with the exponential decrease of the couplings along the chain one can set up an iterative procedure. One begins by diagonalizing a Hamiltonian consisting of the impurity and the '0' site of the chain, and adding subsequent sites of the chain one-by-one, diagonalizing the Hamiltonian after each

[1] A more satisfactory approach than this rather *ad hoc* renormalization of the coupling constant is given in [76] where a modified discretization scheme is used. Section 3.5 gives details of a modified discretization scheme used in this work.

site is added. Wilson was able to show that even by truncating the Hilbert space at each iteration (by keeping only the lowest eigenstates), one can nevertheless obtain accurate thermodynamics on all energy scales — the approximate Hamiltonian at each iteration corresponding to the full system at some effective finite temperature. The truncation procedure ensures the Hilbert space remains at a fixed, manageable size and so, in principle, arbitrarily many iterations can be performed. To begin we consider a series of finite chains of length $N = 0,\ 1,\ 2,\ 3...$ from which we can recover the infinite chain of (3.9). We define a dimensionless Hamiltonian containing the first N sites in the chain by:

$$\begin{aligned}\hat{H}_N^{\mathrm{2LM}} = \Lambda^{(N-1)/2}\Bigg[&\sum_{n=0}^{N-1}\Lambda^{-n/2}\xi_n\left(f_{n\sigma}^\dagger f_{(n+1)\sigma} + f_{(n+1)\sigma}^\dagger f_{n\sigma}\right)\\ &+\sum_i\left(\bar{\epsilon}_{i\sigma}+\frac{\bar{U}}{2}\hat{n}_{i-\sigma}\right)\hat{n}_{i\sigma} + \bar{U}'\hat{n}_1\hat{n}_2 - \bar{J}_H\hat{\mathbf{s}}_1\cdot\hat{\mathbf{s}}_2\\ &+\sum_i\sqrt{\bar{\Gamma}_{ii}}(f_{0\sigma}^\dagger d_{i\sigma} + d_{i\sigma}^\dagger f_{0\sigma})\Bigg],\end{aligned} \tag{3.12}$$

with the dimensionless parameters

$$\begin{aligned}\bar{\Gamma}_{ii} &= \left(\frac{2}{1+\Lambda^{-1}}\right)^2\frac{2A_\Lambda\Gamma_{ii}}{\pi D} \qquad \bar{\epsilon}_{i\sigma} = \left(\frac{2}{1+\Lambda^{-1}}\right)\epsilon_{i\sigma}\\ \bar{U} = \left(\frac{2}{1+\Lambda^{-1}}\right)U &\qquad \bar{U}' = \left(\frac{2}{1+\Lambda^{-1}}\right)U' \qquad \bar{J}_H = \left(\frac{2}{1+\Lambda^{-1}}\right)J_H \quad ,\end{aligned} \tag{3.13}$$

such that (3.9) is recovered by taking the limit

$$\hat{H}^{\mathrm{2LM}} = \lim_{N\to\infty}\tfrac{1}{2}(1+\Lambda^{-1})D\Lambda^{-(N-1)/2}\hat{H}_N^{\mathrm{2LM}}. \tag{3.14}$$

A factor of $\Lambda^{(N-1)/2}$ has been introduced in (3.12) and (3.14); its purpose is to make the coupling between the $N-1$ and N sites of order unity, thereby ensuring the numerical diagonalization is numerically stable. It follows from (3.12) that $\hat{H}_{N+1}$ may be obtained recursively from $\hat{H}_N$ using

$$\hat{H}_{N+1}^{\mathrm{2LM}} = \sqrt{\Lambda}\hat{H}_N^{\mathrm{2LM}} + \xi_n\left(f_{N\sigma}^\dagger f_{(N+1)\sigma} + f_{(N+1)\sigma}^\dagger f_{N\sigma}\right) - E_{G,N+1} \tag{3.15}$$

(measuring energies relative to the ground state $E_{G,N+1}$) which yields an iterative approach to calculating $\hat{H}_N^{\mathrm{2LM}}$ starting from the initial Hamiltonian $\hat{H}_0^{\mathrm{2LM}}$. The initial Hamiltonian itself follows from (3.12) as

$$\begin{aligned}\hat{H}_0^{\mathrm{2LM}} = \Lambda^{-1/2}\Bigg[&\sum_i\left(\epsilon_{i\sigma}+\frac{\bar{U}}{2}\hat{n}_{i-\sigma}\right)\hat{n}_{i\sigma} + \bar{U}'\hat{n}_1\hat{n}_2 - \bar{J}_H\hat{\mathbf{s}}_1\cdot\hat{\mathbf{s}}_2\\ &+\sum_i\sqrt{\bar{\Gamma}_{ii}}(f_{0\sigma}^\dagger d_{i\sigma} + d_{i\sigma}^\dagger f_{0\sigma})\Bigg].\end{aligned} \tag{3.16}$$

At this point it is worth mentioning that to reduce the computational time required to diagonalize each successive $\hat{H}_N^{\mathrm{2LM}}$, the symmetries of the Hamiltonians can be exploited. From (3.1) it can be shown that the Hilbert space can be divided into subspaces according to the total charge Q_N and spin z-projection S_N^z. Further if the impurity level energies are spin independent (as is the case in the absence of a magnetic field) a further computational speed-up can be achieved by using the total spin S_N. We define operators for these quantities via

$$\hat{Q}_N = \sum_{n=0}^{N} (f_{n\sigma}^\dagger f_{n\sigma} - 1) + \sum_i (d_{i\sigma}^\dagger d_{i\sigma} - 1) \tag{3.17a}$$

$$\hat{S}_N = \tfrac{1}{2} \sum_{n=0}^{N} f_{n\sigma}^\dagger \sigma_{\sigma\sigma'} f_{n\sigma'} + \tfrac{1}{2} \sum_i d_{i\sigma}^\dagger \sigma_{\sigma\sigma'} d_{i\sigma'} \tag{3.17b}$$

$$\hat{S}_N^z = \sum_{n=0}^{N} \tfrac{1}{2} (f_{n\uparrow}^\dagger f_{n\uparrow} - f_{n\downarrow}^\dagger f_{n\downarrow}) + \sum_i \tfrac{1}{2} (d_{i\uparrow}^\dagger d_{i\uparrow} - d_{i\uparrow}^\dagger d_{i\uparrow}), \tag{3.17c}$$

with σ the vector of Pauli Matrices. The Hamiltonian $\hat{H}_N$ can now be diagonalized in each subspace independently: full details of this process, for the case of (Q_N, S_N) subspaces, are given in Appendix B of [23].

As mentioned in section 3.2 it is necessary to perform the above iterative process to rather large N in order to capture low-energy excitations. The size of the Hilbert of $\hat{H}_N$ space grows exponentially with N, such that even for modest N this process soon becomes intractable. It is therefore necessary to truncate the Hilbert space from one iteration to the next so that it does not become unmanageably large. We are ultimately interested in the low-energy properties of the system, so it seems reasonable to keep only the lowest N_k states of $\hat{H}_N$ in order that the computational time to diagonalize $\hat{H}_N$ remains fixed when N is large.[2]

Several questions arise at this point. First, how can one calculate $\hat{H}$ using (3.14): even with a suitable truncation procedure, how large must N be to approach the $N \to \infty$ limit? By truncating the Hilbert space, how good is the approximation to the states of $\hat{H}_N$ when all but the lowest few states of $\hat{H}_{N-1}$ are discarded? And finally what useful information, if any, can be gained from the iterative procedure?

As it turns out the answers to these questions are very much related. It is the exponential decrease in the chain couplings which leads to a separation of the energy scales from one iteration to the next [22]. Provided that Λ is suitably greater than 1, the coupling of a further chain orbital can be viewed as causing a small splitting in the eigenstates of the system. This splitting will be smaller than the characteristic spacing of the states (bar any accidental degeneracies), as illustrated in fig. 3.3.

[2] We drop the 2LM from $\hat{H}_N^{\mathrm{2LM}}$ for the remainder of this chapter as the concepts discussed are all rather general.

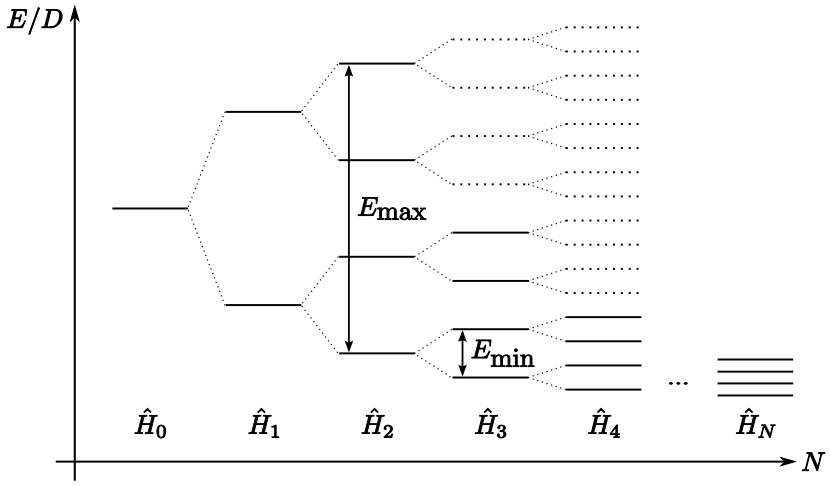

Figure 3.3: NRG eigenstates for successive $\hat{H}_N$. High-energy states of one iteration do not become low-energy states in further iterations. To calculate low-energy properties, only the lowest N_k states need be kept without detrimental effect. $E_{\max}$ and $E_{\min}$ indicate the maximum and minimum temperature scales at which $\hat{H}_2$ is useful for calculating thermodynamics of the system.

Consequently it does not matter if one discards the high-lying states as the states created from them in subsequent iterations will never interfere with the lower-lying states. The lowest eigenstates are then calculated to high accuracy.

From the above, it may seem that all that is achieved is an approximate calculation of the ground state and lowest-lying excitations of the system, since the states required to calculate higher energy excitations have been discarded. In fact this is not correct. Each $\hat{H}_N$ can be used to calculate thermodynamic properties of the system at some effective temperature: if one is interested in the properties of a system at a temperature T, one only needs to know the eigenstates of the system to within the thermal energy $E_T = k_{\mathrm{B}}T$. Any further accuracy is useless due to thermal broadening, the thermal excitation of particles from one state to another of higher energy. Further, one does not need to know anything of the states lying at energies $E \gg k_{\mathrm{B}}T$. Hence useful information can be gathered from each iteration and thermodynamic properties can be calculated for all energy scales up to the bandwidth D simply by piecing together results calculated for each $\hat{H}_N$. As the energy scale associated with $\hat{H}_N$ decreases with increasing N, the effective temperature connected with each $\hat{H}_N$ also decreases.

Having obtained the set of Hamiltonians $\hat{H}_N$, the starting point for calculation of thermodynamic properties is the usual expression for the thermal average of an operator $\hat{O}$:

$$\langle \hat{O} \rangle = \frac{\mathrm{Tr}\, \hat{O} \exp[-\beta \hat{H}]}{\mathrm{Tr} \exp[-\beta \hat{H}]}, \tag{3.18}$$

where Tr denotes a trace over the states of the system and $\beta = 1/k_{\mathrm{B}}T$. As we are usually interested in the properties of the impurity rather than the system as a whole, it is usual to define 'impurity' properties:

$$\langle \hat{O} \rangle_{\mathrm{imp}} = \langle \hat{O} \rangle - \langle \hat{O}^0 \rangle \tag{3.19a}$$

$$= \frac{\mathrm{Tr}\, \hat{O} \exp[-\beta \hat{H}]}{\mathrm{Tr} \exp[-\beta \hat{H}]} - \frac{\mathrm{Tr}\, \hat{O}^0 \exp[-\beta \hat{H}^0]}{\mathrm{Tr} \exp[-\beta \hat{H}^0]}, \tag{3.19b}$$

where $\hat{H}^0$ denotes the Hamiltonian of the system with the impurity removed, and $\hat{O}^0$ an operator acting on this system. Clearly the Boltzmann factor in the above exponentially suppresses states of energy $E_{\mathrm{max}} \gg k_{\mathrm{B}}T$ and so these forms, together with the truncation procedure, immediately provide an upper bound on the temperature T_N at which a Hamiltonian $\hat{H}_N$ may be used to calculate properties of the full system, the $N \to \infty$ limit. A lower bound for T_N may also be established by considering the energy splittings in the iteration $N+1$. As the temperature is reduced the required energy resolution of states naturally increases, as discussed above. The minimum energy scale, E_{min}, for T_N is thereby given by the splittings induced in the levels on going from iteration N to $N+1$; that is to say, at this energy scale one would do better to use the Hamiltonian $\hat{H}_{N+1}$. In reality one can pick a range of overlapping temperature ranges to calculate thermodynamics at each iteration [23]; the differences in results from each iteration give an indication of the accuracy of the NRG calculation. We define [23] the effective temperature for each iteration by:

$$\frac{k_{\mathrm{B}}T_N}{D} = \tfrac{1}{2}(1 + \Lambda^{-1})\Lambda^{-(N-1)/2}/\bar{\beta}, \tag{3.20}$$

where multiple values of the scale $\bar{\beta}$ can be chosen per iteration. Ref. [23] gives details of how $\bar{\beta}$ may be chosen and analyses the error in the procedure, which turns out to be rather small provided $\bar{\beta} \ll \Lambda$. The other Λ-dependent factors are simply those which follow from (3.14).

An NRG calculation can be summarised as follows (see also fig. 3.4). One begins with an initial Hamiltonian ($\hat{H}_0$) as prescribed in (3.16) and uses (3.15) to grow the linear chain. In each iteration the steps taken are:

1. Take the lowest N_k states from the previous iteration.
2. Rescale the energies of the states by $\sqrt{\Lambda}$.
3. Couple an extra site to the chain with coupling strength ξ_N. Rediagonalize the Hamiltonian.
4. Subtract the ground state energy.

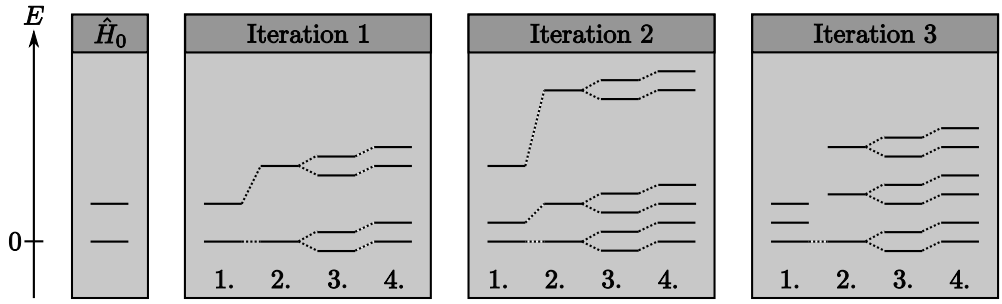

Figure 3.4: Pictorial summary of the NRG procedure as outlined in the text.

Here steps 2. and 4. merely serve to ensure that the range of energies spanned by each $\hat{H}_N$ stays approximately constant. This will prove useful in the following section.

3.4 Renormalization group flows

The previous section has expounded the NRG in terms of a clever mathematical prescription which can calculate an accurate approximation to the ground state and low-lying states of an impurity Hamiltonian, and generate effective Hamiltonians appropriate for the calculation of finite-temperature properties. One could now in principle set up the calculation and analyse the 2LM in quite some detail for arbitrary parameters. However, the NRG is somewhat richer than a computational engine when one realises that the recursion relation of (3.15) is an example of a renormalization group (RG) transformation. In this section we illustrate the underpinning ideas of RG 'flows' between 'fixed points' and the universality which this implies for seemingly distinct Hamiltonians. We will not attempt a full account of RG principles or indeed how these ideas work in practice for the NRG; the intention is rather to prepare the reader with the concepts necessary to understand the language used in the discussion of results in chapters 4–6. Renormalization Group concepts are discussed more thoroughly in the text of Binney *et al.*[77], while a detailed discussion of the classification of the fixed point Hamiltonians relevant here can be found in ref. [23].

Until now we have regarded the iterative procedure to generate successive Hamiltonians as solely a means to an end: to diagonalize accurately and efficiently a linear chain Hamiltonian. We may rewrite (3.15) as

$$\hat{H}_{N+1} = \mathcal{T}[\hat{H}_N], \tag{3.21}$$

where the operator $\mathcal{T}$ is seen to take a Hamiltonian $\hat{H}_N$ and transform it into the new $\hat{H}_{N+1}$. In our case $\mathcal{T}$ is given by a simple mathematical prescription, however there are many examples where $\mathcal{T}$ cannot be so easily written down [77]. The salient point

in either case is that this 'RG transformation' takes existing knowledge of the system at one energy or length scale to glean information at another (usually reduced) scale.

It is often the case that one chooses the operator $\mathcal{T}$ to operate on the Hamiltonian $\hat{H}_N$ in such a way to produce a new Hamiltonian with precisely the same functional form but with a different set of parameters. In this simplifying situation it is helpful to think of a space of Hamiltonians, each Hamiltonian having co-ordinates given by its parameters. Successive use of the operator $\mathcal{T}$ then forms a trajectory in this space, whereby it can be seen that there is nothing in particular special about the initial Hamiltonian $\hat{H}_0$ — a second $\hat{H}_0$ could easily lead to a trajectory which would include the former.

There are however some points in parameter space which are special. Equation (3.21) allows for the possibility of so-called fixed points where the action of $\mathcal{T}$ is to produce precisely the same Hamiltonian:

$$\hat{H}^* = \mathcal{T}[\hat{H}^*], \tag{3.22}$$

with $\hat{H}^*$ the Hamiltonian at the fixed point. The effect of such points on the RG trajectory, or flow, is shown in fig. 3.5, a schematic illustration for a two-parameter Hamiltonian $\hat{H}_N(a, b)$. Three fixed points are shown. The first, $\hat{H}^*_{\mathrm{u}}$, is a so-called unstable fixed point. Exactly at the fixed point, $\mathcal{T}$ has no effect but in the vicinity of this point, the action of $\mathcal{T}$ is to take the flow away from the fixed point; the fixed point is said to 'repel' the flow. In this case $\hat{H}_N$ becomes less like $\hat{H}^*_{\mathrm{u}}$ under renormalization. The second fixed point, $\hat{H}^*_{\mathrm{s}}$, by contrast is stable and attracts nearby flows. The effect is to cause $\hat{H}_N$ to become progressively more similar to $\hat{H}^*_{\mathrm{s}}$. Finally, $\hat{H}^*_{\mathrm{m}}$, has a mixed character. Depending on the direction of approach the action of $\mathcal{T}$ is either to move the flow closer to or further from the fixed point. As we shall see shortly, such fixed points are important in understanding critical phenomena.

To expand on these ideas and to illustrate one method of determining the stabilities of fixed points, we now put these concepts in a more mathematical framework. Consider the situation where the two Hamiltonians $\hat{H}_N$ and $\hat{H}_{N+1}$ are both 'near' a fixed point Hamiltonian $\hat{H}^*$, in the sense that their parameters are similar to those of the fixed point. Using (3.21) we can write the effect of $\mathcal{T}$ on $\hat{H}_N$:

$$\begin{aligned}
\hat{H}_{N+1} = \hat{H}^* + \delta\hat{H}' &= \mathcal{T}[\hat{H}_N] \\
&= \mathcal{T}[\hat{H}^* + \delta\hat{H}] \\
&= \hat{H}^* + \mathcal{T}[\delta\hat{H}] \\
&= \hat{H}^* + \mathcal{M}\delta\hat{H} + \mathcal{O}(\delta\hat{H}^2) \\
\delta\hat{H}' &\approx \mathcal{M}\delta\hat{H},
\end{aligned} \tag{3.23}$$

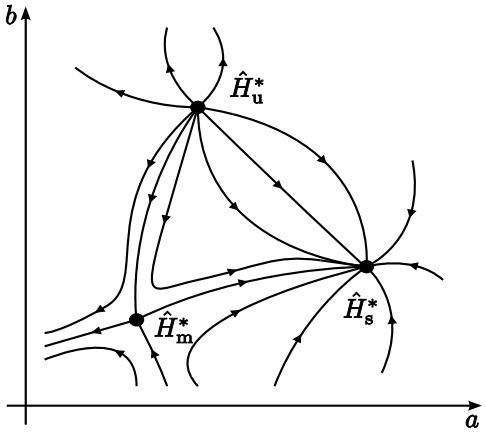

Figure 3.5: A schematic RG flow for a set of Hamiltonians parametrised as $\hat{H}(a, b)$ showing a stable, unstable and mixed fixed point ($\hat{H}^*_{\mathrm{s}}$, $\hat{H}^*_{\mathrm{u}}$ and $\hat{H}^*_{\mathrm{m}}$ respectfully). A stable fixed point attracts nearby RG flows, the Hamiltonian $\hat{H}_N$ becomes progressively more similar to $\hat{H}^*_{\mathrm{s}}$. An unstable fixed points repels nearby flow such that $\hat{H}_N$ becomes less like $\hat{H}^*_{\mathrm{u}}$. Flows near a mixed fixed point can do either of these possibilities depending on the relative position of the flow to the fixed point in co-ordinate space.

where we have expanded $\mathcal{T}$ in a Taylor series about $\hat{H}^*$. The object $\mathcal{M}$ is then a matrix describing the transformation to first order. As the RG flow approaches the fixed point, its behaviour is governed by the eigenvalues and vectors of the matrix $\mathcal{M}$. There are three possibilities for each eigenvalue, λ:

1. $\lambda > 1$. Here $\delta\hat{H}$ increases with each RG iteration and the Hamiltonian $\hat{H}_N$ moves away from the fixed point. This is then an unstable, repulsive fixed point. The corresponding eigenvector is said to be 'relevant'.

2. $\lambda < 1$. The converse is true, $\delta\hat{H}$ decreases with each iteration and $\hat{H}_N$ becomes more like the fixed point. The fixed point is then attracting the RG flow. If this is the sole eigenvector of $\mathcal{M}$ the fixed point is stable. The eigenvector itself is named 'irrelevant'.[3]

3. $\lambda = 1$. In this case $\delta\hat{H}$ remains fixed under renormalization, and the eigenvector is said to be 'marginal'. This does not imply anything about the fixed point itself; only that the approximate linearised transformation does not flow towards or away from the fixed point. One would have to expand $\mathcal{T}$ to higher orders, which in practice leads the analysis to become more complicated.

The existence of fixed point Hamiltonians and RG flows has several immediate consequences. Above we alluded to the fact that one initial Hamiltonian may lead to

[3]These otherwise peculiar names have an obvious meaning: a vector has a relevance in determining whether a fixed point is unstable. One relevant vector is sufficient to deem a fixed point unstable whereas the same cannot be said of irrelevant eigenvectors and stable fixed points.

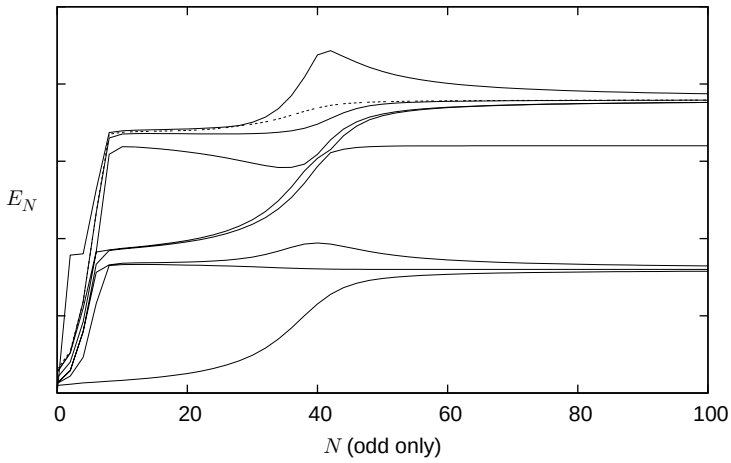

Figure 3.6: NRG results for the energies of the lowest levels of the $(Q_N = 0, S_z = 1)$ subspace of $\hat{H}_N$ for the 2LM, calculated with $\Lambda = 3$ and bare parameters $U = 20\Gamma$, $U' = 10\Gamma$, $J_H = 5\Gamma$, $\epsilon_1 = \epsilon_2 = -20\Gamma$ and $\Gamma = 10^{-2}D$. The levels converge to constant values for large N indicative of the RG flow reaching a stable fixed point.

a trajectory which flows to another choice of initial Hamiltonian. Alternatively one can think of sets of Hamiltonians which all lie on the same flow line [fig. 3.5]. Two systems with different initial, or 'bare', parameters ultimately behave in a similar, even identical, manner after many applications of the transformation. Naturally as the two flows have started on different points on the flow line, this 'universality' occurs at a different energy or temperature scale in the two systems. Here we have simplified the discussion by thinking about Hamiltonians which keep an identical form under renormalization albeit it with changed (renormalized) parameters. However, the same ideas of universality extend to the case where the Hamiltonian changes functional form under renormalization. In this case very different initial Hamiltonians can lead to the same emergent physics with only the characteristic energy scale being changed. A very simple example of this might be a rather complicated Hamiltonian that at a particular energy scale can be projected into one of its subspaces, the neglected eigenvectors and values being unimportant. The projected Hamiltonian is an effective Hamiltonian associated with the particular energy scale. A more concrete example was given in section 2.2. The Schrieffer-Wolff transformation of the Anderson Impurity Model to the Kondo model shows how the former behaves identically to the latter at low energies. One of the main strengths of the NRG is the ability to represent arbitrary Hamiltonians, and not to restrict the form of the Hamiltonian from iteration to iteration. It is for this reason the NRG has been so successful in describing a wide range of quantum impurity Hamiltonians.

From the discussion above it is apparent that a stable fixed point represents a possible $N \to \infty$ solution of the RG procedure, the RG flow will ultimately be

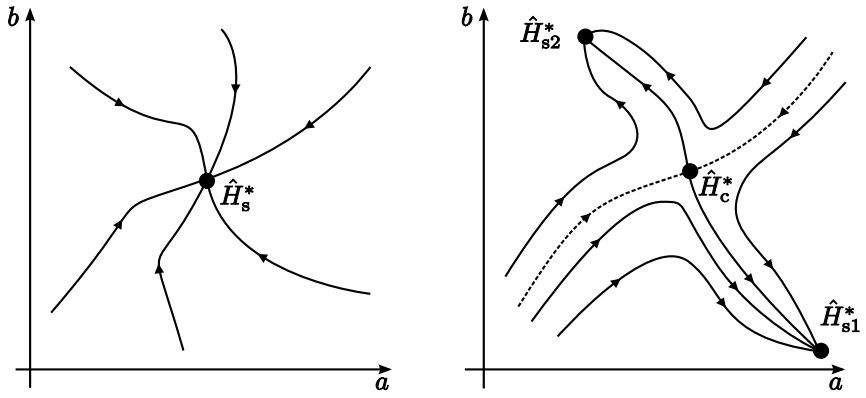

Figure 3.7: *Left:* A system with a single stable fixed point. All systems are ultimately described by the same Hamiltonian under renormalization. *Right:* A system with two stable fixed points. The system possesses a phase transition with the dashed line indicating the phase boundary. RG flows precisely on the dashed line lead to the fixed point $\hat{H}^*_c$.

attracted to it. In the NRG, as the iterations proceed and the effective temperature lowers [(3.20)], the Hamiltonians $\hat{H}_N$ and $\hat{H}_{N+1}$ become increasingly similar. An examples of this is shown in fig. 3.6 where we plot the lowest few energy levels of the $(Q_N = 0, S_z = 1)$ subspace of the 2LM Hamiltonian. (This subspace contains the ground state). It is clear from the figure that there are three distinct regimes of behaviour: a short initial region where all the levels are roughly degenerate, followed by a crossing to a region which lasts until $N \sim 30$. Finally an extended region occurs where groups of levels appear to be converging. It is this last region which represents the approach to a stable fixed point. This convergence to the zero-temperature stable fixed point allows an NRG calculation to be stopped at finite N (corresponding to a small yet finite temperature T_N) whilst still allowing useful information about the true $T_\infty = 0$ ground state to be extracted.

The two earlier regions are indicative of unstable fixed points and it is interesting to see that although these fixed point are ultimately unstable they do attract the RG flow for quite a number of iterations. The unstable fixed points therefore represent effective Hamiltonians suitable for describing a system over a range of temperatures. This will be evidenced in chapters 4–6.

An interesting question arises when one considers the possibility of having more than one stable fixed point, as shown in the right panel of fig. 3.7 for two stable fixed points $\hat{H}^*_{s1}$ and $\hat{H}^*_{s2}$. The RG flow may terminate at either of these giving rise to two distinct ground states at zero temperature; a quantum phase transition can therefore occur between systems with different initial parameters. Each of $\hat{H}^*_{s1}$ and $\hat{H}^*_{s2}$ has a 'basin of attraction' for RG flows. A system, or flow, which starts off inside these basins necessarily terminates at the stable fixed point. There is also a dividing surface between these basins; illustrated by a dashed line in the

figure. Hamiltonians along this flow line tread a fine path between the two stable fixed points. A slight change in parameters would lead the system to one of the stable fixed points. A system precisely on this flow, and therefore precisely at the transition, moves towards the third fixed point $\hat{H}_c^*$.

The fixed point structure of a Hamiltonian determines the RG flows, and hence determines the phase diagram of a physical system. The question arising now is how one determines the fixed points of a given Hamiltonian. It turns out not to be easy to explain this analysis in general terms. Indeed, in some cases [78] fixed points have only been identified by results of numerical procedures: the NRG is particularly well suited to this purpose. We postpone the discussion of the fixed points which arise for the 2LM until section 4.2 in order to separate the more general ideas of this chapter from specific results.

3.5 Calculation of dynamic properties

The previous sections have been concerned with solving the Hamiltonian in (3.9) to obtain its eigensystem and temperature-dependent thermodynamic properties. Of course, having a solution to a Hamiltonian can lead to some very powerful results. In this section we detail how the Hamiltonians acquired from the NRG (the $\hat{H}_N$) may be used to calculate dynamic properties of the system.

We focus on the single-particle spectrum $D_{ij;\sigma}(\omega) = -\frac{1}{\pi}\operatorname{Im} G_{ij;\sigma}(\omega)$, with $G_{ij;\sigma}(\omega)$ an impurity Green function itself given by $G_{ij;\sigma}(\omega) = \langle\langle d_{i\sigma}; d_{j\sigma}^\dagger\rangle\rangle_\omega$.[4] An equivalent and more useful representation of $D_{ij;\sigma}(\omega)$ arises via its Lehmann representation [20]:

$$D_{ij;\sigma}(\omega) = \sum_{a,b}\langle b|d_{i\sigma}|a\rangle\langle a|d_{j\sigma}^\dagger|b\rangle\frac{\exp(-\beta E_a)}{Z}\delta(\omega + E_a - E_b). \tag{3.24}$$

Here $Z = \sum_x \exp(\beta E_x)$ is the system partition function and E_x the energy of the many body state $|x\rangle$. It is seen that the spectral density is just the Boltzmann weighted sum of transition amplitudes between all states of the Hamiltonian. The matrix elements in (3.24) are readily calculable from the NRG Hamiltonians $\hat{H}_N$.

A problem immediately arises when one tries to implement (3.24) with the NRG. In section 3.3 we explained how each $\hat{H}_N$ is only valid for a particular energy scale and so one cannot obtain $D_{ij;\sigma}(\omega)$ from one $\hat{H}_N$ alone. Instead one must piece together information from across all iterations. The simplest method would be to take poles calculated from every iteration. Indeed this method has been used previously to quite some success [79, 80]. However there are some unsatisfactory

[4] The notation $\langle\langle A; B\rangle\rangle_\omega$ denotes the Fourier transform of the retarded correlator $G_{AB}^R(t) = -i\theta(t)\langle[A(t), B(t=0)]_+\rangle$. An advanced correlator is equally defined as $+i\theta(-t)\langle[A(t), B(t=0)]_+\rangle$. The two components are related by $\operatorname{Re} G^A(\omega) = \operatorname{Re} G^R(\omega)$ and $\operatorname{Im} G^A(\omega) = -\operatorname{Im} G^R(\omega)$. We choose to work largely with retarded Green functions and drop the R superscript.

consequences of doing this, not least the conceptual problems which arise. Clearly, there are overcounting ambiguities if one calculates matrix elements between the states of $\hat{H}_N$, retains those states to calculate $\hat{H}_{N+1}$ and then recalculates matrix elements. A simple resolution of this would be to only calculate matrix elements between states which are discarded between iterations. This idea forms part of the method now used, as we will see in due course.

After deciding on an appropriate scheme to form $D_{ij;\sigma}(\omega)$ there is a final step which must be made to realise useful results. The NRG deals with a discretized version of the full system Hamiltonian. The resulting single-particle spectrum is also therefore discrete [as implied by (3.24)]. In reality we expect a continuum form for $D_{ij;\sigma}(\omega)$ and so we broaden the NRG results to obtain a continuous spectra. In the simplest schemes, each pole is replaced with a smooth Gaussian peak of the same weight [81]:

$$g_n\delta(\omega-\omega_n)\rightarrow g_n\frac{e^{-b^2/4}}{b\omega_n\sqrt{\pi}}\exp\left[-\frac{(\ln\omega-\ln\omega_n)^2}{b^2}\right]. \tag{3.25}$$

The index n runs over all the poles with g_n and ω_n the corresponding poles weights and frequencies.[5] The parameter b governs the widths of the Gaussians and is chosen to produce smooth spectra.

The logarithmic discretization of the Hamiltonian and the necessity of broadening the NRG poles are somewhat problematic. Since high-energy scales correspond to low N, the NRG does not capture high-energy features well: one has only a few states from which to calculate poles. This is to be expected since the NRG is designed to access the low-energy properties. At low energies, the NRG poles tend to be clustered around certain energies. This stems naturally from logarithmic discretization and has the consequence that at low frequencies the spectra oscillate periodically on a logarithmic scale (evidenced in fig. 3.8). The choice of b in (3.25) is therefore somewhat delicate. Wide Gaussians will suppress the low frequency oscillations but also potentially 'wash out' narrow spectra features.

As the spectral oscillations result from the logarithmic discretization, it seems sensible to try modifying the discretization procedure. One such way [83–85] is the so-called 'interleaved-NRG' approached (often referred to as the 'z'-trick). This procedure modifies the discretization using a twist parameter z lying in the interval $0<z\leq 1$. The n^{th} logarithmic interval is now chosen to be $\Lambda^{-(z+n+1)}<k<\Lambda^{-(z+n)}$; the effect being to slide (or twist) the intervals away from their usual positions. This also has the effect of sliding the oscillations observed in spectra. By performing several NRG calculations with appropriate values of z, and averaging results, the oscillations can be made to cancel (see fig. 3.8). The limit of choosing

[5] The rather more complicated kernel used in this work can be found in the ref. [82].

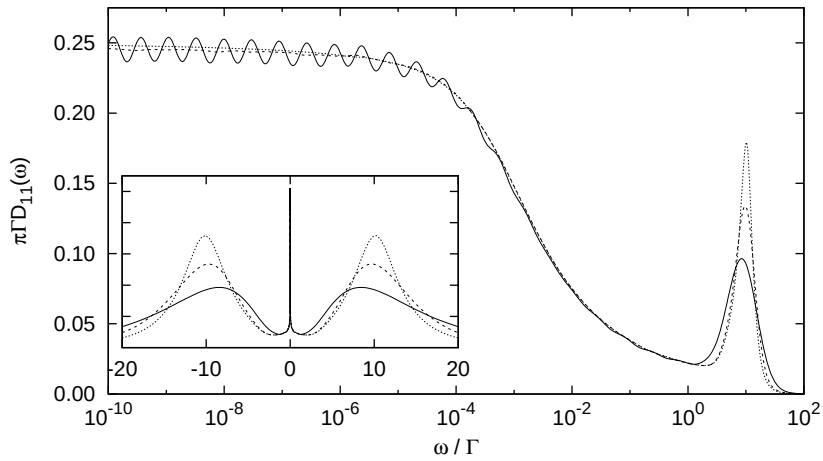

Figure 3.8: Single-particle spectral density $D_{11}(\omega)$ for the 2LM with $U/\Gamma = 20$, $U'/\Gamma = 10$, $J_H/\Gamma = 5$ and $\epsilon_{i\sigma} = -20$. Results from three NRG calculations are shown both on a logarithmic scale and linear scale (inset). *i) Solid line*: A standard NRG calculation. *ii) Dashed line*: A calculation using the interleaved method with five choices of the twist parameter and also a narrower broadening kernel. *iii) Dotted line*: As *ii)* but with an intermediate calculation of the impurity self-energy (section 3.5.1). The oscillations in *i)* are not present in *ii)* despite the choice of a smaller broadening parameter b. The self-energy calculation corrects an undershoot in the zero-frequency value, which should correctly be 0.25, and further sharpens the high-energy features.

infinitely many zs recovers a continuum limit (although it is not precisely the same continuum limit as taking $\Lambda \to 1$ [73]). Use of the z-trick has a secondary advantage: as the oscillations are reduced the broadening parameter can be reduced to improve simultaneously higher energy spectral features.

3.5.1 Green functions and the self-energy

The spectral density is not the only dynamic quantity for understanding the low-energy physics of quantum impurities. A second useful probe is the impurity self-energy $\Sigma_{ij;\sigma}(\omega)$ as embodied in the Dyson equation:

$$\mathbf{G}_\sigma(\omega) = \mathbf{G}^0_\sigma(\omega) + \mathbf{G}^0_\sigma(\omega)\mathbf{\Sigma}_\sigma(\omega)\mathbf{G}_\sigma(\omega), \tag{3.26}$$

where all the quantities appearing are, in general, matrices and the $G^0_{ij;\sigma}(\omega)$ are the non-interacting impurity Green functions *i.e.* those found when the interaction terms in the impurity Hamiltonian (such as U) are set to zero.

To obtain expressions for the Green functions appearing in (3.26) we can use an equation of motion approach, in which the following naturally arises when considering time-dependent (fermion) operators in the Heisenberg picture [20, 86]:

$$\omega^+\langle\langle \hat{A}; \hat{B}\rangle\rangle_\omega = \langle[\hat{A}, \hat{B}]_+\rangle + \langle\langle[\hat{A}, \hat{H}]; \hat{B}\rangle\rangle_\omega, \tag{3.27}$$

with $\omega^+ = \omega + i0^+$. For the impurity and conduction band electrons of the 2LM this gives directly:

$$(\omega^+ - \epsilon_{i\sigma})G^0_{ij;\sigma}(\omega) = \delta_{ij} + \sum_{\mathbf{k}} V_{i\mathbf{k}} G^0_{\mathbf{k}j}(\omega) \tag{3.28a}$$

$$(\omega^+ - \epsilon_{\mathbf{k}})G^0_{\mathbf{k}j}(\omega) = \sum_{l=1,2} V_{\mathbf{k}l} G^0_{lj;\sigma}(\omega). \tag{3.28b}$$

By defining:

$$\Gamma_{ij}(\omega) = \sum_{\mathbf{k}} \frac{V_{i\mathbf{k}} V_{j\mathbf{k}}}{\omega^+ - \epsilon_{\mathbf{k}}} \equiv \Gamma^R_{ij}(\omega) - i\Gamma^I_{ij}(\omega), \tag{3.29}$$

[where $\Gamma^I_{ij}(\omega) = \pi \Sigma_{\mathbf{k}} V_{i\mathbf{k}} V_{j\mathbf{k}} \delta(\omega - \epsilon_{\mathbf{k}})$] and combining (3.28a) and (3.28b) one arrives at

$$\mathbf{G}^0_\sigma(\omega) = \mathbf{g}^0_\sigma(\omega) + \mathbf{g}^0_\sigma(\omega)\mathbf{\Gamma}(\omega)\mathbf{G}^0_\sigma(\omega), \tag{3.30}$$

with $g^0_{ij;\sigma}(\omega) = \delta_{ij}/(\omega^+ - \epsilon_{i\sigma})$ and the non-interacting Green functions given explicitly by:

$$[\mathbf{G}^0_\sigma(\omega)]^{-1} = \begin{pmatrix} \omega^+ - \epsilon_{1\sigma} - \Gamma_{11}(\omega) & -\Gamma_{22}(\omega) \\ -\Gamma_{22}(\omega) & \omega^+ - \epsilon_{2\sigma} - \Gamma_{22}(\omega) \end{pmatrix}. \tag{3.31}$$

The similarity of (3.30) to the Dyson equation of (3.26) informs us of the relation between the non-interacting and fully-interacting cases: $\mathbf{G}_\sigma(\omega)$ has the same algebraic structure as $\mathbf{G}^0_\sigma(\omega)$ except with $\mathbf{\Gamma}(\omega)$ replaced by $\tilde{\mathbf{\Gamma}}(\omega) = \mathbf{\Gamma}(\omega) - \mathbf{\Sigma}_\sigma(\omega)$.[6]

As one can calculate the spectral densities $D_{ij;\sigma}(\omega) = -\frac{1}{\pi} \operatorname{Im} G_{ij;\sigma}(\omega)$, it is possible to calculate the self-energy matrix directly using the Dyson equation and (3.31), the corresponding real parts of the $G_{ij;\sigma}(\omega)$s can be calculated via Hilbert transforms. However there is a rather more elegant approach [81] which we now show. By taking the fully-interacting Hamiltonian and placing it in (3.27) a simple, if lengthy, calculation yields

$$\sum_l \left[(\omega^+ - \epsilon_{i\sigma})\delta_{il} - \Gamma_{il}(\omega)\right] G_{lj;\sigma}(\omega) = \delta_{ij} + \langle\langle [d_{i\sigma}, \hat{H}_D]; d^\dagger_{j\sigma}\rangle\rangle_\omega. \tag{3.32}$$

This is a generalisation of equation (6) of [81] and can be expressed more succinctly in the matrix form

$$[\mathbf{G}^0_\sigma(\omega)]^{-1}\mathbf{G}_\sigma(\omega) = \mathbf{1} + \mathbf{F}_\sigma(\omega). \tag{3.33}$$

Finally using the Dyson equation in the form $[\mathbf{G}^0_\sigma(\omega)]^{-1} = [\mathbf{G}_\sigma(\omega)]^{-1} + \mathbf{\Sigma}_\sigma(\omega)$, equation (3.33) gives:

$$\mathbf{\Sigma}_\sigma(\omega) = \mathbf{F}_\sigma(\omega)[\mathbf{G}_\sigma(\omega)]^{-1}, \tag{3.34}$$

which is the equation we use to calculate self energies from NRG data.

[6] To see this more clearly rearrange (3.26) and (3.30) as $[\mathbf{G}_\sigma(\omega)]^{-1} = [\mathbf{G}^0_\sigma(\omega)]^{-1} - \mathbf{\Sigma}_\sigma(\omega)$ and $[\mathbf{G}^0_\sigma(\omega)]^{-1} = [\mathbf{g}^0_\sigma(\omega)]^{-1} - \mathbf{\Gamma}(\omega)$ respectively.

In the case of the 2LM, $\hat{H}_{\mathrm{D}}$ is given by the separable sum $\hat{H}_D = U\Sigma_i \hat{n}_{i\uparrow}\hat{n}_{i\downarrow} + U'\hat{n}_1\hat{n}_2 - J_H\hat{\mathbf{s}}_1\cdot\hat{\mathbf{s}}_1$. The elements of the matrix $\mathbf{F}$ are thus linearly separable as $F_{ij} = F_{ij}^{U} + F_{ij}^{U'} + F_{ij}^{J_H}$ (in obvious notation). Since each such term is a retarded correlation function, they are Lehmann resolvable [87]. By writing $F_{ij;\sigma}(\omega) = F^R_{ij;\sigma}(\omega) - iF^I_{ij;\sigma}(\omega)$ the general result is:

$$\int_{-\infty}^{+\infty} F^I_{ij;\sigma}(\omega)\,\mathrm{d}\omega = \frac{1}{N_\alpha}\sum_\alpha \langle\psi^N_\alpha|\left[[d_{i\sigma}, \hat{H}_D], d^\dagger_{j\sigma}\right]_+|\psi^N_\alpha\rangle \tag{3.35}$$

where ψ^N_α is the N^{th} state of the N_α-degenerate ground state manifold of the system. Specifically for the present problem, a lengthy calculation yields, for the diagonal components of the $\mathbf{F}_\sigma(\omega)$ matrix:

$$\begin{aligned}
\int_{-\infty}^{+\infty} F^I_{ii;\sigma}(\omega)\,\mathrm{d}\omega &= \frac{1}{N_\alpha}\sum_\alpha \langle\psi^N_\alpha|U\hat{n}_{i-\sigma} + U'\hat{n}_{\bar{i}} - \tfrac{1}{2}J(\delta_{\sigma\uparrow} - \delta_{\sigma\downarrow})\hat{S}^z_{\bar{i}}|\psi^N_\alpha\rangle && \text{(3.36a)}\\
&= U\langle\hat{n}_{i-\sigma}\rangle + U'\langle\hat{n}_{\bar{i}}\rangle - \tfrac{\sigma}{2}J\langle\hat{S}^z_{\bar{i}}\rangle && \text{(3.36b)}\\
&\overset{h=0}{=} \tfrac{1}{2}U\langle\hat{n}_i\rangle + U'\langle\hat{n}_{\bar{i}}\rangle, && \text{(3.36c)}
\end{aligned}$$

(with $\bar{i} = 2$ if $i = 1$, and vice versa) where (3.36c) results only in the absence of a magnetic field ($h = 0$). For the off-diagonal elements we have similarly:

$$\begin{aligned}
\int_{-\infty}^{+\infty} F^I_{ij;\sigma}(\omega)\,\mathrm{d}\omega &= \frac{1}{N_\alpha}\sum_\alpha \langle\psi^N_\alpha| - U'd^\dagger_{j\sigma}d_{i\sigma} + \tfrac{1}{2}J\big(\delta_{\sigma\uparrow}[d^\dagger_{j\downarrow}d_{i\downarrow} + \tfrac{1}{2}d^\dagger_{j\uparrow}d_{i\uparrow}] && \text{(3.37a)}\\
&\qquad + \delta_{\sigma\downarrow}[d^\dagger_{j\uparrow}d_{i\uparrow} + \tfrac{1}{2}d^\dagger_{j\downarrow}d_{i\downarrow}]\big)|\psi^N_\alpha\rangle\\
&\overset{h=0}{=} (-U' + \tfrac{3}{4}J)\langle d^\dagger_{j\sigma}d_{i\sigma}\rangle. && \text{(3.37b)}
\end{aligned}$$

We will make use of these results in chapter 5.

The utility of (3.34) becomes apparent when it is realised that the calculation of the self-energy involves taking quotients of correlation functions calculated via the NRG. As discussed previously the NRG data are prone to oscillations at low frequencies. These oscillations effectively cancel when the division is performed, giving a much smoother representation of the self-energy. A fortunate side effect of the method is that also any systematic constant scaling error in the functions is cancelled. Furthermore, by incorporating the exact non-interacting Green functions the high energy features are more well resolved (see fig. 3.8).

The more elaborate way of calculating the impurity self-energy is therefore superior to the naive use of the Dyson equation; it is at the expense of calculating twice the number of correlation functions however. Once the self-energy has been calculated in this way, improved spectral functions can be obtained by reuse of the Dyson equation. It is the reliable initial calculation of the single-particle densities which we turn to now.

3.5.2 The full density matrix

The methods for calculating dynamical quantities from the NRG have developed considerably since the early 1990s. As outlined previously the earliest methods [80, 88] calculated matrix elements between all the NRG states of each iteration to compile results for the Lehmann resolved spectral density (3.24) — each iteration giving results for frequencies around its characteristic energy scale. An improvement to this method [79] is to find an appropriate weighting function for the poles calculated at each iteration, the weighting function used to increase (decrease) the influence of those poles thought to be most (least) accurately calculated.

As is evident from the preceding paragraph, these methods are conceptually 'standing on thin ice'. The ambiguities in how to combine overlapping results from different iterations are obvious. As already mentioned, the phenomenological patching schemes above neglect the fact (or at best correct for it in an *ad hoc* manner) the completeness of the basis states. This can lead to the total spectral weight being less than or greater than unity. More fundamentally, the states of an NRG iteration N are those of an effective Hamiltonian H_N, valid at a temperature T_N; it is not obvious that these states can be used to calculate dynamic properties of the system at any other temperature. This is particularly true for the case of $T = 0$, where only excitations from the ground state should be considered. The true ground state is only recovered in the limit $N \to \infty$, with the NRG Hamiltonian H_N being a close approximation only when the iterative process has come close to the correct $T = 0$ stable fixed point. A more satisfactory approach would be therefore to work from the correct ground state (or at least the best approximation to it which is available).

There are then two issues to be resolved: the completeness of the basis states used to construct the Lehmann sum and, the determination of a correct, well-defined, prescription for obtaining results across the full energy range. It turns out that the first issue is remarkably easy to resolve [89–91].[7] The states of the initial NRG Hamiltonian H_0 are complete. It is only at iterations $N > N_0$ after the truncation procedure has begun that this property is lost. The states at iteration $N = n$ which are discarded (the 'D' states) are necessarily orthogonal to those states which are kept ('K' states). It follows that the D states of iteration n are also orthogonal to all of the states (both K and D) of all iterations $m > n$, since these are formed from the K states of iteration n. The states of iterations $m > n$, eigenstates of $\hat{H}_m$, form a better approximation to the low-energy states of the full Hamiltonian $\hat{H}$ than those of $\hat{H}_n$. It is not difficult to see that the set of states formed by all D states across all

[7] These original papers discuss the reformulation of the Wilson chain as a system and environment — language which stems from the comparison of NRG with DMRG. We will avoid this language here.

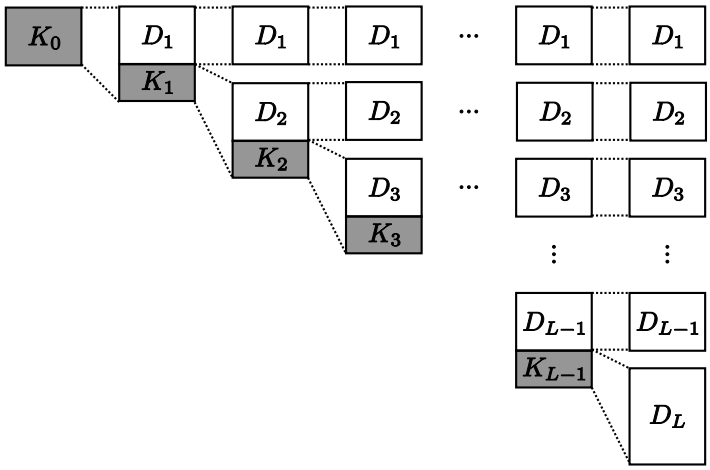

Figure 3.9: Illustration of the Anders-Schiller basis used in the accurate calculation of dynamic quantities from the NRG Hamiltonians. States of each iteration are classified as discarded 'D' or kept 'K' according to whether they are used in the calculation of the next iteration of the NRG. The set of D states across all iterations (the rightmost column) is complete and is the most accurate approximation to the exact Hamiltonian.

iterations, with the states of the final iteration $N = L$ being considered as discarded, forms the best approximation available to the exact Hamiltonian $\hat{H}$ whilst also being complete — inclusion of the K states would lead to overcounting. A mathematically rigorous formulation of the ideas above can be found in [91]. This basis has become known as the Anders-Schiller basis (AS) and is illustrated in fig. 3.9.

The complete AS basis allows one to accurately represent arbitrary local impurity operators, and hence calculate correlation functions between pairs of operators. From the discussion above the unity operator in the AS basis can be constructed as the sum of all states labelled D, *viz.*:

$$\hat{1} = \sum_{N>N_0}^{L} \sum_{s} |s\rangle_{N}^{D\,D} \langle s| \tag{3.38}$$

and is used to construct an operator $\hat{A}$ given by [82]:

$$\hat{A} = \sum_{ss'} |s\rangle_{N_0}^{K} [A_{KK}^{N_0}]_{ss'} {}_{N_0}^{K}\langle s'| = \sum_{N>N_0}^{L} \sum_{XX'}^{\neq KK} \hat{A}_{XX'}^{N}. \tag{3.39}$$

Here $XX' = \{KK, KD, DK, DD\}$ with the restricted sum excluding the KK terms which are refined in later iterations where a better approximation to the true states of the Hamiltonian is found. The left equality represents the operator $\hat{A} = \hat{A}_{KK}^{N_0}$ in the last complete NRG basis. The right-hand side by contrast expresses an iterative

construction of $\hat{A}$ in the AS basis, the KK part at iteration N being discarded in favour of the XX' terms of the next iteration:

$$\hat{A}^{N-1}_{KK} = \sum_{XX'} \hat{A}^{N}_{XX'} = \sum_{ss'} \sum_{XX'} |s\rangle^{X}_{N} [A^{N}_{XX'}]_{ss'} {}^{X'}_{N}\langle s'|. \tag{3.40}$$

A second important feature of operators constructed in this way is that their time-dependent forms, $\hat{A}(t) = e^{i\hat{H}t}\hat{A}e^{-i\hat{H}t}$, contain energy differences between states of the same iteration *i.e.* calculated to the same level of accuracy [82]. Thus, the issues outlined above have largely been resolved.

To obtain thermal averages of operators required in the calculation of correlation functions,[8] we construct the density matrix of the system [82]:

$$\begin{aligned} \hat{\rho} &= \sum_{N>N_0}^{L} \sum_{s} |s\rangle^{D}_{N} \frac{e^{-\beta E^{N}_{s}}}{Z} {}^{D}_{N}\langle s| \\ &= \sum_{N>N_0}^{L} w_N \rho^{N}_{DD}, \end{aligned} \tag{3.41}$$

where in the second line we have split the sum into a sum of density matrices, one for the discarded states at each iteration. The weighting factor $w_N = 4^{(L-N)} Z^{D}_{N}/Z$ with $Z^{D}_{N} = \sum^{D}_{s} e^{-\beta E^{N}_{s}}$ performs the task of selecting the appropriate iterations for a given temperature; it is smooth and contains a peak spanning 5-10 iterations around the iteration with $k_{\mathrm{B}}T_N = 1/\beta$. By expressing correlation functions in terms of similar sums $\mathcal{F}_{ij;\sigma} = \sum_N \mathcal{F}^{N}_{ij;\sigma}$, we are now in a position to calculate such functions via analogous relations to (3.24) [82]:

$$\begin{aligned} \mathcal{F}^{N}_{ij;\sigma} &= \langle\langle \hat{A}_{ij;\sigma}; \hat{B}_{ij;\sigma} \rangle\rangle_{\omega} \\ &= \sum_{M>N_0}^{L} \sum_{ss'} \sum_{XX'}^{\neq KK} [B^{M}_{X'X} \rho^{[MN]}_{XX}]_{s's} [A^{M}_{XX'}]_{ss'} \delta(\omega - E_s + E_{s'}), \end{aligned} \tag{3.42}$$

the structure of which is simply a sum of delta function poles with weights given by the elements of the matrix product $(B\rho)^{\dagger} \circ A$.[9]

Equation (3.42) contains one feature which deserves further explanation: the appearance of the $\rho^{[MN]}_{XX}$ density matrices. These ultimately allow determination of excitations between not only the D states of each iteration, but also between the low-energy K states and the high energy D states. Creating such matrices in the AS basis is non-trivial. As shown in ref. [82] one must iterate backwards from the

[8] Recall that the NRG is inherently a finite temperature technique and so thermal averaging is required conceptually for the calculation of any quantity, static or dynamic.

[9] The Hadamard (or Schur) product is an element wise product $[A \circ B]_{ij} = A_{ij} B_{ij}$

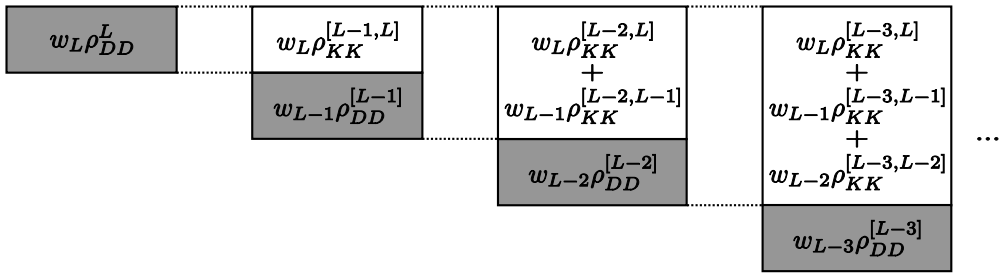

Figure 3.10: Iterative calculation of the full density matrix utilising the Anders-Schiller basis. One starts at the last NRG iteration L, and perform a unitary transforms to acquire the density matrix in the original NRG basis of interation $L-1$. The unrefined discarded (DD) part of the matrix is added and the process iterated until the first iteration where no states were discarded.

final NRG iteration performing similarity transforms. Figure 3.10 illustrates this process. One starts with $\rho_{DD}^{N=L}$, the (diagonal) density matrix for all states of the last iteration. The unitary eigenvector matrix of iteration L is used to transform this into $\rho_{KK}^{[L-1,L]}$; the matrix now being in the NRG basis of iteration $L-1$ and non-diagonal. The total ρ^{L-1} is then formed by adding ρ_{DD}^{L-1}. The general form for the full density matrix at iteration M is thereby:

$$\rho^M = w_M \rho_{DD}^M + \sum_{N>M}^{L} w_N \rho_{KK}^{M,L}. \tag{3.43}$$

The iterative calculation stops at iteration N_0, at which point there is no DD contribution. These density matrices are often termed 'reduced' as they relate to the 'system' comprised of the impurity and the first M sites of the Wilson chain, as distinct from the 'environment' comprising the as yet uncoupled sites of the chain; the reduced matrix represents a 'partial trace' of the density matrix of the whole system [89]. (In fact, without the approximation $\hat{H}_L = \hat{H}$, the final density matrix calculated is also a partial trace over the infinite Wilson chain).

This concludes our outline of how reliable dynamic properties may be calculated from the NRG. Whilst being important theoretically, single-particle densities are rarely measured directly in experimental quantum dot systems. A far more important quantity is the differential conductance, to which we now turn.

3.5.3 Differential conductance

The starting point for the calculation of the differential conductance ('the conductance' henceforth) is the Landauer formula for the steady-state current J through an interacting electron region, as derived by Meir and Wingreen [92]. The result is

given generally by [92]:

$$J = \frac{2ie}{h}\int_{-\infty}^{+\infty} \mathrm{Tr}\left\{[f_L(\omega)\mathbf{\Gamma}_L^I(\omega) - f_R(\omega)\mathbf{\Gamma}_R^I(\omega)][\mathbf{G}^r(\omega) - \mathbf{G}^a(\omega)]\right\} + \mathrm{Tr}\left\{[\mathbf{\Gamma}_L^I(\omega) - \mathbf{\Gamma}_R^I(\omega)]\mathbf{G}^<(\omega)\right\}\mathrm{d}\omega. \tag{3.44}$$

Here the Fermi functions $f_\nu(\omega) = [e^{\beta(\omega-\mu_\nu)}+1]^{-1}$ (with $\nu = L, R$) describe two non-interacting electron regions (leads) positioned to the left (L) and to the right (R) of the interacting region of interest (*i.e.* quantum dot), with μ_ν their respective chemical potentials. The couplings to these regions are given by $[\mathbf{\Gamma}_\nu^I(\omega)]_{ij} = \pi V_{i\nu}V_{j\nu}\rho(\omega)$ (where i, j denote the dot levels).[10] Finally $\mathbf{G}^r(\omega)$, $\mathbf{G}^a(\omega)$ and $\mathbf{G}^<(\omega)$ are the retarded, advanced and non-equilibrium Keldysh 'lesser' Green functions, the latter defined as $G_{AB}^<(t) = i\langle B(t=0)A(t)\rangle$.

We now derive a simplified version of this fundamental equation appropriate for the 2LM. Equation (3.44) is simply a sum of two terms: $J = \frac{1}{2}(J_L - J_R)$ where the current *to* the left is J_L, and *from* the right is $-J_R$. At steady state these are both equal to the total current J and so we can write:

$$J = \frac{1}{1+\lambda}J_L + \frac{\lambda}{1+\lambda}(-J_R), \tag{3.45}$$

for an arbitrary parameter λ. Equation (3.44) then becomes:

$$J = \frac{4ie}{h}\int_{-\infty}^{+\infty}\frac{1}{1+\lambda}\mathrm{Tr}\left\{[f_L(\omega)\mathbf{\Gamma}_L^I(\omega) - \lambda f_R(\omega)\mathbf{\Gamma}_R^I(\omega)][\mathbf{G}^r(\omega) - \mathbf{G}^a(\omega)] + [\mathbf{\Gamma}_L^I(\omega) - \lambda\mathbf{\Gamma}_R^I(\omega)]\mathbf{G}^<(\omega)\right\}\mathrm{d}\omega. \tag{3.46}$$

In section 2.3.3 we considered the 2LM for the case where the couplings to the left and right leads were proportional *i.e.* that

$$\mathbf{\Gamma}_L^I(\omega) = \lambda\mathbf{\Gamma}_R^I(\omega). \tag{3.47}$$

Hence only the first term of (3.46) remains giving:

$$J = \frac{4e}{h}\frac{1}{1+\lambda}2\pi\int_{-\infty}^{+\infty}[f_L(\omega) - f_R(\omega)]\,\mathrm{Tr}[\mathbf{\Gamma}_L^I(\omega)\mathbf{D}(\omega)]\mathrm{d}\omega, \tag{3.48}$$

where we have used $\mathbf{G}^r(\omega) - \mathbf{G}^a(\omega) = -2\pi i\mathbf{D}(\omega)$, the spectral density. Equivalently, using (3.47), we can write

$$J = \frac{2e}{h}G_0\int_{-\infty}^{+\infty}[f_L(\omega) - f_R(\omega)]\,\mathrm{Tr}[\pi\mathbf{\Gamma}^I(\omega)\mathbf{D}(\omega)]\mathrm{d}\omega, \tag{3.49}$$

[10] The original paper defines $[\mathbf{\Gamma}_\nu^I(\omega)]_{ij}$ as double the quantity defined here, we choose our definition to maintain consistency with (3.3).

Figure 3.11: The current through an interacting electron region coupled to two non interacting reservoirs is composed of two terms: J_L and J_R. At steady state $J = J_L = -J_R$

where $G_0 = 4\lambda/(1+\lambda)^2$ and $\mathbf{\Gamma}^I(\omega) = \mathbf{\Gamma}^I_L(\omega) + \mathbf{\Gamma}^I_R(\omega)$ [as given by (3.29)]. The prefactor $G_0 \in [0,1]$ reflects the relative asymmetry in the tunnel coupling to the leads and reaches a maximum for symmetric coupling. It is most easily expressed in terms of the angle appearing in (2.41) *viz.*: $G_0 = \sin^2 2\theta$ with $\theta \in [0, \pi/2]$. Now the current through the 2LM system is known it is straightforward to find the differential conductance. One simply differentiates (3.49) with respect to a bias voltage $V_{\rm sd}$ applied across the left (source) and right (drain) leads, with $\mu_L - \mu_R = eV_{\rm sd}$. In the limit that this voltage tends to zero (zero-bias) the conductance is readily shown to be:

$$G_C(T, V_{\rm sd}=0) = \frac{2e^2}{h} G_0 \int_{-\infty}^{+\infty} \frac{-\partial f(\omega)}{\partial \omega} \sum_{ij} \pi \Gamma^I_{ij}(\omega) D_{ji}(\omega; T) \mathrm{d}\omega, \tag{3.50}$$

expressed in terms of a single Fermi function $f(\omega) = (e^{\beta\omega}+1)^{-1}$ with chemical potential $\mu = 0$. The non-trivial quantities appearing in (3.50) are the equilibrium spectral densities $D_{ij}(\omega; T)$ (with their temperature dependence now explicit) which, as we have seen in the previous section, can be reliably calculated using the NRG.

Whilst this is an important result, experiments are not confined to measuring systems at equilibrium, *i.e.* under the condition that the chemical potentials of the two leads are equal $\mu_L = \mu_R$. It is now becoming possible to use the NRG to calculate non-equilibrium and time-dependent quantities [90, 91, 93–95], however, the calculations are extremely demanding and as yet not very accurate: essentially one performs NRG calculations for multiple discrete time intervals. Here we use the common approximation of neglecting the explicit bias dependence of the impurity self-energies. It is easily shown from (3.49) that the finite-bias conductance is given by:

$$G_C(T, V_{\rm sd}) \approx \frac{2e^2}{h} G_0 \int_{-\infty}^{+\infty} \left[\frac{-\partial f_L}{\partial \omega} + \frac{-\partial f_R}{\partial \omega} \right] \sum_{ij} \Gamma^I_{ij}(\omega) \pi D_{ji}(\omega) \mathrm{d}\omega. \tag{3.51}$$

The bias voltage enters only via the Fermi functions $f_\nu(\omega)$: $\mu_L \neq \mu_R$. This approximation becomes exact for $V_{\rm sd} \to 0$, where (3.50) is recovered (so we might reasonably expect it to work well in practice for relatively low bias voltages); and it is also exact

in the non-interacting limit. Care must be taken however when analysing fine details of experiment, as even at low voltages Hewson has shown [96] that including the effect of the bias voltage on $D_{ij}(\omega)$ can alter the appearance of spectral features of interest.

Having discussed the NRG is some detail, both as a numerical tool for solving complex many-body Hamiltonians and as a framework for understanding the physical properties of such systems, we now turn to applying it to study the behaviour of model quantum dot systems via the 2LM.

CHAPTER 4

Two-Level Quantum Dots

In chapter 2 we introduced the Anderson impurity model and the Kondo model as prototypical quantum impurity models. We outlined a few early advances in obtaining solutions to these models, illustrating the fundamental ideas of universality and scaling. In the $T \to 0$ limit the effective Kondo coupling between the impurity and itinerant electrons runs to infinity, and so perturbative techniques ultimately failed to successfully describe the correct behaviour of these models in this limit.

Towards the end of chapter 2 we introduced also the two-level model (2LM) for describing more accurately the physics of semiconductor and molecular quantum dot devices, whilst in chapter 3 we developed the machinery necessary to calculate physical properties of this model.

In this chapter we survey the basic thermodynamic properties of the 2LM. We begin by examining the atomic limit (AL) of the model. We will examine the symmetries of the model which will later assist in the understanding of some subtle physical points. The experimentally relevant RG fixed points of the model will be explored: most importantly we will identify *two* stable fixed points — indicating the possibility of a quantum phase transition (QPT) between two non-equivalent ground states. Indeed a QPT is found to arise for physically reasonable parameters of the model, and so a large proportion of this chapter will focus on the detailed study of this phase transition.

4.1 The atomic limit

The atomic limit (AL) describes the isolated impurity, detached from the conduction band, and is of course exactly soluble. An equation for it is given by (2.44c), repeated below. By analysing its properties in detail we will gain some headway in understanding the full 2LM with $V_i \neq 0$.

By ignoring the disconnected conduction band parts of (2.44) the AL Hamilto-

nian is simply:[1]

$$\hat{H}_{\rm D} = \sum_{i\sigma} \left(\epsilon_{i\sigma} + \frac{U}{2} \hat{n}_{i-\sigma} \right) \hat{n}_{i\sigma} + U' \hat{n}_1 \hat{n}_2 - J_H \hat{\mathbf{s}}_1 \cdot \hat{\mathbf{s}}_2. \tag{4.1}$$

Equation (4.1) contains two symmetries which we now examine. The particle-hole transformation (p-ht)

$$d^\dagger_{i\sigma} \leftrightarrow d_{i\sigma}, \tag{4.2}$$

exchanges particles for holes and vice-versa[2] and transforms (4.1) into the Hamiltonian

$$\begin{aligned} \hat{H}^{\rm ph}_{\rm D} = & \sum_{i\sigma} \left[\left(-\epsilon_{i\sigma} - U - 2U' \right) + \frac{U}{2} \hat{n}_{i-\sigma} \right] \hat{n}_{i\sigma} + U' \hat{n}_1 \hat{n}_2 - J_H \hat{\mathbf{s}}_1 \cdot \hat{\mathbf{s}}_2 \\ & + 2U + 4U' + \sum_{i\sigma} \epsilon_{i\sigma}. \end{aligned} \tag{4.3}$$

The above has the same form as (4.1) (modulo the constant terms on the second line) but with

$$\epsilon_{i\sigma} \to -(\epsilon_{i\sigma} + U + 2U'). \tag{4.4}$$

For zero magnetic field, as considered throughout this chapter, it is therefore useful to define rescaled parameters

$$x = \epsilon_1 + \tfrac{1}{2}U + U' \tag{4.5a}$$

$$y = \epsilon_2 + \tfrac{1}{2}U + U', \tag{4.5b}$$

such that the ph-t performs $x \to -x$ and $y \to -y$ and

$$\hat{H}_{\rm D}(x,y) \xrightarrow{\text{ph-t}} \hat{H}_{\rm D}(-x,-y) + 2(x+y). \tag{4.6}$$

The AL Hamiltonian is thereby invariant under the ph-t for $x = 0 = y$, or equivalently $\epsilon_1 = \epsilon_2 = -\frac{1}{2}U - U'$, which is the p-h symmetric point. The consequences of the ph-t are intuitively quite simple: it is a canonical transform and as such is just a different way of representing the particles in the system. The expectation value of any operator $\hat{O}(x,y)$ is identical to its transformed counterpart:

$$\langle \hat{O}(x,y) \rangle = \frac{\operatorname{Tr} \hat{O} \exp[-\beta \hat{H}(x,y)]}{\operatorname{Tr} \exp[-\beta \hat{H}(x,y)]} = \frac{\operatorname{Tr} \hat{O} \exp[-\beta \hat{H}^{\rm ph}(x,y)]}{\operatorname{Tr} \exp[-\beta \hat{H}^{\rm ph}(x,y)]} \tag{4.7a}$$

[1] The 2LM label will be dropped from $\hat{H}^{\rm 2LM}_{\rm D}$ for the remainder of the thesis, and we will make it clear when $\hat{H}_{\rm D}$ does not refer to the 2LM.

[2] $\hat{H}_{\rm D}$ is not in general invariant under this transformation; the transformation changes the sign of the total spin projection S_z. This fact is important when considering the case of an applied magnetic field. The ph-t then requires incorporating spin flips into (4.2): $d^\dagger_{i\sigma} \leftrightarrow d_{i-\sigma}$, or equivalently we might require $h \to -h$ in addition to (4.2) to maintain $\epsilon_{i\sigma} = \epsilon_i - \sigma h$ constant under the transformation.

$$\langle \hat{O}(x,y)\rangle = \langle \hat{O}^{\rm ph}(-x,-y)\rangle, \tag{4.7b}$$

where (4.7b) results from using (4.6), the constant term cancelling. Expressions for the partition function and free energy follow similarly:

$$Z(x,y) = Z(-x,-y)e^{-2\beta(x+y)} \tag{4.8a}$$

$$F(x,y) = F(-x,-y) + 2(x+y). \tag{4.8b}$$

There is also a second obvious "1–2" symmetry expressed formally by the canonical transformation

$$(d_{1\sigma}, d_{2\sigma}) \rightarrow (d_{2\sigma}, d_{1\sigma}), \tag{4.9}$$

and application of which gives $\hat{H}_{\rm D}^{12}(x,y) = \hat{H}_{\rm D}^{21}(y,x)$. Naturally the Hamiltonian, and the physical properties above, are invariant under the simultaneous exchange $1 \leftrightarrow 2$ and $x \leftrightarrow y$. The line $y = x$ thereby bisects, with regards to the physical properties of the system, the $x-y$ plane into two equivalent regions. Coupled with the ph-t (which corresponds to inversion through the origin), this second symmetry implies a third: the plane can be further bisected by the line $y = -x$. Thus in general we can confine our interests to only one quadrant of the $x-y$ plane.

We briefly note that to maintain the symmetries above in the full 2LM two further considerations must be made. Equation (4.2) must be supplemented by $c^\dagger_{\mathbf{k}\sigma} \rightarrow c_{-\mathbf{k}\sigma}$. This requires a symmetric conduction band, as we use within the NRG framework for the 2LM [24]. The full model also requires $V_1 = V_2$ to maintain the 1–2 symmetry. We take this second condition for much of our work but will briefly examine the case $V_1 \neq V_2$ in section 4.3.3.

Having discussed the underlying symmetries of (4.1) we now move to outline the AL eigenstates and ground state phase diagram. Each of the dot levels may in principle be empty, singly- or doubly-occupied. There are therefore 16 possible states with the ground state containing between zero and four electrons. The impurity parameters (ϵ_1, ϵ_2, U, U', and J_H) form, in general, a five dimensional space. However in studying the 2LM it is most useful to consider the effect of changing the level energies ϵ_1 and ϵ_2 whilst holding the other parameters fixed. To this end we will consider phase diagrams in the $\epsilon_1 - \epsilon_2$ plane (equivalently the $x-y$ plane).

The possible impurity states are listed in table 4.1. In the case of $J_H = 0$ all the states of $\hat{H}_{\rm D}$ are simultaneous eigenstates of the impurity level charges $n_i = \langle \hat{n}_i \rangle$ since the $\hat{n}_i$ clearly commute with the remaining terms of the Hamiltonian. It is therefore convenient to label the states by these occupations. For finite J_H ambiguity only arises in the $(n_1 = 1, n_2 = 1)$ sector where the four states are no longer eigenstates of the n_i with spin-singlet and triplet combinations arising. However, as is obvious from the energies given in table 4.1, it is not possible for both the singlet and triplet states to simultaneously exist as the ground state: the energy of one of these combinations

n_1	n_2	Energy
0	0	0
1	0	ϵ_1
0	1	ϵ_2
1	1	Singlet: $\epsilon_1 + \epsilon_2 + U' + \frac{3}{4}J_H$
		Triplet: $\epsilon_1 + \epsilon_2 + U' - \frac{1}{4}J_H$
2	0	$2\epsilon_1 + U$
0	2	$2\epsilon_2 + U$
2	1	$2\epsilon_1 + \epsilon_2 + U + 2U'$
1	2	$\epsilon_1 + 2\epsilon_2 + U + 2U'$
2	2	$2\epsilon_1 + 2\epsilon_2 + 2U + 4U'$

Table 4.1: Energy levels of the atomic limit Hamiltonian.

will be lower than the other throughout the $\epsilon_1 - \epsilon_2$ plane. We will largely consider $J_H > 0$ [see section 2.3.2] and so the ground state will be the triplet combination.

In fig. 4.1 we show the AL phase diagram for the generic (and physically relevant) case $U > U' > J_H$. The dotted lines indicate the boundaries between the various phases, labelled by their charges as above. The boundaries correspond to degeneracy points between the states of table 4.1 and can be obtained simply by equating the energy of the states.

There are several observations to make about the phase diagram. First an obvious point: as x and y are lowered the impurity levels progressively fill, being empty in the top right of the diagram and completely full in the bottom left. More interesting is the interplay between U' and J_H. As drawn in fig. 4.1 there is a direct transition between the $(1,0)$ and $(0,1)$ states, a consequence of $U' > \frac{1}{4}J_H$. In fact for $\frac{1}{4}J_H < U'$ this boundary is removed and the $(1,1)$ and $(0,0)$ have a direct boundary instead. For $\frac{1}{4}J_H = U'$ precisely the states $(1,1)$, $(1,0)$, $(0,1)$, and $(0,0)$ are quadruply degenerate at the point $x = y = U/2 + U'$.

A related effect is that of U' on the shape of the $(1,1)$ in the transverse direction; that is the stability of the $(1,1)$ phase with respect to the $(2,0)$ and $(0,2)$ phases. This is illustrated in fig. 4.2. In fig. 4.2a) we show the effect of increasing U' to the point that $U' = U$. This naturally has the effect of destabilising the $(1,1)$ phase with respect to the $(2,0)$ and $(0,2)$ phases. Under this regime it is only the influence of J_H which stabilises the $(1,1)$ phase; the phase collapses completely, to a line, for $J_H = 0$ where the energies of all three states are equal along the line $y = x$.

Conversely the case of $U' = 0$ is shown in fig. 4.2b) where the $(1,1)$ phase forms a more symmetrical squared shape. In this extreme limit the phase diagram becomes four-fold rotationally symmetric due to the additional symmetry lines along $x = 0$ and $y = 0$ resulting from individual p-h transforms the two levels. The effect of J_H is to truncate the corners of this square, indeed for $J_H = 0$ the phase becomes

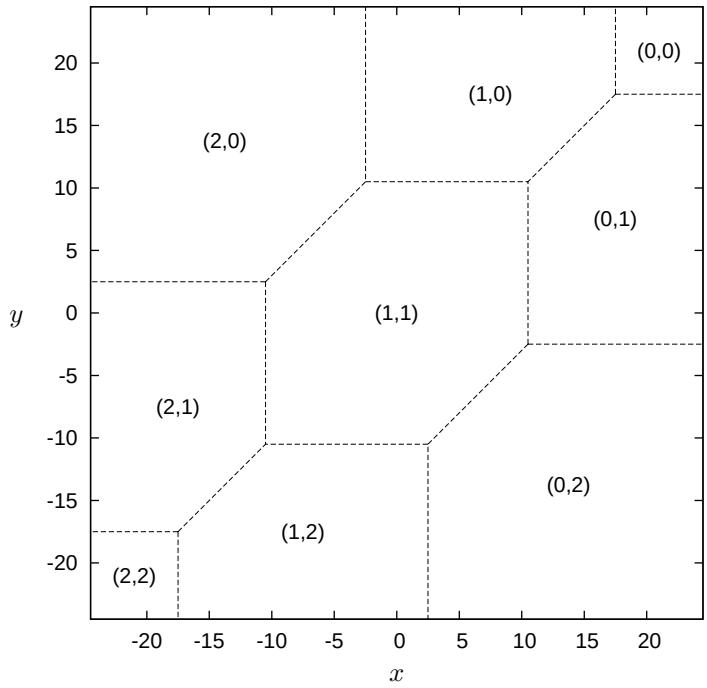

Figure 4.1: Atomic limit phase diagram in the $x - y$ plane (a simple translation of the $\epsilon_1 - \epsilon_2$ plane). Parameters are chosen as $U = 20$, $U' = 7.5$, and $J_H = 2$. All boundaries are inversion symmetric through the origin.

precisely square with the $(1,1)$, $(1,0)$, $(0,1)$, and $(0,0)$ phases (for example) meeting at the point $(x, y) = (U/2, U/2)$.

The AL and the isolated impurity states which result from it are therefore somewhat trivial. In later sections we will consider the phase diagram for the full 2LM with non-zero impurity-lead couplings. In this case only two phases will result. To understand why this should be so, we now consider the RG fixed points of the AIM and of the 2LM.

4.2 RG fixed points of the AIM and 2LM

In this section we survey the possible fixed point Hamiltonians which arise in the 2LM. We give a short summary of each and explain why and when they might be expected to occur. References will be given to sources where a fuller treatment can be found.

As discussed in [23] many of the fixed points of an impurity Hamiltonian can be identified by setting the parameters of the bare model to the special values of zero or infinity. In the section 3.4 it was shown how the RG transformation can

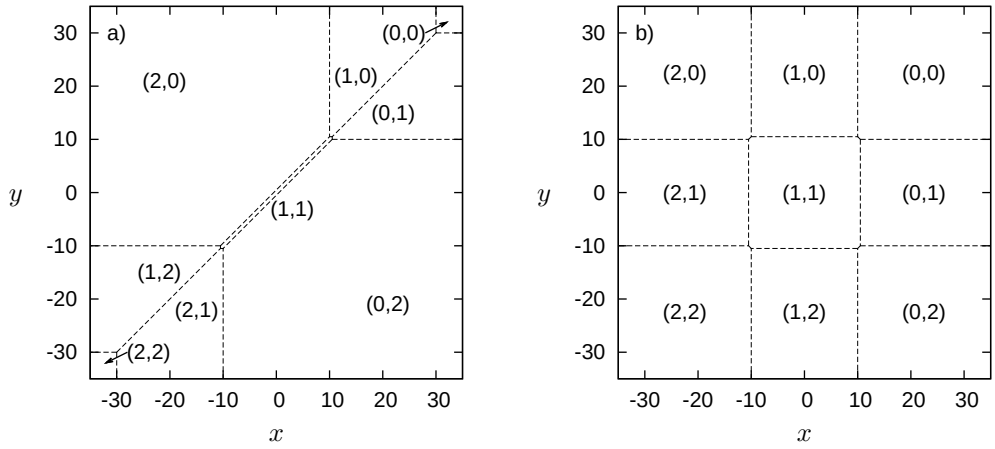

Figure 4.2: Atomic limit diagrams for the case a) $U = U'$ and b) $U' = 0$. All other parameters are the same as in fig. 4.1. The effect of U' is to stretch the phase diagram along the $y = x$ line.

be thought of as taking a Hamiltonian and 'renormalizing' its parameters into new effective parameters. By setting the bare parameters to either zero or infinity we are really saying that the fixed point has these effective parameters.

The 2LM of (2.44) is a direct extension of the more simple single impurity Anderson model (AIM). In fact if one of the impurity levels is removed to well above or well below the Fermi level of the conduction band, it follows that the remaining level acts in effect as the single level of an AIM. (We will see this explicitely in section 4.3). It is worth therefore repeating some of the arguments of [23] to obtain the fixed points of the AIM before discussing the more complex 2LM.

The equation equivalent to (3.12) appropriate for the AIM is:

$$\begin{aligned}\hat{H}_N^{\mathrm{AIM}} = \Lambda^{(N-1)/2}\Bigg[&\sum_{n=0}^{N-1}\Lambda^{-n/2}\xi_n\left(f_{n\sigma}^\dagger f_{(n+1)\sigma} + f_{(n+1)\sigma}^\dagger f_{n\sigma}\right)\\ &+\left(\bar{\epsilon}_{i\sigma}+\frac{\bar{U}}{2}\hat{n}_{i-\sigma}\right)\hat{n}_{i\sigma} + \sqrt{\bar{\Gamma}_{ii}}(f_{0\sigma}^\dagger d_{i\sigma} + d_{i\sigma}^\dagger f_{0\sigma})\Bigg],\end{aligned} \tag{4.10}$$

where i takes a single value and the full Hamiltonian $\hat{H}^{\mathrm{AIM}}$ is recovered by taking the $N \to \infty$ limit as in (3.14). If we suppose that $\bar{\Gamma}_{ii}$, $\bar{U}$, and $\bar{\epsilon}_{i\sigma}$ are set to zero, the resulting Hamiltonian $\hat{H}_{N,\mathrm{FO}}$ is split into an isolated impurity orbital at zero energy and the free-electron conduction band. As shown in [23] the initial Hamiltonian $\hat{H}_{0,\mathrm{CB}} = f_{0\sigma}^\dagger f_{0\sigma}$, *i.e.* the Hamiltonian corresponding to a free conduction band, leads to energy levels of $\hat{H}_{N,\mathrm{CB}}$ which converge as $N \to \infty$. It follows that the free conduction band Hamiltonian is a stable fixed point of the NRG transformation. We denote this fixed point $\hat{H}^*_{\mathrm{CB}}$.[3] In the limit $N \to \infty$ it is clear then that $\hat{H}_{N,\mathrm{FO}}$

[3] Actually there is an asymmetry between odd and even N iterations which gives rise to two

also corresponds to a fixed point Hamiltonian: one can construct the states of free orbital fixed point, $\hat{H}^*_{\rm FO}$, by combining the states of $\hat{H}^*_0$ with the four degenerate states of the impurity orbital. As we will see in section 4.3 such free orbital fixed points are high temperature unstable fixed points of the NRG transformation when $\bar{\Gamma}_{ii} \neq 0$ [23].

Now consider the case where $\bar{\Gamma}_{ii}$ and $\bar{\epsilon}_{i\sigma}$ are still zero but $\bar{U}$ is allowed to become infinite. As above in the free orbital case the Hamiltonian can be decomposed into the free-electron conduction band and an effective impurity site comprised of only the empty and singly occupied states, the doubly occupied state is excluded since its energy depends on U. Since this decomposition can again be made we can identify this Hamiltonian as a fixed point: the valence fluctuation fixed point $\hat{H}^*_{\rm VF}$. Like $\hat{H}^*_{\rm FO}$ it is ultimately unstable for $\bar{\Gamma}_{ii} \neq 0$ and occurs at intermediate temperatures, specifically $k_B T \lesssim U$ as one might imagine.

We can also imagine the case of $\bar{\Gamma}_{ii}$ and $\bar{U}$ being zero but letting $\bar{\epsilon}_{i\sigma} \to \infty$. The singly and doubly occupied states of the dot are now removed from our consideration. The resulting frozen impurity fixed point $\hat{H}^*_{\rm FI}$ is essentially the free-electron fixed point $\hat{H}^*_{\rm CB}$ with a modified charge due to the unoccupied impurity site. The $\hat{H}^*_{\rm FI}$ fixed point is stable. In essence, as the impurity level is placed increasingly higher in energy, it does not provide a potential for the conduction band electrons to become trapped. The itinerant electrons therefore behave as if the impurity were absent.

A rather more interesting fixed point arises when one considers fixing $\bar{\Gamma}_{ii} = 0$ and $\bar{\epsilon}_{i\sigma} = -\infty$ but varying $\bar{U}$. The lowest energy impurity states are the two singly occupied configurations, the empty and doubly occupied states being $\bar{U}$ higher in energy. Suppose that we let $\bar{U}$ run off to infinity, the impurity will be strictly singly occupied. As in section 2.2 the two impurity states can be used to define a spin-$\frac{1}{2}$ variable uncoupled from the conduction band. This is the local moment fixed point $\hat{H}^*_{\rm LM}$ and is also unstable [23].

Finally consider the case when $\bar{\Gamma}_{ii} \to \infty$ at fixed $\bar{U}$. Here the impurity is not isolated from the conduction band but binds strongly to the first conduction band orbital to form a singlet state (the coupling is antiferromagnetic). This is just as we saw from poor man's scaling with the Kondo model in section 2.2.1. We can therefore strike out the second two terms in (4.10), as these give excited states $\sim \bar{\Gamma}_{ii}^{1/2}$ higher than the ground state, and reduce the sum in the first term to exclude the $n = 0$ orbital. The remaining $(N-1)$ orbitals constitute a free conduction band, albeit with a phase shift [20], and so a fixed point: the strong coupling fixed point $\hat{H}^*_{\rm SC}$.

It would seem from the discussion above that we have five fixed points in the full AIM Hamiltonian: $\hat{H}^*_{\rm FO}$, $\hat{H}^*_{\rm VF}$, $\hat{H}^*_{\rm LM}$, $\hat{H}^*_{\rm FI}$, and $\hat{H}^*_{\rm SC}$, with the final two being stable. However from the discussion above one might deduce that in fact the final two are

distinct fixed points, both fixed points of the RG transform acting twice.

identical as they are both take the form of free-electron Hamiltonians. Indeed, in the above we have neglected the fact that the fixed point Hamiltonians are not in general particle-hole symmetric and so there exists the added complication of potential scattering. As discussed in [24] when this factor is included lines of fixed points are generated: one line each for the five fixed points outlined above. The lines arising in the frozen impurity and strong coupling cases turn out to be identical, this is shown formally in Appendix A of [24]. There is then only one stable fixed point and no phase transition possible in the AIM. A phase transition does however arise in the 2LM which we turn to now.

4.2.1 Low-energy model for the 2LM

Deep in the one-electron $(1,0)$ regime of the 2LM (fig. 4.1), the appropriate low-energy model is obviously the spin-$\frac{1}{2}$ Kondo model, a normal Fermi liquid with a fully screened spin and the same strong coupling fixed point derived above for the AIM. But what of the other isolated impurity states, encircling the $(1,1)$ triplet sector as illustrated in fig. 4.1 (and all of which are either singlets or doublets)? The salient point here is that, on coupling to the leads, *all* give rise to Fermi liquid states with a local singlet ground state: as for the asymmetric AIM, their stable low-energy fixed points form a continuous line connecting the strong coupling fixed point arising for the spin-$\frac{1}{2}$ Kondo model to the generic case of the frozen impurity fixed point. These regions of the phase diagram form a single phase in the full 2LM.

We now ask, what of the $(1,1)$ triplet sector? Deep in this sector the effective low-energy model is naturally a spin-1 Kondo model [49, 50], obtained formally by a Schrieffer-Wolff transformation retaining only the $(1,1)$ triplet states of the isolated two-level impurity. In section 4.3.2*ff* we obtain

$$\hat{H}_K^{S=1} = J_K^{S=1}\hat{\mathbf{s}}\cdot\hat{\mathbf{s}}_0 + K\hat{n}_0, \tag{4.11}$$

with $\hat{\mathbf{s}}$ representing the total impurity spin, from a rather more specific case. The Kondo coupling $J_K^{S=1}$ and potential scattering K are given explicitly in terms of the impurity parameters as:

$$J_K^{S=1}(x,y) = \frac{4N}{U+\frac{1}{2}J_H}\left[\frac{V_1^2}{1-\eta(x)^2}+\frac{V_2^2}{1-\eta(y)^2}\right] \tag{4.12a}$$

$$K(x,y) = \frac{2N}{U+\frac{1}{2}J_H}\left[\frac{V_1^2\eta(x)}{1-\eta(x)^2}+\frac{V_2^2\eta(y)}{1-\eta(y)^2}\right], \tag{4.12b}$$

where we have introduced the asymmetry function

$$\eta(z) = \frac{2z}{U+\frac{1}{2}J_H}. \tag{4.13}$$

In direct analogy to the case of the AIM (section 2.2.1), the ratio of K to $J_K^{S=1}$ is solely a function of the asymmetry:

$$\begin{aligned}\eta(x,y) &= \frac{2K(x,y)}{J_K^{S=1}} \\ &= \frac{\eta(x)+\eta(y)}{2-\frac{[\eta(x)-\eta(y)]^2}{1-\eta(x)\eta(y)}},\end{aligned} \tag{4.14}$$

thus the physical properties of the spin-1 Kondo model are wholly specified by $J_K^{S=1}$ and $\eta(x,y)$. Moreover, systems with fixed $\eta(x,y)$ [which is satisfied, but does not necessitate, fixed $\eta(x)$ and fixed $\eta(y)$] will lie on the same RG flow and their properties will show universal scaling as a function of $J_K^{S=1}$. Further, since $\eta(z)$ in (4.13) is an odd function of z, it follows from (4.12b) that K vanishes for all points along the line $y=-x$. The effective spin-1 Kondo model therefore displays an effective particle-hole symmetry along this line, not only at the p-h symmetric point $x=0=y$.

The implications made above are that the physics of the 2LM in the $(1,1)$ sector are that of a spin-1 Kondo model and are somewhat similar to that of the spin-$\frac{1}{2}$ Kondo model we have seen previously. There are crucially some notable differences, particularly the nature of the $T=0$ ground state as we now elucidate.

4.2.2 The underscreened fixed point

Nozières and Blandin [97] surveyed the possible Kondo effects that could occur in 'real metals'. They considered transition metal impurities within bulk metals, including effects of crystal field splittings and various occupancies of the impurity d-orbitals. To this end they studied spin-S Kondo impurities connected to n conduction band channels. For the case $S=\frac{1}{2}$ and $n=1$, the ordinary spin-$\frac{1}{2}$ Kondo model, we have seen that the ground state forms from the antiferromagnetic coupling of the impurity local moment with the zero orbital of the Wilson chain resulting in a state with $S'=S-\frac{n}{2}=0$. At this strong coupling fixed point the conduction band electrons fully screen the impurity moment. However for $S>\frac{n}{2}$, as is the case for the spin-1 Kondo model of (4.11), the impurity is not fully screened by the same process leaving a residual non-zero spin at the impurity [97]. The obvious question now is how does this state couple to the remaining sites of the Wilson chain? We consider this question in fig. 4.3. The impurity 'traps' a single electron with an antiparallel spin to give a $S'=\frac{1}{2}$ Kondo doublet state, fig. 4.3. By considering virtual second order hopping between the zero and first Wilson sites we can generate a second Kondo effect with *weak* ferromagnetic coupling. However, only up spin electrons on the $\hat{f}_1$ site have their energy lowered by such processes due to the exclusion principle: the coupling between the Kondo doublet and remaining conduction band states is

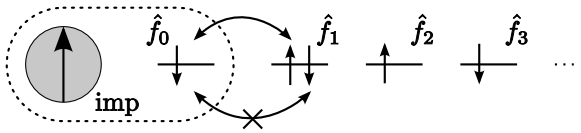

Figure 4.3: Representation of the spin-1 Kondo strong coupling fixed point. The impurity traps a single electron in the zero orbital of the Wilson chain forming a net $S = \frac{1}{2}$ residual moment. To second order, only down spin electrons on the second Wilson site have their energy lowered by hopping the zero orbital: the coupling to the Kondo state is thereby ferromagnetic.

thereby *ferro*magnetic and no further screening of the impurity spin takes place.

For reasons that will become apparent later, the stability of the underscreened (USC) fixed point described above is most easily determined by numerical calculations using the NRG. The first NRG calculations for spin-1 Kondo models [40], showed the USC fixed point to be stable: the energy levels of the system converging with iteration number to those expected for a doubly degenerate state. In fig. 3.6 we showed similar results for the 2LM. Parameters were chosen such that the system was deep in the (1,1) triplet sector and at the particle-hole symmetric point, *i.e.* precisely where the spin-1 Kondo model is expected to be the correct low-energy model. In that case, the energy levels were also seen to converge. We can therefore be confident that the USC fixed point is a stable fixed point of the 2LM. The thermodynamic calculations of section 4.3 will further confirm the identity of the stable fixed point in fig. 3.6.

The 2LM therefore contains two distinct stable fixed points. The first of these points is the strong coupling (SC) fixed point,[4] which also arises in the AIM, describes a regular Fermi liquid (FL) state. The USC fixed point described in this section, and particular to the 2LM, describes a more exotic so-called singular Fermi liquid [54, 98, 99]. The quantum phase transition between two $T = 0$ states described by these distinct stable points is now studied throughout the rest of this chapter. The general structure of the phase diagram in the $x - y$ plane is expected to consist of a closed continuous line of quantum phase transitions separating an underscreened spin-1 phase from a continuously connected Fermi liquid phase. We begin in section 4.3 by examining various thermodynamic properties and studying the evolution of the phase boundaries from the atomic limit to the $V \neq 0$ case. In section 4.3.1 we will investigate how the symmetries of the 2LM Hamiltonian identified earlier affect the nature of the transition from the FL to the USC state.

[4] We include here the generic, equivalent case of the frozen impurity (FI) fixed point when the impurity charge is non-integral.

4.3 Phase transitions and thermodynamics

In this section we focus on the impurity contribution to thermodynamic properties as defined in (3.19). We will use the impurity free energy

$$F = k_{\mathrm{B}} T \ln\left(\frac{Z}{Z^0}\right) \tag{4.15}$$

(with Z and Z^0 the system partition function with and without the impurity present) to calculate the impurity entropy $S_{\mathrm{imp}}(T) = k_{\mathrm{B}}(\langle\beta\hat{H}\rangle_{\mathrm{imp}} - F)$. We will also calculate the temperature scaled magnetic spin susceptibility: $T\chi_{\mathrm{imp}}(T) = \langle(\hat{S}^z)^2\rangle_{\mathrm{imp}} - (\langle\hat{S}^z\rangle_{\mathrm{imp}})^2$. The temperature dependence of these quantities provides clear signatures of the fixed points reached during the RG procedure on progressive reduction of the characteristic energy scale [22, 23, 73]. We also consider the $T = 0$ 'excess impurity charge' n_{imp}: the difference in the charge of the entire system with and without the impurity present, *i.e.* from (3.19):

$$n_{\mathrm{imp}} \equiv \langle\hat{Q}\rangle_{\mathrm{imp}} \tag{4.16a}$$

$$= \langle\hat{Q}\rangle - \langle\hat{Q^0}\rangle, \tag{4.16b}$$

with $\hat{Q}$ the total charge operator (for the impurity and conduction band combined), and Q^0 the charge operator in the absence of the impurity. In practice n_{imp} corresponds closely to the overall impurity charge: $n_{\mathrm{imp}} \simeq \langle\hat{n}_1 + \hat{n}_2\rangle$, but is not identical to it.[5] Under the particle-hole and $1-2$ transformations of section 4.1 (and for $V_1 = V_2$) n_{imp} transforms, respectively, as:

$$n_{\mathrm{imp}}(x, y) = 4 - n_{\mathrm{imp}}(-x, -y), \tag{4.17a}$$

$$= n_{\mathrm{imp}}(y, x), \tag{4.17b}$$

which we will use later.

The numerical calculations presented in this chapter were typically performed using an NRG discretization parameter $\Lambda = 3$ and retaining the lowest $N_k = 2000$ states at each iteration. The results are not affected by decreasing Λ or increasing N_k. We assume $V_1 = V_2 = V$ such that $\Gamma_{ii} = \pi\rho V_{ii}^2 = \Gamma$. It is thereby convenient to express the remaining parameters of the 2LM in terms of Γ, *viz.*:

$$\tilde{\epsilon}_i = \frac{\epsilon_i}{\Gamma}, \qquad \tilde{U} = \frac{U}{\Gamma}, \qquad \tilde{U}' = \frac{U'}{\Gamma}, \qquad \tilde{J}_H = \frac{J_H}{\Gamma}. \tag{4.18}$$

Figure 4.4 shows the temperature dependence of the impurity entropy (left) and susceptibility (right) for fixed $\tilde{U} = 20$, $\tilde{U}' = 7$, and $\tilde{J}_H = 2$, taking a vertical cut

[5] When evaluating (4.16a) the expectation value of the band charge operator $\sum_{\mathbf{k}\sigma} c^\dagger_{\mathbf{k}\sigma} c_{\mathbf{k}\sigma}$, which contributes to both $\langle\hat{Q}\rangle$ and $\langle\hat{Q^0}\rangle$, remains approximately equal when the impurity is removed. A formal definition of n_{imp} in terms of the impurity Green functions will be given in chapter 5.

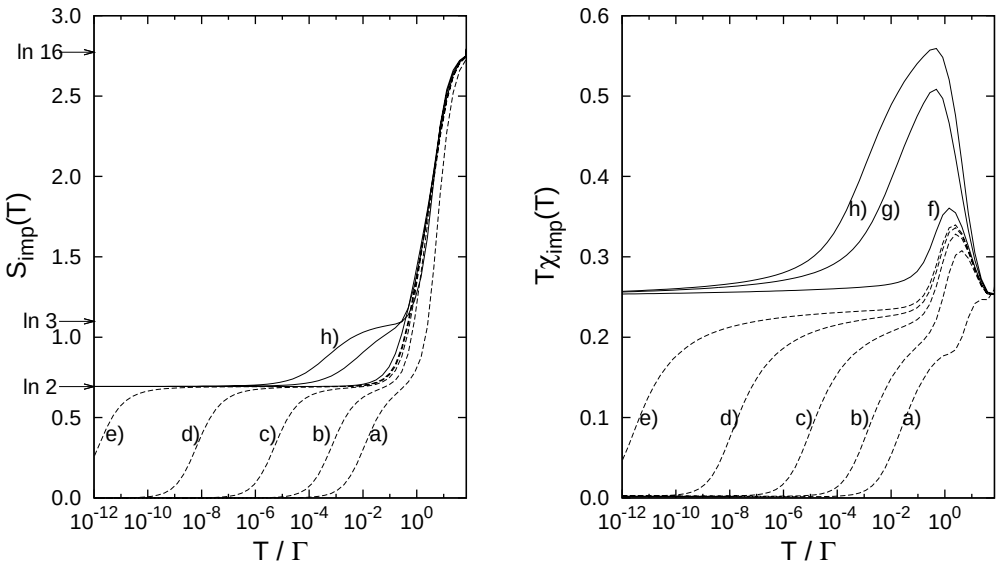

Figure 4.4: Temperature dependence of the impurity entropy $S_{\rm imp}(T)$ (left) and spin susceptibility $T\chi_{\rm imp}(T)$ (right) for fixed level energy $\tilde{\epsilon}_1 = \frac{1}{2}\tilde{U} - \tilde{U}'$ with $\tilde{U} = 20$, $\tilde{U}' = 7$, and $\tilde{J}_H = 2$. The energy of level 2 is progressively decreased: a) $\tilde{\epsilon}_2 = +5$, b) -5, c) -6, d) -6.3, e) -6.43, f) $\tilde{\epsilon}_2 = -7$, g) -10 and h) -17. Inset: the corresponding impurity charge $n_{\rm imp}$ vs. $\tilde{\epsilon}_2$ is seen to change smoothly as the nature of the ground state changes.

through the $x - y$ plane: we have fixed $\tilde{\epsilon}_1 = -\frac{1}{2}\tilde{U} - \tilde{U}' = 17$ (*i.e.*, $x = 0$) and varied $\tilde{\epsilon}_2$. Let us first examine the results in the $T \to 0$ limit in order to illustrate that a quantum phase transition does indeed exist in the 2LM. Two distinct $T = 0$ behaviours are seen depending on the value of $\tilde{\epsilon}_2$ chosen. For curves a) $\tilde{\epsilon}_2 = +5$, b) -5, c) -6, d) -6.3, and e) -6.43 in the figure, the impurity contribution to the system entropy ultimately falls to zero as $T = 0$ is approached. On the lowest temperature scales $T\chi_{\rm imp}(T)$ is likewise seen to approach zero. We conclude that the ground state for these parameters is therefore a non-magnetic singlet state. From the analysis of the previous section we can deduce that these results correspond to RG flows which terminate at fixed points along the continuous line connecting the strong coupling (SC) fixed points to the more generic frozen impurity (FI) fixed point.

In contrast to the behaviour above the curves f)-h) corresponding to $\tilde{\epsilon}_2 = -7$, -10, and -17 respectively, show that $S_{\rm imp}(T)$ very definitely approaches a value of $\ln 2$ whilst $T\chi_{\rm imp}(T)$ approaches $1/4$.[6] These are precisely the results that one would predict for the USC fixed point being indicative of an asymptotically free spin-$\frac{1}{2}$ — a magnetic, degenerate doublet ground state.

The NRG data therefore confirm the assertions of the previous section: the 2LM supports a quantum phase transition (QPT) between two fundamentally distinct states. On one side of the QPT the stable low-energy fixed point is a FI fixed point which gives rise to a Fermi liquid (FL) ground state. We will label this side of the

[6] It is implied that $S_{\rm imp}(T)$ is given in units of the Boltzmann constant $k_{\rm B}$.

transition the FL phase. By contrast on the other side of the transition, systems are described by different physics: the physics of the USC fixed point, which as we will see throughout the course of this chapter displays some very interesting and subtle characteristics. It has been described previously as a singular Fermi liquid state [54, 98, 99]. We will refer to this side of the transition as the USC phase. This is not to say that the underlying low-energy model is ubiquitously a pure underscreened spin-1 Kondo model [as in (4.11)] throughout the phase, indeed we shall see shortly that such a model is not always entirely appropriate. We could equally well label this phase the singular Fermi liquid (SFL) phase, but we see the USC label as more distinctive.

Before analysing the particulars of the transition further, we can further inspect the finite temperature results presented in fig. 4.4. In all cases a)-h) the high temperature behaviour is governed by the free orbital fixed point, which corresponds to all 16 states of the isolated dot being thermally accessible and hence $S_{\rm imp}(T) = \ln 16$. On the FL side of the QPT and in the extreme case a), $\tilde{\epsilon}_2 = +5$ is sufficiently large that level 2 is in essence irrelevant: population of the level incurs a large energy cost and does not occur for $T/\Gamma < \tilde{\epsilon}_2 - \tilde{\epsilon}_1$. The 2LM thus reduces to an effective single-level AIM in this limit, the physics of which we have explored in sections 2.2 and 4.2. Hence, on decreasing T, $S_{\rm imp}(T)$ first flows toward the spin-$\frac{1}{2}$ local moment (LM) fixed point with $S_{\rm imp}(T) = \ln 2$. In this case we see a weak plateau at $T/\Gamma \lesssim 1$, reflecting the modest thermal excitation between the $(2,0)$ and $(1,0)$ states of the isolated dot at energy $\tilde{\epsilon}_1 + \tilde{U} = 3\Gamma$ (see table 4.1). On further decreasing the temperature the Kondo effect takes place whence the system arrives at the stable SC/FI fixed point. A Kondo scale T_K may be identified from this final crossover, and is in practice defined via $S_{\rm imp}(T_K) = 0.1$. For the cases b)-e) in fig. 4.4 the same essential pattern of fixed points is seen; the only difference being that the $S_{\rm imp}(T) = \ln 2$ LM plateau is progressively lengthened and the associated T_K diminishes and *vanishes* at the QPT itself. We will return to the precise behaviour of T_K vs. $\tilde{\epsilon}_2$ later.

The behaviour on the USC side of the transition [cases f)-h)] is distinct from that shown above in the FL phase. At intermediate temperatures, $T/\Gamma \sim 1 \times 10^{-2}$, an $S_{\rm imp}(T) = \ln 3$ plateau is observed whilst $T\chi_{\rm imp}(T)$ increases from its FI value towards values approaching 0.6. It therefore seems the case that the system reaches a spin-1 LM fixed point associated with an effective spin-1 impurity detached from the conduction band. For a completely free spin-1 we would of course expect $T\chi_{\rm imp}(T) = S(S+1)/3 = 2/3$, the fact that this limit is not reached in any of the examples shown is indicative of a residual coupling of the impurity to the conduction band, that the spin-1 LM fixed point is unstable and consequently that the RG flow does not precisely reach this fixed point. On decreasing the temperature further the impurity entropy and susceptibility fall to $S_{\rm imp}(T) = \ln 2$ and $1/4$ respectively indicative of the USC spin-1 fixed point, or equivalently the spin-$\frac{1}{2}$ LM fixed point, there being no distinction between them as fixed point Hamiltonians. As in the FL phase we can

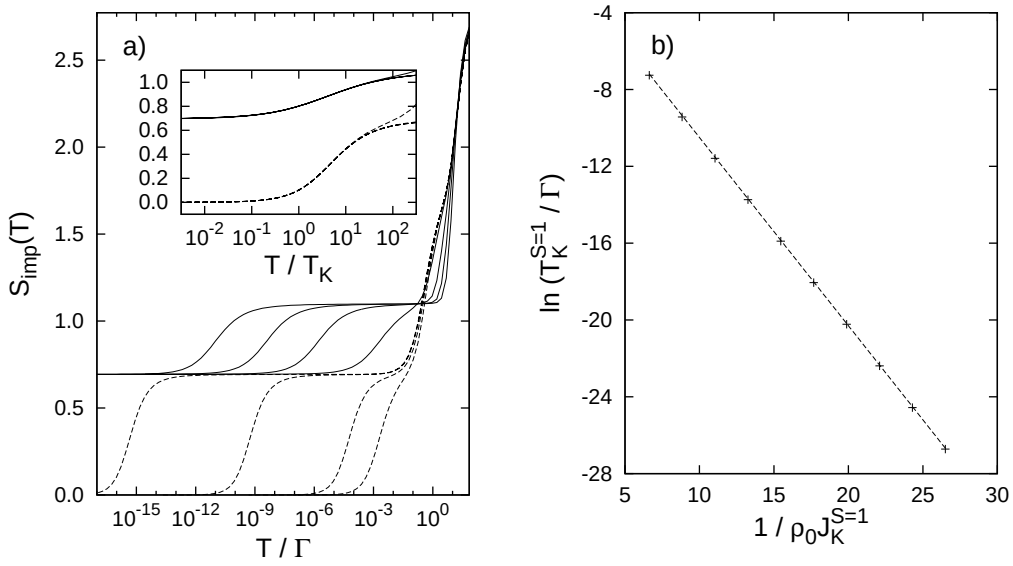

Figure 4.5: a) Universal scaling displayed in the impurity entropy for a system with $\tilde{U} = 60$, $\tilde{U}' = 30$, $\tilde{J}_H = 15$, $\tilde{\epsilon}_1 = -30$, and $\tilde{\epsilon}_2 = -60$, -40, -34, -30, -27.85, -27.8, -27.6, and -27.3, the transition occurring here at $\tilde{\epsilon}_{2,c} \sim -27.9$. *Main*: In the USC phase (solid lines) and FL phase (dashed lines), the Kondo scales, $T_K^{S=1}$ and T_K respectively, vary widely for different $\tilde{\epsilon}_2$. *Inset*: When results are scaled in terms of $T_K^{S=1}$ (or T_K) a single universal form results. b) Relation between the Kondo coupling $J_K^{S=1}$ [from (4.12a)] and $T_K^{S=1}$, shown for systems with $\tilde{U} = 20$, 25...55, 60, and $\tilde{U} = 2\tilde{U}' = 4\tilde{J}_H$ at particle symmetry.

define the USC Kondo scale via the crossover: $S_{\rm imp}(T_K^{S=1}) = 0.8$, a value suitably between $\ln 3$ and $\ln 2$ (the values at the two relevant fixed points).

Earlier in sections 2.2.1 and 3.4 we saw how the Kondo scale T_K (or $T_K^{S=1}$), arises as a scaling invariant. As such T_K fully characterises the system at low energies and systems with different Kondo scales behave identically when their temperature dependent properties are rescaled. Figure 4.5a) gives a specific example of this universality. Again we show $S_{\rm imp}(T)$ for a system with $\tilde{U} = 60$, $\tilde{U}' = 30$, $\tilde{J}_H = 15$, and $\tilde{\epsilon}_1 = -30$ and for various values of $\tilde{\epsilon}_2$ straddling the QPT. As found previously the low temperature results flow toward either the FI or USC fixed point, shown by dashed and solid lines respectively. Which fixed point, and on which temperature scale is determined by the value of $\tilde{\epsilon}_2$. When the results are scaled in terms of T_K (or $T_K^{S=1}$), as in the inset, the results scale onto functional forms indicative of the two phases. We can see that this scaling is lost for $T \gtrsim \Gamma$, *i.e.* the lowest non universal scale, at which point the lines naturally diverge. Finally we note one further point. The results throughout the USC phase scale onto a single universal form indicating that the asymmetry $\eta(x, y)$ plays little role in scaling — there is no discernible difference in the scaling forms found for different values of the asymmetry.

What of the Kondo scale itself? In the USC phase (4.12a) gives a simple relation between the Kondo coupling $J_K^{S=1}$ and the impurity parameters. Let us focus specifically on the case of particle-hole symmetry such that we can be certain that

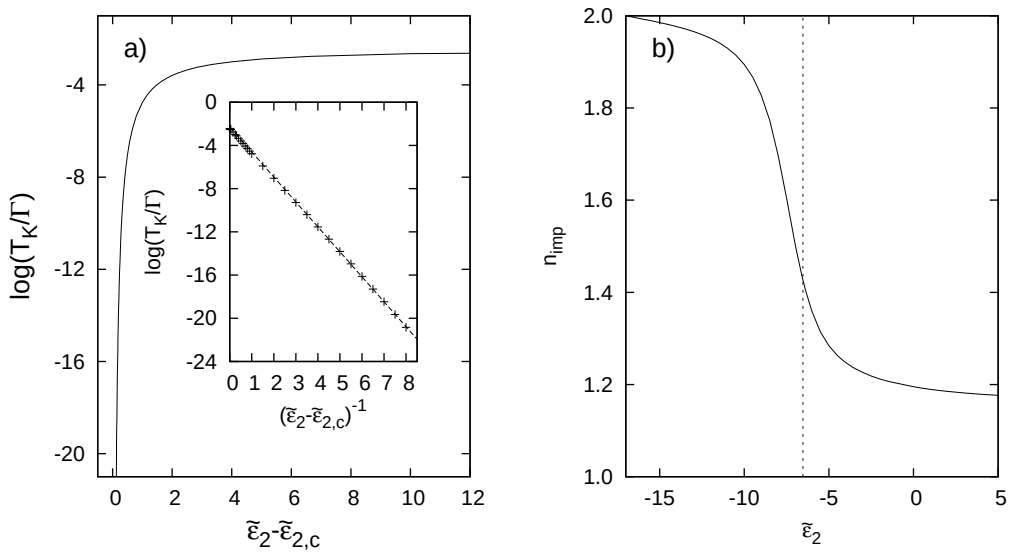

Figure 4.6: a) The Kondo scale T_K on approaching the QPT on the FL side for the same parameters as fig. 4.4. b) The transition occurs in a mixed valent regime of non-integral impurity charge n_{imp}.

the correct underlying low-energy model is a pure spin-1 Kondo model as in (4.11) with no potential scattering. In section 2.2.1 we found that in the case of the spin-$\frac{1}{2}$ Kondo model perturbative scaling gave $T_K \sim D\exp(-1/\rho_0 J_K)$. Perturbative scaling for the spin-1 Kondo model yields a similar result [20], with the exponential dependence as usual of the essence, and the prefactor immaterial. Thus, a plot of $\ln T_K^{S=1}/\Gamma$ vs. $1/\rho_0 J_K^{S=1}$ yields a straight line, fig. 4.5b). Results for $\tilde{U} = 20$, 25...55, and 60 with $\tilde{U} = 2\tilde{U}' = 4\tilde{J}_H$ are shown, although arbitrarily chosen values of these parameters lie on the same straight line.

Above it was noted that T_K rapidly diminishes as the transition is approached on the FL side. We now examine this more closely in fig. 4.6a) which plots T_K against the 'distance' from the transition $\tilde{\epsilon}_2 - \tilde{\epsilon}_{2,c}$, with $\tilde{\epsilon}_{2,c} = -6.536...$ the value of $\tilde{\epsilon}_2$ at the transition. As is clear from the main figure, T_K vanishes in an exponential fashion as $\tilde{\epsilon}_2 - \tilde{\epsilon}_{2,c}$ decreases rather than as a power law. The form of the exponent is elucidated in the inset to fig. 4.6a) where a plot of $\ln T_K$ vs. $(\tilde{\epsilon}_2 - \tilde{\epsilon}_{2,c})^{-1}$ results in a straight line: $T_K \propto \exp(-a/|\tilde{\epsilon}_2 - \tilde{\epsilon}_{2,c}|)$ with $a \sim \mathcal{O}(1)$. In contrast to these observations the low-energy scale of the USC phase, $T_K^{S=1}$, plays no role in the QPT and nothing remarkable happens to it on approaching the transition. We can draw an analogy to the phase transition of the classical XY-model, which displays similar traits in its critical phenomena, and label the transition in the 2LM as being of Kosterlitz-Thouless (KT) type. The phase transition is continuous and there is no separate unstable critical fixed point distinct from the two stable fixed points mentioned above (as characteristic of KT transitions) [52, 53].

The KT behaviour is not confined to the particular trajectory in the $x-y$ plane

chosen above. Almost all trajectories lead to the same observation of a vanishing T_K on approaching the QPT on the FL side. (We will examine the exception to this rule in section 4.3.1.) Hofstetter and Schoeller [52] have previously considered the 2LM with $U = U'$ along the line $y = -x$. A KT transition is found in this case also. Along this line $n_{\rm imp} = 2$ results from (4.17a). It is therefore possible [52] to construct an effective spin model via a Schrieffer-Wolff transformation by forming a low-energy manifold composed of the $(1,1)$ and $(2,0)$ atomic limit states. The result is a two-spin spin-$\frac{1}{2}$ Kondo model, as illustrated in fig. 4.11, known [53] to exhibit a KT transition. In the present (general) case however the transition occurs in a mixed-valent regime of nonintegral $n_{\rm imp}$, illustrated in fig. 4.6b). Here it is shown that $n_{\rm imp}$ varies continuously as the transition is crossed, with $n_{\rm imp} \simeq 1.4$ at the transition itself. It is therefore not in general possible to construct via a Schrieffer-Wolff transformation an effective low-energy spin model applicable in the vicinity of the QPT.

Phase boundaries for the full 2LM are shown in fig. 4.7. In a) we compare NRG results (solid) to those of the atomic limit (dashed) — we show only the boundary of the $(1,1)$ sector of the AL, the other boundaries being replaced by continuous crossovers in the full model as explained previously. The AL is indeed a good indicator of the stability of the USC phase in the full model. The transition is of KT form throughout the plane except at the two special points denoted by filled circles. We examine these points more closely in the next section. The result of varying $\tilde{U}'$ is shown in fig. 4.7b). As in the AL the phase boundary shows four-fold symmetry for the case of $\tilde{U}' = 0$ (solid). On progressively increasing $\tilde{U}'$ the USC phase is 'stretched' along the line $y = x$ becoming a narrow strip for $\tilde{U}' = \tilde{U}$ (short dash), again easily understood in terms of the AL states. Finally fig. 4.7c) depicts the effect of decreasing $\tilde{J}_H$ from positive values (outside) through zero (short dash) and one example of antiferromagnetic $\tilde{J}_H$ (dotted). The important point here is that even for weakly antiferromagnetic $\tilde{J}_H$ the USC persists throughout a large proportion of the $x - y$ plane. This phenomena will be explored further in section 4.3.2.

The results presented above reflect those found for most choices of the impurity parameters. In the following sections we will examine more unusual behaviours found along specific lines of symmetry and less generic choices of the impurity parameters.

4.3.1 First-order transitions

In the proceeding section the QPT between the USC and FL phases was found generally to be of KT form with an associated vanishing of the low-energy Kondo scale T_K as the transition is approached on the FL side. However, as noted in section 4.1 the 2LM Hamiltonian transforms under the $1-2$ transformation as $\hat{H}(x,y) \to \hat{H}(y,x)$ and is hence invariant on the line $y = x$ (or equivalently $\epsilon_1 = \epsilon_2$). Along this line all states of the entire system therefore have a definite parity under

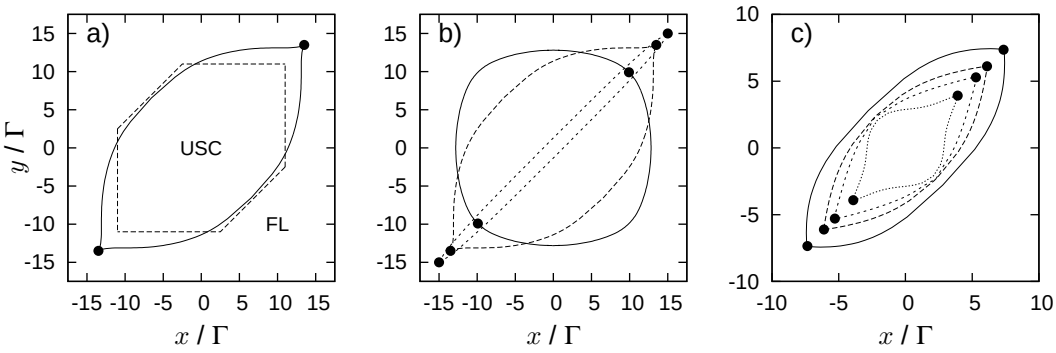

Figure 4.7: Phase boundaries as derived from NRG calculations of the impurity entropy. a) Comparison to atomic limit (dashed) for $\tilde{U} = 20$, $\tilde{J}_H = 5$, and $\tilde{U}' = 7.5$. The QPT in the full model mirrors the AL and is of KT form except at special points denoted by filled circles. b) The effect of varying $\tilde{U}' = 0$, 7.5, and 20, outside to inside respectively. c) Now for $\tilde{U} = 10$ and $\tilde{U}' = 5.25$ and varying $\tilde{J}_H = 5$, 1, 0, and -0.5, outside to inside. The USC phase persists even for antiferromagnetic $\tilde{J}_H$.

the $1-2$ transformation. The Hilbert space of the Hamiltonian is then separable into disjoint parity sectors. As we now investigate, a first-order transition must thus occur when the global many-body ground state changes parity.

The temperature dependence of $S_{\rm imp}(T)$ and $T\chi_{\rm imp}(T)$ are shown in fig. 4.8 for fixed $\tilde{U} = 20$, $\tilde{U}' = 7$, and $\tilde{J}_H = 2$ along the line $y = x$ such that $\tilde{\epsilon}_1 = \tilde{\epsilon}_2 = \tilde{\epsilon}$. Results are given for $\tilde{\epsilon} = \tilde{\epsilon}_c \pm 10^{-n}$ with b) $n = 4$, c) 6, d) 8, and e) 10 as well as at the transition f) $\tilde{\epsilon} = \tilde{\epsilon}_c \simeq -4.7$. For comparison we also show results for a) deep in the FL phase $\tilde{\epsilon} = +5$ where the impurity is essentially unoccupied ($n_{\rm imp} \simeq 0.25$ in the left inset) and g) at particle-hole symmetry $\tilde{\epsilon} = -17$.

The stable low-temperature fixed points remain as before: for $\tilde{\epsilon} > \tilde{\epsilon}_c$ the FI fixed point gives a singlet ground state whilst for $\tilde{\epsilon} < \tilde{\epsilon}_c$ the ground state is a doublet as governed by the USC fixed point. Close to the transition however the energy separation of these two states T_* is tending to zero such that the singlet and doublet states appear effectively degenerate for $T \gtrsim T_*$. An entropy plateau of $S_{\rm imp}(T) = \ln 3$ is then clearly visible in fig. 4.8. A similarly new plateau is observed in the magnetic susceptibility with $T\chi_{\rm imp}(T) = \frac{1}{6}$. This value can be readily understood in terms of the mean value $\langle (S_z)^2 \rangle = \frac{1}{3}(1\times 0 + 2\times\frac{1}{4})$ over the quasidegenerate states. These are signatures of the 'transition fixed point' TFP characteristic of systems exhibiting a level crossing transition [100]. On further reducing T below T_*, the system is seen to cross from the TFP to one or other of the stable fixed points — this crossover in effect defines T_*, specifically we choose $S_{\rm imp}(T_*) = 0.8$. As the transition is approached T_* vanishes linearly in $\tilde{\epsilon} - \tilde{\epsilon}_c$ as is evident from the equally spaced entropy and susceptibility curves and shown explicitly in the right inset. Precisely at the transition, $T_* = 0$, the ground state consists of the precisely degenerate singlet and doublet states, as evident in case f) of fig. 4.8.

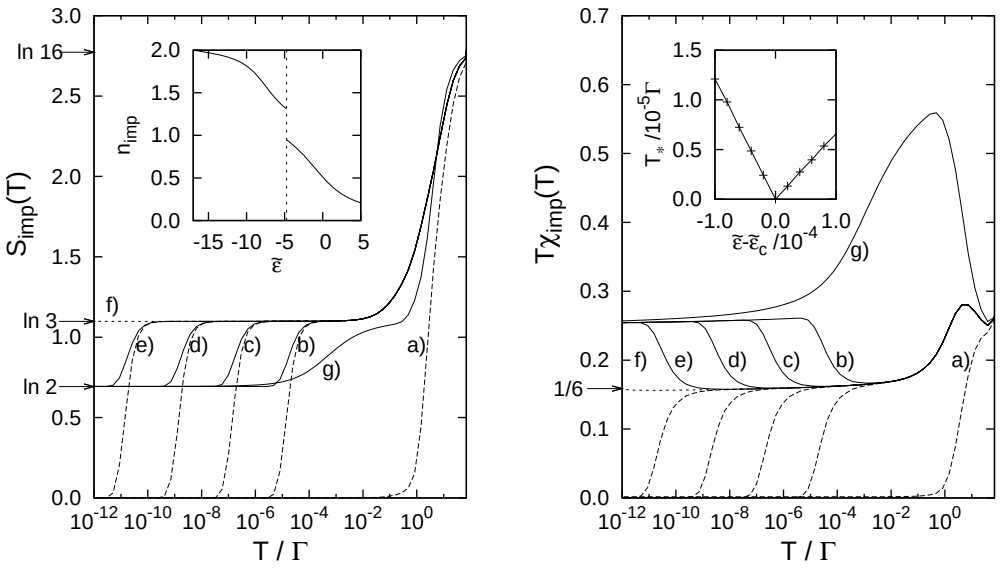

Figure 4.8: Temperature dependence of the impurity entropy and susceptibility as the first-order transition on the line $\tilde{\epsilon}_1 = \tilde{\epsilon}_2 = \tilde{\epsilon}$ is approached and crossed; for fixed $\tilde{U} = 20$, $\tilde{U}' = 7$, and $\tilde{J}_H = 2$, the transition here occurring at $\tilde{\epsilon}_c = -4.738\ 648\ 563\ 029\ 29$. Solid lines refer to the USC phase ($\tilde{\epsilon} < \tilde{\epsilon}_c$) and dashed lines to the FL phase. Shown for a) $\tilde{\epsilon} = +5$ deep in the FL phase; b)-e) $\tilde{\epsilon} = \tilde{\epsilon}_c \pm 10^{-n}$ with $n = 4$, 6, 8, and 10, respectively, f) $\tilde{\epsilon} = \tilde{\epsilon}_c$, as well as for g) $\tilde{\epsilon} = -17$ at the particle-hole symmetric point deep in the USC phase. The transition fixed point has a characteristic $S_{\rm imp}(T) = \ln 3$ and $T\chi_{\rm imp}(T) = \frac{1}{6}$, as indicated, and persists down to $T = 0$ precisely at the transition. *Left inset*: impurity charge $n_{\rm imp}$ vs. $\tilde{\epsilon}$. It changes discontinuously at the transition (dashed vertical line). *Right inset* The low-energy scale T_* associated with the transition fixed point vanishes linearly as the transition is approached, symptomatic of the level-crossing nature of the transition.

The behaviour of the excess impurity charge $n_{\rm imp}$ as the first-order transition is crossed is shown in the left inset to fig. 4.8. In contrast to the KT transitions seen previously, $n_{\rm imp}$ is seen to change *discontinuously* when the phase boundary is crossed. A progenitor of this behaviour can in fact be found in the noninteracting limit, $U = 0 = U' = J_H$. On taking even (e) and odd (o) combinations of the impurity levels, *viz.*, $d_{e\sigma} = (d_{1\sigma} + d_{2\sigma})/\sqrt{2}$ and $d_{o\sigma} = (d_{1\sigma} - d_{2\sigma})/\sqrt{2}$, only the e-orbital tunnel couples directly to the conduction band and the noninteracting Hamiltonian $\hat{H}^0$ [(2.38) with U, U', and J_H set to zero] reduces to

$$\hat{H}^0 = \sum_{\mathbf{k}\sigma} \epsilon_{\mathbf{k}} c^\dagger_{\mathbf{k}\sigma} c_{\mathbf{k}\sigma} + \tfrac{1}{2}(\epsilon_1 + \epsilon_2)(\hat{n}_e + \hat{n}_o) + \sum_{\mathbf{k}\sigma} \sqrt{2} V (c^\dagger_{\mathbf{k}\sigma} d_{e\sigma} + d^\dagger_{e\sigma} c_{\mathbf{k}\sigma}) + \sum_\sigma \tfrac{1}{2}(\epsilon_1 - \epsilon_2)(d^\dagger_{e\sigma} d_{o\sigma} + d^\dagger_{o\sigma} d_{e\sigma}) \quad (4.19)$$

In general, the e and o orbitals are coupled by the final term in the above. For the case of $\epsilon_1 = \epsilon_2$, however, the final term clearly vanishes and the Hamiltonian is separable, $\hat{H}^0 = \hat{H}^0_e + \hat{H}^0_o$ with $\hat{H}^0_o$ a free orbital with energy ϵ. A transition in this

limit thus trivially occurs for $\epsilon = 0$. This is the particle-hole symmetric point of the noninteracting limit. For all $\epsilon > 0$ the o-orbital is unoccupied while for $\epsilon < 0$ it is doubly occupied; only at precisely $\epsilon = 0$ is it singly occupied. The total impurity occupation $n_{\rm imp}$ thus changes discontinuously from 1 to 3 as the transition is crossed.

With interactions present the situation is of course much less simple. The o-orbital remains uncoupled from the conduction band for $\epsilon_1 = \epsilon_2$ but it now becomes coupled to the e-orbital via the nontrivial interactions terms of (4.1), which acquire a rather complex, unenlightening, form when expressed in terms of the e and o operators.

This concludes our analysis of the thermodynamics of first-order transitions along the line $y = x$. We will return to this case when we consider the single-particle dynamics of the 2LM and analyse the renormalized e and o levels in section 5.3.1. The important result is that when the Hamiltonian can be separated into distinct sectors, a level crossing must result at some point in the $x - y$ plane.

4.3.2 Weakly Antiferromagnetic J_H

As we saw in fig. 4.7 the USC phase survives even for weak antiferromagnetic coupling $J_H < 0$. Clearly this behaviour cannot persist for large, negative J_H when one expects that only the *singlet* state of the impurity in the $(1, 1)$ sector to be relevant. On coupling to the leads a singlet ground state should result with a stable FI fixed point which is continuously connected to that of the normal FL phase: the USC phase will be destroyed and the QPT eliminated.

To begin fig. 4.9 shows phase boundaries in the $x - y$ plane for fixed $\tilde{U} = 10$ and $\tilde{U}' = 5.25$ for antiferromagnetic $\tilde{J}_H = -0.55$, -0.558, -0.56, and -0.6. For $\tilde{J}_H = -0.55$ (long dash) the phase boundary has a familiar form: consisting of the USC phase centred on $(x, y) = (0, 0)$, separated from the FL phase by a single boundary line of KT transitions (except on the line $y = x$ where a first order QPT arises).

On decreasing $\tilde{J}_H$ slightly to -0.558 (solid) however, the USC phase is seen to split into four distinct domains. Naturally these domains remain symmetric under both inversion through $(x, y) = (0, 0)$ and reflection about $y = x$. Perhaps surprisingly the particle-hole symmetric point is now part of the FL phase. Decreasing $\tilde{J}_H$ further sees the two domains straddling the line $y = x$ disappear leaving only those straddling $y = -x$. The latter domains are diminished in extent until they finally disappear entirely by $\tilde{J}_H = -1$, leaving a single FL phase and no QPT. As indicated in the figure, first-order level-crossing transitions occur not only along the line $y = x$ as discussed in the previous section but also along $y = -x$ on the inner surfaces of the phase boundaries, near the particle-hole symmetric point.

To understand the above observations note that the difference in energy between

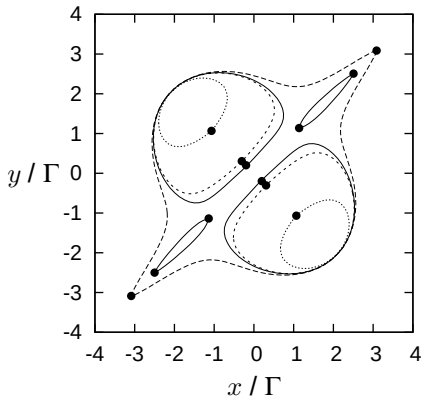

Figure 4.9: Evolution of the phase boundaries in the $x-y$ plane for antiferromagnetic $\tilde{J}_H < 0$. shown for fixed $\tilde{U} = 10$ and $\tilde{U}' = 5.25$ with $\tilde{J}_H = -0.55$ (long dash), -0.558 (solid), -0.56 (short dash), and -0.6 (dotted). Interior regions in each case are the USC phase and exterior regions the FL phase. First Order transitions are indicated by dots and occur along the lines $y = +x$ and $y = -x$.

the $(1,1)$ singlet and triplet states of the isolated dot is $|E_S - E_T| = |J_H|$. So for $|J_H| = -J_H \lesssim \mathcal{O}(\Gamma)$, and at least close enough to particle-hole symmetry (where $n_{\rm imp} = 2$), one expects it necessary to include both the $(1,1)$ triplet *and* singlet states in the low-energy manifold [higher dot states, such as $(2,0)$, lie considerably higher in energy provided U' in not within $\mathcal{O}(J_H)$ of U]. We therefore now construct, via a Schrieffer-Wolff transformation as in section 2.2 for the AIM, an effective low-energy spin model within this subspace.

The projection operator for the ground state manifold [the four $(1,1)$ impurity states] is simply:

$$\hat{P} = \hat{P}_S + \hat{P}_T \tag{4.20}$$

with

$$\hat{P}_S = |S=0, S_z=0\rangle\langle S=0, S_z=0| \tag{4.21a}$$

$$\hat{P}_T = \sum_{S_z} |S=1, S_z\rangle\langle S=1, S_z|. \tag{4.21b}$$

An entirely equivalent, and useful form, is the uncoupled representation

$$\hat{P} = \sum_{\sigma_1\sigma_2} |\sigma_1, \sigma_2\rangle\langle\sigma_1, \sigma_2|, \tag{4.22}$$

and the following identities can be noted:

$$\hat{P}_S = -\hat{\mathbf{s}}_1 \cdot \hat{\mathbf{s}}_2 + \tfrac{1}{4}\hat{P} \tag{4.23a}$$

$$\hat{P}_T = +\hat{\mathbf{s}}_1 \cdot \hat{\mathbf{s}}_2 + \tfrac{3}{4}\hat{P}. \tag{4.23b}$$

Finally the perturbing Hamiltonian is the one electron tunneling Hamiltonian of (2.44d):

$$\hat{H}_1 = \sum_{i\mathbf{k}\sigma} V_{i\mathbf{k}}(d^\dagger_{i\sigma}c_{\mathbf{k}\sigma} + c^\dagger_{\mathbf{k}\sigma}d_{i\sigma}) \tag{4.24}$$

We now have everything required to evaluate the effective low-energy Hamiltonian (2.7). The zeroth order term is simple to calculate:

$$\begin{aligned}\hat{H}^{(0)}_{\text{eff}}\hat{P} &= E_S\hat{P}_S + E_T\hat{P}_T \\ &= E_S\hat{P} + (E_T - E_S)\hat{P}_T \\ &= (\tfrac{1}{4}E_S + \tfrac{3}{4}E_T)\hat{P} + (E_T - E_S)\hat{\mathbf{s}}_1\cdot\hat{\mathbf{s}}_2 \\ &= (\epsilon_1 + \epsilon_2 + U')\hat{P} - J_H\hat{\mathbf{s}}_1\cdot\hat{\mathbf{s}}_2,\end{aligned} \tag{4.25}$$

the first term of which is a constant which we will drop. As for the AIM transformation, the first order term in the perturbative expansion is zero: a single application of the tunneling Hamiltonian does not return the system to the ground state manifold. Again it is the second order term which is important, it can be decomposed into three terms:

$$\hat{H}^{(2)}_{\text{eff}} = \hat{H}^{S}_{\text{eff}} + \hat{H}^{T}_{\text{eff}} + \hat{H}^{ST}_{\text{eff}}. \tag{4.26}$$

The first term is that for excitations from the singlet (S) subspace of the ground state manifold with subsequent return to this subspace. The second term is the analogue of the first but for the triplet (T) subspace. Finally the third term captures the processes which mix the singlet and triplet states under the perturbation. Naturally, to return to the ground state manifold electron addition to the impurity under the first application of $\hat{H}_1$ must be followed by electron removal, and vice versa. Furthermore, these processes must involve the same impurity level, as illustrated in fig. 4.10. It is useful to define the following energy differences which appear in (2.7):

Removal Processes:

$$\begin{aligned}\Delta E^T_1 &= E(0,1) - E_T \\ &= -\epsilon_1 - U' + \tfrac{1}{4}J_H \qquad (4.27a)\\ \Delta E^T_2 &= E(1,0) - E_T \\ &= -\epsilon_2 - U' + \tfrac{1}{4}J_H \qquad (4.27b)\\ \Delta E^S_1 &= E(0,1) - E_S \\ &= -\epsilon_1 - U' - \tfrac{3}{4}J_H \qquad (4.27c)\\ \Delta E^S_2 &= E(1,0) - E_S \\ &= -\epsilon_2 - U' - \tfrac{3}{4}J_H \qquad (4.27d)\end{aligned}$$

Addition Processes:

$$\begin{aligned}\Delta \tilde{E}^T_1 &= E(2,1) - E_T \\ &= \epsilon_1 + U + U' + \tfrac{1}{4}J_H \qquad (4.27e)\\ \Delta \tilde{E}^T_2 &= E(1,2) - E_T \\ &= \epsilon_2 + U + U' + \tfrac{1}{4}J_H \qquad (4.27f)\\ \Delta \tilde{E}^S_1 &= E(2,1) - E_S \\ &= \epsilon_1 + U + U' - \tfrac{3}{4}J_H \qquad (4.27g)\\ \Delta \tilde{E}^S_2 &= E(1,2) - E_S \\ &= \epsilon_2 + U + U' - \tfrac{3}{4}J_H \qquad (4.27h)\end{aligned}$$

With these energies defined it is simple to evaluate $\hat{H}^S_{\text{eff}}$ and $\hat{H}^T_{\text{eff}}$ using (2.7) and

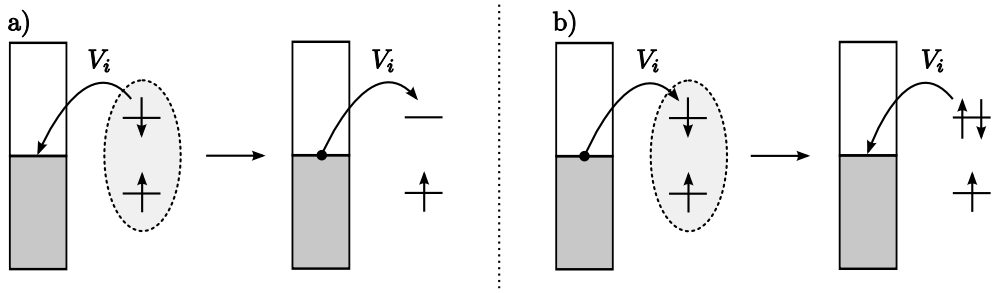

Figure 4.10: Schematic representations of the second order contributions to the effective Hamiltonian. a) Initially the impurity has a well defined total spin (singlet or triplet). An electron hops from one of the levels to a conduction band state near the Fermi level. A second electron then hops in the reverse direction to the same level leaving the impurity a spin state uncorrelated with the initial state. b) An electron first hops onto the impurity before return to the singly occupied manifold. Again the total impurity spin can change.

(4.24). As discussed above, only two terms each arise for $\alpha = S, T$:

$$\hat{H}^{\alpha}_{\text{eff}} = \hat{H}^{\alpha-}_{\text{eff}} + \hat{H}^{\alpha+}_{\text{eff}} \tag{4.28a}$$

$$\hat{H}^{\alpha-}_{\text{eff}} = \sum_i \sum_{\substack{\mathbf{k}\mathbf{k}' \\ \sigma\sigma'}} \frac{V_i^2}{-\Delta E_i^{\alpha}} \hat{P}_{\alpha} d^{\dagger}_{i\sigma'} c_{\mathbf{k}'\sigma'} c^{\dagger}_{\mathbf{k}\sigma} d_{i\sigma} \hat{P}_{\alpha} \tag{4.28b}$$

$$\hat{H}^{\alpha+}_{\text{eff}} = \sum_i \sum_{\substack{\mathbf{k}\mathbf{k}' \\ \sigma\sigma'}} \frac{V_i^2}{-\Delta \tilde{E}_i^{\alpha}} \hat{P}_{\alpha} c^{\dagger}_{\mathbf{k}'\sigma'} d_{i\sigma'} d^{\dagger}_{i\sigma} c_{\mathbf{k}\sigma} \hat{P}_{\alpha}, \tag{4.28c}$$

where $\hat{H}^{\alpha-}_{\text{eff}}$ describes the situation where an electron hops off of the impurity before a second hops on and $\hat{H}^{\alpha+}_{\text{eff}}$ is the opposite process. The above can be reorganised using the usual fermion anticommutation relations, together with the fact that $\hat{P}_{\alpha}(\sum_{\sigma} d^{\dagger}_{i\sigma} d_{i\sigma})\hat{P}_{\alpha} = \hat{P}_{\alpha}$ when the levels are singly occupied, to give

$$\begin{aligned} \hat{H}^{\alpha}_{\text{eff}} = &- \sum_i \frac{N V_i^2}{\Delta E_i^{\alpha}} \hat{P}_{\alpha} + \sum_i \frac{-V_i^2}{\Delta \tilde{E}_i^{\alpha}} \sum_{\substack{\mathbf{k}\mathbf{k}' \\ \sigma}} c^{\dagger}_{\mathbf{k}\sigma} c_{\mathbf{k}'\sigma} \hat{P}_{\alpha} \\ &+ \sum_i \sum_{\substack{\mathbf{k}\mathbf{k}' \\ \sigma\sigma'}} V_i^2 \left(\frac{1}{\Delta E_i^{\alpha}} + \frac{1}{\Delta \tilde{E}_i^{\alpha}} \right) c^{\dagger}_{\mathbf{k}\sigma} c_{\mathbf{k}'\sigma'} \hat{P}_{\alpha} d^{\dagger}_{i\sigma'} d_{i\sigma} \hat{P}_{\alpha}. \end{aligned} \tag{4.29}$$

(where N is the number of conduction band states). Finally we must evaluate $\hat{H}^{ST}_{\text{eff}}$. It too can be broken down into a sum of two terms as in (4.28). Unlike the equations above where the same energy denominator appears twice, the mixing of the singlet and triplet states gives two distinct energy denominators. Using the results $\hat{P}_T(\sum_{\sigma} d^{\dagger}_{i\sigma} d_{i\sigma})\hat{P}_S = 0$ and $\hat{P}_T(d_{i\sigma} d^{\dagger}_{i\sigma'})\hat{P}_S = -\hat{P}_T(d^{\dagger}_{i\sigma'} d_{i\sigma})\hat{P}_S$, a slightly more

lengthy calculation yields:

$$\hat{H}_{\text{eff}}^{ST} = \sum_i \sum_{\substack{\mathbf{k}\mathbf{k}' \\ \sigma\sigma'}} \tfrac{1}{2} V_i^2 \left(\frac{1}{\Delta E_i^T} + \frac{1}{\Delta \tilde{E}_i^T} + \frac{1}{\Delta E_i^S} + \frac{1}{\Delta \tilde{E}_i^S} \right) \times$$
$$c_{\mathbf{k}\sigma}^\dagger c_{\mathbf{k}'\sigma'} (\hat{P}_T d_{i\sigma'}^\dagger d_{i\sigma} \hat{P}_S + \hat{P}_S d_{i\sigma'}^\dagger d_{i\sigma} \hat{P}_T). \quad (4.30)$$

Equations (4.25), (4.29) and (4.30) form the basic result for the low-energy effective Hamiltonian. In this form however, they do not form a useful physical description. We now attempt to rewrite these expressions in terms of impurity and conduction band spin operators. By constructing the fully symmetric combination of conduction band orbitals (the first site of the Wilson chain — the zero orbital),

$$f_{0\sigma}^\dagger = \frac{1}{\sqrt{N}} \sum_{\mathbf{k}} c_{\mathbf{k}\sigma}^\dagger, \quad (4.31)$$

and defining the couplings

$$J_i^\alpha = N V_i^2 \left(\frac{1}{\Delta E_i^\alpha} + \frac{1}{\Delta \tilde{E}_i^\alpha} \right), \quad (4.32)$$

the second order term becomes:

$$\begin{aligned} \hat{H}_{\text{eff}}^{(2)} = &- \sum_{\alpha i} \frac{N V_i^2}{\Delta E_i^\alpha} \hat{P}_\alpha - \sum_{\alpha i} \frac{N V_i^2}{\Delta \tilde{E}_i^\alpha} \hat{P}_\alpha \sum_\sigma f_{0\sigma}^\dagger f_{0\sigma} \\ &+ \sum_{i\sigma\sigma'} \tfrac{1}{2} (J_i^T - J_i^S) f_{0\sigma}^\dagger f_{0\sigma'} \left[\hat{P}_T d_{i\sigma'}^\dagger d_{i\sigma} \hat{P}_T - \hat{P}_S d_{i\sigma'}^\dagger d_{i\sigma} \hat{P}_S \right] \\ &+ \sum_{i\sigma\sigma'} \tfrac{1}{2} (J_i^T + J_i^S) f_{0\sigma}^\dagger f_{0\sigma'} \left[(\hat{P}_T + \hat{P}_S) d_{i\sigma'}^\dagger d_{i\sigma} (\hat{P}_T + \hat{P}_S) \right] \end{aligned} \quad (4.33)$$

This still requires some simplification. Let's begin by examining the first line of (4.33). By using $\hat{n}_0 = f_{0\sigma}^\dagger f_{0\sigma}$, the occupation of the zero orbital, we have:

$$\begin{aligned} &\sum_{\alpha i} \frac{N V_i^2}{\Delta E_i^\alpha} \hat{P}_\alpha + \sum_{\alpha i} \frac{N V_i^2}{\Delta \tilde{E}_i^\alpha} \hat{P}_\alpha \sum_\sigma \hat{n}_0 \\ &= \sum_{\alpha i} N V_i^2 \left(\frac{1}{\Delta E_i^\alpha} + \frac{1}{\Delta \tilde{E}_i^\alpha} \right) \hat{P}_\alpha + (\hat{n}_0 - 1) \sum_{\alpha i} \frac{N V_i^2}{\Delta \tilde{E}_i^\alpha} \hat{P}_\alpha \\ &= \sum_{\alpha i} J_i^\alpha \hat{P}_\alpha + (\hat{n}_0 - 1) \sum_{\alpha i} \frac{N V_i^2}{\Delta \tilde{E}_i^\alpha} \hat{P}_\alpha \\ &= \sum_i \tfrac{1}{2} (J_i^T + J_i^S) \hat{P} + \sum_i \tfrac{1}{2} (J_i^T - J_i^S) (\hat{P}_T - \hat{P}_S) + (\hat{n}_0 - 1) \sum_{\alpha i} \frac{N V_i^2}{\Delta \tilde{E}_i^\alpha} \hat{P}_\alpha \end{aligned} \quad (4.34)$$

Now for the second line of (4.33). For $\sigma = \sigma'$ we have

$$\begin{aligned}\hat{P}_T d^\dagger_{i\sigma} d_{i\sigma} \hat{P}_T - \hat{P}_S d^\dagger_{i\sigma} d_{i\sigma} \hat{P}_S &= \hat{P}_T(\tfrac{1}{2}\hat{n}_i + \sigma \hat{s}^z_i)\hat{P}_T - \hat{P}_S(\tfrac{1}{2}\hat{n}_i + \sigma \hat{s}^z_i)\hat{P}_S \\ &= \tfrac{1}{2}(\hat{P}_T - \hat{P}_S) + \sigma(\hat{P}_T \hat{s}^z_i \hat{P}_T - \hat{P}_S \hat{s}^z_i \hat{P}_S) \\ &= \tfrac{1}{2}(\hat{P}_T - \hat{P}_S) + \tfrac{1}{2}\sigma \hat{P}(\hat{s}^z_1 + \hat{s}^z_2)\hat{P}, \end{aligned} \tag{4.35}$$

whilst for $\sigma = \uparrow$ and $\sigma' = \downarrow$ we find

$$\begin{aligned}\hat{P}_T d^\dagger_{i\sigma'} d_{i\sigma} \hat{P}_T - \hat{P}_S d^\dagger_{i\sigma'} d_{i\sigma} \hat{P}_S &= \hat{P}_T \hat{s}^-_i \hat{P}_T - \hat{P}_S \hat{s}^-_i \hat{P}_S \\ &= \hat{P}_T \hat{s}^-_i \hat{P}_T \\ &= \tfrac{1}{2}\hat{P}_T(\hat{s}^-_1 + \hat{s}^-_2)\hat{P}_T \\ &= \tfrac{1}{2}\hat{P}(\hat{s}^-_1 + \hat{s}^-_2)\hat{P}. \end{aligned} \tag{4.36}$$

The result for $\sigma = \downarrow$ and $\sigma' = \uparrow$ follows by replacing $\hat{s}^-_i$ with $\hat{s}^+_i$ in the above and so overall the second line of (4.33) becomes:

$$\begin{aligned}\sum_i \tfrac{1}{2}(J^T_i - J^S_i) \Bigg[&\tfrac{1}{2}(\hat{P}_T - \hat{P}_S) \sum_\sigma \hat{n}_{0\sigma} + \hat{s}^z_0 \hat{P}(\hat{s}^z_1 + \hat{s}^z_2)\hat{P} \\ &+ \tfrac{1}{2}\hat{s}^-_0 \hat{P}(\hat{s}^+_1 + \hat{s}^+_2)\hat{P} + \tfrac{1}{2}\hat{s}^+_0 \hat{P}(\hat{s}^-_1 + \hat{s}^-_2)\hat{P} \Bigg] \\ = \sum_i \tfrac{1}{2}(J^T_i - J^S_i) \Bigg[&\tfrac{1}{2}(\hat{P}_T - \hat{P}_S) \sum_\sigma \hat{n}_{0\sigma} + \hat{\mathbf{s}}_0 \cdot (\hat{\mathbf{s}}_1 + \hat{\mathbf{s}}_2) \Bigg] \end{aligned} \tag{4.37}$$

We thereby begin to see an effective spin model forming with a scalar coupling between the conduction band spin density at the impurity, $\hat{\mathbf{s}}_0$, and impurity moments on the individual levels. It is straightforward to simplify the third line of (4.33) by using $\hat{n}_{i\sigma} = \frac{1}{2} + \sigma \hat{s}^z_i$ and (4.20) to give:

$$\sum_{i\sigma\sigma'} \tfrac{1}{2}(J^T_i + J^S_i) f^\dagger_{0\sigma} f_{0\sigma'} \hat{P} d^\dagger_{i\sigma'} d_{i\sigma} \hat{P} = \sum_i \tfrac{1}{2}(J^T_i + J^S_i) \Bigg(\tfrac{1}{2} \sum_\sigma \hat{n}_0 + 2\hat{\mathbf{s}}_0 \cdot \hat{\mathbf{s}}_i \Bigg). \tag{4.38}$$

Combining (4.34), (4.37) and (4.38) we can rewrite (4.33):

$$\begin{aligned}\hat{H}^{(2)}_{\text{eff}} = &- \sum_i \tfrac{1}{2}(J^T_i + J^S_i)\hat{P} - \sum_i \tfrac{1}{2}(J^T_i - J^S_i)(\hat{P}_T - \hat{P}_S) - (\hat{n}_0 - 1) \sum_{\alpha i} \frac{N V_i^2}{\Delta \tilde{E}^\alpha_i} \hat{P}_\alpha \\ &+ \sum_i \tfrac{1}{2}(J^T_i - J^S_i) \Bigg[\tfrac{1}{2}(\hat{P}_T - \hat{P}_S) \sum_\sigma \hat{n}_{0\sigma} + \hat{\mathbf{s}}_0 \cdot (\hat{\mathbf{s}}_1 + \hat{\mathbf{s}}_2) \Bigg], \end{aligned} \tag{4.39a}$$

and continue with

$$\begin{aligned}\hat{H}^{(2)}_{\text{eff}} &= +\sum_i \tfrac{1}{2}(J_i^T + J_i^S)\left(\tfrac{1}{2}\sum_\sigma \hat{n}_0 + 2\hat{\mathbf{s}}_0 \cdot \hat{\mathbf{s}}_i\right) \\ &= J_1 \hat{\mathbf{s}}_1 \cdot \hat{\mathbf{s}}_0 + J_2 \hat{\mathbf{s}}_2 \cdot \hat{\mathbf{s}}_0 - (\hat{P}_T - \hat{P}_S)\sum_i \tfrac{1}{4}(J_i^T - J_i^S) \\ &\quad + \left[(\hat{P}_T - \hat{P}_S)\sum_i \tfrac{1}{4}(J_i^T - J_i^S) + \sum_i \tfrac{1}{4}(J_i^T + J_i^S) - \sum_{\alpha i} \frac{NV_i^2}{\Delta \tilde{E}_i^\alpha}\hat{P}_\alpha\right](\hat{n}_0 - 1) \\ &\quad - \sum_i \tfrac{1}{4}(J_i^T + J_i^S)\hat{P}\end{aligned} \tag{4.39b}$$

The above result is now expressed in terms of the individual exchange couplings for the two impurity levels:

$$J_1 = \tfrac{1}{2}(3J_1^T + J_2^T + J_1^S - J_2^S) \tag{4.40a}$$

$$J_2 = \tfrac{1}{2}(3J_2^T + J_1^T + J_2^S - J_1^S). \tag{4.40b}$$

Equation (4.39b) can be further simplified by noting from (4.23) that $\hat{P}_T - \hat{P}_S = 2\hat{\mathbf{s}}_1 \cdot \hat{\mathbf{s}}_2 + \frac{1}{2}\hat{P}$, this combination of projection operators can thereby be removed from (4.39b) to give, after association with (4.25):

$$\begin{aligned}\hat{H}_{\text{eff}} &= J_1 \hat{\mathbf{s}}_1 \cdot \hat{\mathbf{s}}_0 + J_2 \hat{\mathbf{s}}_2 \cdot \hat{\mathbf{s}}_0 - I\hat{\mathbf{s}}_1 \cdot \hat{\mathbf{s}}_2 \\ &\quad + \left[\sum_i \tfrac{1}{2}(J_i^T - J_i^S)\hat{\mathbf{s}}_1 \cdot \hat{\mathbf{s}}_2 + \sum_i \tfrac{1}{8}(3J_i^T + J_i^S) - \sum_{\alpha i} \frac{NV_i^2}{\Delta \tilde{E}_i^\alpha}\hat{P}_\alpha\right](\hat{n}_0 - 1) \\ &\quad - \tfrac{1}{8}\sum_i (3J_i^T + J_i^S)\hat{P}\end{aligned} \tag{4.41}$$

with the inter-impurity exchange coupling

$$I = J_H + \tfrac{1}{2}(J_1^T + J_2^T - J_1^S - J_2^S). \tag{4.42}$$

The factor J_H appearing here is that which arises in the initial Hamiltonian $\hat{H}_0$. The third line of (4.41) is simply a constant, which we ignore, whilst the second line describes scattering of the zero orbital electrons off of the impurity levels. By defining the constants

$$K_i^\alpha = NV_i^2\left(\frac{1}{\Delta E_i^\alpha} - \frac{1}{\Delta \tilde{E}_i^\alpha}\right) \tag{4.43}$$

[*cf.* (4.32) for J_i^α] the final result for the effective low-energy model in the $(1,1)$

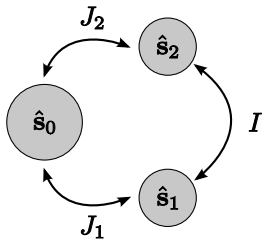

Figure 4.11: The effective low-energy spin model. The two impurity spins each couple separately to the conduction band spin density at the impurity in an antiferromagnetic fashion. A ferromagnetic coupling, $I > J_H$ also exists between the impurity spins.

sector of the 2LM is:

$$\begin{aligned}\hat{H}_{\text{eff}} &= J_1\hat{\mathbf{s}}_1\cdot\hat{\mathbf{s}}_0 + J_2\hat{\mathbf{s}}_2\cdot\hat{\mathbf{s}}_0 - I\hat{\mathbf{s}}_1\cdot\hat{\mathbf{s}}_2 \\ &+ \left[\sum_i \tfrac{1}{8}(3K_i^T + K_i^S) + \tfrac{1}{2}(K_i^T - K_i^S)\hat{\mathbf{s}}_1\cdot\hat{\mathbf{s}}_2\right](\hat{n}_0 - 1).\end{aligned} \tag{4.44}$$

This Hamiltonian is represented schematically in fig. 4.11, it consist of two mutually coupled impurity spins (corresponding to the local moments formed on the original levels) each of which is also independently coupled to the conduction band spin density at the impurity. The model is of the same form as the model derived by Hofstetter and Schoeller [52] appropriate for the situation when the $(1,1)$ triplet and $(2,0)$ singlet states of the atomic limit are near degenerate. The only difference between this model and the current case is the form of the couplings. In the current case the impurity spins $\hat{\mathbf{s}}_1$ and $\hat{\mathbf{s}}_2$ are real impurity spins, whereas in the Hofstetter-Schoeller case these spins are composite, fictitious spins. Both formulations are useful in understanding the properties of the 2LM.

The spin only model consisting of solely the first line of (4.44) has been studied previously [53] as a quantum impurity model in its own right and so the physics of it are understood. A QPT transition is naturally driven by the direct exchange I. For ferromagnetic $\Delta I = I - I_c > 0$, the spins 1 and 2 form a spin 1 which is underscreened on coupling to the lead spin density, resulting in a residual spin $\frac{1}{2}$. For antiferromagnetic $\Delta I = I - I_c < 0$ by contrast, the local-singlet Fermi liquid phase arises. The QPT transition is in general of KT form. This spin model therefore captures the essence of the full 2LM in this regime. Furthermore, (4.42) admits the possibility that the effective direct exchange coupling I remains ferromagnetic for even when the bare J_H is antiferromagnetic. It is therefore not surprising that the USC phase persists for weak $J_H < 0$. Naturally as J_H is decreased further to the point at which $|J_H| > \frac{1}{2}(J_1^T + J_2^T - J_1^S - J_2^S)$ a local impurity singlet state is to be expected.

Before moving on to discuss examples of thermodynamic properties for weakly

antiferromagnetic J_H, we note the symmetries of the couplings arising in (4.44). From (4.27) and (4.32) it is clear that J_1^α is solely a function of ϵ_1 (or x) whilst J_2^α depends only on ϵ_2 (or y). Further both quantities are odd in their arguments, for example:

$$J_1^\alpha(x) = NV_1^2\left(\frac{1}{\frac{1}{2}U+\gamma J_H - x} + \frac{1}{\frac{1}{2}U+\gamma J_H + x}\right) = J_1^\alpha(-x) \tag{4.45}$$

with $\gamma = \frac{1}{4}$ or $-\frac{3}{4}$ for $\alpha = T$ or S. It follows from (4.40) and (4.42) that the three exchange couplings appearing in (4.44) are inversion symmetric:

$$J_i(x,y) = J_i(-x,-y) \tag{4.46a}$$

$$I(x,y) = I(-x,-y). \tag{4.46b}$$

Similar comments can be made of the potential scattering couplings and so the effective Hamiltonian is therefore also inversion symmetric: $\hat{H}_{\text{eff}}(x,y) = \hat{H}_{\text{eff}}(-x,-y)$. These conclusions are general and conform to the symmetries we know exist in the full 2LM from examination of the atomic limit. By setting $V_1 = V_2 = V$ a 1–2 symmetry also arises. A single function now characterises both J_i^α, specifically:

$$J_1^\alpha \equiv J^\alpha(x), \qquad J_2^\alpha \equiv J^\alpha(y). \tag{4.47}$$

In this limit we find

$$J_1(x,y) = J_2(y,x), \tag{4.48a}$$

$$I(x,y) = I(y,x), \tag{4.48b}$$

and so $\hat{H}_{\text{eff}}(x,y) \rightarrow \hat{H}_{\text{eff}}(y,x)$ under the 1–2 transformation. The potential scattering terms however are not similarly invariant under such a transformation and so whilst the spin part of $\hat{H}_{\text{eff}}$ [the first line of (4.44)] is invariant the full effective Hamiltonian is not. This of course echoes the symmetries of the atomic limit in the case of $U' \neq 0$.

It is worth noting a final point concerning the symmetry of the couplings. Along the lines $y = \pm x$ in the $x-y$ plane, and again for $V_1 = V_2$, it follows from (4.48) that $J_1(x,\pm x) = J_2(x,\pm x)$ and hence from (4.40), (4.45) and (4.47) that

$$J_2(x,\pm x) = J_1(x,\pm x) = 2J^T(x), \tag{4.49}$$

with $I(x,\pm x) = J_H + [J^T(x) - J^S(x)]$ following similarly from (4.42). It is therefore only the impurity triplet spin combination which couples to the conduction band, the singlet combination completely decoupling. This decoupling can be shown explicitly by projecting (4.44) with $\hat{P} = \hat{P}_T + \hat{P}_S$. Defining the total impurity spin $\hat{\mathbf{s}}$ and using

$\hat{\mathbf{s}}_1 \cdot \hat{\mathbf{s}}_2 \equiv \frac{1}{2}(\hat{S}^2 - \frac{3}{2})$ together with $\hat{\mathbf{s}}\hat{P}_S \equiv 0$ for all components of $\hat{\mathbf{s}}$ we find:

$$\hat{H}_{\text{eff}} = \hat{P}_T(J_1\hat{\mathbf{s}} \cdot \hat{\mathbf{s}}_0 - \tfrac{1}{4}I)\hat{P}_T + \tfrac{3}{4}I\hat{P}_S, \tag{4.50}$$

which contains no term mixing the singlet and triplet sectors. As in the case of the line $y = x$ where the Hilbert space of the 2LM can be separated into disjoint even and odd parity sectors, the effective spin model derived here is separable into a triplet sector and a singlet sector; thus explaining the remaining first order transitions in fig. 4.9. Why, however, are similar first-order transitions not found on the exterior sides of the domains straddling the line $y = -x$? The effective model is simply not applicable in this region. The correct model in this case is formed by retaining also the $(2, 0)$ [or $(0, 2)$] states of the isolated impurity. Whilst the resulting low-energy model takes the same form as that used here [52], the couplings do not display the same symmetries and the transition is of KT form.

Finally we comment on the observation that the USC survives away from the particle hole symmetric point after it has been destroyed at this point. This is consistent with the couplings in the low-energy model derived above. Considering the lines $y = \pm x$ for simplicity, for a given J_H both $J^T(x)$ and $I(x, \pm x)$ grow on increasing $|x|$ to favour a local impurity triplet state.

Figure 4.12 shows results for the impurity thermodynamics at particle hole symmetry as J_H is switched from ferromagnetic to antiferromagnetic for the same $\tilde{U} = 10$ and $\tilde{U}' = 5.25$ as fig. 4.9. In case a) $\tilde{J}_H = 5$ a weak intermeadiate $S_{\text{imp}}(T) = \ln 3$ plateau is seen indicative of the spin-1 LM fixed point. For b) $\tilde{J}_H = 0$ and c) -0.55 this plateau rises such that $S_{\text{imp}}(T)$ approaches values nearer $\ln 4$, corresponding to the approximate degeneracy of the four $(n_1, n_2) = (1, 1)$ states, an $SU(2) \times SU(2)$ fixed point. In all three cases the stable zero temperature behaviour is governed by the USC fixed point with $S_{\text{imp}}(T) = \ln 2$ and $T\chi_{\text{imp}}(T) \to \frac{1}{4}$. Cases d) $\tilde{J}_H = -0.558$, e) -0.56, and f) -0.6 by contrast show a stable FI fixed point with $S_{\text{imp}}(T) = 0$ and $T\chi_{\text{imp}}(T) = 0$ at zero temperature. The crossover to the stable fixed point occurs from the same $SU(2) \times SU(2)$ fixed point as arises on the USC side of the transition. The transition itself is first order, the parameters here putting the system on the $y = \pm x$ lines, with the crossover scale being a linear function of $\tilde{J}_H$ near the transition, inset to fig. 4.12.

We have not attempted a thorough comparison of the numerical results with the functional form of $I(x, y)$. In the full 2LM we expect additional higher order processes to supplement I, modifying both its magnitude and sign. Specifically an effective RKKY interaction can be generated [53, 101] by considering fourth-order V processes, resulting in $I_{\text{eff}} = I + I_{\text{RKKY}}$.

The sign of I_{RKKY} is generally expected [101–104] to be ferromagnetic. It has recently been suggested however, that for a double quantum dot coupled in parallel

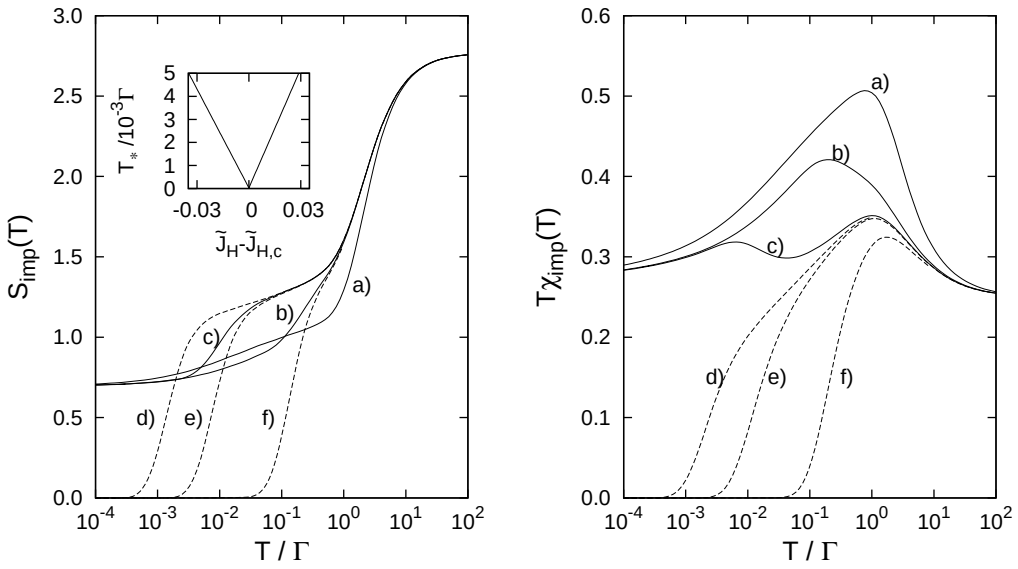

Figure 4.12: Evolution of thermodynamic properties as $\tilde{J}_H$ changes sign. a) The USC phase with ferromagnetic $\tilde{J}_H = +5$, the $S = 1$ LM fixed point is observed. b) $\tilde{J}_H = 0$ and c) -0.55, development of the $SU(2)\times SU(2)$ fixed point. d)-f) The FL phase with $\tilde{J}_H = -0.588, -0.56$, and -0.6 respectively. *Inset*: The associated low-energy scale T_* is linear in $\tilde{J}_H$.

the RKKY interaction is in fact antiferromagnetic [105–107]. Further, it has been argued due to the antiferromagnetic nature of I_{RKKY}, that the ground state of the 2LM presented here should in fact be a Fermi liquid, with no USC phase. The authors suggest that the fundamental approximation of the NRG [to neglect the second line of (3.8)] is the cause of the NRG's deficiencies, and that removing this approximation will introduce a second conduction band that will fully screen the impurity local moment. However such a supposition, if true, would put the NRG at odds with exact Bethe-Ansatz results for the spin-1 Kondo model, found to possess an underscreened ground state. The extra 'conduction band' generated by including higher terms in the NRG approximation does not in fact constitute a second independent screening channel: as in section 2.3.3 the two bands can be combined into a single conduction band.

As a by product of (4.44), we can derive the pure spin-1 Kondo model appropriate for the case that J_H is large and positive. In this case only the triplet impurity state is energetically relevant and we may discard the singlet states. We can rework the calculation using only the triplet states or more simply project (4.44) with $\hat{P}_T$. By writing $J_1\hat{\mathbf{s}}_1\cdot\hat{\mathbf{s}}_0 + J_2\hat{\mathbf{s}}_2\cdot\hat{\mathbf{s}}_0 = \frac{1}{2}(J_1+J_2)(\hat{\mathbf{s}}_1+\hat{\mathbf{s}}_2)\cdot\hat{\mathbf{s}}_0 + \frac{1}{2}(J_1-J_2)(\hat{\mathbf{s}}_1-\hat{\mathbf{s}}_2)\cdot\hat{\mathbf{s}}_0$ and recognising that $\hat{P}_T(\hat{\mathbf{s}}_1-\hat{\mathbf{s}}_2)\hat{P}_T = 0$ we arrive at a spin-1 Kondo model:

$$\begin{aligned}\hat{H}_K^{S=1} &= \hat{P}_T\hat{H}_{\mathrm{eff}}\hat{P}_T \\ &= J_K^{S=1}\hat{\mathbf{s}}\cdot\hat{\mathbf{s}}_0 + K\hat{n}_0,\end{aligned} \tag{4.51}$$

(as given in section 4.2.1) with $\hat{\mathbf{s}}$ representing the total impurity spin, $J_K^{S=1} = \frac{1}{2}(J_1 + J_2)$ the Kondo coupling and $K = \Sigma_i 2K_i^T$ the potential scattering matrix element

In this section we have explored how the USC phase is robust to moderate antiferromagnetic J_H. The low-energy spin model derived previously concurs with the NRG results — the separability of the model leading to first-order transitions, and the functional forms of the exchange couplings dictating how the USC fractionates and eventually disappears.

4.3.3 Unequal dot-lead couplings

So far, and throughout the rest of this thesis, we have simplified the numerical study of the 2LM by examining the limit $V_1 = V_2$. So called side-coupled quantum dots, systems where only one of the two impurity levels is tunnel coupled to the host (*i.e.* one of the V_i is set to zero), have attracted previous research [108–112]. For completeness we now briefly examine the evolution of the phase boundary in the 2LM on varying the impurity-conduction band couplings V_1 and V_2 between these two limits.

In considering the case of unequal coupling we consider only the relative values of the couplings; we define the ratio $\gamma = \Gamma_{22}/\Gamma_{11}$ and maintain Γ_{11} constant. We continue to specify the remaining impurity parameters in units of $\Gamma \equiv \Gamma_{11}$.

Phase boundaries for diminishing γ are shown in fig. 4.13 for systems with common $\tilde{U} = 10$, $\tilde{U}' = 7.5$, and $\tilde{J}_H = 5$. In all cases we show also the atomic limit boundaries (dotted). Figure 4.13a) displays the results for symmetric couplings $\gamma = 1$ — the phase boundary displays both inversion symmetry and reflection symmetry in the line $y = x$. This latter symmetry is lost on moving to b) $\gamma = 0.6$. Two lobes (related by inversion) develop with the phase boundary growing into the $(n_1, n_2) = (2, 1)$ and $(0, 1)$ regions of the atomic limit. These lobes extend and widen for c) $\gamma = 0.5$. Finally the case of $\gamma = 0$ is depicted in d) where it is seen that the entire phase boundary follows closely the AL.

It is clear then that as γ is lowered (and the coupling of level 2 decreases), level 2 progressively behaves increasingly as it does in the atomic limit. The effect is to stabilise the USC phase for regimes where $n_2 = 1$; level 2 is responsible for carrying the impurity local moment, being coupled to the conduction band only via level 1. This is most strongly seen of course for $V_2 = 0$ where an impurity local moment is always found in regions of the $x - y$ plane corresponding to the $(2, 1)$ and $(0, 1)$ sectors of the AL. For $|x|/\Gamma \gg 0$ the low-energy physics of the USC phase are not now well described by a spin-1 Kondo model, rather one must view the system as a two-spin spin-$\frac{1}{2}$ Kondo model with one spin strongly coupled to the conduction band and with the second essentially decoupled. The system still possesses a local

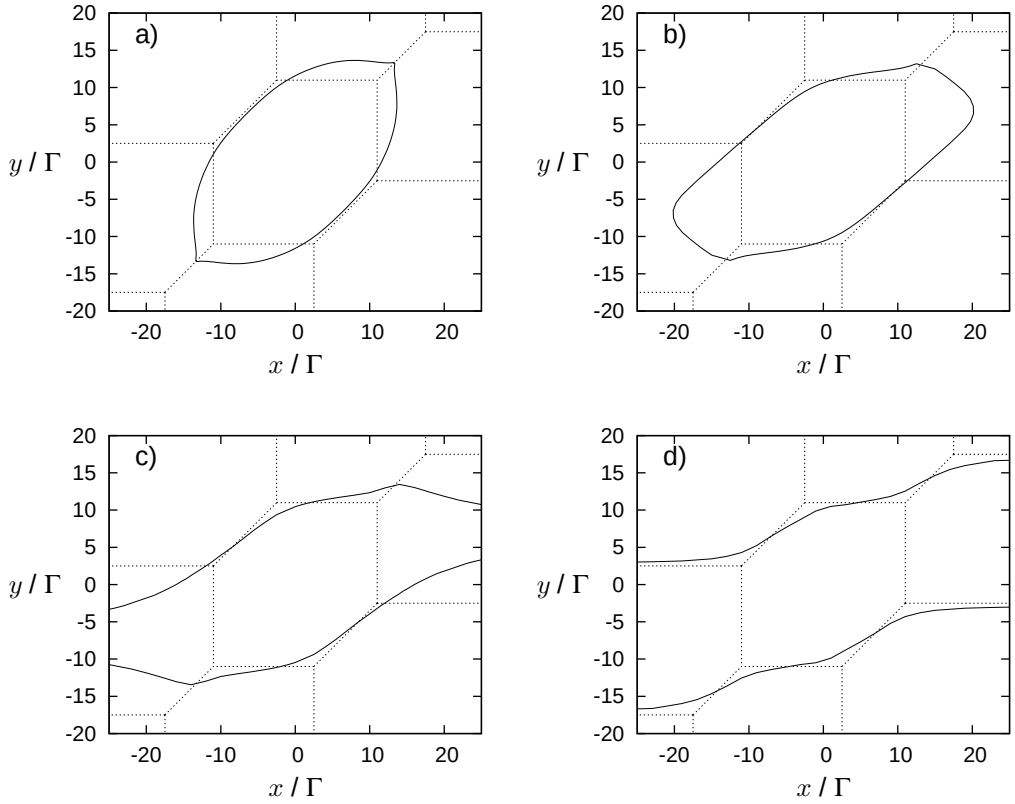

Figure 4.13: Phase boundaries (solid) in the $x-y$ plane for $\tilde{U}=10$, $\tilde{U}'=7.5$, $\tilde{J}_H=5$, and a) $\gamma=V_2/V_1=1$, b) 0.6, c) 0.5, and d) 0. Dotted lines indicate the atomic limit boundaries and dashed lines give $n_{\rm imp}=2$. On decreasing γ the USC phase evolves into the atomic limit regions with $n_2=1$, with the phase boundaries being coincident with the $n_{\rm imp}=2$ lines for $V_2=0$.

moment ground state, however the physical origin of this state is somewhat different.

The main conclusion of this brief section is therefore that a lack of symmetry in the tunnel couplings V_1 and V_2 does not crucially affect the physics of the 2LM. The major effect is to deform the shape of the phase boundary; the underlying fixed point structure of the model remains identical. We shall say no more about the asymmetric case and we shall continue studying the case of $V_1=V_2$ with impunity

This concludes our results for the thermodynamic properties of the 2LM. The NRG is well suited to detecting the phase boundary between the usual FL phase and the more exotic USC phase. We have illustrated the stability of the USC fixed point to various changes in the parameters of the model. The nature of the transition has been investigated. It is generally of KT form with an associated exponential vanishing of the low-energy Kondo scale T_K on approaching the transition in the FL phase. However, along special lines of symmetry first-order transitions are found due to the separability of the Hamiltonian into distinct sectors. The next chapter will be devoted to the study of the dynamic properties of the 2LM.

CHAPTER 5

Dynamics and Transport in Two-Level Quantum Dots

In the previous chapter the NRG was shown to be a useful tool for calculating temperature-dependent thermodynamic properties of quantum impurity models and specifically the 2LM studied in this thesis. In this chapter we will study the dynamic properties of the 2LM starting with simple properties of the impurity Green functions and spectral densities, before in section 5.2 introducing some new ideas about the so-called Luttinger integral. We will examine in detail the evolution of the single-particle densities across the phase transition before finally comparing our results (favourably) with those of experiments with real quantum dot devices.

With regard to the dynamics of quantum impurity systems the fundamental quantities of interest are the impurity single-particle propagators introduced briefly in section 3.5. We will now embark on a more fulsome treatment of these central quantities, after reiterating some of the basic results. In section 3.5.1 we outlined the link between the non-interacting limit, where all parameters U, U', and J_H are set to zero, and the fully interacting case. This relation is embodied by the impurity self-energy and the Dyson equation:

$$\mathbf{G}_\sigma(\omega) = \mathbf{G}^0_\sigma(\omega) + \mathbf{G}^0_\sigma(\omega)\mathbf{\Sigma}_\sigma(\omega)\mathbf{G}_\sigma(\omega). \tag{5.1}$$

By using equations of motion methods [20, 86] one can find expressions for the single-particle propagators describing the behaviour of the electrons as they move between the impurity levels, and from the impurity to the conduction band:

$$(\omega^+ - \epsilon_{i\sigma})G^0_{ij;\sigma}(\omega) = \delta_{ij} + \sum_{\mathbf{k}} V_{i\mathbf{k}} G^0_{\mathbf{k}j}(\omega) \tag{5.2a}$$

$$(\omega^+ - \epsilon_{\mathbf{k}\sigma})G^0_{\mathbf{k}j;\sigma}(\omega) = \sum_{l=1,2} V_{\mathbf{k}l} G^0_{lj;\sigma}(\omega). \tag{5.2b}$$

The host-impurity hybridization function is given generally by (3.29):

$$\Gamma_{ij}(\omega) = \sum_{\mathbf{k}} \frac{V_{i\mathbf{k}} V_{j\mathbf{k}}}{\omega^+ - \epsilon_{\mathbf{k}}} \equiv \Gamma^R_{ij}(\omega) - i\Gamma^I_{ij}(\omega), \tag{5.3}$$

In practice (as in sections sections 2.3.3 and 3.1), we consider explicitely the standard case [20, 23] of a symmetric flat-band conduction band/lead with $V_{i\mathbf{k}} = V_i$. In this case, (5.3) yields

$$\Gamma^I_{ij}(\omega) = \Gamma_{ij} = \pi\rho V_i V_j \tag{5.4}$$

(for $|\omega| < D$, and zero otherwise) with ρ the total density of states of the lead, $\Gamma^R_{ij}(\omega = 0) = 0$ at the Fermi level, and:

$$\Gamma^2_{12}(\omega) = \Gamma_{11}(\omega)\Gamma_{22}(\omega) \tag{5.5}$$

By combining (5.1) and (5.2) and defining

$$\tilde{\mathbf{\Gamma}}(\omega) = \mathbf{\Gamma}(\omega) + \mathbf{\Sigma}(\omega) \tag{5.6}$$

one obtains the fully interacting propagators as:

$$G_{11;\sigma}(\omega) = [\omega^+ - \epsilon_{2\sigma} - \tilde{\Gamma}_{22}(\omega)] \det \mathbf{G}_\sigma(\omega) \tag{5.7a}$$

$$G_{22;\sigma}(\omega) = [\omega^+ - \epsilon_{1\sigma} - \tilde{\Gamma}_{11}(\omega)] \det \mathbf{G}_\sigma(\omega) \tag{5.7b}$$

$$G_{12;\sigma}(\omega) = G_{21;\sigma}(\omega) = \tilde{\Gamma}_{12}(\omega) \det \mathbf{G}_\sigma(\omega), \tag{5.7c}$$

with the determinant given explicitly by:

$$\det \mathbf{G}_\sigma(\omega) = \left\{ [\omega^+ - \epsilon_{1\sigma} - \tilde{\Gamma}_{11}(\omega)][\omega^+ - \epsilon_{2\sigma} - \tilde{\Gamma}_{22}(\omega)] - [\tilde{\Gamma}_{12}(\omega)]^2 \right\}^{-1} \tag{5.8}$$

It is convenient at this point to note a formal expression for the 'excess impurity charge' n_{imp} introduced in section 4.3 as the difference in charge of the entire system with and without the impurity present. This quantity is then, by definition, given by:

$$n_{\text{imp}} = \frac{-1}{\pi} \operatorname{Im} \sum_\sigma \int_{-\infty}^{0} \left\{ \sum_{\mathbf{k}} \left[G_{\mathbf{kk};\sigma}(\omega) + G_{11;\sigma}(\omega) + G_{22;\sigma}(\omega) \right] - \sum_{\mathbf{k}} \frac{1}{\omega^+ - \epsilon_{\mathbf{k}\sigma}} \right\} \mathrm{d}\omega. \tag{5.9}$$

To simplify the above we write the final term here, the number of electrons in an isolated conduction band, in terms of the impurity propagators of (5.2a). In the non-interacting limit, an equations of motion approach then gives

$$(\omega^+ - \epsilon_{\mathbf{k}\sigma}) G^0_{\mathbf{kk}';\sigma}(\omega) = \delta_{\mathbf{kk}'} + \sum_i V_{\mathbf{k}i} G^0_{\mathbf{k}i;\sigma}(\omega). \tag{5.10}$$

Now by inserting (5.2b) into the above one finds:

$$\sum_{\mathbf{k}} G^0_{\mathbf{kk};\sigma}(\omega) = \sum_{\mathbf{k}} \frac{1}{\omega^+ - \epsilon_{\mathbf{k}\sigma}} - \sum_{ij} \frac{\partial \Gamma_{ij}(\omega)}{\partial \omega} G^0_{ji;\sigma}(\omega). \tag{5.11}$$

In the fully interacting case $G_{\mathbf{kk};\sigma}(\omega)$ will be the same functional of $\{G_{ij;\sigma}(\omega)\}$ as $G^0_{\mathbf{kk};\sigma}(\omega)$ is of $\{G^0_{ij;\sigma}(\omega)\}$, since interactions occur solely on the impurity. We therefore have

$$\sum_{\mathbf{k}} G_{\mathbf{kk};\sigma}(\omega) - \sum_{\mathbf{k}} \frac{1}{\omega^+ - \epsilon_{\mathbf{k}\sigma}} = \sum_{ij} \frac{\partial \Gamma_{ij}(\omega)}{\partial \omega} G_{ji;\sigma}(\omega) \tag{5.12}$$

such that (5.9) becomes

$$\begin{aligned} n_{\mathrm{imp}} = \frac{-1}{\pi} \operatorname{Im} \sum_{\sigma} \int_{-\infty}^{0} \Bigg\{ G_{11;\sigma}(\omega) \left[1 - \frac{\partial \Gamma_{11}(\omega)}{\partial \omega} \right] + G_{22;\sigma}(\omega) \left[1 - \frac{\partial \Gamma_{22}(\omega)}{\partial \omega} \right] \\ - 2 G_{12;\sigma}(\omega) \frac{\partial \Gamma_{12}(\omega)}{\partial \omega} \Bigg\} \mathrm{d}\omega. \end{aligned} \tag{5.13}$$

The structure of the above is very natural — it contains two 'one-level' contributions and a cross term. For the present case of a flat band, if we assume that the bandwidth is much larger than any other energy scale (as we use within the NRG in practice) then the derivatives in the above are all equal to zero, and the expression for n_{imp} reduces to:

$$n_{\mathrm{imp}} \simeq \frac{-1}{\pi} \operatorname{Im} \sum_{\sigma} \int_{-\infty}^{0} [G_{11;\sigma}(\omega) + G_{22;\sigma}(\omega)] \mathrm{d}\omega \tag{5.14a}$$

$$= \sum_{\sigma} \int_{-\infty}^{0} [D_{11;\sigma}(\omega) + D_{22;\sigma}(\omega)] \mathrm{d}\omega, \tag{5.14b}$$

now given in terms of the spectral densities $D_{ij}(\omega) = \frac{-1}{\pi} \operatorname{Im} G_{ij}(\omega)$. Equation (5.14b) is the result stated previously, namely that n_{imp} is approximately related to the charge on the impurity, the sum to the Fermi level of the spectral densities.[1]

5.1 The even-even spectral density

The previous section has introduced some basic results for the impurity propagators and spectral densities of the 2LM. Before showing FDM-NRG results for these functions we will further develop our understanding of the 2LM via analytic methods.

We will be ultimately interested in the differential conductance of the 2LM, as given in (3.50). To this end we note that (3.50) contains the symmetric linear

[1] Equation (5.14) is often taken in the NRG literature to be an equality. It is not, only (5.13) is exact. Formally (5.14) requires an infinitely flat band. In practice n_{imp} and $\langle \hat{n}_1 + \hat{n}_2 \rangle$ very nearly coincide but are not identical.

combination of impurity spectral densities:

$$\sum_{ij} \pi\Gamma^I_{ij}(\omega) D_{ji}(\omega) \equiv \sum_{ij} \pi\Gamma_{ij} D_{ji}(\omega), \tag{5.15}$$

as discussed above for a flat conduction band. We therefore define even and odd combinations of the impurity orbitals, *viz.*:

$$d^\dagger_{e\sigma} = \frac{1}{\sqrt{V_1^2 + V_2^2}} (V_1 d^\dagger_{1\sigma} + V_2 d^\dagger_{2\sigma}) \tag{5.16a}$$

$$d^\dagger_{o\sigma} = \frac{1}{\sqrt{V_1^2 + V_2^2}} (V_2 d^\dagger_{1\sigma} - V_1 d^\dagger_{2\sigma}) \tag{5.16b}$$

from which follow the 'even-even', 'odd-odd' and 'even-odd' impurity propagators:

$$G_{ee}(\omega) = \frac{1}{V_1^2 + V_2^2} \left[V_1^2 G_{11}(\omega) + V_2^2 G_{22}(\omega) + 2V_1 V_2 G_{12}(\omega) \right] \tag{5.17a}$$

$$G_{oo}(\omega) = \frac{1}{V_1^2 + V_2^2} \left[V_2^2 G_{11}(\omega) + V_1^2 G_{22}(\omega) - 2V_1 V_2 G_{12}(\omega) \right] \tag{5.17b}$$

$$G_{eo}(\omega) = G_{oe}(\omega) = \frac{1}{V_1^2 + V_2^2} \left[V_1 V_2 G_{11}(\omega) - V_1 V_2 G_{22}(\omega) + (V_2^2 - V_1^2) G_{12}(\omega) \right]. \tag{5.17c}$$

By using $\Gamma_{ij} = \pi\rho V_i V_j$ [(5.4)], (5.15) can be rewritten:

$$\sum_{ij} \pi\Gamma_{ij} D_{ji}(\omega) = \pi(\Gamma_{11} + \Gamma_{22}) D_{ee}(\omega). \tag{5.18}$$

Thus the conductance through the 2LM system is governed solely by the even-even spectral density. The immediate question of why might this be so is quickly answered by transforming the impurity-lead tunneling Hamiltonian (2.44d) into the basis of the even and odd operators. To achieve this we employ

$$d^\dagger_{1\sigma} = \frac{1}{\sqrt{V_1^2 + V_2^2}} (V_1 d^\dagger_{e\sigma} + V_2 d^\dagger_{o\sigma}) \tag{5.19a}$$

$$d^\dagger_{2\sigma} = \frac{1}{\sqrt{V_1^2 + V_2^2}} (V_2 d^\dagger_{e\sigma} - V_1 d^\dagger_{o\sigma}), \tag{5.19b}$$

to give:

$$\begin{aligned} \hat{H}_{\mathrm{T}} &= \sum_{i\mathbf{k}\sigma} V_i (d^\dagger_{i\sigma} c_{\mathbf{k}\sigma} + c^\dagger_{\mathbf{k}\sigma} d_{i\sigma}) \\ &= \sum_{\mathbf{k}\sigma} \sqrt{V_1^2 + V_2^2} \left(d^\dagger_{e\sigma} c_{\mathbf{k}\sigma} + c^\dagger_{\mathbf{k}\sigma} d_{e\sigma} \right), \end{aligned} \tag{5.20}$$

which shows a complete detachment of the odd impurity channel from the lead, as seen previously in section 4.3.1. This is not to say the odd channel is not now

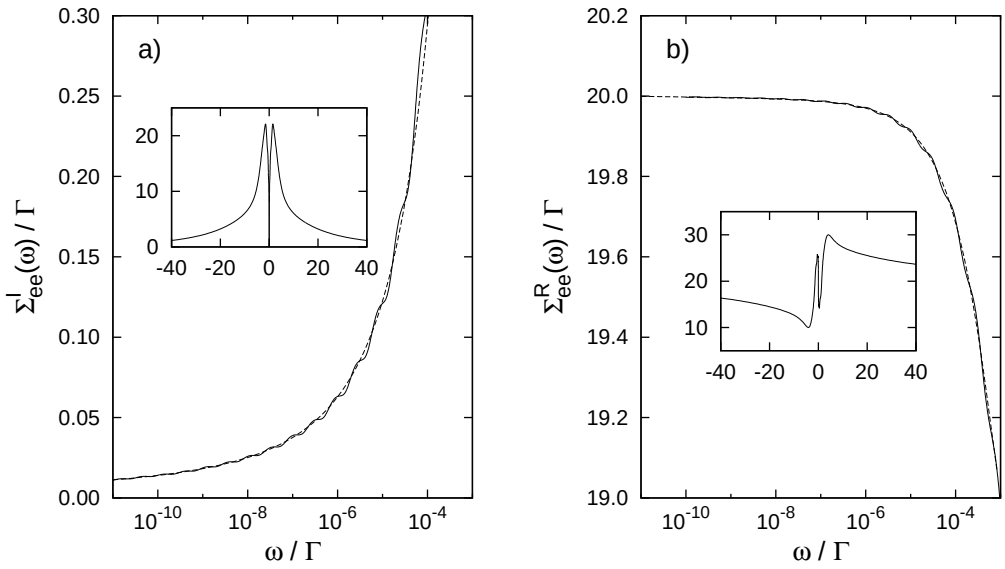

Figure 5.1: Low frequency asymptotics of the even-even impurity self-energy $\Sigma_{ee}(\omega) = \Sigma^R_{ee}(\omega) - i\Sigma^I_{ee}(\omega)$ for a system with $\tilde{U} = 20$, $\tilde{U}' = 10$, and $\tilde{J}_H = 5$ at particle-hole symmetry (and thus in the USC phase). Solid lines are results from the FDM-NRG, dashed lines are functional forms as given by (5.23). a) The imaginary part logarithmically approaches zero for $\omega \to 0$ whilst b) the real part approaches a non-vanishing value. The characteristic oscillations present in the FDM-NRG results can be suppressed by utilising the 'z-trick' [83–85].

important, for the impurity Hamiltonian $\hat{H}_{\rm D}$ contains interactions between even and odd channels as embodied in the self-energy $\Sigma_{oo}(\omega)$. We will see later in section 5.3 that the odd impurity orbital plays a particularly important role in describing the first order transitions along the line $y = x$.

To proceed further we might wish to obtain an analytic expression for the spectral densities as an entire function of ω. Of course, if this were possible the NRG would be somewhat redundant! However, we can make progress by considering the zero-temperature conductance, for which one only need know the zero frequency properties of the impurity spectral functions: from (3.50) and (5.18),

$$G_C(T = 0, V_{\rm sd} = 0) = \frac{2e^2}{h} G_0 \pi(\Gamma_{11} + \Gamma_{22}) D_{ee}(\omega = 0). \tag{5.21}$$

We will make use of a fundamental, underpinning result of Fermi liquid theory: that the imaginary part of the impurity self-energy vanishes at the Fermi level [20]

$$\Sigma^I_{ij}(\omega = 0) = 0. \tag{5.22}$$

For the 2LM this relation certainly holds in the normal FL phase. In the USC phase we also expect (5.22) to hold precisely at the Fermi level $\omega = 0$, since a singular Fermi liquid also has purely elastic scattering at the Fermi level [99]. There are however important differences in the ω-dependence of $\Sigma^I_{ij}(\omega)$ for a normal and a singular Fermi liquid: for a normal FL, $\Sigma^I_{ij}(\omega) \propto \omega^2$ as $\omega \to 0$ [20] whereas in the

USC phase a rather slower logarithmic approach to zero occurs [54], with the form

$$\Sigma^I_{ee}(\omega) = \frac{a_1}{\log^2 \omega/T_K^{S=1}} + \frac{a_2}{\log^4 \omega/T_K^{S=1}} + \dots \tag{5.23a}$$

$$\Sigma^R_{ee}(\omega) = \Sigma^R_{ee}(0) + \frac{b_1}{\log^3 \omega/T_K^{S=1}} + \frac{b_2}{\log^5 \omega/T_K^{S=1}} + \dots . \tag{5.23b}$$

where the real part of the self-energy at the Fermi level, $\Sigma^R_{ee}(\omega = 0)$, is in general non-vanishing. The validity of (5.23) is illustrated in fig. 5.22, where the FDM-NRG has been used to calculate both the real and imaginary parts of the even-even self-energy in the USC phase.

As in (5.21), the $T = 0$ zero-bias conductance is determined solely by $\pi(\Gamma_{11} + \Gamma_{22})D_{ee}(0)$ at the Fermi level. This in turn follows from simple algebra. We define the renormalized levels [20]

$$\epsilon_i^* = \epsilon_i + \Sigma^R_{ii}(0) \tag{5.24}$$

and by using (5.3) and (5.6) to give $\tilde{\mathbf{\Gamma}}(0) = -i\mathbf{\Gamma} + \mathbf{\Sigma}^R(0)$, the even-even spectra is obtained by combining (5.7) and (5.8). This simple if lengthy calculation yields (for convenience we drop the spin label σ from now on)

$$\pi(\Gamma_{11} + \Gamma_{22})D_{ee}(0) = \frac{1}{1 + \left\{ \frac{\epsilon_1^*\epsilon_2^* - \left[\Sigma^R_{12}(0)\right]^2}{\epsilon_1^*\Gamma_{22} + \epsilon_2^*\Gamma_{11} - 2\Gamma_{12}\Sigma^R_{12}(0)} \right\}^2} \tag{5.25}$$

or equivalently

$$\pi(\Gamma_{11} + \Gamma_{22})D_{ee}(0) = \sin^2 \delta(0) \tag{5.26}$$

with δ given explicitly by

$$\delta(0) = \arctan \left\{ \frac{\epsilon_1^*\Gamma_{22} + \epsilon_2^*\Gamma_{11} - 2\Gamma_{12}\Sigma^R_{12}(0)}{\epsilon_1^*\epsilon_2^* - \left[\Sigma^R_{12}(0)\right]^2} \right\}. \tag{5.27}$$

The zero frequency even-even spectral density, and so the $T = 0$ zero-bias conductance, is thus wholly characterised by a single number, an angle δ. The quantity δ is thus central to calculating the zero-bias conductance, in *both* the FL and USC phase of the 2LM [since (5.26) and (5.27) are entirely general, applying to both phases]. In the next section we consider an alternative but entirely equivalent definition of δ that will lead us to a rather profound result.

5.2 Friedel-Luttinger sum rule

The quantity δ which has emerged in the previous section to characterise the zero frequency value of the even-even spectral density is simply the static ($\omega = 0$) scattering phase shift. The phase shift arises naturally when considering the scattering

of plane-wave electron states from an impurity [113], and is given alternatively by

$$\delta(\omega) = \mathrm{Im}\ln[\det \mathbf{G}(\omega)]. \tag{5.28}$$

Before continuing we will show the equivalence of (5.27) and (5.28) (with $\omega = 0$). From (5.3), (5.6) and (5.8), and taking $\Gamma_{ij} = \Gamma$ (merely for algebraic simplicity), we have:

$$\begin{aligned}\frac{1}{\det \mathbf{G}(\omega)} = &\Big\{[\omega^+ - \epsilon_1 - \Sigma^R_{11}(\omega)][\omega^+ - \epsilon_2 - \Sigma^R_{22}(\omega)] - [\Sigma^R_{12}(\omega)]^2 + [\Sigma^I_{12}(\omega)]^2 \\ &\qquad + \Gamma[2\Sigma^I_{12}(\omega) - \Sigma^I_{11}(\omega) - \Sigma^I_{22}(\omega)]\Big\} \\ &+ i\Big\{[\Gamma + \Sigma^I_{11}(\omega)][\omega^+ - \epsilon_2 - \Sigma^R_{22}(\omega)] + [\Gamma + \Sigma^I_{22}(\omega)][\omega^+ - \epsilon_1 - \Sigma^R_{11}(\omega)] \\ &\qquad + 2\Sigma^R_{12}(\omega)[\Gamma + \Sigma^I_{12}(\omega)]\Big\},\end{aligned} \tag{5.29}$$

where we have separated the real and imaginary parts. Now by taking $\omega = 0$, and using $\Sigma^I_{ij}(\omega = 0) = 0$, we obtain:

$$\frac{1}{\det \mathbf{G}(\omega)} = \Big\{\{\epsilon^*_1\epsilon^*_2 - [\Sigma^R_{12}(0)]^2\} - \eta^2 - 2\eta\Gamma\Big\} + i\Big\{ - \eta(\epsilon^*_1 + \epsilon^*_2) + \Gamma[2\Sigma^R_{12}(0) - \epsilon^*_1 - \epsilon^*_2]\Big\}. \tag{5.30}$$

Finally by considering the general case in which $\epsilon^*_1 + \epsilon^*_2 - 2\Sigma^R_{12}(0)$ and $\epsilon^*_1\epsilon^*_2 - [\Sigma^R_{12}(0)]^2$ are not simultaneously zero,[2] such that we can neglect the $\eta = 0^+$ factors in the above, we arrive at:

$$\delta(0) = \mathrm{Im}\ln\det \mathbf{G}(0) = \mathrm{Im}\ln\frac{\{\epsilon^*_1\epsilon^*_2 - [\Sigma^R_{12}(0)]^2\} + i\Gamma\{\epsilon^*_1 + \epsilon^*_2 - 2\Sigma^R_{12}(0)\}}{\{\epsilon^*_1\epsilon^*_2 - [\Sigma^R_{12}(0)]^2\}^2 + \Gamma^2\{\epsilon^*_1 + \epsilon^*_2 - 2\Sigma^R_{12}(0)\}^2} \tag{5.31}$$

$$= \arctan\frac{\Gamma\{\epsilon^*_1 + \epsilon^*_2 - 2\Sigma^R_{12}(0)\}}{\{\epsilon^*_1\epsilon^*_2 - [\Sigma^R_{12}(0)]^2\}}. \tag{5.32}$$

Thus the quantity $\delta(0)$ appearing in (5.26) and (5.27) is the same as that which follows from the definition (5.28).

In the above we have considered only the static phase shift $\delta(\omega = 0)$. We will now examine the value of the phase shift in the limit $|\omega| \to \infty$. In this limit all the $\Sigma^I_{ij}(\omega)$ vanish whilst the corresponding real parts tend towards finite constants.

[2] The simultaneous equations $\epsilon^*_1 + \epsilon^*_2 - 2\Sigma^R_{12}(0) = 0$ and $\epsilon^*_1\epsilon^*_2 - [\Sigma^R_{12}(0)]^2 = 0$ have solution $\epsilon^*_1 = \epsilon^*_2 = \Sigma^R_{12}(0)$. In section 5.3.1 we will see that this condition is fulfilled solely at the phase boundary between the FL and USC phases along the line $y = x$. In that case an alternative formulation of the analysis here will however avoid this complication.

Equation (5.8) then gives:

$$\det \mathbf{G}(\omega) \overset{|\omega|\to\infty}{=} \frac{1}{(\omega^+)^2} \tag{5.33a}$$

By defining the principal range of δ to be $[0, 2\pi]$ we thus obtain:

$$\delta(-\infty) = 0, \tag{5.34a}$$
$$\delta(+\infty) = 2\pi. \tag{5.34b}$$

Having established the value of the phase shift $\delta(\omega)$ in the limits of $\omega = 0$ and $\omega = -\infty$ we will now use the definition given in (5.28) to derive a general result for the static phase shift. From (5.7) and (5.8) it follows that

$$\frac{\partial}{\partial\omega} \ln\det \mathbf{G}(\omega) = -\left[1-\frac{\partial\tilde{\Gamma}_{11}(\omega)}{\partial\omega}\right] G_{11}(\omega) - \left[1-\frac{\partial\tilde{\Gamma}_{22}(\omega)}{\partial\omega}\right] G_{11}(\omega) + 2\frac{\partial\tilde{\Gamma}_{12}(\omega)}{\partial\omega} G_{12}(\omega). \tag{5.35}$$

By integrating from $\omega = -\infty$ to 0 and using (5.6) we naturally obtain a relation for the phase shifts in terms of the impurity Green functions and self-energies, *viz.*:

$$\mathrm{Im}\int_{-\infty}^{0} \frac{\partial}{\partial\omega} \ln\det \mathbf{G}(\omega)\, \mathrm{d}\omega = \delta(0) - \delta(-\infty) \equiv \delta(0) \tag{5.36a}$$

$$\begin{aligned} &= -\,\mathrm{Im}\int_{-\infty}^{0} \left\{ G_{11}(\omega)\left[1-\frac{\partial\Gamma_{11}(\omega)}{\partial\omega}\right] + G_{22}(\omega)\left[1-\frac{\partial\Gamma_{22}(\omega)}{\partial\omega}\right] - 2G_{12}(\omega)\frac{\partial\Gamma_{12}(\omega)}{\partial\omega} \right\} \mathrm{d}\omega \\ &\quad + \mathrm{Im}\int_{-\infty}^{0} \left\{ G_{11}(\omega)\frac{\partial\Sigma_{11}(\omega)}{\partial\omega} + G_{22}(\omega)\frac{\partial\Sigma_{22}(\omega)}{\partial\omega} - 2G_{12}(\omega)\frac{\partial\Sigma_{12}(\omega)}{\partial\omega} \right\} \mathrm{d}\omega \end{aligned} \tag{5.36b}$$

The first line of (5.36b) can be recognised from (5.13) as being proportional to the excess impurity charge n_{imp}, whilst the second line is the Luttinger integral [114] defined generally to be

$$I_L = \mathrm{Im}\,\mathrm{Tr}\int_{-\infty}^{0} \frac{\partial\boldsymbol{\Sigma}(\omega)}{\partial\omega}\mathbf{G}(\omega)\, \mathrm{d}\omega. \tag{5.37}$$

By using (5.34a) we thus arrive at the very simple result

$$\delta(0) = \frac{\pi}{2} n_{\mathrm{imp}} + I_L, \tag{5.38}$$

relating the static phase shift to the excess impurity charge and the Luttinger integral. Equation (5.38) is entirely general: applicable to *both* the FL and USC phases of the 2LM.

For a normal Fermi liquid, Luttinger's integral theorem gives $I_L = 0$ [20, 114]; reflecting adiabatic continuity to the non-interacting limit — the fact that pertur-

bation theory in the interactions about this limit converges order by order. In this case (5.38) reduces to the usual Friedel sum rule [20, 113], $\delta(0) = \frac{\pi}{2} n_{\mathrm{imp}}$, relating the phase shift to the excess impurity charge (with $n_{\mathrm{imp}} \in [0, 4]$ for the 2LM, hence our definition of the principal range of δ). More generally however the phase shift and impurity charge are related by (5.38), which we refer to as a *Friedel-Luttinger sum rule*.

The Luttinger integral is then a characteristic of a Fermi liquid state in any system: provided only the system *is* a (normal) Fermi liquid, $I_L = 0$ holds independently of the underlying bare model parameters and indeed structure of the model Hamiltonian. The Luttinger integral is thus a hallmark of a Fermi liquid state in a rather deep sense.

The USC phase of the 2LM is not a regular Fermi liquid. There is no reason to suspect that $I_L = 0$ here and indeed it can be shown that the USC phase is not perturbatively connected to the noninteracting limit of the model. An obvious question arises however: as for a normal Fermi liquid, does an analogous situation arise for a singular Fermi liquid whereby the Luttinger integral has a characteristic, constant value for this type of state?

This question can be most easily answered by appealing to results from the FDM-NRG. The Luttinger integral can be calculated numerically in several ways. As the self-energies $\mathbf{\Sigma}(\omega)$ and Green functions $\mathbf{G}(\omega)$ can be calculated within in the FDM-NRG framework, we can calculate I_L directly from (5.37) by performing the integration. Alternatively we may obtain n_{imp} from a thermodynamic calculation as in section 4.3 and $\delta(0)$ from the *ee*-spectral density at the Fermi level [or via (5.31)]; the difference of these quantities then gives the Luttinger integral, $I_L = \delta(0) - \frac{\pi}{2} n_{\mathrm{imp}}$. These two methods naturally give essentially identical answers, illustrating the self-consistency of the FDM-NRG numerics.

Figure 5.2 displays typical results for the Luttinger integral calculated using (5.37)[3] We have taken a system with fixed $\tilde{U} = 20$, $\tilde{U}' = 10$, and $\tilde{J}_H = 5$. We have varied ϵ_1 and maintained $\Delta\epsilon = \epsilon_2 - \epsilon_1 = 2\Gamma$ for simplicity, such that we take a trajectory parallel to the $y = x$ line in the phase diagram. Four distinct regions are seen. For $x \ll 0$ we expect the system to be in the FL phase. Indeed this is found and $I_L = 0$ results, as expected. The FDM-NRG recovers the Luttinger theorem result really rather well: the calculated I_L/π being equal to zero to within ± 0.001. On crossing into the USC phase (the transition occurring here at $x \sim -12.6\Gamma$) the Luttinger integral takes a new constant value $I_L = -\pi/2$. The quantity remains at this value until the $y = -x$ line is crossed, at which point we find $I_L = +\pi/2$, and again constant. Finally on crossing the transition back into the FL phase the FDM-NRG results correctly show $I_L = 0$ once again.

[3] We find this method to be slightly superior in practice.

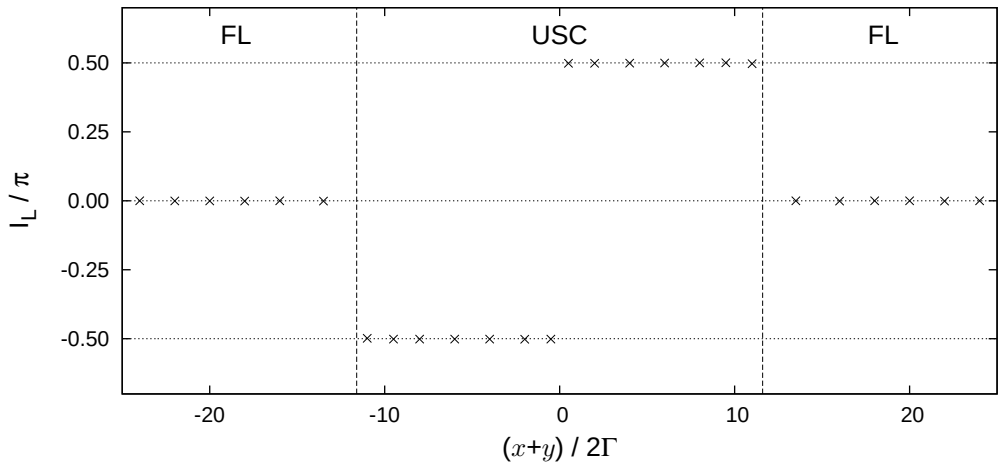

Figure 5.2: The Luttinger integral I_L calculated via the FDM-NRG method for the 2LM for a system with $\tilde{U} = 20$, $\tilde{U}' = 10$, and $\tilde{J}_H = 5$ and fixed level spacing $\Delta\epsilon = \epsilon_2 - \epsilon_1 = y - x = 2\Gamma$. Throughout the FL phase $I_L = 0$ as prescribed by Luttinger's theorem. In the USC phase $|I_L| = \pi/2$ and I_L changes sign discontinuously across the line $y = -x$.

In summary, the FDM-NRG recovers correctly $I_L = 0$ in the Fermi liquid phase of the 2LM. In the USC by contrast we find that $|I_L|$ is a non-zero constant that likewise characterises this phase:

$$|I_L| = \frac{\pi}{2}. \tag{5.39}$$

This result is found for many different values of the bare interaction parameters $\tilde{U}$, $\tilde{U}'$, and $\tilde{J}_H$. Whilst the numerical results cannot amount to a proof, we are confident of the general validity of (5.39). That the sign of the Luttinger integral should change across the line $y = -x$ is a natural consequence of symmetry, as we now show.

In appendix A we explore the symmetries of the Green functions and self-energies under the particle-hole transformation $(x, y) \to (-x, -y)$. The key results are:

$$\mathbf{G}(-\omega; -x, -y) = -\mathbf{G}^\dagger(\omega; x, y) \tag{5.40a}$$

$$\mathbf{\Sigma}(-\omega; -x, -y) = -\mathbf{\Sigma}^*(\omega; x, y) + (U + 2U')\mathbf{1}. \tag{5.40b}$$

Using (5.40) directly in (5.37) gives:

$$I_L(-x, -y) = \operatorname{Im}\operatorname{Tr}\int_{-\infty}^{0} \frac{\partial}{\partial\omega}\mathbf{\Sigma}(\omega; -x, -y)\mathbf{G}(\omega; -x, -y)\,\mathrm{d}\omega \tag{5.41a}$$

$$= \operatorname{Im}\operatorname{Tr}\int_{-\infty}^{0} \frac{\partial}{\partial\omega}\mathbf{\Sigma}^\dagger(\omega; x, y)\mathbf{G}^\dagger(\omega; x, y)\,\mathrm{d}\omega \tag{5.41b}$$

$$= \operatorname{Im}\operatorname{Tr}\int_{0}^{\infty} \frac{\partial}{\partial\omega}\mathbf{\Sigma}(\omega; x, y)\mathbf{G}(\omega; x, y)\,\mathrm{d}\omega, \tag{5.41c}$$

where on the third line we have made the substitution $\omega \to -\omega$. From (5.37) we have then

$$I_L(x,y) + I_L(-x,-y) = \mathrm{Im}\,\mathrm{Tr}\int_{-\infty}^{\infty} \frac{\partial}{\partial\omega}\mathbf{\Sigma}(\omega;x,y)\mathbf{G}(\omega;x,y)\,\mathrm{d}\omega. \tag{5.42}$$

In precise parallel to the calculation of the static phase shift $\delta(0)$ from (5.36a) we may calculate the right hand side of (5.42):

$$\mathrm{Im}\int_{-\infty}^{+\infty} \frac{\partial}{\partial\omega}\ln\det\mathbf{G}(\omega)\,\mathrm{d}\omega = \delta(+\infty) - \delta(-\infty) \tag{5.43a}$$

$$= 2\pi + \mathrm{Im}\,\mathrm{Tr}\int_{-\infty}^{+\infty} \frac{\partial\mathbf{\Sigma}(\omega)}{\partial\omega}\mathbf{G}(\omega)\,\mathrm{d}\omega, \tag{5.43b}$$

and from using (5.34) we find

$$\mathrm{Im}\,\mathrm{Tr}\int_{-\infty}^{+\infty} \frac{\partial\mathbf{\Sigma}(\omega)}{\partial\omega}\mathbf{G}(\omega)\,\mathrm{d}\omega = 0. \tag{5.44}$$

Using this result in (5.42) then gives

$$I_L(-x,-y) = -I_L(x,y), \tag{5.45}$$

showing that the Luttinger integral changes sign under the particle-hole transform (inversion through the origin). A further symmetry can be deduced for the Luttinger integral by considering the $1 \leftrightarrow 2$ transformation (applicable to the case $V_1 = V_2$ considered explicitely in practice). This yields the rather obvious result that

$$I_L(y,x) = I_L(x,y) \tag{5.46}$$

such that by combining the two symmetries $|I_L|$ can take only a single value throughout the $x-y$ plane, in the USC phase. In summary, and from fig. 5.2, we have:

$$I_L(x,y) = \begin{cases} +\frac{\pi}{2} & \text{if } y > -x \\ -\frac{\pi}{2} & \text{if } y < -x \end{cases} \qquad \text{(USC)}. \tag{5.47}$$

We conclude this section by examining the important consequences of the above for the even-even spectral density. By combining (5.26) and (5.38) for a system with $V_1 = V_2$ we have simply that:

$$2\pi\Gamma D_{ee}(\omega = 0) = \sin^2\left(\frac{\pi}{2}n_{\mathrm{imp}} + I_L\right), \tag{5.48}$$

relating the zero-frequency spectral density to the two 'simple' quantities n_{imp} and I_L. The situation is simplified further by noting that in each of the two phases, $|I_L|$

takes on a characteristic value. As $\sin^2[\frac{1}{2}\pi(n_{\rm imp}\pm 1)] = \cos^2(\frac{1}{2}\pi n_{\rm imp})$ it follows that:

$$2\pi\Gamma D_{ee}(0) = \begin{cases} = \sin^2\left(\frac{\pi n_{\rm imp}}{2}\right) & \text{FL}, \\ = \cos^2\left(\frac{\pi n_{\rm imp}}{2}\right) & \text{USC}. \end{cases} \tag{5.49}$$

On crossing the Kosterlitz-Thouless transitions from the FL to the USC, we saw in section 4.3 how $n_{\rm imp}$ varied continuously. Hence from (5.49), the zero-frequency spectral density must vary *discontinuously* on crossing the transition, the discontinuity being $\cos(\pi n_{\rm imp})$. Equation (5.49) is of course equally well satisfied at the first order transitions occurring along the lines $y = \pm x$, however here $n_{\rm imp}$ does not vary continuously (fig. 4.8). The veracity of (5.49) will be tested explicitely in the next section where we turn to examine numerical results for the single-particle dynamics of the 2LM.

5.3 Single-particle dynamics

The preceding sections have focused on establishing analytic properties of the Green functions of the 2LM. We have established the importance of the even-even spectral density in determining the differential conductance of the system. Further we have derived a Friedel-Luttinger sum rule relating the static phase shift to the impurity charge and the Luttinger integral, a number characteristic of the thermodynamic phase of the impurity model.

In this section we present representative numerical results for the single-particle dynamics, focussing largely on the even-even spectral density and principally the USC phase. In section 5.3.1 we will examine in some detail the dynamics of the 2LM along the line $y = x$. Whilst not being of generic interest with regard to experimental results, this peculiar line more than warrants theoretical study, as we will see.

Throughout this section we again take $V_1 = V_2$ such that $\Gamma_{ij} = \Gamma$. This is unlikely to occur in experiment but serves to simplify the parameter regime to be studied; from section 4.3.3 we know that tolerable deviations from $V_1 = V_2$ do not critically effect the physical behaviour of the system.

Figure 5.3 shows an overview of $2\pi\Gamma D_{ee}(\omega)$ on all scales for $\tilde{U} = 20$, $\tilde{U}' = 7$, and $\tilde{J}_H = 2$ at zero-temperature.[4] We take a vertical cut through the $x - y$ plane above the particle-hole symmetric point $\tilde{\epsilon}_1 = \frac{1}{2}\tilde{U} - \tilde{U}' = -17$ (*i.e.*, $x = 0$) and $\tilde{\epsilon}_2$ is progressively decreased through the FL phase toward the QPT — the same trajectory as figs. 4.4 and 4.6. The transition itself occurs here at $\tilde{\epsilon}_2 \sim -6.536$.

[4] Remembering that the FDM-NRG is inherently a finite temperature technique, by zero-temperature we really mean a temperature significantly below all energy scales of the 2LM including the Kondo scale.

The most important spectral feature is of course the Kondo resonance straddling the Fermi level at $\omega = 0$. We will consider this later and first comment on the origin of the higher energy features. For $\tilde{\epsilon}_2 = +1$ fig. 4.6b) indicates that $n_{\rm imp} \simeq 1.2$, suitably close to unity that we may interpret the high-energy spectral features as removal or addition excitations from the singly occupied $(n_1, n_2) = (1, 0)$ atomic limit state. The removal excitation from level 1, contributing to $D_{ee}(\omega)$ via its $D_{11}(\omega)$ component, thus corresponds to the difference between the energies of the $(1, 0)$ and $(0, 0)$ states: $E(1, 0) - E(0, 0) = \epsilon_1$. The excitation therefore lies at negative frequencies and is clearly seen in fig. 5.3 as the lower 'Hubbard satellite' (arrowed). The position of this peak is dependent solely on ϵ_1 in this level of description explaining why the peak position varies little on lowering ϵ_2.

Two addition excitations lying above the Fermi level are also seen in fig. 5.3 for $\tilde{\epsilon}_2 = +1$. The lowest corresponds to electron addition to level 1 and hence shows itself, via $D_{11}(\omega)$, at an energy $E(2, 0) - E(1, 0) = \epsilon_1 + U = +3\Gamma$, as clearly seen in the figure. The second excitation corresponds to addition to level 2 and contributes to $D_{ee}(\omega)$ via the latter's $D_{22}(\omega)$ component, and occurs at an energy $E(1, 1) - E(1, 0)$. As there are two distinct $(1, 1)$ impurity states — singlet and triplet — two such excitations exist in principle separated by an energy $\tilde{J}_H$. However, as is evident from the figure, coupling to the conduction band in practice blurs these excitations so that only a single spectral feature is seen. This feature moves towards the Fermi level on decreasing $\tilde{\epsilon}_2$ from $+1$ to -3 (long dash) and -6 (short dash), its characteristic energy being a function of $\tilde{\epsilon}_2$. For $\tilde{\epsilon}_2 = -6$ the high energy features merge into a single intense band.

As commented above, the single-particle spectrum in the vicinity of the Fermi level is dominated by the Kondo resonance — the sharp distinctive feature in fig. 5.3. The evolution of the Kondo resonance as the transition is approached is displayed in fig. 5.4. For $\tilde{\epsilon}_2 \to \epsilon^+_{2,c}$ the Kondo resonance progressively narrows reflecting the vanishing of the Kondo scale T_K found in section 4.3. Precisely at the transition T_K vanishes and the Kondo resonance collapses 'on the spot' into the background spectral density arising from the high energy features. Just on the other side of the transition, in the USC phase, the Kondo resonance is simply absent, as seen in fig. 5.4 where for $\tilde{\epsilon}_2 = -6.54$ the USC spectrum (short dash) is constant throughout the range shown. The inset to fig. 5.3 also shows this USC spectrum on an expanded scale. Whilst the Kondo resonance is absent here, the high-energy features discussed previously evolve in a continuous manner on crossing the transition. The resonance above the Fermi level whose width $\mathcal{O}(\Gamma)$ reflects the mixed valent nature of the USC phase at this point.

In section 4.3 we saw that thermodynamic properties in the FL phase show uni-

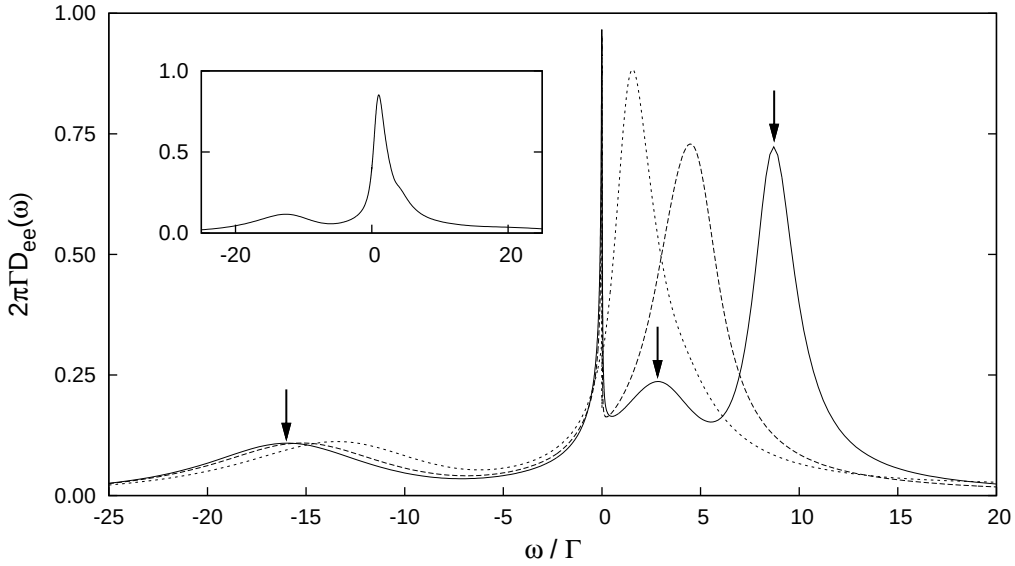

Figure 5.3: Single-particle spectrum $2\pi\Gamma D_{ee}(\omega)$ vs. ω/Γ in the FL phase for fixed level energy $\tilde{\epsilon}_1 = -\frac{1}{2}\tilde{U} - \tilde{U}'$ (*i.e.* $x = 0$) on progressively decreasing $\tilde{\epsilon}_2$ toward the QPT occurring at $\tilde{\epsilon}_2 \sim -6.536$. Shown for $\tilde{U} = 20$, $\tilde{U}' = 7$, and $\tilde{J}_H = 2$, as in fig. 4.4, with $\tilde{\epsilon}_2 = +1$ (solid), -3 (long dash), and -6 (short dash). In all three cases a narrow Kondo resonance is present, straddling the Fermi level $\omega = 0$. Vertical arrows mark excitations interpretable in terms of the atomic limit states, as discussed in text. *Inset*: spectrum at $\tilde{\epsilon}_2 = -6.6$ on just entering the USC phase showing the absence of a Kondo resonance.

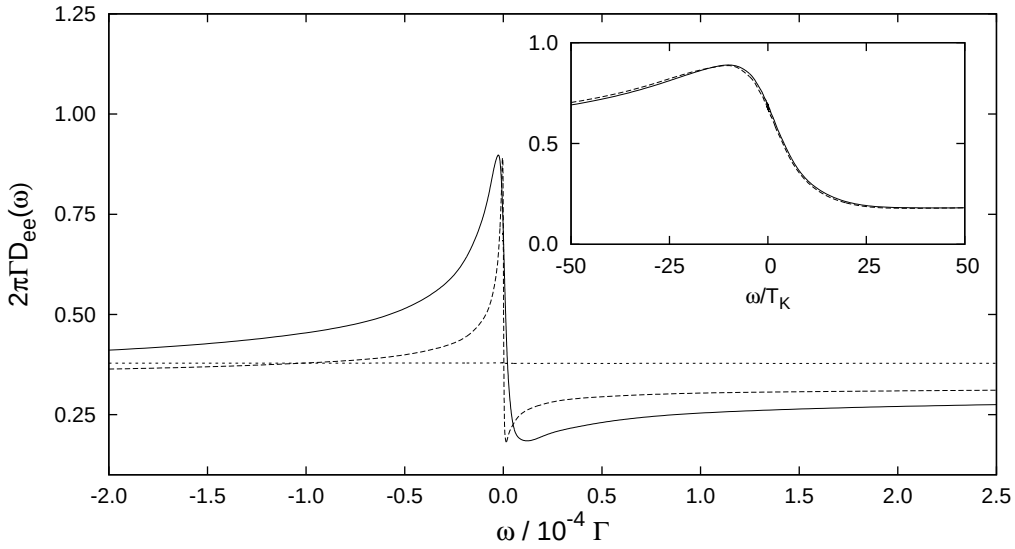

Figure 5.4: A close up view of the Kondo resonance straddling the Fermi level for the same parameters as fig. 5.3 excepting $\tilde{\epsilon}_2 = -6.1$ (solid) and -6.2 (long dash). The Kondo resonance collapses on the spot as the QPT is approached and the Kondo scale T_K vanishes. Just on entering the USC phase at $\tilde{\epsilon}_2 = -6.54$ (short dash) the spectrum is featureless on these scales with no Kondo resonance. *Inset*: Scaling of the Kondo resonance on approaching the QPT from the FL side. Both FL spectra of the main figure collapse to the same universal scaling resonance as a function of ω/T_K.

versal scaling in terms of the Kondo scale T_K. That the dynamic properties exhibit scaling is shown in the inset to fig. 5.4. When scaled in terms of T_K the results of the main figure give the same universal form as a function of ω/T_K despite their individual T_K's differing by more than an order of magnitude. We note here that we have scaled the results by the Kondo temperature obtained from the thermodynamic results. We could equally have used a spectral definition for the Kondo scale — *e.g.* via the width of the Kondo resonance — to obtain a universal form. The salient point is that there is only a single universal scale and that different practical definitions of it are fundamentally equivalent, being related by simple multiplicative factors.

The subsequent evolution of the even-even spectrum in the USC phase is shown in fig. 5.5. For $\tilde{\epsilon}_2 = -7$ (short dashed line), not far into the USC phase, the spectrum lacks a Kondo resonance, as in the example near the transition shown above. However, on further decreasing $\tilde{\epsilon}_2$, a second Kondo resonance straddling the Fermi level arises. It is well developed by $\tilde{\epsilon}_2 = -10$ and fully developed at particle-hole symmetry $\tilde{\epsilon}_2 = \tilde{\epsilon}_1 = -17$ (solid line). Further, the width of the resonance progressively narrows on approaching particle-hole symmetry. This behaviour can be explained in terms of the increasing $n_{\rm imp}$ [fig. 4.6b)] and decreasing $T_K^{S=1}$ [fig. 4.5a)] on approach to particle-hole symmetry. While the QPT occurs in the mixed valent regime with $n_{\rm imp} \simeq 1.4$, the impurity charge rapidly increases on entering the USC phase such that by $\tilde{\epsilon}_2 = -10$ it is very close to 2. The 2LM is then expected to be described asymptotically at low energies by a spin-1 Kondo model as derived in section 4.2.1. This second Kondo resonance is then distinct from that found in fig. 5.4: we will discuss it further in the context of fig. 5.8*ff*. The higher energy features occurring in the USC phase spectra are naturally interpretable in terms of the atomic limit states. At particle-hole symmetry all addition, and removal, excitations to, and from, both levels 1 and 2 have the same magnitude $|\tilde{\epsilon}_1 + \tilde{U}' - \frac{1}{4}\tilde{J}_H|$. The spectra is therefore an even function of energy with Hubbard satellites occurring, in this case, at $\tilde{\omega} \simeq 10.5$.

Finally, and importantly, in this general section we verify numerically the Friedel-Luttinger sum rule derived in section 5.2. Figure 5.6 tracks the behaviour of the zero-frequency spectral density from the particle-hole symmetric point in the USC phase, across the QPT and into the FL phase. The solid line is the result of application of (5.49) with $n_{\rm imp}$ obtained from an independent thermodynamic NRG calculation, whilst crosses display direct results for $2\pi\Gamma D_{ee}(\omega = 0)$. The agreement between the two sets of data is clearly excellent. We note that on entering the USC phase the spectral density *decreases* discontinuously as a result of $n_{\rm imp}$ being in the range $\frac{1}{2} < n_{\rm imp} < \frac{3}{2}$ [see (5.49))]. We will now examine a case where a discontinuous *increase* in $D_{ee}(0)$ occurs on entering the FL phase.

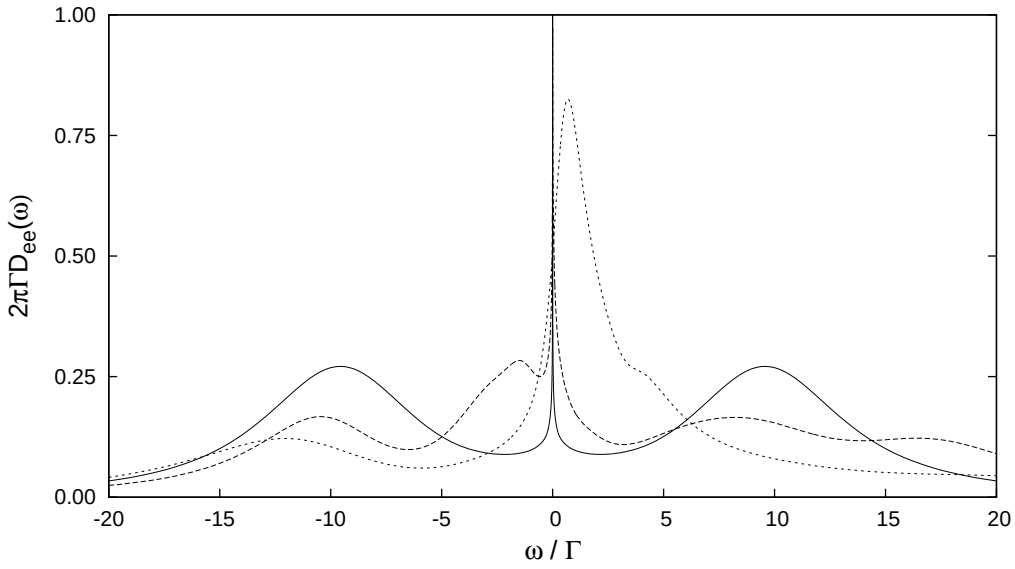

Figure 5.5: Spectra in the USC phase for the same parameters as figs. 5.3 and 5.4 for $\tilde{\epsilon}_2 = -7$ (short dash), -10 (long dash), and the centre of the USC phase $\tilde{\epsilon}_2 = -17$ (solid line, the particle-hole symmetric point). The Kondo resonance that develops here is that for a spin-1 Kondo model.

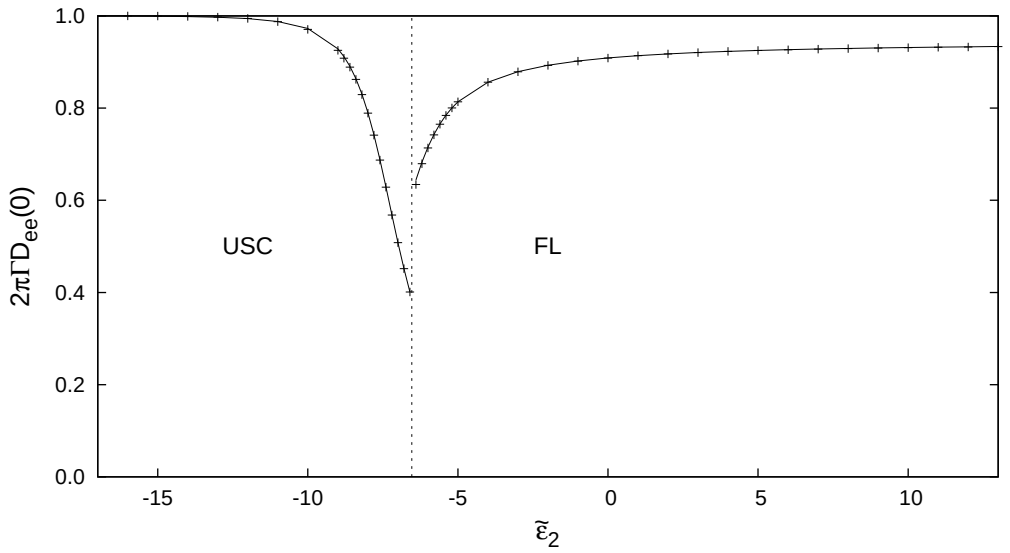

Figure 5.6: The zero-frequency spectral density $2\pi\Gamma D_{ee}(\omega = 0)$ in both phases either side of the Kosterlitz-Thouless transition (the transition indicated by a dashed vertical line), with the same parameters as figs. 5.3–5.5. Crosses show the direct result from the FDM-NRG calculation of the spectral density whilst solid lines indicate the result of (5.49) with $n_{\rm imp}$ obtained from a thermodynamic NRG calculation. The agreement is excellent. At the QPT $n_{\rm imp} = 1.43$ and hence the spectrum decreases discontinuously on entering the USC phase from the FL phase; $n_{\rm imp}$ itself evolves continuously [fig. 4.5b)].

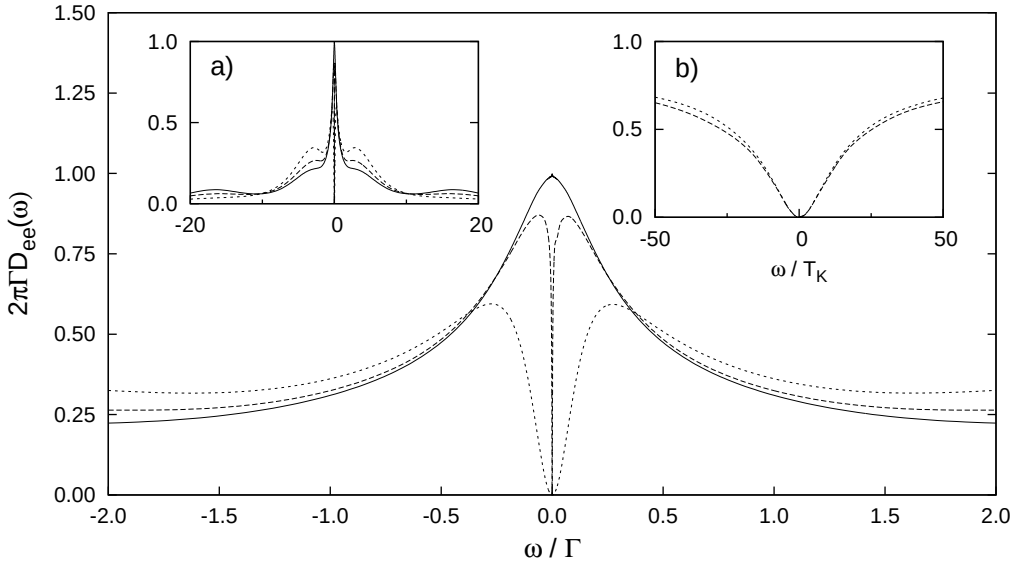

Figure 5.7: The even-even spectral density along the line $y = -x$ for the same interaction parameters as studied figs. 5.3–5.6, decreasing $\tilde{y}$ through the QPT (at $\tilde{y}_c \sim 6.36$) from the FL side $y > y_c$. Shown for $\tilde{y} = 6.55$ (short dash) and 6.40 (long dash) in the FL phase, and $\tilde{y} = 6.30$ (solid) just into the USC phase. A clear Kondo antiresonance is seen with $2\pi\Gamma D_{ee}(0) = 0$. It collapses on the spot as $T_K \to 0$ as the QPT is approached. a) An expanded frequency scale illustrating the symmetry of the higher energy features. b) Scaling of the antiresonance as a function of ω/T_K. Quadratic behaviour is observed at low frequencies.

The line $y = -x$ and Kondo antiresonances

The generic example considered above sees a collapsing Kondo resonance in the FL phase and hence a natural decrease in $D_{ee}(0)$ on crossing into the USC phase. If $n_{\rm imp}$ lies not in the range $\frac{1}{2} < n_{\rm imp} < \frac{3}{2}$ but instead between $\frac{3}{2}$ and $\frac{5}{2}$ then (5.49) predicts an *increase* in the spectral density on crossing from the FL to the USC phase. In this case one might expect such behaviour to be associated with a vanishing *Kondo antiresonance* as the transition is approached from the FL side.

This behaviour does indeed arise [52] and is particularly evident along the line $y = -x$ for which $n_{\rm imp} = 2$ is guaranteed by symmetry, regardless of the phase [(4.17a)]. The spectra are likewise symmetric in ω along this line due to the effective particle-hole symmetry discussed in section 4.2.1. Figure 5.7 shows results for $2\pi\Gamma D_{ee}(\omega)$ again for bare interaction parameters $\tilde{U} = 20$, $\tilde{U}' = 7$, and $\tilde{J}_H = 2$. We decrease $y/\Gamma = \tilde{y}$ across the transition occurring at the critical value $\tilde{y}_c \sim 6.36$ from the FL side ($y > y_c$) to the USC phase.

As shown in the main figure, $D_{ee}(\omega)$ does indeed contain a characteristic Kondo antiresonance in the FL phase with $2\pi\Gamma D_{ee}(0)$ equal to precisely zero along the line $y = -x$ [as indeed follows from (5.49) with $n_{\rm imp} = 2$]. The antiresonance vanishes on the spot as the transition is approached from the FL side and the Kondo

scale T_K diminishes — the antiresonance 'closes up' and the two maxima positioned symmetrically about $\omega = 0$ move toward each other. Figure 5.7b) exhibits the scaling nature of the spectral density in the FL phase: a characteristic $D_{ee}(\omega) \propto (\omega/T_K)^2$ form symptomatic of a normal Fermi liquid.

The general predictions of (5.49) are again confirmed by these results, and in a rather clear fashion. As $n_{\rm imp} = 2$ for all systems along the line $y = -x$, (5.49) gives $2\pi\Gamma D_{ee}(0) = 1$ in the USC phase and 0 in the FL phase.

Figure 5.8 continues fig. 5.7 into the USC, phase showing the even-even spectral density for $\tilde{y} = 5$, 3, and 0. The striking resonance found to straddle zero frequency is of course the same spin-1 Kondo resonance as found in fig. 5.5. The width of this resonance again decreases toward its smallest (but nonzero) value as the particle-hole symmetric point is approached, due to the decreasing Kondo scale $T_K^{S=1}$. Particularly evident from the main figure is also the convergence of the Hubbard satellites as the bare level energies become equal at the particle-hole symmetric point.

The inset to fig. 5.8 shows the clear scaling behaviour of $2\pi D_{ee}(\omega)$ in terms of $\omega/T_K^{S=1}$. All the spectra of the main figure scale beautifully onto the same universal form for many multiples of the Kondo scale. Also apparent is the sharp cusp-like form of the Kondo resonance known from the study of a pure spin-1 Kondo model [54].[5] This behaviour is symptomatic of the singular Fermi liquid [99] nature of the underscreened spin-1 phase; the weak ferromagnetic coupling of the spin $\frac{1}{2}$ to the metallic lead resulting in logarithmic corrections to Fermi liquid behaviour as in (5.23).

In fig. 5.9 we consider the precise low-frequency form of the spectral density. From the low-frequency forms of the impurity self-energies [(5.23)] and the Dyson equation we expect to find:

$$2\pi\Gamma D_{ee(\omega)} \sim 1 - \frac{a}{\ln^2(\omega/T_K^{S=1})}, \tag{5.50}$$

as is indeed the case shown in the figure and is in agreement with the results found for the spin-1 Kondo model [99]. We note one final aspect of the scaling form of $D_{ee}(\omega)$ in the inset to fig. 5.9 where we compare the results at the particle-hole symmetric point to those at $\tilde{\epsilon}_1 = -17$ and $\tilde{\epsilon}_2 = -12$, *i.e.* a point above particle-hole symmetry (as in the previous section) and where $n_{\rm imp} = 1.95$. The salient point here is that, as found for the thermodynamic results in fig. 4.5, the scaling form found varies little with the asymmetry [which here takes the values $\eta(x, y) = 0$ and ~ 0.25, see (4.14)]. Of course the form of the spectra does alter further from particle-hole

[5] Single-particle spectra do not exists as such for the Kondo model, the impurity being described strictly by spin operators. However one may define an impurity Green function in terms of the scattering t-matrix; the latter being well defined in an analogous Anderson model from which a correspondence can be drawn and a spectral density examined.

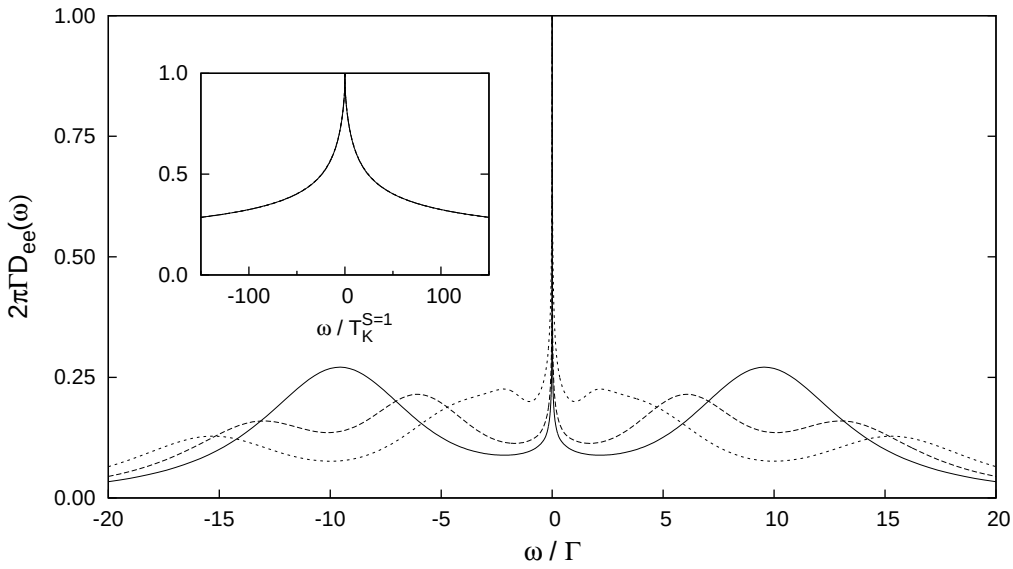

Figure 5.8: The even-even spectra density in the USC phase along the line $y = -x$ for $\tilde{U} = 20$, $\tilde{U}' = 7$, and $\tilde{J}_H = 2$ and for $y = 0$ (solid), 5 (long dash), and 3 (short dash). The spin-1 Kondo resonance is much sharper in form than the spin-$\frac{1}{2}$ resonance seen in the FL phase. *Inset*: Rescaled spectra showing only the universal, cusp-like Kondo resonance.

symmetry when n_{imp} deviates significantly from the value 2, under which conditions the USC phase is no longer adequately described by the same spin-1 Kondo model.

This section has considered the properties and behaviour of the single-particle dynamics along a generic trajectory (above the particle-hole symmetric point) and along the simplifying $y = -x$ line. We have seen that the high energy features are largely interpretable in terms of the atomic limit states: broad Hubbard satellites result in the fully interacting 2LM with the coupled conduction band. On low-energy scales the spectra is dominated by the Kondo resonance. The form of this resonance is distinct for each of the two phases. In the USC phase the resonance takes a sharp cusp-like form, indicative of the singular nature of the USC fixed point. In the FL phase, a more rounded resonance is seen which narrows significantly as the QPT is approached. Further throughout the USC the same scaling form is observed for the Kondo resonance regardless of the value of the asymmetry $\eta(x, y)$. In the next section we focus specifically along the line $y = x$, which contains the particle-hole symmetric point and along which a first-order transition between the FL and USC phases is observed.

5.3.1 The line $y = x$

In section 4.3.1 in regard to thermodynamics, the transition occurring along the line $\epsilon_1 = \epsilon_2$, *i.e.* the line $y = x$, was seen to be first-order level-crossing transition. The special nature of the QPT along this line occurs only for $V_1 = V_2$. We now consider

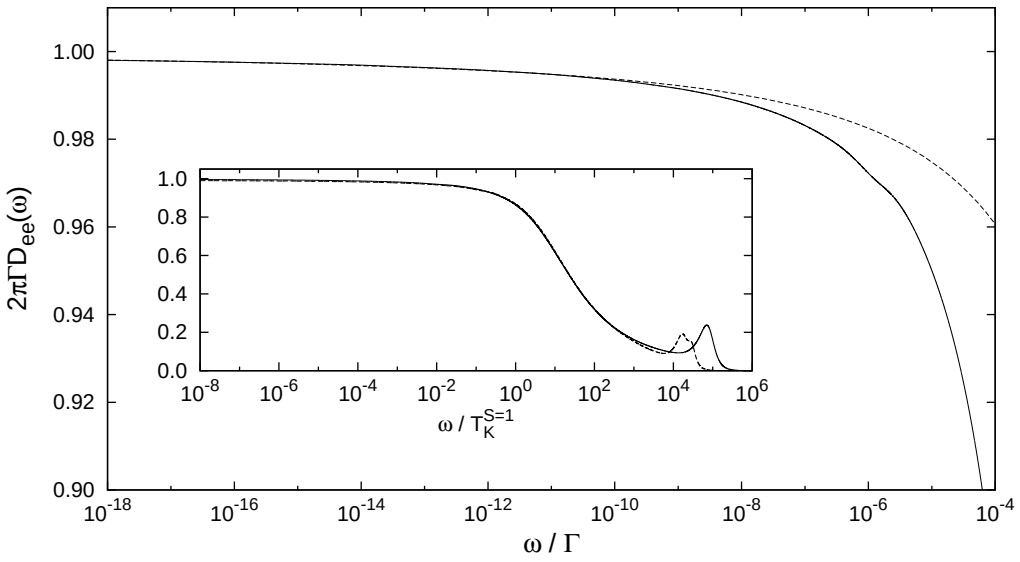

Figure 5.9: Low frequency asymptotics of the spectral density $2\pi\Gamma D_{ee}(\omega)$ (solid) for $\tilde{U} = 20$, $\tilde{U}' = 7$, and $\tilde{J}_H = 2$ at the particle hole symmetric point $\tilde{\epsilon}_1 = \tilde{\epsilon}_2 = -17$. A logarithmically slow approach to unity is seen a $\omega = 0$, as governed by (5.50) (dashed). *Inset*: Comparison between the spectra at (solid) and away from (dashed, $\eta(x, y) \simeq 0.25$) particle-hole symmetry. The same low frequency form is found throughout the USC phase in the region where $n_{\rm imp} \sim 2$ and where the full 2LM is consequently described well by the spin-1 Kondo model.

this line from the perspective of single-particle dynamics and the separability arising in the even-odd representation of the 2LM.

In the previous section the elements of the Green function matrix $\mathbf{G}(\omega)$ have been considered to be the propagators for the two impurity levels, *i.e.* $G_{ij}(\omega)$ with $i, j \in \{1, 2\}$. Along the line $y = x$ it is in fact more convenient, and enlightening, to work with $\mathbf{G}(\omega)$ in the basis of the even and odd impurity level combinations, as defined in (5.16). Away from this line, where $\epsilon_1 \neq \epsilon_2$, there is no particular advantage to working in this basis. However along the line $\epsilon_1 = \epsilon_2$ the two impurity levels are equivalent as a natural consequence of symmetry and so the diagonal components of the (symmetric) $\mathbf{G}(\omega)$ matrix are equal in the 1-2 basis. Therefore from (5.17c) the off-diagonal elements in the *e*-*o* basis, $G_{eo}(\omega)$ and $G_{oe}(\omega)$, are not only equal to each other but also vanish identically. The matrix $\mathbf{G}(\omega)$ is then purely diagonal for *all* frequencies and from (5.17a) and (5.17b) has elements:[6]

$$\underset{oo}{G^{ee}}(\omega) = G_{11}(\omega) \pm G_{12}(\omega). \tag{5.51}$$

The analytic forms of the propagators in this basis have similarly simple forms. By

[6] Away from $y = x$ one can of course diagonalise the matrix $\mathbf{G}(\omega)$, however a different transformation is in general required for each value of ω.

using (5.7) and (5.6) in (5.51) one obtains:

$$G_{ee}(\omega) = \left[\omega^+ - \epsilon - 2\Gamma(\omega) - \Sigma_{ee}(\omega)\right]^{-1} \tag{5.52a}$$

$$G_{oo}(\omega) = \left[\omega^+ - \epsilon - \Sigma_{oo}(\omega)\right]^{-1} \tag{5.52b}$$

where the hybridisation function $\Gamma(\omega) \equiv \Gamma_{ij}(\omega)$ appears only in $G_{ee}(\omega)$ (and we have defined $\epsilon = \epsilon_1 = \epsilon_2$ the common level energy); and the even-even and odd-odd self-energies are given explicitly by:

$$\Sigma_{\substack{ee\\oo}}(\omega) = \Sigma_{11}(\omega) \pm \Sigma_{12}(\omega). \tag{5.53}$$

That the hybridisation $\Gamma(\omega)$ does not appear in $G_{oo}(\omega)$ is a reflection of the fact that the odd orbital is not directly coupled to the lead (see section 5.1); its only coupling is to the even orbital. In the non-interacting limit the odd level thus becomes entirely free: $G^0_{oo}(\omega) = \left[\omega^+ - \epsilon\right]^{-1}$. In the interacting case, the coupling to the even orbital is of course embodied in $\Sigma_{oo}(\omega) \neq 0$.

It is useful to note further that the calculation of the impurity self-energies can be simplified along the line $y = x$. From section 3.5.1 we have (generally) that $\mathbf{\Sigma}(\omega) = \mathbf{F}(\omega)\mathbf{G}^{-1}(\omega)$, *i.e.* :

$$\Sigma_{11}(\omega) = \frac{F_{11}(\omega)G_{22}(\omega) - F_{12}(\omega)G_{21}(\omega)}{G_{11}(\omega)G_{22}(\omega) - G_{12}(\omega)G_{21}(\omega)} \tag{5.54a}$$

$$\Sigma_{12}(\omega) = \frac{F_{12}(\omega)G_{11}(\omega) - F_{11}(\omega)G_{12}(\omega)}{G_{11}(\omega)G_{22}(\omega) - G_{12}(\omega)G_{21}(\omega)}. \tag{5.54b}$$

Noting that $G_{11}(\omega) = G_{22}(\omega)$ [and $G_{12}(\omega) = G_{21}(\omega)$] along $y = x$, and defining the diagonal elements of the $\mathbf{F}(\omega)$ matrix in the even-odd basis, *viz.*:

$$F_{ee}(\omega) = F_{11}(\omega) + F_{12}(\omega) \tag{5.55a}$$

$$F_{oo}(\omega) = F_{11}(\omega) - F_{12}(\omega), \tag{5.55b}$$

the calculation of the self-energies reduces from (5.53) to a simple 'scalar' problem:

$$\Sigma_{ee}(\omega) = \frac{F_{ee}(\omega)}{G_{ee}(\omega)} \tag{5.56a}$$

$$\Sigma_{oo}(\omega) = \frac{F_{oo}(\omega)}{G_{oo}(\omega)}, \tag{5.56b}$$

as occurs in a simple single-level Anderson Model [81].

In section 5.2 we developed the Friedel-Luttinger sum rule relating the static phase shift, the excess impurity occupation and the Luttinger integral. We now show that by separating each of these quantities into even and odd components,

useful results can be established. We begin by examining the Luttinger integral as given in (5.37). By the virtue of the trace appearing in (5.37) and that $\mathbf{G}(\omega)$ is diagonal in the even-odd basis, the Luttinger integral trivially becomes:

$$I_L = \mathrm{Im}\int_{-\infty}^{0}\left[\frac{\partial\Sigma_{ee}(\omega)}{\partial\omega}G_{ee}(\omega)+\frac{\partial\Sigma_{oo}(\omega)}{\partial\omega}G_{oo}(\omega)\right]\,\mathrm{d}\omega \tag{5.57a}$$

$$= I_L^e + I_L^o, \tag{5.57b}$$

which defines separate Luttinger integrals in each channel. Consider first just I_L^e in the above. From (5.52a) we have:

$$\Sigma_{ee}(\omega) = \omega^+ - \epsilon - 2\Gamma(\omega) - G_{ee}^{-1}(\omega) \tag{5.58a}$$

$$\frac{\partial\Sigma_{ee}(\omega)}{\partial\omega} = 1 - 2\frac{\partial\Gamma(\omega)}{\partial\omega} + G_{ee}^{-2}(\omega)\frac{\partial G_{ee}(\omega)}{\partial\omega}, \tag{5.58b}$$

which gives on substitution into (5.57):

$$I_L^e = \mathrm{Im}\int_{-\infty}^{0}\left\{\left[1-2\frac{\partial\Gamma(\omega)}{\partial\omega}\right]G_{ee}(\omega)+\frac{\partial\ln G_{ee}(\omega)}{\partial\omega}\right\}\,\mathrm{d}\omega. \tag{5.59}$$

As in the case of the total Luttinger integral, there are two distinct terms under the integral. By rewriting (5.13) for n_{imp} in terms of the even and odd Green functions, *viz.*

$$n_{\mathrm{imp}} = -\frac{2}{\pi}\,\mathrm{Im}\int_{-\infty}^{0}\left\{\left[1-2\frac{\partial\Gamma(\omega)}{\partial\omega}\right]G_{ee}(\omega)+G_{oo}(\omega)\right\}\,\mathrm{d}\omega \tag{5.60a}$$

$$= n_{\mathrm{imp}}^e + n_{\mathrm{imp}}^o, \tag{5.60b}$$

the first term in (5.59) is simply equal to $-\frac{\pi}{2}n_{\mathrm{imp}}^e$. Also by analogy to the previous results we expect the second term in (5.59) to be proportional to a phase shift. Indeed this is the case. From the definition of the phase shift [(5.28)] and again that the $\mathbf{G}(\omega)$ matrix is diagonal in the even-odd basis such that $\det\mathbf{G}(\omega) = G_{ee}(\omega)G_{oo}(\omega)$, the phase shift is likewise separable into even and odd components:

$$\delta(\omega) = \delta_e(\omega) + \delta_o(\omega), \tag{5.61}$$

with

$$\delta_\alpha(\omega) = \mathrm{Im}\ln G_{\alpha\alpha}(\omega) \equiv \arg G_{\alpha\alpha}(\omega). \tag{5.62}$$

The even channel Luttinger integral is then given by:

$$I_L^e = -\frac{\pi}{2}n_{\mathrm{imp}}^e + \delta_e(0) - \delta_e(-\infty). \tag{5.63}$$

Our final task is to calculate the phase shifts appearing in the above. To this end

return to (5.52a) for $G_{ee}(\omega)$. Note again that as $|\omega| \to 0$, the imaginary parts $\Gamma^I(\omega)$ and $\Sigma^I_{ee}(\omega)$ both vanish [as too does $\Gamma^R(\omega)$], while $\Sigma^R_{ee}(\omega)$ tends to a finite constant. Hence (5.52a) yields $G_{ee}(\omega) = 1/\omega^+$ as $|\omega| \to \infty$; from which $\delta_e(-\infty) = \arg G_{ee}(-\infty)$ follows as

$$\delta_e(-\infty) = -\pi \tag{5.64}$$

We need also the static phase shift $\delta_e(0)$. For this we use $\Sigma^I_{ee}(\omega = 0) = 0$, and define the renormalized even and odd levels:

$$\epsilon^*_\alpha = \epsilon + \Sigma^R_{\alpha\alpha}(\omega = 0) \qquad \alpha \in \{e, o\}. \tag{5.65}$$

With these results (5.52a) becomes:

$$G_{ee}(0) = \frac{-\epsilon^*_e - 2i\Gamma}{(\epsilon^*_e)^2 + 4\Gamma^2} \tag{5.66}$$

and hence the phase shift is given by

$$\delta_e(0) = \operatorname{Im} \ln G_{ee}(0) = \arctan \frac{2\Gamma}{\epsilon^*_e} \qquad \in [-\pi, 0]. \tag{5.67}$$

It is useful to note than as ϵ^*_e changes sign, the phase shift $\delta_e(0)$ evolves continuously reflecting the fact $\Gamma \neq 0$. Finally by combining (5.64) and (5.67) we write

$$\delta_e = \delta_e(0) - \delta_e(-\infty) \tag{5.68a}$$

$$= \arctan \frac{2\Gamma}{\epsilon^*_e} \qquad \in [0, \pi] \tag{5.68b}$$

(since adding π to an angle is equivalent to inversion through the origin) such that (5.59) becomes:

$$I^e_L = -\frac{\pi}{2} n^e_{\text{imp}} + \delta_e. \tag{5.69}$$

A similar result for the odd channel may be derived in a parallel fashion to that above, with the natural result that:

$$I^o_L = -\frac{\pi}{2} n^o_{\text{imp}} + \delta_o. \tag{5.70}$$

However the phase shift $\delta_o = \delta_o(0) - \delta_o(-\infty)$ contains some subtle behaviour. In the limit $\omega = -\infty$ we have $\delta_o(-\infty) = -\pi$ by analogy to the calculation for $\delta_e(-\infty)$. At $\omega = 0$ by contrast we have (with $\eta = 0^+$):

$$\delta_o(0) = \operatorname{Im} \ln \frac{-\epsilon^*_o - i\eta}{(\epsilon^*_o)^2 + \eta^2} \tag{5.71a}$$

$$= \arctan \frac{\eta}{\epsilon^*_o} \qquad \in [-\pi, 0] \tag{5.71b}$$

such that δ_o changes *discontinuously* as ϵ_o^* changes sign *viz.*:

$$\delta_o = \delta_o(0) - \delta_o(-\infty) = \begin{cases} 0 & \text{if } \epsilon_0^* > 0 \\ \frac{\pi}{2} & \text{if } \epsilon_0^* = 0 \\ \pi & \text{if } \epsilon_0^* < 0 \end{cases} \tag{5.72}$$

and the Luttinger integral is then given from (5.70) by

$$I_L^o = -\frac{\pi}{2} n_{\text{imp}}^o + \frac{\pi}{2}\big[1 - \text{sgn}(\epsilon_o^*)\big]. \tag{5.73}$$

We have therefore established the Friedel-Luttinger sum rules in the even and odd channels separately. Before analysing numerical results from the FDM-NRG we comment on the symmetries of the quantities derived above. By an entirely analogous process as that leading to (5.45) it is possible to show that

$$I_L^\alpha(-x) = -I_L^\alpha(x) \qquad \alpha \in \{e, o\}, \tag{5.74}$$

so the Luttinger integrals in the even and odd channels are separately odd functions of x. Similarly from (5.40) both the self-energies, and so renormalized levels in the even-odd basis, are odd functions, specifically:

$$\underset{oo}{\Sigma_{ee}}(\omega = 0; -x) = U + 2U' - \underset{oo}{\Sigma_{ee}}(\omega = 0; +x) \tag{5.75a}$$

$$\begin{aligned} \underset{o}{\epsilon_e^*}(-x) &= -(\tfrac{1}{2}U + U') - x + \underset{oo}{\Sigma_{ee}^R}(\omega = 0; -x) \\ &= -\underset{o}{\epsilon_e^*}(+x) \end{aligned} \tag{5.75b}$$

That these renormalized levels are odd in x implies either that they must be equal to zero at $x = 0$ or diverge at this point. The FDM-NRG results in the next section will indeed show this to be the case. Next, the symmetry of the excess impurity charges. Under the particle-hole transformation given by $d_{\alpha\sigma} \leftrightarrow d_{\alpha\sigma}^\dagger$ and $c_{-\mathbf{k}\sigma} \leftrightarrow c_{\mathbf{k}\sigma}^\dagger$ (see section 4.1), n_{imp}^e and n_{imp}^o obey:

$$n_{\text{imp}}^\alpha(-x) = 2 - n_{\text{imp}}^\alpha(x) \qquad \alpha \in \{e, o\} \tag{5.76}$$

(arising because we take a symmetric conduction band density of states) with $n_{\text{imp}}^\alpha = 1$ at the particle-hole symmetric point $x = 0$. Finally, it follows from (5.69) and (5.70), using (5.74) and (5.76), that the phase shifts have the property that:

$$\delta_\alpha(x) + \delta_\alpha(-x) = \pi \qquad \alpha \in \{e, o\} \tag{5.77}$$

so we only need consider $x > 0$ in the following.

Numerical results

We begin by examining the even and odd excess impurity charges, which may be calculated as above from FDM-NRG for the associated spectral densities [see (5.60)]:

$$n^e_{\rm imp} = -\frac{2}{\pi}\,{\rm Im}\int_{-\infty}^{0}\left[1-\frac{\partial\Gamma(\omega)}{\partial\omega}\right]G_{ee(\omega)}\,{\rm d}\omega \tag{5.78a}$$

$$n^o_{\rm imp} = -\frac{2}{\pi}\,{\rm Im}\int_{-\infty}^{0}G_{oo}(\omega)\,{\rm d}\omega \tag{5.78b}$$

Figure 5.10 shows the evolution of $n^e_{\rm imp}$ and $n^o_{\rm imp}$ on increasing x (or equivalently ϵ) for the representative case $\tilde{U}=20$, $\tilde{U}'=7$, and $\tilde{J}_H=2$ as in fig. 4.8 for the thermodynamic results. The results of this section are general, applying to arbitrary choices of these parameters. The first-order level-crossing transition occurs here at $x_c\sim 12.26\Gamma$ ($\tilde{\epsilon}_c=-4.73$). Throughout the USC phase we find $n^o_{\rm imp}=1$ precisely. It decreases discontinuously to a value close to (but not equal to) zero on crossing the transition into the FL phase.[7] For the even channel by contrast, $n^e_{\rm imp}$ is not fixed in the USC phase and decreases steadily as the QPT is approached from the USC side. In common with the odd channel, $n^e_{\rm imp}$ jumps discontinuously on crossing the QPT, increasing as $n^o_{\rm imp}$ decreases. This behaviour is physically natural. On crossing the transition from the FL phase, the sudden piling of charge in the odd orbital increases the Coulomb repulsions with electrons in the even orbital — a reduction in $n^e_{\rm imp}$ serves to mitigate this effect. The two effects do not cancel however and $n_{\rm imp}=n^e_{\rm imp}+n^o_{\rm imp}$ (as shown in fig. 4.8) decreases discontinuously as the system crosses from the USC to FL phase.

The above behaviour is qualitatively reminiscent of that found in the noninteracting limit discussed in section 4.3.1. On decreasing ϵ through zero in this limit, $n^o_{\rm imp}$ jumps discontinuously from 0 to 2 but with no concomitant change in $n^e_{\rm imp}$ since there are no interactions present. Moreover in the interacting case, since the transition is generically accompanied by an increased occupancy of the odd orbital, one might intuitively expect that the transition occurs at $\epsilon<0$, in order to offset the increased interactions, as indeed found above.

We consider now the static renormalized levels given by (5.65). Results are presented in fig. 5.11 where we have used the FDM-NRG results for the self-energies appearing in (5.65). First we comment briefly on the results for the even channel [inset to fig. 5.11]. At the particle-hole symmetric point ($x=0$) the renormalized even level sits precisely at zero, indicating that $\Sigma^R_{ee}(0)=-\epsilon$. This is precisely as occurs for single impurity level in the AIM at particle-hole symmetry [20]. As x

[7] This is a different result to that presented in ref. [64] and is in agreement with the results of ref. [63].

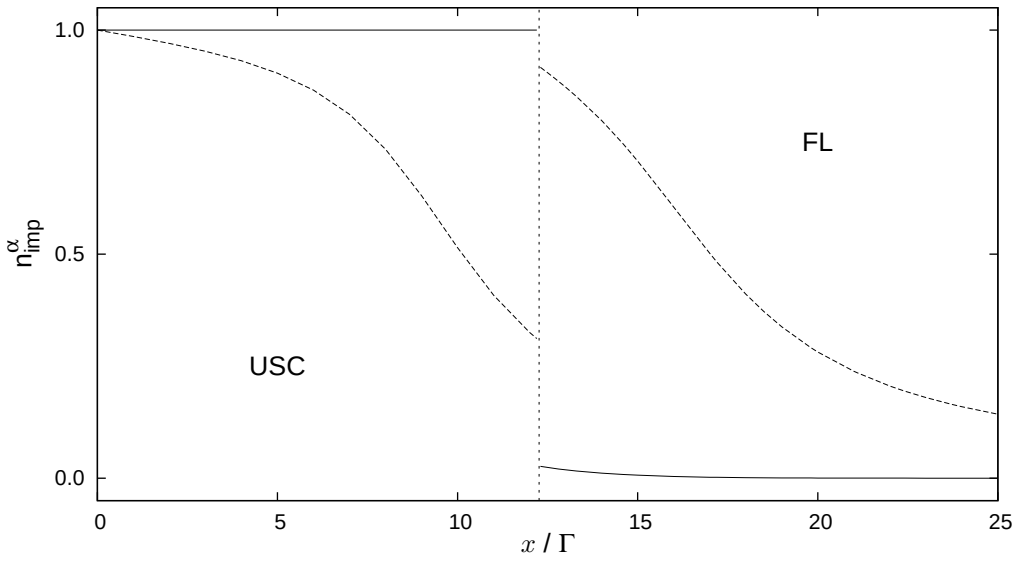

Figure 5.10: Excess impurity charges in the odd (solid) and even (dashed) channels for $\tilde{U} = 20$, $\tilde{U}' = 7$, and $\tilde{J}_H = 2$ along the line $y = x$. Throughout the USC phase $n^o_{\rm imp}$ remains fixed at unity and decreases discontinuously as the first-order QPT is crossed at $x_c \sim 12.26\Gamma$, indicated by the vertical dashed line. The even impurity orbital is gradually depopulated as the level energy is increased, but increases discontinuously on crossing the transition when the sudden change in $n^o_{\rm imp}$ reduces Coulombic interactions between the two levels.

is increased away from the particle-hole symmetric point, the renormalized level increases also. At the transition into the FL phase however a discontinuous jump downwards is seen in ϵ^*_e before the level rises in energy once more. For $\epsilon \gg 0$ (or equivalently $x \gg U/2 + U' = 17$) the impurity levels are in practice empty and interaction effects embodied in $\Sigma_{ee}(\omega)$ are thus irrelevant, such that $\epsilon^*_e \to \epsilon$ [the 'bare' level energy, see (5.65)]. We will defer the explanation of the discontinuous jump in ϵ^*_e until the end of this section.

With regards to rationalising the level-crossing transition occurring along the $y = x$ line, it is the odd renormalized level which is more important, as will now be demonstrated. Results for it are shown in the main panel of fig. 5.11. In the vicinity of the particle-hole symmetric point ($x = 0$), ϵ^*_o diverges: it is positive for $x < 0$ and negative for $x > 0$, consistent with the symmetry (5.75b). This divergence in ϵ^*_o can be related to the behaviour of $F_{oo}(\omega = 0)$ [as given by (5.55b)] as x is varied. To this end, substitute (5.52b) for $G_{oo}(\omega)$ into (5.56b) to obtain:

$$\Sigma_{oo}(\omega) = \frac{(\omega^+ - \epsilon)F_{oo}(\omega)}{1 + F_{oo}(\omega)}. \tag{5.79}$$

The function $F_{oo}(\omega) = F^R_{oo}(\omega) - iF^I_{oo}(\omega)$ may be calculated via the FDM-NRG; results for the zero frequency values of both $F^I_{oo}(\omega)$ and $F^R_{oo}(\omega)$ are shown in fig. 5.12. The

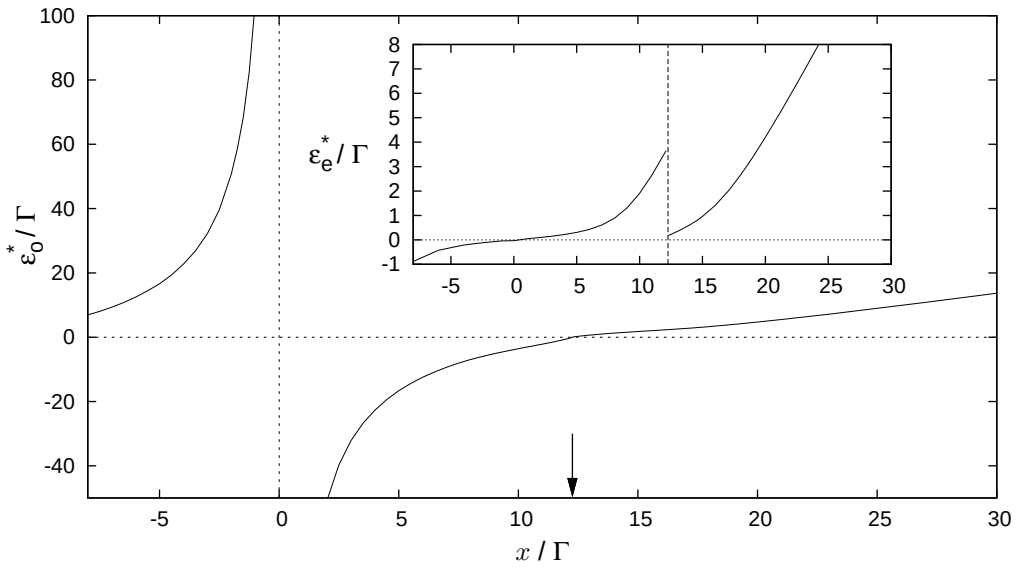

Figure 5.11: The renormalized odd impurity level ϵ_o^* for the same parameters as fig. 5.10. It is an odd function of x and diverges at the particle-hole symmetric point $x = 0$. At the QPT, indicated by a vertical arrow, ϵ_o^* vanishes linearly in x reflecting the first-order nature of the transition. *Inset*: The renormalized even impurity level ϵ_e^*. It too is an odd function of x and is positive for $x > 0$. On crossing the QPT ϵ_e^* decreases discontinuously as dictated by (5.85).

former is ubiquitously zero along the line $y = x$. Equations (5.79) and (5.65) then yield

$$\epsilon_o^* = \frac{\epsilon}{1 + F_{oo}^R(0)} \tag{5.80}$$

for the renormalized odd level. The divergent behaviour of $\epsilon_o^*(x)$ at $x = 0$ is now seen to reflect the fact that $F_{oo}^R(0) \to -1$ as $x \to 0^{\pm}$, as shown in fig. 5.12b).

As x increases away from the particle-hole symmetric point ($x = 0$), so too does ϵ_o^* (fig. 5.11). At the quantum phase transition we find $\epsilon_o^* = 0$ precisely, with the level vanishing linearly as the QPT is crossed:

$$\epsilon_o^* \overset{x \to x_c}{\sim} x - x_c. \tag{5.81}$$

As in the even channel we find $\epsilon_o^* \sim \epsilon$ for $x \gg U/2 + U' = 17$. This is reflected in the fact that $F_{oo}^R(0) \to 0$ in this limit [fig. 5.12 and (5.80)].

Now a brief aside. In deriving (5.31), the general result for the total impurity phase shift throughout the $x - y$ plane, we implicitely removed the case of $\epsilon_o^* = 0$ from consideration. The separation into even and odd channels in this section automatically handles this case.

The results above for the renormalized level energies and level charges allow the behaviour of the Luttinger integrals to be deduced. From the result that $\epsilon_o^* < 0$ in

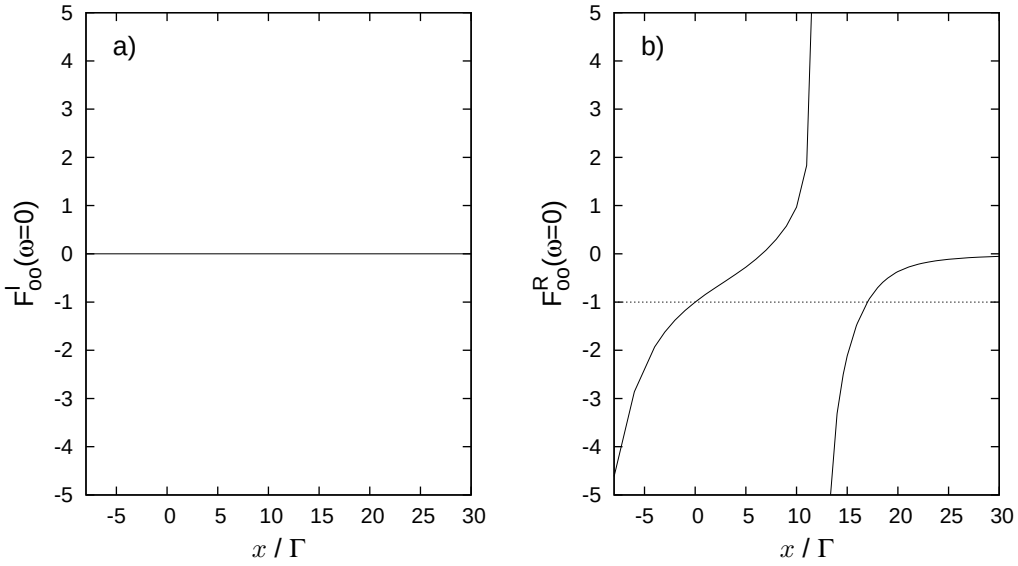

Figure 5.12: a) Imaginary and b) real parts of the function $F_{oo}(\omega) = F^R_{oo}(\omega) - iF^I_{oo}(\omega)$ along the $y = x$ line for the same parameters as fig. 5.11. The imaginary part is ubiquitously zero along this trajectory. For the real part we find $F^R_{oo}(0) \to -1$ as $x \to 0^{\pm}$.

the USC phase for $x > 0$, (5.72) informs that the odd phase shift is given by $\delta_o = \pi$ throughout this phase. Further from (5.73) (together with $n^o_{\rm imp} = 1$ in the USC phase, see fig. 5.10) we have that the odd Luttinger integral is simply:

$$I^o_L = \begin{cases} +\frac{\pi}{2} & \text{if } x > 0 \\ -\frac{\pi}{2} & \text{if } x < 0, \end{cases} \tag{5.82}$$

the result for $x < 0$ arising by symmetry, or from direct substitution into (5.73). Direct calculation of I^o_L via the FDM-NRG confirms these results, as demonstrated in fig. 5.13. Knowledge of I^o_L allows the value of the even Luttinger integral in the USC phase to be deduced, since $I_L = I^o_L + I^e_L = \pm\pi/2$ (fig. 5.2):

$$I^e_L = 0, \tag{5.83}$$

holding throughout the USC phase.

What of the Luttinger integrals in the FL phase for $x > 0$? Here $n^o_{\rm imp}$ does not take a single characteristic value throughout the phase and so nothing can be said about the value of I^o_L in general. However we can deduce its sign. Again from (5.73) and now that $\epsilon^*_o > 0$ in the FL phase we have:

$$I^o_L = -\frac{\pi}{2} n^o_{\rm imp}, \tag{5.84}$$

which is always negative. Hence, since $I_L = I^e_L + I^o_L = 0$ in the FL phase (fig. 5.2),

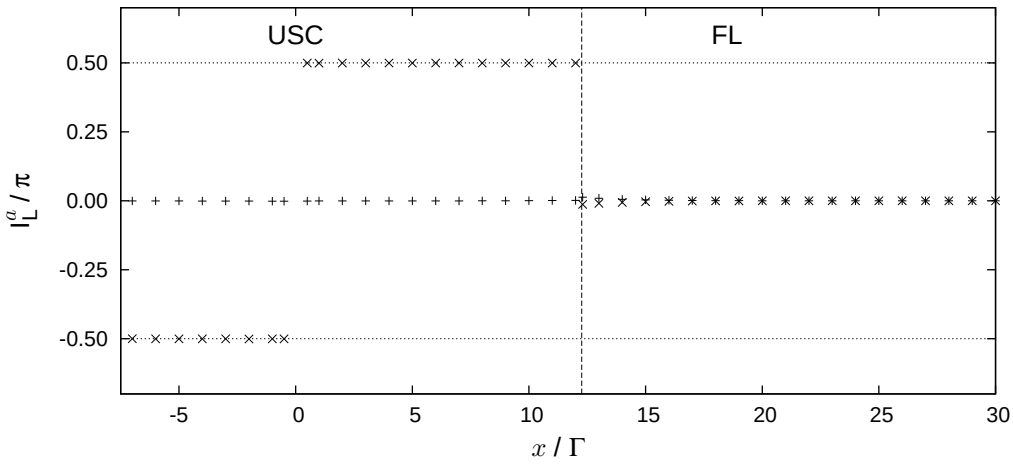

Figure 5.13: The Luttinger integral in the even (+) and odd (×) channels for the same parameters as fig. 5.10, as calculated directly from (5.69) and (5.70). In the USC phase we find $|I_L^o| = \pi/2$ and $I_L^e = 0$ in agreement with the general result $|I_L| = I_L^o + I_L^e = \pi/2$. As discussed in the text, the situation in the FL phase is more complicated; the numerical results show $I_L^e = -I_L^o$, also in agreement with the general result for a FL phase.

the even Luttinger integral must always be positive. As illustrated in fig. 5.13, these results are confirmed by the FDM-NRG calculations. This result brings us full circle, and we can now analyse the behaviour of the renormalized even level. From (5.68b) and (5.69) the renormalized even level can be expressed as:

$$\epsilon_e^* = 2\Gamma\big[\frac{\pi}{2}(1 - n_{\rm imp}^e) - I_L^e\big]. \tag{5.85}$$

In the USC phase we have $I_L^e = 0$ such that ϵ_e^* is solely a function of $n_{\rm imp}^e$ and increases as the level becomes depopulated. In the FL phase we cannot say anything in general since I_L^e cannot be assigned a single value. However we typically find that the discontinuity in I_L^e on crossing the phase boundary is small (for all choices of the impurity parameters), and certainly much smaller than the discontinuity in $n_{\rm imp}^e$ (fig. 5.10). The behaviour of ϵ_e^* is thus controlled by $n_{\rm imp}^e$ and thus from (5.85) decreases discontinuously on passing into the FL phase from the USC phase.

As a brief illustration of the single-particle dynamics along the line $y = x$, fig. 5.14 shows the o-orbital spectrum on decreasing $\tilde{x}$ through the FL phase (main), across the transition, and into the USC phase [b)]. In the FL phase and in the vicinity of the transition, a strong low-frequency spectral resonance is seen to develop above the Fermi level [whilst little spectral density is observed below the Fermi level, indicative of $n_{\rm imp}^o$ being close to zero, fig. 5.10]. The feature becomes a pole at $\omega = 0$ precisely at the transition, and crosses smoothly to $\omega < 0$ in the USC phase. The position of the spectral maximum closely tracks the vanishing renormalized level ϵ_o^*: the $\omega = 0$ pole at $x = x_c$ reflecting $\epsilon_o^* = 0$ at this point. From (5.52b) and using $\Sigma_{oo}(0) = \Sigma_{oo}^R(0)$

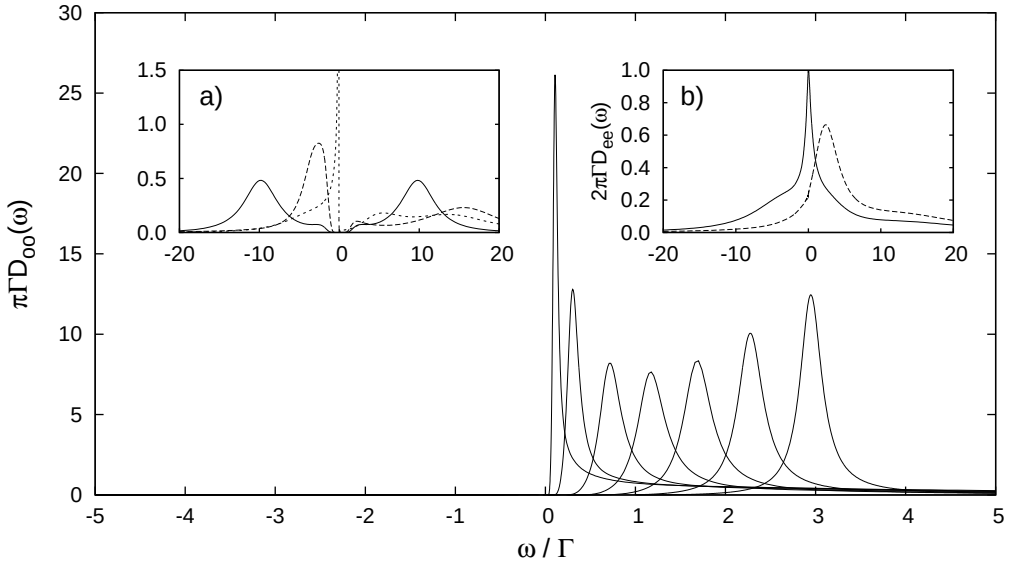

Figure 5.14: The odd orbital spectrum $\pi\Gamma D_{oo}(\omega)$ vs. ω/Γ for the same parameters as fig. 5.10 on decreasing x through the FL phase towards the QPT at $x_c \simeq 12.26$. Shown for $\tilde{x} = 18$, 17, 16, 15, 14, 13, and 12.5 (from right to left). a) As main figure but in the USC phase for $\tilde{x} = 12$ (dotted), 7 (dashed), and at the particle-hole symmetric point $\tilde{x} = 0$ (solid). The o-spectrum evolves continuously as the transition is crossed, a pole occurring at the Fermi level precisely at the transition where ϵ_o^* vanishes. b) The $D_{ee}(\omega)$ spectral density just on either side of the QPT for $\tilde{x} = 12.261\,351\,440$ in the FL phase (solid) and $\tilde{x} = 12.261\,351\,420$ in the USC phase (dashed). Here the entire spectrum changes abruptly on crossing the transition.

the Fermi level spectrum is given generally by $D_{oo}(0) = \delta(\epsilon_o^*)$. In the vicinity of the transition, the renormalized level ϵ_o^* is the counterpart of the low energy scale T_* introduced in section 4.3.1 in respect of thermodynamics (see *e.g.* fig. 4.8); T_* and ϵ_o^* both vanish linearly as the transition is approached, and control the low-energy behaviour of appropriate thermodynamics or single-particle dynamics.

In contrast to the above behaviour of the $D_{oo}(\omega)$, the even channel spectrum $D_{ee}(\omega)$ illustrated in fig. 5.14a) naturally shows no sign of the vanishing renormalized odd level. Equally naturally it changes in a wholly discontinuous fashion, commensurate with the first-order nature of the transition.

This concludes our discussion of the single-particle dynamics along the line $y = x$ and indeed throughout the $x - y$ plane as a whole. In the next section we aim to make contact with experiments in real quantum dot devices. The findings of this chapter will be used along with the tools developed in chapter 3 to calculate the finite-bias differential conductance of such devices.

5.4 Conductance of real devices

Thus far we have concerned ourselves with model quantum dot systems. In this section we now attempt to rationalise, explain and guide experiment by comparison of such models to real laboratory systems. We will focus on the experiments of Kogan *et al.*[45] measuring the conductance of a GaAs-based single-electron transistor at low temperature. Before embarking on a study of the experimental results we will first highlight briefly the rather general effects that both the temperature and bias-voltage applied across a quantum dot may have. A more substantial examination of the behaviour of the conductance will be undertaken in section 6.2.2, where we also analyse the effect of a magnetic field on the conductance.

Our central equation for calculating the equilibrium (*i.e.* zero source-drain bias, $V_{\rm sd} = 0$) differential conductance in the 2LM is (3.50), which together with (5.4) gives:

$$G_C(T, V_{\rm sd} = 0) = \frac{2e^2}{h} G_0 \int_{-D}^{+D} \frac{-\partial f(\omega)}{\partial \omega} 2\pi\Gamma D_{ee}(\omega; T) \mathrm{d}\omega, \tag{5.86}$$

with D the conduction-band band width, and where $2\pi\Gamma D_{ee}(\omega;T) = \Sigma_{ij}\pi\Gamma_{ij}D_{ji}(\omega;T)$ (see section 5.1, we consider explicitely $V_1 = V_2$ and hence $\Gamma_{11} = \Gamma_{22} = \Gamma$). The most significant quantity appearing in (5.86) is of course the even-even spectral density $D_{ee}(\omega;T)$. The temperature dependence of this spectrum can be determined within the FDM-NRG framework in a well defined manner, something not accurately possible before the advent of the FDM-NRG method [82, 89–91, 115]. Hence the full temperature dependence of the conductance can also be calculated, not only the $T = 0$ result. Figure 5.15 illustrates the effect of increasing temperature T on the conductance, shown for the 2LM at particle-hole symmetry for simplicity, and for three values of the impurity parameters with $\tilde{U} = 2\tilde{U}' = 4\tilde{J}_H$. We have defined the Kondo scale $\omega_K^{S=1}$ in terms of the HWHM of the Kondo resonance in the $D_{ee}(\omega; T = 0)$ spectral density.

In this particle-hole symmetric example, the conductance approaches its maximal value $2e^2G_0/h$ in the $T \to 0$ limit (for all values of the impurity parameters). This is a natural consequence of the Friedel-Luttinger sum rule, section 5.2. For $T \to 0$ the derivative of the Fermi function appearing in (5.86) approaches a delta function centred on $\omega = 0$. The integral therefore 'picks out' only the zero frequency (Fermi level) value of the spectral density. At particle-hole symmetry we have $n_{\rm imp} = 2$ such that in the USC phase $2\pi\Gamma D_{ee}(0) = 1$ [from (5.49)], hence the conductance maximum. This maximum is reached only logarithmically slowly, symptomatic of the singular nature of the USC fixed point and the form of $D_{ee}(\omega)$ discussed in section 5.3, hence this maximum is not recovered exactly for the temperatures shown in fig. 5.15.

For the parameters chosen, the 2LM is in a strong coupling, spin-1 Kondo, regime

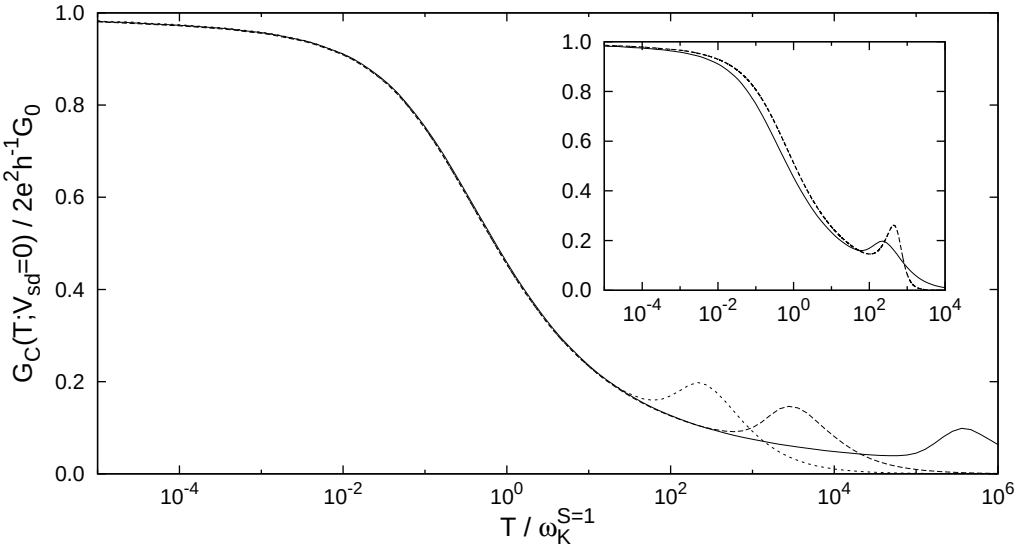

Figure 5.15: The zero-bias differential conductance for the 2LM at particle-hole symmetry (and hence in the USC phase) for $\tilde{U} = 2\tilde{U}' = 4\tilde{J}_H$ with $\tilde{U} = 30$ (solid), 20 (long dash), and 15 (short dash). The temperature T is scaled by $\omega_K^{S=1}$ defined as the HWHM of the Kondo resonance occurring in the $T = 0$ spectral density $D_{ee}(\omega)$, and given by $\omega_K^{S=1} = 2.06 \times 10^{-5}$, 1.64×10^{-3}, and 1.47×10^{-2} in the three cases respectively. A universal scaling form is found for $T \ll \Gamma$ with the maximal conductance at $T = 0$. Incoherent tunneling peaks occur on the scale $T \sim |\epsilon| = U + U'$ and can be understood in terms of a contribution to the conductance arising from the Hubbard satellites of the spectra. *Inset*: comparison of $G_C(T; V_{sd} = 0)/2e^2h^{-1}G_0$ vs. $T/\omega_K^{S=1}$ and the $T = 0$ spectral density $2\pi\Gamma D_{ee}(\omega)$ vs. $\omega/\omega_K^{S=1}$. The functions have similar but not identical forms: most notably the incoherent tunneling peak in the conductance is broader than the Hubbard satellite appearing in the spectra.

entirely characterised by the low-energy scale $\omega_K^{S=1}$. We therefore expect [20, 23] the temperature dependent conductance to be a universal function of $T/\omega_K^{S=1}$. Indeed this is found in fig. 5.15: results for different impurity parameters obey the same universal form for temperatures $T \ll \Gamma$, the lowest non-universal energy scale. Above this non-universal temperature scale, the results naturally deviate from the scaling form. Most noticeable are the conductance peaks occurring on a scale $T \sim |\epsilon_1|$ $(= |\epsilon_2|)$, and therefore at distinct values of $T/\omega_K^{S=1}$ for the different parameter sets. These incoherent tunneling peaks must clearly arise from the spectral Hubbard satellites. We note however that the features in the conductance as a function of T are broader than those appearing in the $(T = 0)$ spectra as a function of ω, as illustrated inset to fig. 5.15; the incoherent tunneling peak in the conductance (solid line) is reduced in height compared to the spectral Hubbard satellite (dashed line).

The thermal broadening of $G_C(T; V_{\rm sd} = 0)$ has two components. The first is that arising from the inclusion of the Fermi function in (5.86) whilst the second is that occurring due to the explicit temperature dependence of the spectral density. This second effect is illustrated in fig. 5.16, showing $2\pi\Gamma D_{ee}(\omega; T)$ vs. ω/Γ for the case

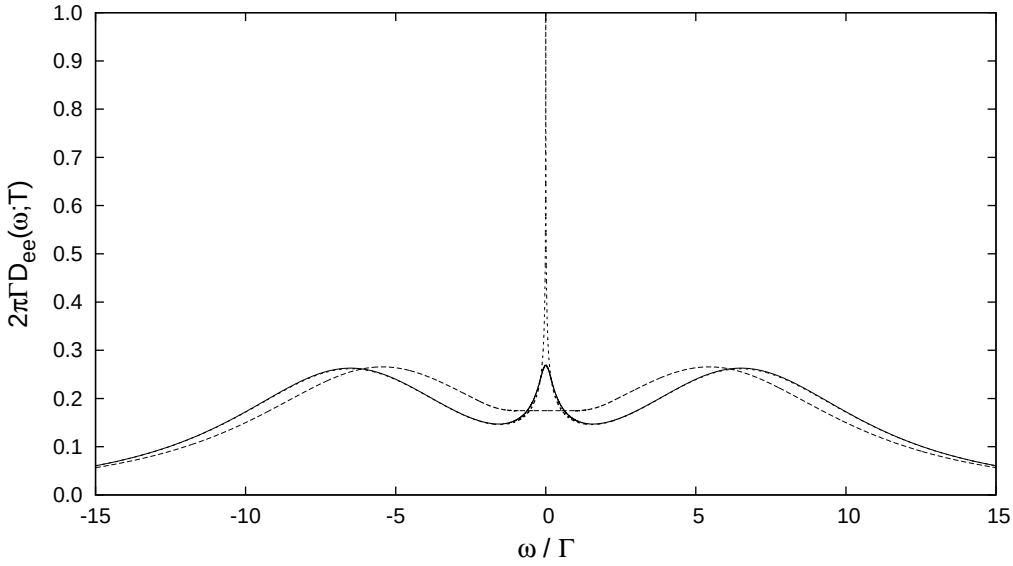

Figure 5.16: Effect of temperature on the spectral density $D_{ee}(\omega;T)$ for $\tilde{U} = 2\tilde{U}' = 4\tilde{J}_H = 15$ at particle-hole symmetry and with $T = 0$ (short dash), $10\omega_K^{S=1}$ (solid), and 5Γ (long dash), where $\omega_K^{S=1} = 1.47 \times 10^{-2}$. Temperature plays no role for frequencies $|\omega| \gg T$. The Kondo resonance is eroded on a scale $T \sim \omega_K^{S=1}$ and is completely destroyed in the case $T = 5\Gamma$.

$\tilde{U} = 2\tilde{U}' = 4\tilde{J}_H = 15$ with $T = 0$, $10\omega_K^{S=1}$, and 5Γ ($\simeq 350\omega_K^{S=1}$). As is clear from the figure the spectrum is only strongly affected by temperature on scales $|\omega| \lesssim T$: the results for $T = 0$ and $T = 10\omega_K^{S=1}$ are coincident for much of the range shown, differing appreciably only for $|\omega/\Gamma| < 1$, where in the later case the Kondo resonance has been noticeably eroded. For $T = 5\Gamma$ the Kondo resonance is simply absent, and the maxima of the Hubbard satellites have shifted toward $\omega = 0$.

The two thermal broadening effects outline above, combine to 'smooth out' the conductance when compared to the spectrum, inset to fig. 5.15. We note that it is largely through use of the self-energy method [81], leading to an enhanced resolution of the Hubbard satellites, that the incoherent tunneling peaks can be observed in the conductance. Without this method the features form merely a shoulder to the larger Kondo peak or are simply absent [52, 57].

This concludes our brief analysis of the effect of temperature on the zero-bias conductance $G_C(T; V_{\rm sd} = 0)$. The basic results are that for strongly correlated systems the conductance is a universal function of $T/\omega_K^{S=1}$ (or equivalently $T/T_K^{S=1}$) for temperature scales less than all non-universal scale (*i.e.* Γ, U, *etc.*), and that its features can be largely interpreted in terms of those arising in the single-particle spectra $D_{ee}(\omega)$, as evident from the inset to fig. 5.15. We will examine these effects in more detail when comparing FDM-NRG results for the conductance of the 2LM to those of experiments.

We now turn to examine the effect of the bias voltage on the conductance

$G_C(T;V_{\rm sd})$, given approximately from (3.51) and (5.4) by:

$$G_C(T;V_{\rm sd}) \simeq \frac{2e^2}{h} G_0 \int_{-D}^{+D} \left[\frac{-\partial f_s}{\partial \omega} + \frac{-\partial f_d}{\partial \omega}\right] 2\pi\Gamma D_{ee}(\omega;T)\mathrm{d}\omega. \tag{5.87}$$

with the Fermi functions $f_\nu(\omega) = [e^{\beta(\omega-\mu_\nu)}+1]^{-1}$. We consider a bias voltage $V_{\rm sd}$ asymmetrically partitioned across the impurity such that the Fermi levels of the source and drain leads are positioned respectively at

$$\mu_s = +\lambda e V_{\rm sd} \tag{5.88a}$$

$$\mu_d = -(1-\lambda) V_{\rm sd}. \tag{5.88b}$$

The case of a symmetric voltage drop is encompassed by setting $\lambda = \frac{1}{2}$, whilst $\lambda = 1$ corresponds to the maximal asymmetry. To understand how spectra features give rise to features in the finite-bias conductance we now examine the specific case of $T = 0$ such that (5.87) reduces to a sum of the spectral densities evaluated at the chemical potentials of the two leads:

$$G_C(T=0;V_{\rm sd}) = \frac{2e^2}{h} G_0 \big[\lambda 2\pi\Gamma D_{ee}(\omega = \lambda e V_{\rm sd}) + (1-\lambda) 2\pi\Gamma D_{ee}(\omega = -[1-\lambda] e V_{\rm sd})\big]. \tag{5.89}$$

Figure 5.17 displays results for a system with $\tilde{U} = 2\tilde{U}' = 4\tilde{J}_H = 30$ at the particle-hole symmetric point ($\tilde{\epsilon}_1 = \tilde{\epsilon}_2 = -30$) for $\lambda = 0.5$, 0.8, and 1 (solid, long dash, and short dash). The left inset shows $2\pi\Gamma D_{ee}(\omega)$ vs. ω/Γ as a guide to the features appearing in the main figure. For all values of λ the conductance is an even function of the bias, reflecting the fact that the spectrum at particle-hole symmetry is also an even function of its argument: $G_C(T=0;-V_{\rm sd}) = G_C(T=0;V_{\rm sd})$ for $D_{ee}(-\omega) = D_{ee}(\omega)$, as can be seen from (5.89). In the particle-hole symmetric limit illustrated, and in the extreme symmetric ($\lambda = \frac{1}{2}$) and asymmetric ($\lambda = 1$) cases, the conductance takes a particularly simple form mirroring that of the spectrum, specifically:

$$\frac{G_C(T=0;eV_{\rm sd})}{(2e^2/h)G_0} = 2\pi\Gamma D_{ee}(\omega = \lambda e V_{\rm sd}) \qquad : \lambda = \tfrac{1}{2} \text{ or } 1. \tag{5.90}$$

Between these two limits the conductance develops extra features over the spectrum. On decreasing λ from 1 (dotted) to the $\lambda = 0.8$ (dashed) intermediate case in fig. 5.17, the incoherent tunneling peaks develop weak shoulders, also readily interpretable by examination of (5.89). For example the shoulder at $eV_{\rm sd}/\Gamma = +75$ arises due a contribution to the conductance from the *lower* spectral satellite (occurring

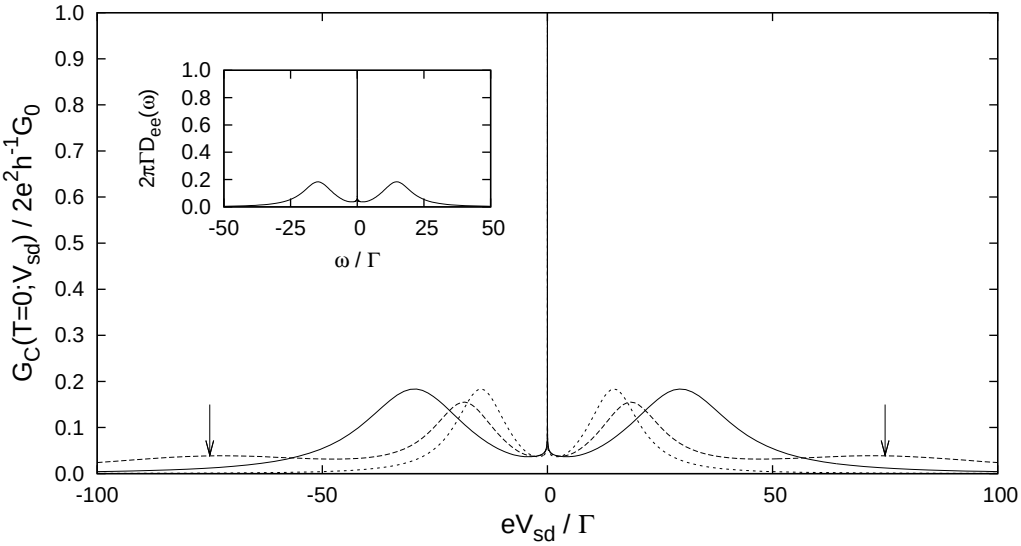

Figure 5.17: Dependence of the $T = 0$ finite-bias conductance on the bias asymmetry λ for $\tilde{U} = 2\tilde{U}' = 4\tilde{J}_H = 30$ at the particle-hole symmetric point ($\tilde{\epsilon}_1 = \tilde{\epsilon}_2 = -30$), shown for $\lambda = 0.5$ (solid), 0.8 (long dash), and 1 (short dash). As discussed in the text, the $T = 0$ conductance can be understood in terms of the feature appearing in the spectral density $D_{ee}(\omega)$, as shown in the inset. Between the extreme limits $\lambda = 0.5$ and $\lambda = 1$, additional weak high-energy shoulders (indicated by an arrow) are seen on the incoherent tunneling peaks of the conductance.

at $\omega/\Gamma \simeq -15$, inset to fig. 5.17), as is clear from (5.89) which gives:

$$\frac{G_C(T=0; eV_{\rm sd} = 75\Gamma)}{(2e^2/h)G_0} = 1.6\pi\Gamma D_{ee}(\omega = 60\Gamma) + 0.4\pi\Gamma D_{ee}(\omega = -15\Gamma). \qquad (5.91)$$

That this shoulder is weak reflects the small prefactor in the second term of the above.

The form of the conductance at particle-hole symmetry is therefore quite predictable once one has knowledge of the spectral density $D_{ee}(\omega)$. A more complicated example away from particle-hole symmetry is depicted in fig. 5.18 for the same bias asymmetries as fig. 5.17. We choose $\tilde{\epsilon}_1 = -30$ and $\tilde{\epsilon}_2 = -10$, in the FL phase of the 2LM. For the asymmetric case $\lambda = 1$ (short dash) the conductance $G_C(T = 0; V_{\rm sd})$ is given equivalently by the spectra $2\pi\Gamma D_{ee}(\omega)$, (5.90). It contains a large central peak at $eV_{\rm sd}/\Gamma \simeq -0.5$ and a smaller band at $eV_{\rm sd}/\Gamma \simeq 5$. For a symmetrical bias split $\lambda = 0.5$ (solid) the conductance is a symmetrised version of the spectral density, resulting from the fact that $\partial f_s(\omega)/\partial\omega + \partial f_d(\omega)/\partial\omega$ is an even function of ω in this limit.[8] We therefore observe a split central peak in the conductance with weak shoulders at $eV_{\rm sd}/ = \pm 10\Gamma$. The situation between these two limits can become quite complicated as shown in the case $\lambda = 0.8$. Thus it is not, in the general case,

[8] This holds for all temperatures, not only $T = 0$.

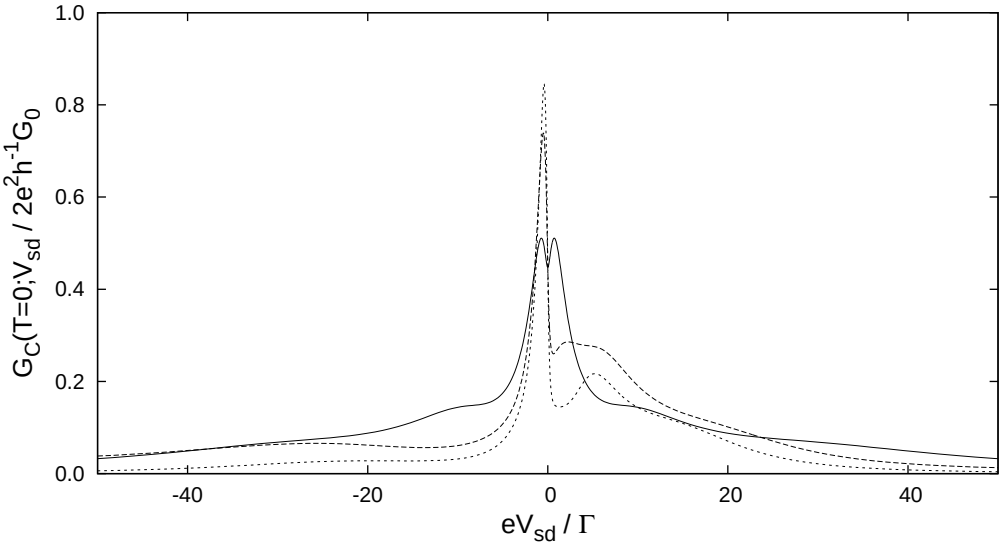

Figure 5.18: The finite-bias conductance for the same interaction parameters as fig. 5.17, and again with $\lambda = 0.5$ (solid), 0.8 (long dash), and 1 (short dash), but away from particle-hole symmetry. We take $\tilde{\epsilon}_1 = -30$ and $\tilde{\epsilon}_2 = -10$. At this point the system is in the FL phase of the 2LM. The conductance has a much more complicated dependence on the bias asymmetry than at particle-hole symmetry.

appropriate to naively associate features of the finite-bias conductance with features appearing in $D_{ee}(\omega)$.

Both the temperature and bias asymmetry therefore have a profound effect on the calculated differential conductance of quantum impurity models. The major effect of temperature is to thermally smear features of the conductance over and above those arising spectrally, as above in the inset to fig. 5.15. This can ultimately lead to either an enhancement or reduction in the zero-bias conductance, as we shall see shortly in the experimental results. The bias voltage has a yet more complicated effect. In general the asymmetry parameter λ is as important as the other impurity parameters ($\tilde{U}$, $\tilde{U}'$, etc) in determining the full bias dependence of the conductance. One must therefore be careful in naively taking either of the limits $\lambda = \frac{1}{2}$ or $\lambda = 1$ when comparing numerical results to those of experiments, as we move to do now.

5.4.1 Phase transition in a GaAs quantum dot

We now consider the experiments of Kogan *et al.*[45] on a GaAs-based single-electron transistor at low temperatures, embodied in the differential conductance as a function of gate voltage ΔV_g (measured relative to a reference voltage) and also the bias voltage $V_{\rm sd}$, considered briefly in the previous section. We will begin by describing the experimental results, before moving to detail how comparison between theoretical results for the 2LM and experiment can be made. Finally we show numerical results and provide a rationale for the experimental findings.

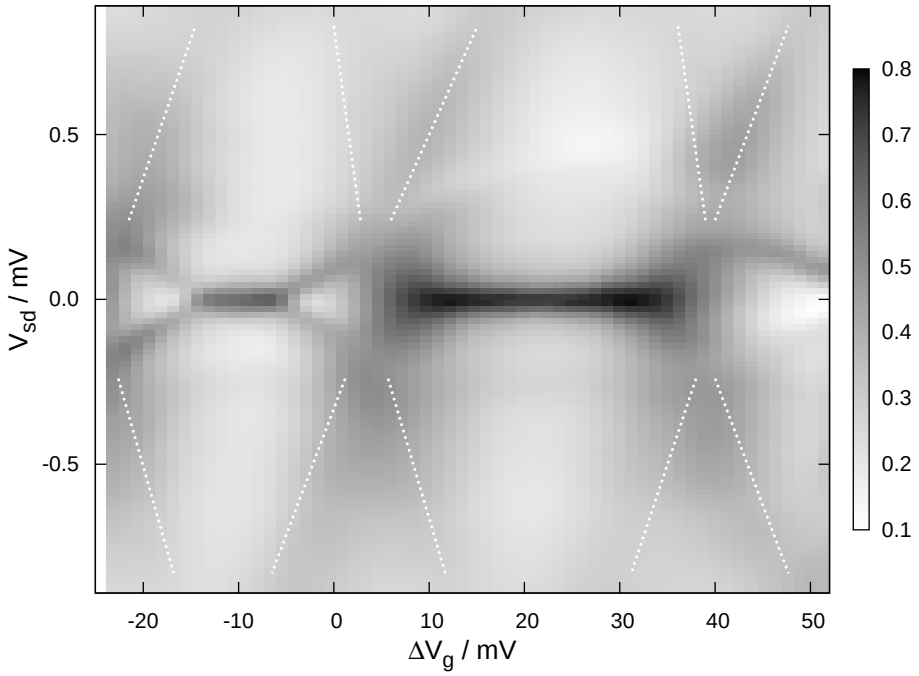

Figure 5.19: Experimental results [45] for the differential conductance (in units of $2e^2/h$) of a quantum dot device in the $(\Delta V_g, V_{\rm sd})$ plane. Results are black/white shaded (as indicated) in units of $2e^2/h$, darker shading indicating higher conductance. Dotted white lines are a guide indicating the Coulomb-blockade diamonds. Two clear zero-bias peaks are seen in adjacent Coulomb blockade valleys — one must therefore correspond to odd impurity occupation (right) whilst the other to even occupation (left). Finite bias peaks symmetrically disposed about $V_{\rm sd} = 0$ emanate from the even valley zero-bias peak and are interpreted, by the authors, as an excited-state triplet Kondo effect.

The experimental results are shown in fig. 5.19. On varying the gate voltage clear zero-bias Kondo peaks are seen in the centres of *adjacent* Coulomb blockade valleys, one valley thus being associated with an odd number of quantum dot electrons and the other with an even number. The former valley, in the relatively wide range $5 \lesssim \Delta V_g/\text{mV} \lesssim 40$, is interpreted [45] as that occurring for odd occupation and thus a usual spin-$\frac{1}{2}$ Kondo effect: the normal FL, or 'singlet phase'. The second valley, extending over the much narrower range $-20 \lesssim \Delta V_g/\text{mV} \lesssim 5$, is then interpreted [45] as the even occupation valley. In this second valley a zero-bias peak occurs in the range $-15 \lesssim \Delta V_g/\text{mV} \lesssim -5$ concomitant with the expectation of Kondo screening of a triplet quantum dot state; the 'triplet phase' (*i.e.* the USC phase). It was suggested [45] that a transition to a singlet ground state occurs (within this second valley) at $\Delta V_g = -5$ mV, and speculated that the peaks displaced symmetrically about $V_{\rm sd} = 0$ in the range $-5 \lesssim \Delta V_g/\text{mV} \lesssim 0$ arise from 'Kondo screening of the excited triplet state'. In comparing these findings with numerical results we will provide a coherent explanation of the experiment.

In order to compare our theoretical results with those of experiment we must first

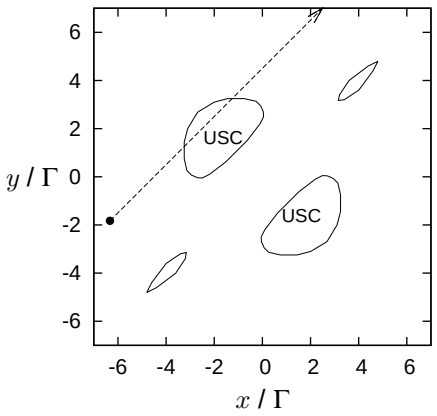

Figure 5.20: Phase boundary for the 2LM with parameters as fitting to experiment: $\tilde{U} = 12$, $\tilde{U}' = 6$, $\Delta\tilde{\epsilon} = 4.5$, and $\tilde{J}_H = -0.5$. The experimental trajectory (dashed arrow) begins in the singlet (FL) phase at $(x/\Gamma, y/\Gamma) = (-6.3, -1.8)$ runs parallel to the $y = x$ line cutting through the triplet (USC) phase before returning to the singlet phase and finishing outside of the area shown at $(x/\Gamma, y/\Gamma) = (14.6, 19.1)$.

make a correspondence between the parameters of the 2LM and those of experiment. As before, and for simplicity, we assume that all the quantum dot levels are equally coupled to the metallic leads so we have $V_1 = V_2$ in the 2LM. Under application of a gate voltage, we expect the energy levels (ϵ_1 and ϵ_2) of the quantum dot device to be shifted in energy relative to the Fermi energy of the leads. Further we make the assumption that each level is equally affected and so the level spacing remains essentially fixed. For the 2LM model we have then that $\Delta\epsilon = \epsilon_2 - \epsilon_1$ is constant. One can of course relax this restriction but we do not find it necessary to do so in order to explain the experimental results.[9] The experimental trajectory in the (ϵ_1, ϵ_2) [or (x,y)] plane upon varying ΔV_g is then one which runs parallel to the $y = x$ line ($y = x + \Delta\epsilon$), as depicted in fig. 5.20 which shows also the phase boundary for the dot parameters determined below.

A distinctive feature of the experimental results is the approximate symmetry with respect to the bias voltage $V_{\rm sd}$. This is particularly noticeable in the vicinity of $V_{\rm sd} = 0$, for example the symmetrically disposed peaks in the regions $\Delta V_g = -5$ mV and $\Delta V_g = -15$ mV. From the previous discussion this symmetry can only occur for all values of the gate voltage ΔV_g for a symmetric bias drop. We therefore take $\lambda = \frac{1}{2}$. This symmetry implies a second: under the particle-hole and $1 - 2$ transformations we have, from (5.40a), that $D_{ee}(-\omega; -x, -y) = D_{ee}(\omega; x, y)$. Coupled with the even symmetry of $\partial f_s(\omega)/\partial\omega + \partial f_d(\omega)/\partial\omega$ for $\lambda = \frac{1}{2}$ the conductance [(5.87)] must then obey:

$$G_C(T, V_{\rm sd}; -y, -x) = G_C(T, V_{\rm sd}; x, y), \tag{5.92}$$

[9]The modification of the excitation spectra on changing ΔV_g is generally considered [45] to be a much weaker effect than the shifting of the energy levels.

that is the conductance is symmetric under reflection about the line $y = -x$. Now, the trajectory $y = x + \Delta\epsilon$ discussed above is perpendicular to the line $y = -x$ and intersects it for $x = -\frac{1}{2}\Delta\epsilon$, *i.e.* for $\epsilon_1 = -\frac{1}{2}\Delta\epsilon - \frac{1}{2}U - U' \equiv \epsilon_{1,m}$. Since the phase boundaries in the 2LM are also symmetric under reflection about the line $y = -x$ (see fig. 5.20) this value $\epsilon_1 = \epsilon_{1,m}$ is the midpoint of the triplet phase, such that the conductance is an even function of $\epsilon_1 - \epsilon_{1,m}$, or equivalently $\Delta V_g - \Delta V_{g,m}$. This symmetry is quite well satisfied in the experimental results of fig. 5.19, with $\Delta V_{g,m} = -10$ mV.

To compare results for the 2LM directly to experiment we must also specify the dimensionless interactions $\tilde{U} = U/\Gamma$, $\tilde{U}'$, and $\tilde{J}_H$, $\Delta\tilde{\epsilon} = \Delta\epsilon/\Gamma$, the relation between $\tilde{\epsilon}_1$ and ΔV_g and finally the hybridisation strength Γ in terms of physical units (*i.e.* in units of meV). This is clearly a large parameter space and so our intent here is simply to employ a reasonable set of parameters. As discussed in section 2.3.2 we expect the relative hierarchy of energies to satisfy [116] $|\tilde{J}_H| \ll \Delta\tilde{\epsilon} \ll \tilde{U}$. Here we employ $|\tilde{J}_H| = 0.5$, $\Delta\tilde{\epsilon} = 4.5$, and $\tilde{U} = 12$ such that (since $U > \Gamma$) charge quantization occurs toward the centres of the Coulomb blockade valleys. Further, single occupation of two distinct quantum dot levels is promoted over double occupation of a single level by $\Delta\tilde{\epsilon} < \tilde{U} - U' + \frac{1}{4}J_H$. In determining $\tilde{U}'$ no attempt to explain experiment on the assumption that $\tilde{U}' = \tilde{U}$ was found to be successful. The main reason for this is evident in fig. 4.7b) where for $\tilde{U}' = \tilde{U}$ the resultant width of the triplet phase (in $\tilde{\epsilon}_1$ or ΔV_g) is much too large compared to that of the singlet phase. This assumption is therefore not qualitatively consistent with experiment. For the results shown here we have used $\tilde{U}' = 6$ although tolerable variations from this value give comparable agreement with experiment.

Figure 5.21 shows our comparison with experiment for both b) the zero-bias and c) the finite-bias conductance along with the variation of the Kondo scale T_K [a)] as ΔV_g is varied. From the discussion above, the relation between ΔV_g and $\tilde{\epsilon}_1$ is of the form $\Delta V_g = c(\tilde{\epsilon}_1 - \tilde{\epsilon}_{1,m}) + \Delta V_{g,m}$ where the constant of proportionality is to be determined. For a chosen set of $\tilde{U}$, $\tilde{U}'$, $\tilde{J}_H$ and $\Delta\tilde{\epsilon}$ the theoretical zero-bias conductance is calculated as a function of $\tilde{\epsilon}_1$. It is then scaled onto the experimental results shown in fig. 5.21b) over the range $35 < \Delta V_g/\text{mV} < 40$. This range is chosen because not only is it a relatively simple feature of the overall curve but also because here the system is beginning the approach to the 'empty orbital' regime [20] of $n_{\text{imp}} \ll 1$ where we do not expect the conductance to have any appreciable temperature dependence. With this procedure the constant $c = 14.25$ can be determined and is then fixed for all values of ΔV_g and T. The final parameter which must be specified to fully determine the zero-bias conductance is the prefactor G_0, reflecting the relative coupling asymmetry of the quantum dot levels to the source and drain leads, which serves to scale the vertical axis in fig. 5.21b). A value of $G_0 \simeq 0.8$ can be seen from even a cursory examination of the experimental data in fig. 5.21b).

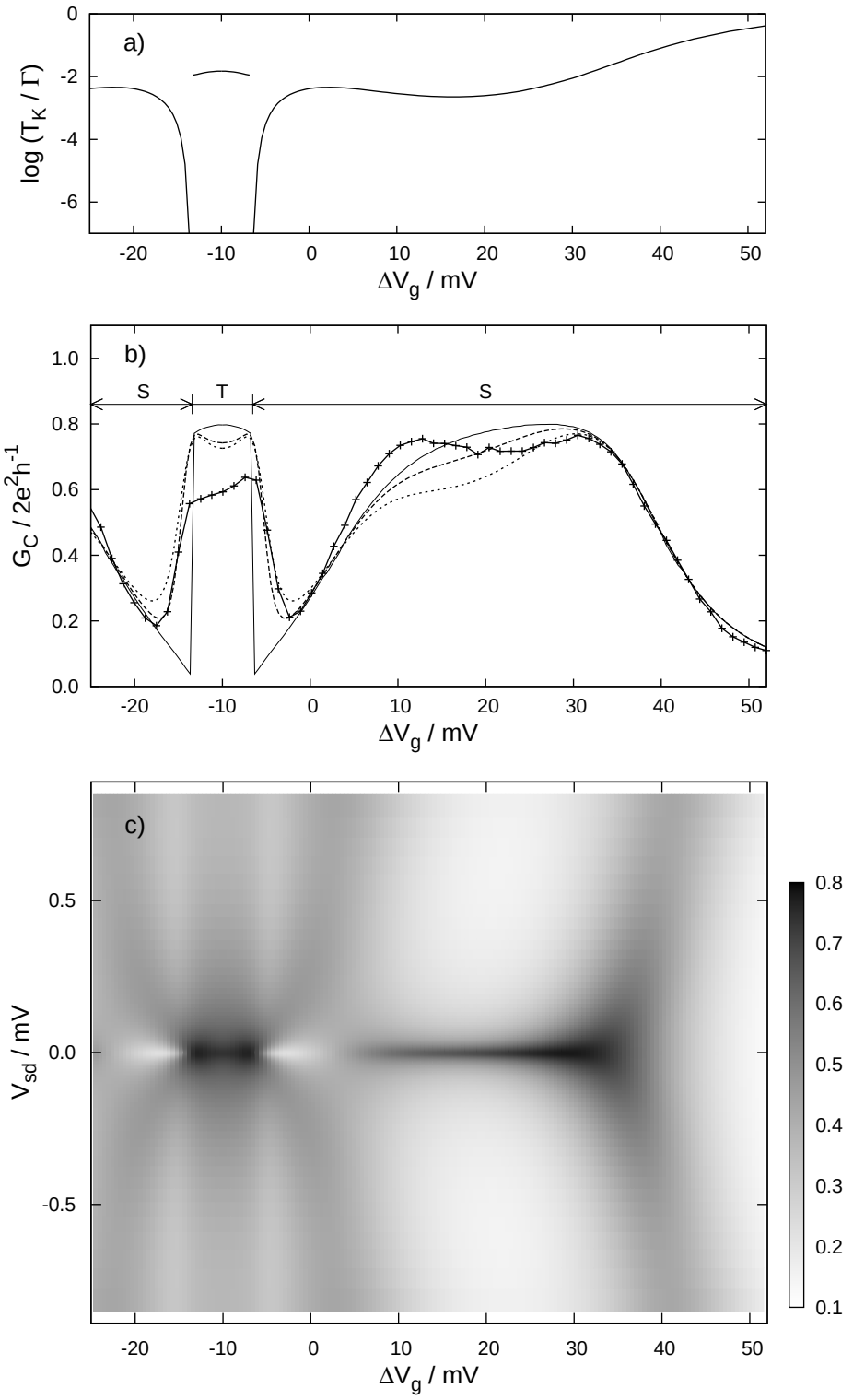

Figure 5.21: a) Theoretical results for the Kondo scale T_K [$\equiv T_K^{S=1}$ in the USC triplet (T) phase] as the relative gate voltage ΔV_g is varied in a quantum dot device. b) Experimental results (+) [45] for the zero-bias conductance compared with theory for $T/\Gamma = 0$ (solid), 5×10^{-3} (long dash), and 1×10^{-2} (short dash) corressponding to $T = 0$, 30, and 60 mK. Positions of the $T = 0$ phase boundaries between the USC triplet (T) and FL singlet (S) state are indicated. c) Theoretical counterpart to fig. 5.19 shown for $T = 30$ mK. The same conductance scale is used as fig. 5.19.

In comparing to experiment an obvious key element is the relative widths (in ΔV_g) of the singlet and triplet phases [labelled S and T respectively in fig. 5.21b)], the former being considerably wider than the latter in experiment. This is naturally influenced by the exchange interaction $\tilde{J}_H$ as well as the interlevel Coulomb repulsion $\tilde{U}'$ and the level spacing $\Delta\tilde{\epsilon}$. These parameters are therefore optimised accordingly. For the results shown here we choose $\tilde{J}_H = -0.5$. The magnitude of this coupling is therefore small as expected, although its sign is antiferromagnetic. This is not however unreasonable as on coupling to the leads the *effective* interimpurity exchange coupling can be ferromagnetic [see *e.g.* (4.42)] such that the triplet phase may still arise as in section 4.3.2; and indeed the USC phase does arise as seen in fig. 5.20.

With the parameters derived above we calculate the $T = 0$ zero-bias conductance [solid line in fig. 5.21b)]. The two triplet/singlet (USC/FL) phase boundaries are indicated in the figure. The triplet (T) phase is, as discussed above, symmetrically disposed about the midpoint $\Delta V_{g,m} = -10$ mV. It occurs in the interval $-13.45 < \Delta V_g/\text{mV} < -6.55$, corresponding to $-3.2 < x/\Gamma < -1.3$ as seen in fig. 5.20. At the upper phase boundary we find $n_{\text{imp}} = 1.87$ while by symmetry at the lower boundary we find $n_{\text{imp}} = 4 - 1.87 = 2.13$ such that from (5.49) the zero-bias conductance increases on crossing from the singlet to the triplet phase. At this stage the agreement between theory and experiment is good but not remarkable, particularly in the region of the transition.

In determining the effect of temperature on the zero-bias conductance it is useful to consider the Kondo scale T_K (with $T_K \equiv T_K^{S=1}$ for the triplet phase) as a function of ΔV_g, shown in fig. 5.21a). Since T_K vanishes as the QPT is approached from the singlet (FL) side, finite temperature effects are naturally most significant in the vicinity of the transition. Figure 5.21b) thus shows the zero-bias conductance at two nonzero temperatures, $T/\Gamma = 5 \times 10^{-3}$ and 1×10^{-2}. Whilst there is not much net difference between the two, each has the effect of significantly increasing the conductance in the vicinity of the transition. This effect arises not only from the vanishing Kondo scale but also from the asymmetry of the Kondo antiresonance, shown explicitely in fig. 5.22 below. At finite temperatures the Fermi functions appearing in (5.86) thereby increase the conductance by including a larger proportion of this important spectral feature in the integral. The end result is rather good overall agreement with experiment. Over the temperature range shown the conductance in the triplet phase does not erode as rapidly as we might like, reflecting the fact that $T_K \equiv T_K^{S=1}$ is in excess of the temperatures shown. The situation could be improved by varying the bare impurity parameters to reduce $T_K^{S=1}$ below the temperatures used. The experimental temperature is not known with certainty, for although the experiments were performed at the refrigerator temperature of ~ 12 mK, the effec-

tive electron temperature was not determined but believed to be $\gtrsim 40$ mK.[10] With $\Gamma = 0.5$ meV (as we use below) the temperatures shown here correspond to $T = 30$ and 60 mK, in agreement with the expected experimental value.

Using (5.87) we now calculate the finite-bias conductance [*cf.* fig. 5.19]. To do this we must make correspondence between the energy scales used in the theoretical model and those of experiment, *i.e.* we must find the energy unit Γ. This can be done in a variety of ways, some more quantitative than others, depending on the experimental data available. Often, as in the current case, the charging energies (U) and level spacings ($\Delta\epsilon$) of quantum dots are not known with certainty and only broad, often conflicting [45] estimates can be made of the parameters. The Coulomb-blockade charging peaks, such as those highlighted in fig. 5.19, are often a good indicator of the dot-lead hybridization, having width $1-2\Gamma$ [117, 118]. Here we choose the typical value $\Gamma = 0.5$ meV [1, 45, 119] but note that comparison between theory and experiment is not critically dependent on this choice, with values in the range of $0.3-0.6$ meV being quite acceptable. The resultant theoretical conductance map is shown in fig. 5.21c) for $T = 30$ mK and is in rather good overall agreement with the experimental results.

In addition to the clear zero-bias Kondo ridges discussed above associated with both the triplet and singlet phases, the theoretical conductance map shows some of the other features noted in experiment. In particular, the symmetrically disposed peaks attached to the triplet Kondo peak separated by an area of low conductance, the bright white region in fig. 5.21c). We now provide an explanation of the occurrence of these peaks based on our study of the single-particle dynamics of the 2LM.

As seen in fig. 5.21b) the $T = 0$ zero-bias conductance increases on passing from the singlet (FL) to the triplet (USC) phase. In section 5.3 we showed that such behaviour was indicative of a vanishing Kondo antiresonance in the single-particle spectrum, as the transition is approached from the singlet side. This is the origin of the ridges seen in the conductance maps, as shown by considering cuts through the conductance map of fig. 5.21b) for a sequence of different gate voltages. Figure 5.22a) accordingly shows the conductance *vs.* the bias voltage $V_{\rm sd}$ for five different values of ΔV_g: -10 mV (at the midpoint of the triplet phase), and $\Delta V_g = -6$, -5, -3, and $+2$ mV (in the singlet phase). The transition into the singlet phase occurs for $\Delta V_g = -6.5$ mV. For $\Delta V_g = -10$ mV the conductance naturally peaks for $V_{\rm sd} = 0$. On entering the singlet phase a clear antiresonance in the conductance is seen to develop, just setting in by $\Delta V_g = -6$ mV. The antiresonance widens and deepens as ΔV_g increases, indicative of the associated Kondo scale T_K increasing above the temperature T. Further into the singlet phase the antiresonance disappears,

[10] From private communication with A. Kogan and D. Goldhaber-Gordon.

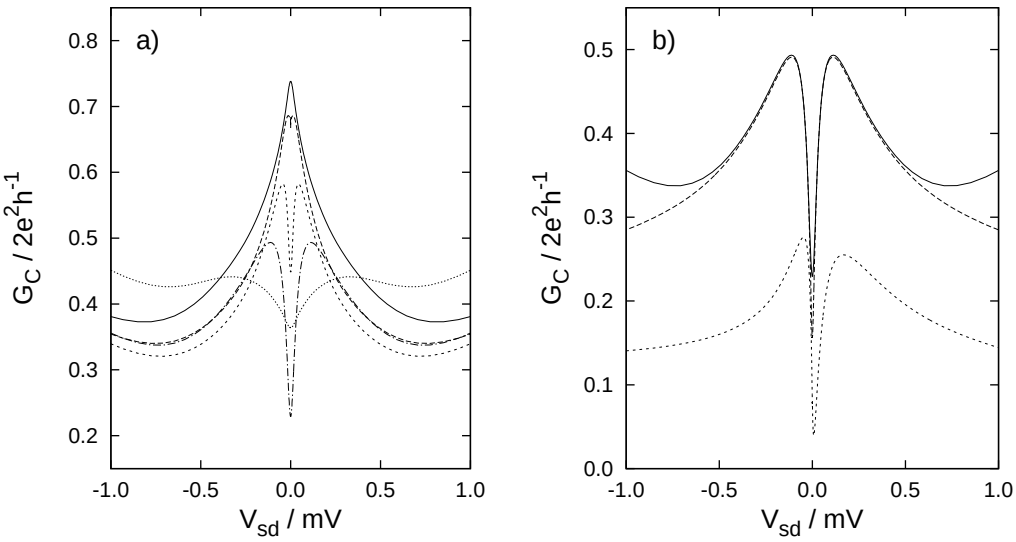

Figure 5.22: a) $V_{\rm sd}$ dependence of the conductance, taking cuts through the conductance map of fig. 5.21c) for a sequence of different fixed gate voltages: $\Delta V_g/\mathrm{mV} = -10$ (solid), -6 (long dash), -5 (short dash), -3 (point dash), and $+2$ (dotted) on moving into and through the singlet phase. A clear antiresonance develops in the singlet phase, as discussed in the text. The peaks in the conductance, symmetrical about $V_{\rm sd} = 0$, lie at the centre of the ridges seen in the conductance map. b) Focus on the $\Delta V_g/\mathrm{mV} = -3$ case. Solid: conductance as in a). Long dash: corresponding $T = 0$ conductance proportional to $D_{ee}(\omega = +\frac{1}{2}eV_{\rm sd}) + D_{ee}(\omega = -\frac{1}{2}eV_{\rm sd})$. Short dash: contribution from $D_{ee}(\omega = +\frac{1}{2}eV_{\rm sd})$ alone, showing a clear Kondo antiresonance in the single-particle spectrum.

as illustrated by the $\Delta V_g = +2$ mV example. The peaks in these conductance profiles, symmetrically disposed about $V_{\rm sd} = 0$, lie at the centre of the ridges in the conductance map.

To show that the above behaviour indeed reflects a Kondo antiresonance in the single-particle spectra itself, fig. 5.22b) focuses on the $\Delta V_g = -3$ mV example. The solid line again gives the conductance shown in fig. 5.22a), while the long dashed line shows the corresponding $T = 0$ conductance obtained from (5.89) with $\lambda = \frac{1}{2}$ (a symmetric bias voltage split), and thus proportional to the symmetrised spectra $[D_{ee}(\omega = +\frac{1}{2}eV_{\rm sd}) + D_{ee}(\omega = -\frac{1}{2}eV_{\rm sd})]$. The later clearly captures well the former, only a small amount of thermal smearing of the kind discussed in the previous section is apparent. Because the conductance is proportional to the symmetrised spectra (for $\lambda = 0.5$), it is not *a priori* clear that the single-particle spectrum itself contains a Kondo antiresonance — $D_{ee}(\omega)$ may contain only a single peak displaced slightly from $\omega = 0$. That an antiresonance does occur in the spectra is seen from the short dashed line, which shows the contribution from $D_{ee}(\omega = +\frac{1}{2}eV_{\rm sd})$ itself, seen to contain a clear Kondo antiresonance centred on the Fermi level. This antiresonance is naturally asymmetric, unlike those studied previously along the $y = -x$ line of the 2LM. We emphasise that since the ridges in the conductance stem from the peaks

inherent to the Kondo antiresonance in $D_{ee}(\omega)$, they are *not* interpretable naively in terms of the isolated dot states, contrary to the original paper [45].

The zero-bias Kondo ridge in the conductance map — formed as described above from the merging of the $V_{\rm sd} \neq 0$ conductance ridges and concomitant vanishing of the conductance antiresonance — reflects of course the existence of the triplet phase and transition to it from the Fermi liquid phase commonly observed in experiments. However, one can readily envisage a situation where the underlying parameters of the quantum dot device are such that on varying the gate voltage the transition is not seen. For example, fig. 5.20 indicates that by taking the same parameters as above but making a small change in the level separation (from $\Delta\epsilon = 4.5\Gamma$ to say 5.5Γ) the resultant trajectory would come close to but 'miss' the singlet/triplet phase boundary; the system would remain in the singlet phase. In this case no zero-bias Kondo ridge associated with the triplet phase can arise. Instead, from the discussion above, we expect that the Kondo antiresonance persists on decreasing ΔV_g, with attendant finite-bias conductance ridges that never quite merge together. That this indeed occurs is shown in fig. 5.23 where the conductance map for $T = 30$ mK is shown for the same parameters as fig. 5.21 except for a slight change in $\tilde{J}_H$ to -0.6. This more antiferromagnetic $\tilde{J}_H$ has the effect of 'shrinking' the triplet phase, as in fig. 4.9, such that for the same $\Delta\epsilon$ a transition to the triplet phase is not made. The qualitative behaviour seen here is similar to that observed in a second device shown in fig. 3 of ref. [45], although in this case we have not attempted a quantitative comparison.

This chapter has shown the single-particle dynamics to be very rich. Our focus has been on the even-even spectral density $D_{ee}(\omega)$ due to its intimate relation to the differential conductance. In the USC phase the associated self-energy $\Sigma_{ee}(\omega)$ displays properties symptomatic of a singular Fermi liquid: its imaginary part vanishing at the Fermi level only logarithmically slowly rather than being quadratic in frequency. We have introduced the Friedel-Luttinger sum rule relating the static phase shift $\delta(0)$ to the excess impurity charge and the Luttinger integral. We have shown also that the latter takes a value characteristic to the quantum phase of the 2LM. In the FL phase the well known result $I_L = 0$ is found whilst in the USC phase by contrast we find $|I_L| = \frac{1}{2}\pi$. The sum rule has immediate consequences for the spectral density on crossing the Kosterlitz-Thouless phase transitions: it must jump discontinuously except in the very rare cases of $n_{\rm imp} = n/2$ with n an odd integer. We have illustrated representative results for $D_{ee}(\omega)$ on crossing both the generic second-order QPTs and along the lines $y = -x$ and $y = x$. The spectral density shows universal scaling independent of the asymmetry $\eta(x, y)$ in the region of the USC phase where the low-energy effective model is the spin-1 Kondo model. Along the line $y = -x$ a Kondo antiresonance, which appears to be experimentally relevant, develops in the FL phase on approaching the transition. It too shows universal scaling. On the line $y = x$ where a first-order QPT arises, the Hilbert space

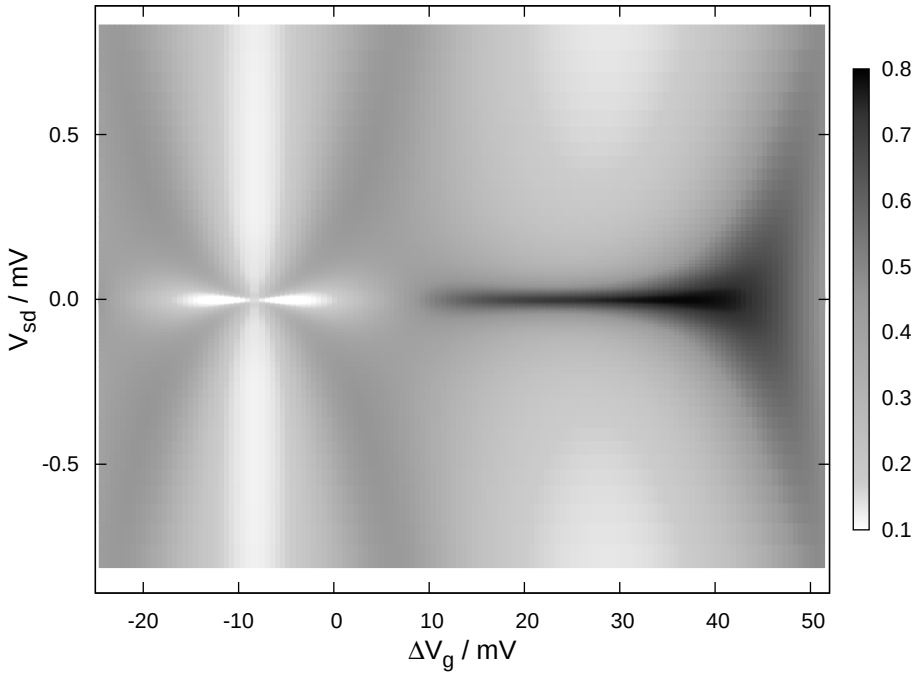

Figure 5.23: As discussed in the test, conductance map in the $(V_{\rm sd}, \Delta V_g)$ plane shown for $T = 30$ mK and the same parameters as fig. 5.21 except for a slight change in $\tilde{J}_H$ to -0.6. In this case no singlet/triplet transition arises, the system remaining throughout in the singlet phase. The zero-bias Kondo ridge associated with the triplet phase is therefore absent and replaced by a persistent Kondo antiresonance.

of the Hamiltonian is entirely separable into even and odd sectors. The spectral densities, self-energies, phase shifts and Luttinger integrals may therefore be separated into even and odd components. In doing so the first-order transition can be interpreted as the crossing through the Fermi level of the odd renormalized level $\epsilon_o^* = \epsilon + \Sigma_o^R(\omega = 0)$. Numerical results from the FDM-NRG have been shown to be consistent with analytical results. Finally we have examined results for the differential conductance both at zero and finite bias. In the USC phase the zero-bias conductance as a function of temperature shows universal scaling in $T/T_K^{S=1}$ up to temperatures of the order Γ where non-universal effects begin to have an effect. Use of the self-energy in calculating the single-particle densities allows better resolution of these non-universal peaks in the conductance. The effects of temperature and the bias asymmetry λ on the finite-bias conductance have been examined. The latter can lead to non-trivial results for the conductance if the bias-dependence of the conductance is interpreted in terms of the spectral density, as is often performed when rationalising experimental results. Care must therefore be taken with this approach. A comparison of numerical results for the 2LM with those of experiment has been performed with a favourable outcome and has led to a better understanding of the experimental findings. The next chapter departs slightly from the work thus far and examines the effect of a local magnetic field applied to the impurity in the 2LM.

CHAPTER 6

The Role of Local Magnetic Fields

Thus far in this thesis we have examined the physics of quantum dot systems in the absence of an applied magnetic field. Many interesting experiments [44, 46, 47, 112, 120–124] are however performed by varying an applied field, and so it is appropriate that we should address theoretically this issue.

We start by examining the field dependent magnetization of both the AIM and 2LM under an applied field. This property is quite well understood for the AIM [20] and hence we do not cover it so extensively in this thesis. We will however use these results to illustrate the accuracy and reliability of current NRG methods when a magnetic field is present in the system. Our focus in section 6.2 will be on the dynamic properties of both the AIM and 2LM in a magnetic field. We will examine the magnitude of the shift in the spectral maximum away from zero as a function of the field strength. In this area we hope to clarify the existing literature [115, 125–131]. We will also extend the Friedel-Luttinger sum rule of section 5.2 to the case of broken spin symmetry. Experimental results [46, 123] are analysed towards the end of the chapter.

In considering a magnetic field applied to a quantum dot system, we assume that only the impurity couples to the field — specifically we ignore the effect of the field on the conduction band states. This simplification is valid provided the band width D is well in excess of all energy scales; the field then simply shifts all conduction band levels by some small, essentially imperceptible amount such that the gross structure of the band is little altered. For simplicity we assume a field directed in the $+z$ direction, $B \equiv B_z$, such that a scalar coupling of the impurity spin to the field yields impurity levels at:

$$\epsilon_{i\sigma} = \epsilon_i - \sigma h. \tag{6.1}$$

Here $2h = g\mu_B B$ is the Zeeman splitting and $\sigma = +\,(-)$ for $\uparrow$-spin ($\downarrow$-spin) electrons. Throughout this chapter we will invariably refer to h as 'the field'.

6.1 The impurity magnetization

The magnetization of a quantum impurity level i may be defined through the difference in the spin-dependent expectation values of the level occupation number, *viz.*:

$$m_i(h) = \langle \hat{n}_{i\uparrow} \rangle - \langle \hat{n}_{i\downarrow} \rangle \tag{6.2a}$$

$$= \int_{-\infty}^{0} [D_{ii;\uparrow}(\omega) - D_{ii;\downarrow}(\omega)] \; \mathrm{d}\omega. \tag{6.2b}$$

For the 2LM, $i = 1$ or 2, while for the single-level AIM, $i = 1$ only. This quantity can be determined accurately using the FDM-NRG [73, 82, 89], the complete Fock space approach circumventing known problems arising in the original NRG [115, 127].

Figure 6.1 shows the total dot magnetization $m(h) \equiv m_1(h)$ vs. h/T_K for the symmetric single-level AIM with $\tilde{U} = 50$ and $\tilde{\epsilon} = -\frac{1}{2}\tilde{U}$. As in section 4.3 we define T_K via $S_{\mathrm{imp}}(T_K) = 0.1$, in the case $h = 0$. The accuracy of the FDM-NRG is confirmed by the clear agreement with the exact result known from the Bethe ansatz for the Kondo model [31, 132]. At a field $h \sim T_K$ the magnetization rises rapidly from its zero-field (Kondo screened) value $m(0) = 0$, before turning over to a slow asymptotic approach to saturation of the form [31, 132] $m(h) \sim 1 - [2\ln(h/T_K)]^{-1}$. The inset to fig. 6.1 gives results for $\tilde{U} = 30$, 20, and 10, showing the inevitable deviation from the universal Kondo magnetization curve at sufficiently high fields $h \gtrsim \mathcal{O}(\Gamma)$.

In comparison to the above, fig. 6.2 shows results for the 2LM with $\tilde{U} = 40$, $\tilde{U}' = 0$, and $\tilde{J}_H = 10$ at particle-hole symmetry, such that the model is in the USC phase at $h = 0$. Strikingly $m(h) = m_1(h) + m_2(h)$ is greater than unity for any non-zero field, with $m(h) \to 1$ as $h \to 0$. This is a natural consequence of the USC fixed point containing a free spin-$\frac{1}{2}$ local moment [97]. Upon application of any field $h \neq 0$, complete polarization of this spin occurs. This is in contrast to the $h = 0$ case where the magnetization vanishes by symmetry. The magnetization rises above unity for $h \sim T_K^{S=1}$ [again with $T_K^{S=1}$ defined as in section 4.3 via $S_{\mathrm{imp}}(T_K^{S=1}) = 0.8$] and turns to a slow asymptotic form $m(h) \sim 2 - [\ln(h/T_K)]^{-1}$ [31, 132]. We compare again to the exact Bethe ansatz result for the spin-1 Kondo model [31, 132][1] with excellent agreement (non-universal effects are not encountered for the field strengths shown).

In the case of the 2LM the quantum phase transition studied throughout chapters 4 and 5 between the USC and FL phase is destroyed for any finite field — it is replaced by a smooth crossover, as we demonstrate shortly. In terms of the fixed

[1] We have only compared to the exact results for $h/T_K^{S=1} > 1$. Equations given in refs. [31, 132] for the case $h/T_K^{S=1} < 1$ are contradictory, and each appears to be wrong.

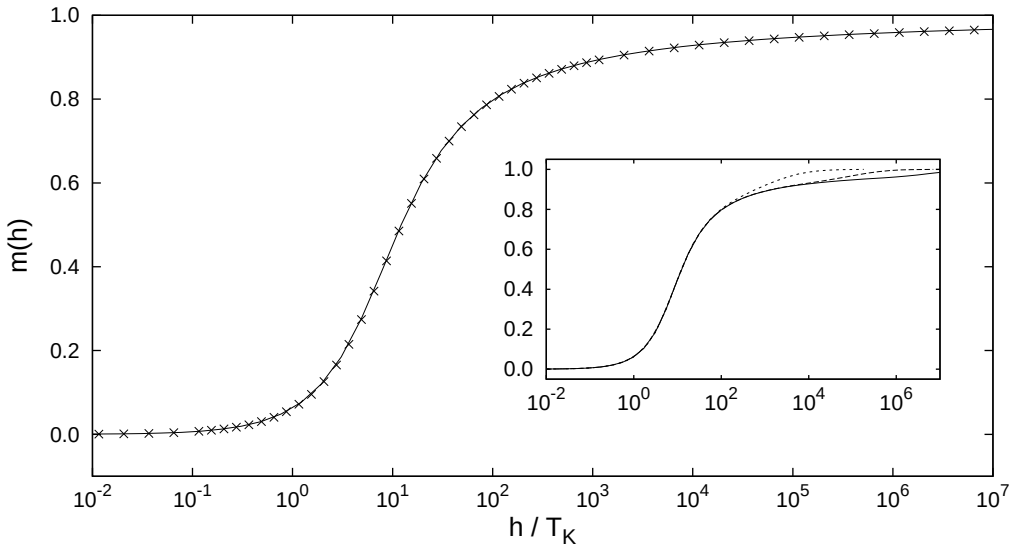

Figure 6.1: Magnetization of the AIM vs. h/T_K for $\tilde{U} = -2\tilde{\epsilon} = 50$. Comparison between FDM-NRG results (crosses) calculated via (6.2), and the Bethe ansatz result for the Kondo model (line) [31, 132]. *Inset*: $\tilde{U} = -2\tilde{\epsilon} = 30$ (solid), 20 (long dash), and 10 (short dash) corresponding to $T_K/\Gamma = 1.8\times10^{-6}$, 8.0×10^{-5}, and 3.1×10^{-3}. Deviations from universality occur for $h \gtrsim \mathcal{O}(\Gamma)$.

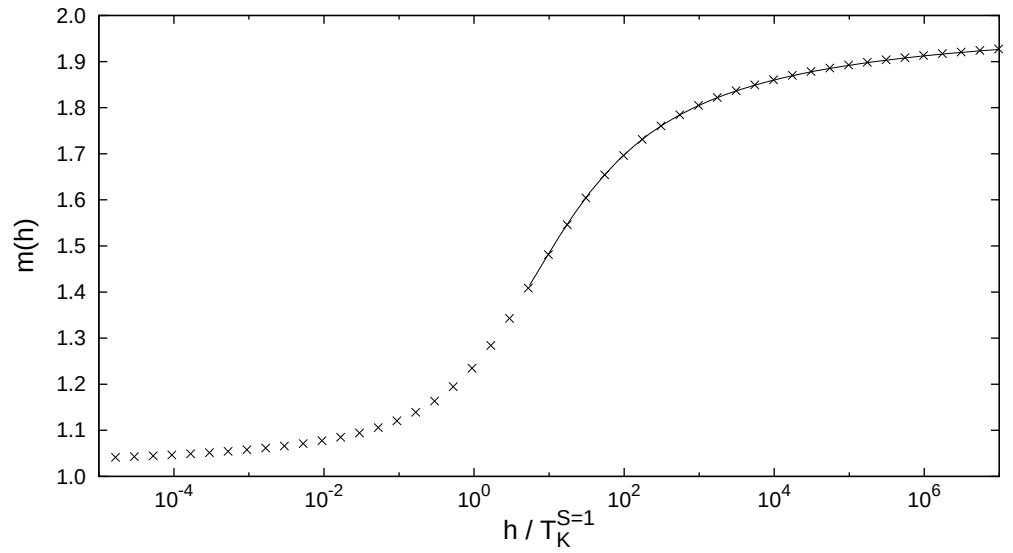

Figure 6.2: The universal magnetization $m(h) = m_1(h) + m_2(h)$ scaling curve for the 2LM at particle-hole symmetry. Numerical FDM-NRG results (crosses) are shown for $\tilde{U} = 40$, $\tilde{U}' = 0$, and $\tilde{J}_H = 10$. We are only able to compare with the high field Bethe ansatz results (line) [31, 132]. A form distinct from that for the single-level AIM is found. In the limit $h \to 0$ a non-zero magnetization results from full polarization of the spin-$\frac{1}{2}$ local moment associated with the underscreened impurity.

point structure of the renormalization group, the breaking of spin symmetry associated with a non-zero magnetic field renders the USC fixed point unstable for all $h \neq 0$. All NRG flows therefore tend toward a Fermi liquid, strong coupling fixed point, with spin-dependent potential scattering. We study now this crossover.

The total impurity magnetization $m(h)$ in the 2LM as the $h = 0$ quantum phase transition is crossed in the $\epsilon_1 - \epsilon_2$ plane is shown in fig. 6.3a). We choose $\tilde{U} = 2\tilde{U}' = 4\tilde{J}_H = 20$ and fix $\epsilon_1 = -\frac{1}{2}U - U'$ (*i.e.* its value at the particle-hole symmetric point, $x = \epsilon_1 + \frac{1}{2}U + U' = 0$) and increase ϵ_2 (or $y = \epsilon_2 + \frac{1}{2}U + U'$) away from its particle-hole symmetric value. Along this trajectory the zero-field transition from the USC phase to the FL phase occurs at a critical $\tilde{\epsilon}_{2,c} \simeq -9.94$. Curves i) to iii) correspond to $\epsilon_2 < \epsilon_{2,c}$ and hence the USC phase at $h = 0$. As in fig. 6.2, the magnetization rises monotonically from the zero field limit $m(h \to 0) = 1$ on the scale $h \sim T_K^{S=1}$, crossing over towards $m(h) = 2$ as the field destroys the underscreened Kondo effect and singles out the $S_z = +1$ component of the dot triplet state. On moving away from the particle-hole symmetric point, section 4.3 showed how the spin-1 Kondo scale increases (see *e.g.* fig. 4.5), explaining the higher field required to destroy the underscreened Kondo effect for iii) compared to i).

For larger level separations, $\epsilon_2 > \epsilon_{2,c}$ [lines iv)-viii)], the system possesses a Fermi liquid ground state at zero field. Here the low-field behaviour more closely resembles that of fig. 6.1. At zero-field the impurity is fully screened by the conduction band, and remains essentially so until $h \sim T_K$. Above this field strength the spin-$\frac{1}{2}$ Kondo effect is progressively destroyed and $m(h)$ crosses over to $m(h) \sim 1$ associated with a spin-polarized $S = \frac{1}{2}$ impurity state. As in the cases i)-iii), further increasing the field causes a second marked increase in $m(h)$ when the $S_z = +1$ components of the two-electron triplet state is favoured.

Figure 6.3b) shows the magnetization at various fixed values of the field as a function of ϵ_2 in the vicinity of the zero field transition at $\epsilon_{2,c}$ (indicated by the dotted vertical line). At any finite field the magnetization decreases monotonically with increasing $\tilde{\epsilon}_2$. In the limit $h \to 0$ the curve approaches the step function $m(\epsilon_2) \to \theta(\epsilon_{2,c} - \epsilon_2)$ [56]. Again we stress that in the absence of a field the magnetization vanishes, and hence the limit $h \to 0$ and the specific case of $h = 0$ are quite distinct.

In sections 4.3 and 5.3 we showed that the universal scaling forms of the impurity entropy (as a function of temperature) and single-particle spectra (as a function of frequency) are in pratice essentially independent of the system asymmetry $\eta(x, y)$, defined in (4.14), the ratio of the potential scattering K to the Kondo coupling $J_K^{S=1}$. We now show that a similar situation arises for the form of the magnetization as a function of the field strength. Figure 6.4 examines the scaling form of the magnetization in the 2LM away from particle-hole symmetry. In the inset to fig. 6.4 we consider the line $y = -x$, for all points on which $\eta(x, y) = 0$ [(4.13) and (4.14)]

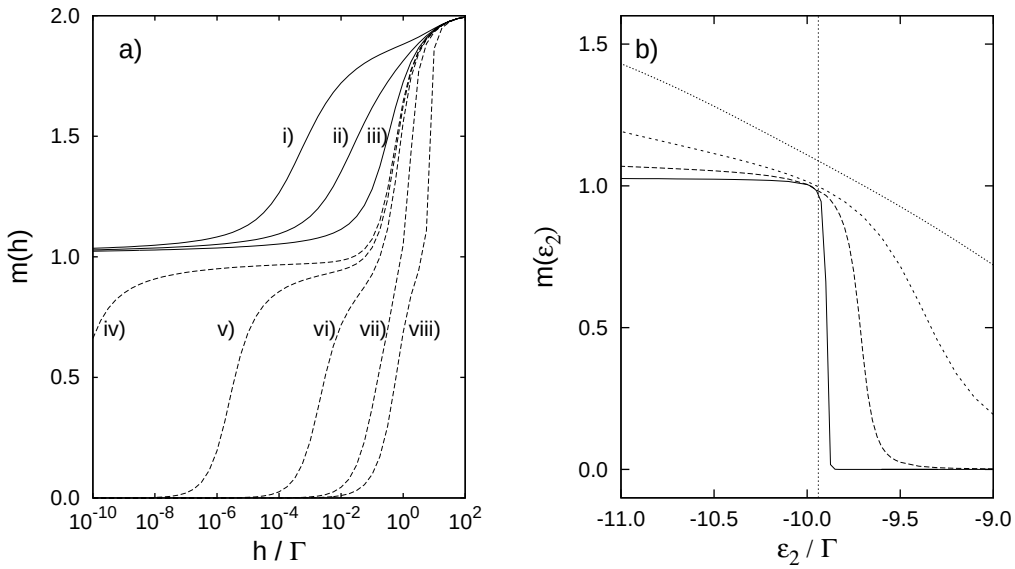

Figure 6.3: a) Total magnetization $m(h) = m_1(h) + m_2(h)$ of the 2LM with $\tilde{U} = 2\tilde{U}' = 4\tilde{J}_H = 20$, $\tilde{\epsilon}_1 = -\frac{1}{2}\tilde{U} - \tilde{U}' = -20$, and i) $\tilde{\epsilon}_2 = -20$, ii) -12, iii) -10.5, iv) -9.9, v) -9.8, vi) -9.5, vii) -8, and viii) -2. At zero-field i)-iii) correspond to the USC phase of the model. A clear distinction is seen between these three curves and the cases iv)-viii) in which at zero-field the system is in the FL phase. The results mirror those found for $S_{\rm imp}(T)$ found in section 4.3. b) Magnetization near the crossover for $h/\Gamma = 10^{-10}$ (solid), 10^{-4} (long dash), 10^{-2} (short dash), and 10^{-1} (dotted). The $h = 0$ transition is marked by a vertical line at $\tilde{\epsilon}_{2,c} \simeq -9.94$. For $h \to 0$ the magnetization jumps discontinuously at $\tilde{\epsilon}_{2,c}$, while for finite fields this step is smeared.

and hence there is no potential scattering. We show universal results for $x = 0 = -y$ (line), compared to that obtained some distance away from the particle-hole symmetric point at $x = -6\Gamma = -y$. The two scaling curves clearly coincide.

The main panel of figure fig. 6.4 illustrates universality for non-vanishing asymmetry, showing $m(h)$ vs. $h/T_K^{S=1}$ for $\tilde{U} = 2\tilde{U}' = 4\tilde{J}_H = 30$ (solid), 20 (long dash), and 15 (short dash), and for $\eta(x) = 0$ and $\eta(y) = 0.5$ in all cases [*i.e.* $\eta(x, y) \simeq 0.29$]. The three curves scale perfectly in the universal regime, beginning to deviate only at high fields $h \sim \mathcal{O}(\Gamma)$. Moreover the resultant universal $m(h)$ is found numerically to be identical to that arising for $\eta(x, y) = 0$ (crosses), and as such thus appears to be *independent* of the asymmetry $\eta(x, y)$; a result we have further confirmed for a wide range of η-values.

Before moving to consider field dependent dynamic properties, we present one final result for the impurity magnetization. Previously in section 5.3.1 we saw how it was useful to think it terms of even and odd combinations of the impurity orbitals. To that end, fig. 6.5 compares results for the even and odd channel magnetizations $m_e(h)$ and $m_o(h)$ [such that $m(h) = m_e(h)+m_o(h)$] in the case $\tilde{U} = 2\tilde{U}' = 4\tilde{J}_H = 20$. The odd orbital is clearly polarized to a greater extent than the even orbital by an

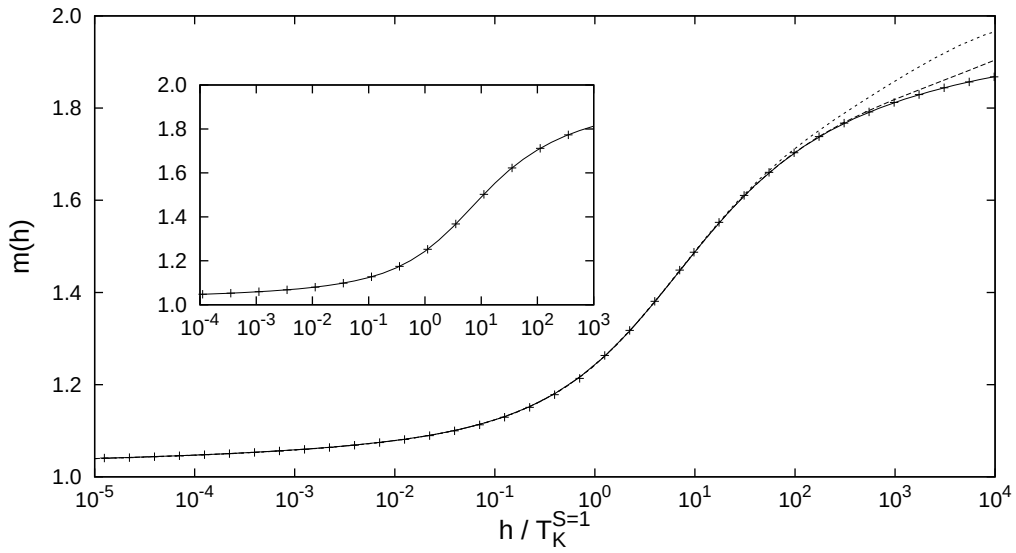

Figure 6.4: Magnetization away from the particle-hole symmetric point, deep in the USC phase, for $\tilde{U} = 2\tilde{U}' = 4\tilde{J}_H = 30$ (solid), 20 (long dash), and 15 (short dash), corresponding to $T_K^{S=1}/\Gamma = 1.0 \times 10^{-6}$, 7.7×10^{-5}, and 6.8×10^{-4} respectively. We maintain $\eta(x) = 0$ and $\eta(y) = 0.5$. The results show the same scaling form as at particle-hole symmetry (crosses). *Inset*: Results along the line $y = -x$ in the $\tilde{U} = 30$ for $x = 0$ (line) and -6Γ (crosses). Universal results are again found, *i.e.* the universal scaling form is independent of $\eta(x, y)$.

infinitesimal field, and $m_o(h)$ reaches saturation more quickly that either $m_e(h)$ or $m_1(h)$. This reflects the fact that the odd orbital does not couple directly to the conduction band, only interacting with it via the even orbital (section 5.1). The odd orbital as such contributes more to the local moment of the underscreened impurity than the even orbital.

This concludes our brief survey of the static field-dependent properties of the AIM and 2LM. In the latter case a magnetic field renders the USC fixed point unstable. Systems which would otherwise have an underscreened local moment ground state described by the USC fixed point, flow to a Fermi liquid strong coupling fixed point on an energy scale $\mathcal{O}(h)$.

6.2 Field dependent dynamics

We turn now to the field dependence of the single-particle dynamics for the AIM and the 2LM. Much is already known [115, 125–131] about the former case, but it serves as a useful comparison to the 2LM and both are experimentally relevant, as we shall see in section 6.3. The spin-resolved impurity spectrum is first considered, with a two-fold focus: the field-induced redistribution of weight in the Hubbard satellites, and the shift of the spectral maximum from zero.

Figure 6.6 shows results for the spectral density $D_{ee;\downarrow}(\omega)$ of the 2LM (main

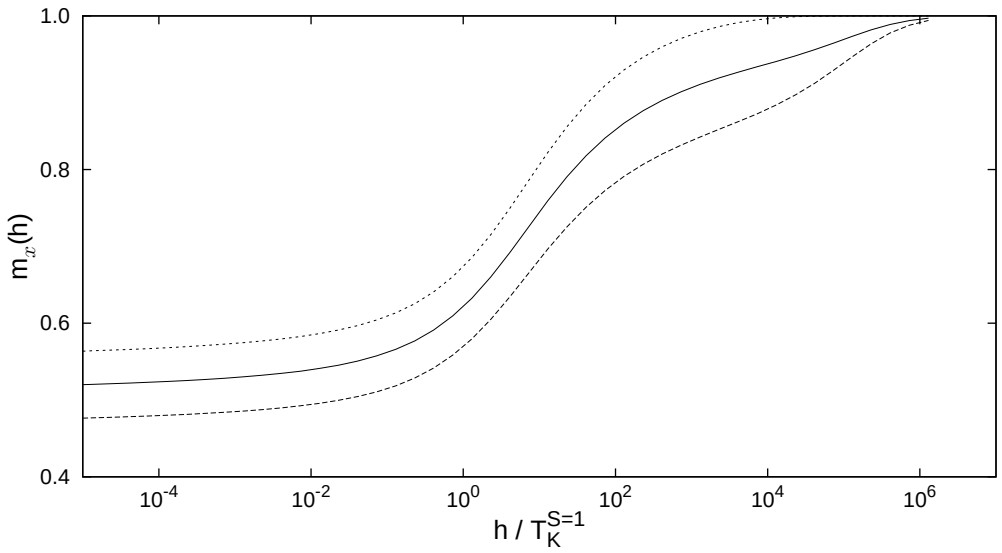

Figure 6.5: Comparison of the magnetization in the even and odd impurity channels at particle-hole symemtry for $\tilde{U} = 2\tilde{U}' = 4\tilde{J}_H = 20$. The odd orbital (short dash) contributes more to the impurity local moment than does the even orbital (long dash). Consequently $m_o(h)$ reaches saturation more quickly than $m_e(h)$ or indeed $m_1(h)$ (solid).

figure) and $D_{11;\downarrow}(\omega)$ for the AIM (inset), for a range of fields strengths. In both cases we show results deep in the Kondo regime, and at particle-hole symmetry such that $D_\uparrow(\omega;h) = D_\downarrow(-\omega;h)$. In each case the familiar three peak structure is evident: upper and lower Hubbard satellites due to local charge excitations on the impurity, and a central low energy Kondo resonance. As in section 5.4 we denote the half-width at half-maximum of the $h = 0$ Kondo resonance by ω_K ($\equiv \omega_K^{S=1}$ for the 2LM in the USC phase).

In both cases, increasing the applied field causes spectral weight to be redistributed from the lower to the upper Hubbard satellite, corresponding to a destabilisation of $\downarrow$-spin electrons on the dot. The striking difference between the two is that for the 2LM (main figure), a significant redistribution occurs upon introducing an infinitesimal field (*e.g.* $h/\omega_K^{S=1} \sim 1 \times 10^{-6}$), whereas for the AIM this occurs only when $h/\omega_K \sim \mathcal{O}(1)$ (inset). This reflects directly the behaviour of the magnetization in fig. 6.3 [see (6.2)]: the free spin associated with the USC fixed point is fully polarized by an infinitesimal field, while a finite $h \sim \omega_K$ is required to disrupt the Kondo singlet associated with the strong coupling fixed point of the AIM.

6.2.1 The Kondo peak: universality and the 'Zeeman' splitting

The high-frequency behaviour is then relatively easy to understand and is readily interpretable in terms of the total magnetization. We consider now the more complex behaviour arising on lower energy scales $\omega \sim \omega_K$. The low-frequency behaviour of

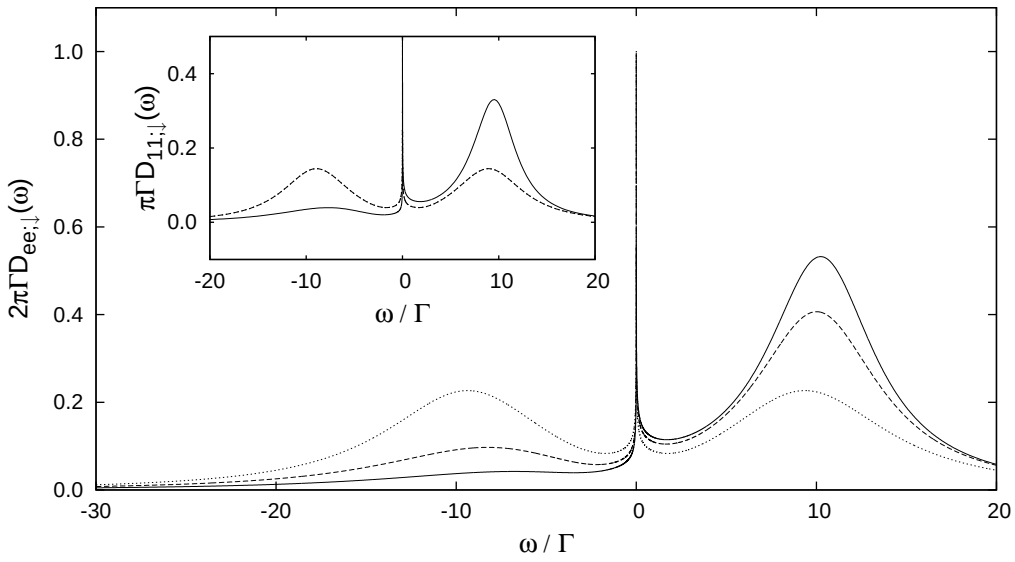

Figure 6.6: Redistribution of spectral weight in the Hubbard bands for the 2LM with $\tilde{U} = 2\tilde{U}' = 4\tilde{J}_H = 20$ at particle-hole symmetry with $h/\omega_K^{S=1} = 0$ (dotted), 1×10^{-6} (dashed) and 1 (solid). Even at the smallest field strength significant redistribution occurs. *Inset*: Analogous results for the AIM with $\tilde{U} = 20$. The result for $h/\omega_K = 1 \times 10^{-6}$ is coincident with that for $h = 0$.

the AIM spectrum in a magnetic field has received significant attention using various techniques [115, 125–131], yet there is still some disagreement in the literature. Here we present results from accurate FDM-NRG calculations, with the aim of clarifying the issue.

At zero field the Kondo resonance at particle-hole symmetry is centered on $\omega = 0$ and is symmetric upon reflection about this point. The zero-frequency value obeys the Friedel sum rule [20, 113]: $\pi\Gamma D_{11;\sigma}(\omega = 0) = 1$. Introduction of a finite field h is well known to shift the resonance in $D_{11;\sigma}(\omega; h)$ away from the Fermi level and diminish its height [127]. We define Δ_σ as the magnitude of this shift as illustrated in the inset to fig. 6.7.

The spin-summed spectra $D_{11}(\omega; h) = \frac{1}{2}\Sigma_\sigma D_{11;\sigma}(\omega; h)$ is distinct from the individual spin resolved spectra, since the $\sigma = \uparrow$ and $\downarrow$ Kondo resonances are shifted in opposite directions by the field. At sufficiently high fields, the two resonances are far apart and $D_{11}(\omega; h)$ contains two peaks separated by 2Δ (defined also in the inset to fig. 6.7). As h is reduced these peaks approach each other and are known [127] to coalesce at a field we denote h_c. Our FDM-NRG calculations yield a universal value $h_c \simeq 0.27\omega_K$ in the Kondo scaling regime ($U/\Gamma \gg 1$). In terms of the quasiparticle weight $Z = [1 - \partial\Sigma_{11}(\omega = 0)/\partial\omega]^{-1}$ [20], easily extracted from FDM-NRG results for the self-energy $\Sigma_{11}(\omega)$, we obtain $h_c \simeq 0.40Z\Gamma$. This is in good agreement with the exact result $h_c/Z\Gamma = 0.39...$ [96].

Accurate FDM-NRG calculations for both Δ_σ/h and Δ/h in the Kondo regime

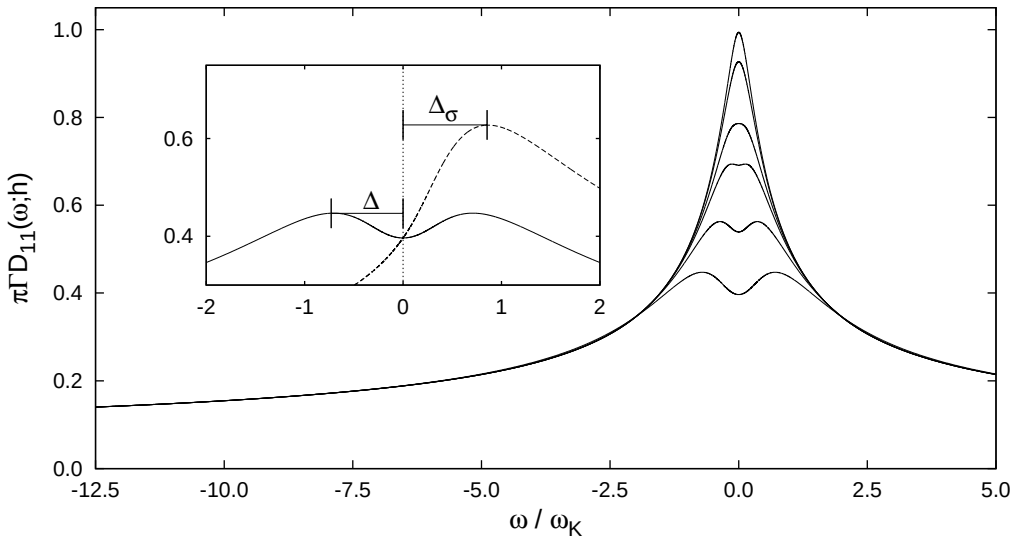

Figure 6.7: Kondo resonance splitting in the spin-summed spectrum $D_{11}(\omega;h)$ for the AIM at particle-hole symmetry with $\tilde{U} = 20$ on application of a magnetic field $h/h_c = 0$, 1/2, 1, 4/3, 2, and 3 (top to bottom respectively), with $h_c = 0.27\omega_K$ the peak coalescence point. *Inset*: Kondo peaks in $D_{11}(\omega;h)$ (solid) and $D_{11;\downarrow}(\omega;h)$ (dashed).

of the AIM are presented in fig. 6.8, as a function of h/ω_K. Before discussing these results it is worth explaining the procedure used to obtain results over the full range of h/ω_K. We find that to calculate Δ_σ and Δ over the large range of h/ω_K shown, it is necessary to combine results for different values of $\tilde{U}$ (and so ω_K). For a given $\tilde{U}$ one cannot obtain universal results for arbitrarily high h/ω_K because universality arises only when h is much smaller than the other non-universal scales Γ and U. Since ω_K is small but finite for a given $\tilde{U}$, there will always be a value of h/ω_K for which h itself becomes comparable to the non-universal scales and then the results deviate from universality.

Since ω_K *decreases* exponentially with increasing $\tilde{U}$, this might suggest working with a very large $\tilde{U}$, for then one can reach very high values of h/ω_K before h itself becomes non-universal. However this is subject to a second problem, at the opposite end of the field scale. The energies that enter the Hamiltonian involve combinations of h, U, and Γ. The double precision arithmetic used in the NRG thus places a lower limit on the size of h relative to U and Γ. If ω_K is too small, then low values of h/ω_K shift the dot energy levels by so little that they cannot be accurately represented in double precision.[2]

For a given $\tilde{U}$ there is therefore a range of fields encompassing in practice around 4-5 orders of magnitude, over which universal scaling behaviour can be observed by the NRG. By combining results for different values of $\tilde{U}$ the full scaling curve can be

[2]The accumulation of numerical errors during the iterative NRG procedure can further limit the practical range of h.

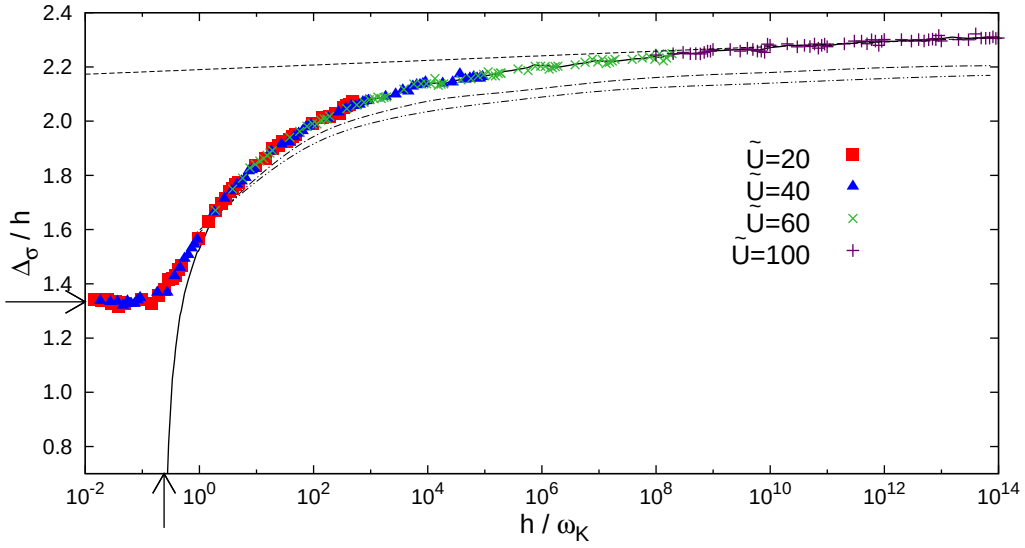

Figure 6.8: Universality in the field-dependence of the spectral maximum Δ_σ in $D_{11;\sigma}(\omega;h)$ for the particle-hole symmetric AIM. Horizontal arrow indicates the exact low-field asymptote $\Delta_\sigma/h = 4/3$. The dashed line shows the high field form $a\log(h/\omega_K)+c$. The position of the maxima in the spin-summed spectra $D_{11}(\omega;h)$ (Δ, solid) approaches h_c (vertical arrow) at low field strength. At high fields we find $\Delta \to \Delta_\sigma$.

built up, and by choosing $\tilde{U}$s appropriately results of the calculations may overlap such that one can obtain a measure of the accuracy of the calculation.

The points in fig. 6.8 show results for $\Delta_\sigma(h)/h$ obtained from a series of FDM-NRG calculations with $\tilde{U} = 20$, 40, 60, and 100. Results for different values of $\tilde{U}$ indeed overlap when plotted as a function of h/ω_K, indicating universal scaling behaviour. At low field we recover the exact result, $\Delta_\sigma/h \to 4/3$ as $h \to 0$, known from Fermi liquid theory [129, 133]. The splitting Δ_σ/h increases with h/ω_K, undergoing a rapid crossing around $h/\omega_K \sim 1$ and tending asymptotically to the limiting form $\Delta_\sigma/h \sim a\log(h/\omega_K) + c$. This latter behaviour agrees with results obtained from the local moment approach [129].

The low-h/ω_K behaviour of the points in fig. 6.8 appears to be numerically exact. Repeating the calculations more accurately does not affect the basic result.[3] However, as the field (and hence location of the spectral maximum) increases further, we find it increasingly difficult to obtain accurate results for Δ_σ. This is a direct consequence of the logarithmic discretization used within the NRG: sharp spectral features away from the Fermi level ($\omega = 0$) cannot be accurately resolved. The problem can be resolved to some extent by using the 'z-trick' [84] (section 3.5), and calculating the impurity self-energy [81] (section 3.5.1). In fig. 6.8 the points were obtained by averaging results over 10 separate logarithmic discretizations (10 values

[3] Clearly some scatter is observed in the data: this is to be expected, broadening of the discrete FDM-NRG spectra results naturally in a finite uncertainty in the peak position.

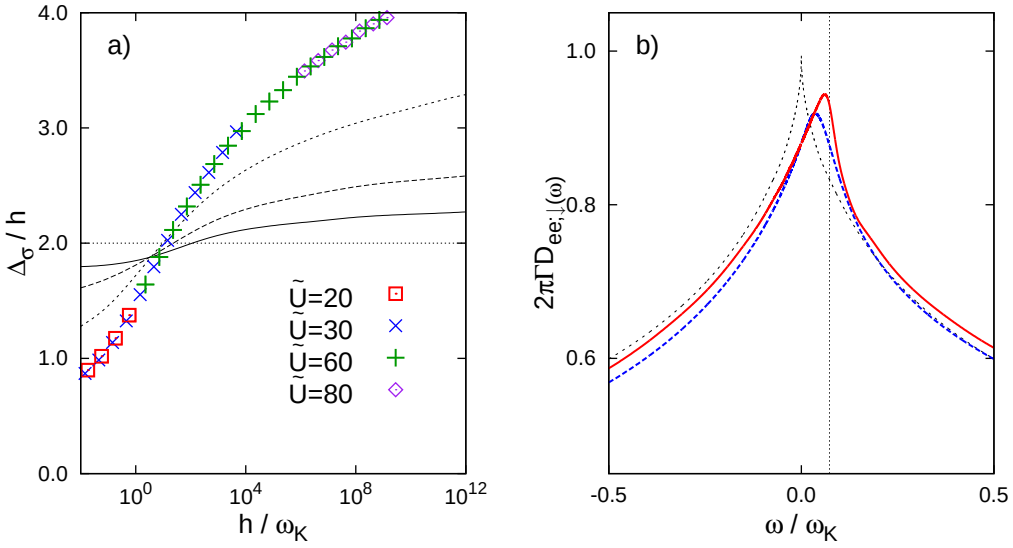

Figure 6.9: a) Field induced shift of the underscreened Kondo resonance in the particle-hole symmetric 2LM, with $\tilde{U} = \tilde{U}' = \tilde{J}_H$. Results appear to converge to $\Delta_\sigma/h = 2$ for all $h/\omega_K^{S=1}$ as the NRG spectral broadening parameter is reduced: $b = 0.7$ (points), 0.4 (short dash), 0.2 (long dash), and 0.1 (solid). b) Representative example of the spectrum $D_{ee;\downarrow}(\omega; h)$ for $h = 0$ (short dash) and $h/\omega_K^{S=1} = 0.366$ with two different broadening parameters $b = 0.2$ (solid red) and 0.7 (dashed blue). The point $\omega = 2h$ is marked by a vertical line.

of the parameter z, section 3.5), with a broadening parameter $b = 0.1$ [see (3.25)]. Increasing the number of zs to 20 and working with $b = 0.07$ and 0.05 (*i.e.* narrower broadening of the discrete spectra) gives the dot-dashed and dot-dot-dashed lines. One might speculate that a high-field limit $\Delta_\sigma/h = 2$ is reached, although we believe the available data do not support this: in each case the qualitative form is the same slow logarithmic increase. An adaptive grid of the kind proposed in ref. [134] could in principle aid further clarification of this issue.

Figure 6.9a) shows analogous results for the spectral shift in $D_{ee;\sigma}(\omega; h)$ for the 2LM at particle-hole symmetry, and hence USC phase for $h = 0$. In this case we find the results to be even more sensitive to the broadening procedure — likely due to the sharp, cusp-like nature of the spin-1 Kondo resonance (see *e.g.* the $h = 0$ case (short dash) in fig. 6.9b)]. The points show the splitting obtained from averaging 10 zs with $b = 0.7$, using four different values of U/Γ as before. Also shown are results for 20 zs and $b = 0.4$ (short dash), 0.2 (long dash), and 0.1 (solid). As the accuracy of the calculation increases the splitting appears to be approaching $\Delta_\sigma/h = 2$ *for all* h, in marked contrast to the behavior of the AIM in fig. 6.8.

As an example of this apparent behaviour, fig. 6.9b) shows $D_{ee;\downarrow}(w; h)$ for a representative low-field case $h/\omega_K^{S=1} \simeq 0.0366$. We compare results obtained for $b = 0.7$ (dashed blue) and 0.2 (solid red). The figure clearly illustrates the sensitivity of the finite-h spectrum to the value of b employed. In line with the conjecture above

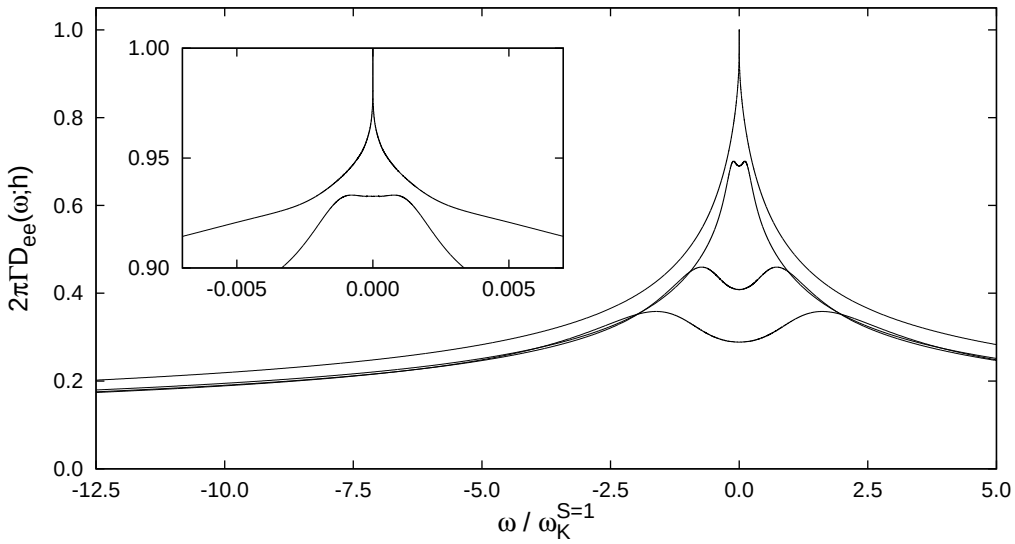

Figure 6.10: The spin-summed spectral density $D_{ee}(\omega;h)$ in the 2LM for $U = 2U' = 4J_H = 30$ at particle-hole symmetry and for $h/\omega_K^{S=1} = 0$, 0.1, 0.5, and 1 ($\omega_K^{S=1}/\Gamma = 2.06 \times 10^{-5}$). The finite frequency peaks are well resolved, having a form reminiscent of $D_{ee;\downarrow}(\omega;h)$. *Inset*: Zero-frequency minima can be observed for all finite fields, here we show $h = \omega_K^{S=1}/1000$, as well as $h = 0$.

it appears that in the limit $b \to 0$ the peak position would lie at $2h$ (marked by a vertical line in the figure). The shape of these finite-h peaks is reminiscent of the $h = 0$ case (as shown by the short dashed line in fig. 6.9b)) studied in chapter 5. It is reasonable to believe that the $h \neq 0$ spectrum should have a qualitatively similar form to the $h = 0$ case, albeit shifted in frequency such that its peak occurs at $\omega = 2h$. Due to the logarithmic discretization used in the NRG, centered on the Fermi level ($w = 0$), it is not possible to confirm or refute this using the techniques employed here.

As a corollary to the above behaviour we examine the spin-summed spectrum $D_{ee}(\omega;h) = \frac{1}{2}\Sigma_\sigma D_{ee,\sigma}(\omega;h)$ in fig. 6.10, analogous to the AIM results in fig. 6.7. From the previous analysis of Δ_σ in the two models above, one might expect that Δ should be larger for the 2LM at comparable fields, and indeed this is the case. Further, it appears that the peaks do not coalesce for any finite h: an example is shown in the inset to fig. 6.10 where a minimum is observed at $\omega = 0$ for $h = \omega_K^{S=1}/1000$. We again take this to be a remnant of the sharp cusp-like nature of the $h = 0$ spectrum discussed previously in section 5.3, and the similarly sharp peaks observed for finite fields [fig. 6.9b)]

In ref. [129] the low field-limit for Δ_σ in the AIM, was found through the Dyson equation by using low frequency Fermi liquid results [20] for the impurity self-energy $\Sigma_{11;\sigma}(\omega;h) = \Sigma^R_{11;\sigma}(\omega;h) - i\Sigma^I_{11;\sigma}(\omega;h)$. To understand the results of fig. 6.9 we might wish to try a similar approach for the 2LM. Figure 6.11 indicates

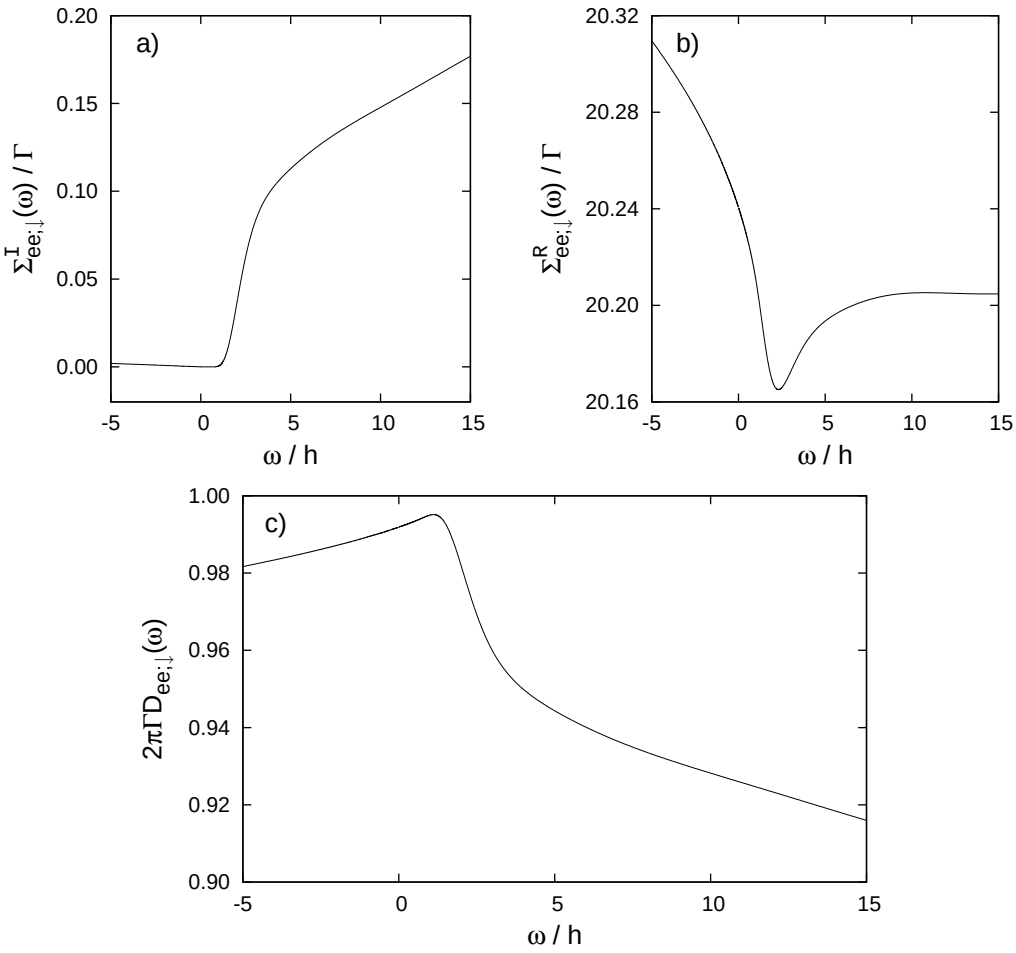

Figure 6.11: Representative examples of the a) imaginary and b) real parts of the impurity self-energy $\Sigma_{ee;\downarrow}(\omega) = \Sigma^{R}_{ee;\downarrow}(\omega) - i\Sigma^{I}_{ee;\downarrow}(\omega)$. The rather complicated form of the self-energy around $\omega = h$ makes it exceedingly difficult to find a low-frequency expansion that captures correctly Δ_σ in the spectra, c).

that finding the required expansion would be a difficult task. We show results for the self-energy $\Sigma_{ee;\downarrow}(\omega) = \Sigma^{R}_{ee;\downarrow}(\omega) - i\Sigma^{I}_{ee;\downarrow}(\omega)$ at particle-hole symmetry in the case $\tilde{U} = 2\tilde{U}' = 4\tilde{J}_H = 20$ for $h/\Gamma = 1 \times 10^{-6}$. For this system we find $\omega_K^{S=1}/\Gamma = 1.64 \times 10^{-3}$, much larger than the energy range shown. However, the self-energy clearly has a complicated form on energy scales $\mathcal{O}(h)$. Finding analytically the required expansion would therefore appear to be a formidable task.[4]

In this section we have been concerned purely with the question: how does the *equilibrium spectrum* evolve with magnetic field in single and two-level impurities? Here we have deliberately not related the equilibrium spectrum to the finite-bias conductance, because (5.87) is approximate and (as shown explicitely later in relation to experiments) can give quantitatively wrong results for field strengths in excess of

[4] In fact in attempting to fit numerically determined power law forms to the self-energies, we find it necessary to use terms up to $(\omega/h)^5$ to replicate successfully the observed peak in $D_{ee;\downarrow}(\omega)$.

a few multiples of the Kondo scale [128]. The figures shown here should *not* therefore be translated naively into quantitative predictions of conductance splittings. The only predictions for experiment that we can make with real certainty are those involving the zero-bias conductance, which we discuss now.

6.2.2 Conductance scaling

The temperature and field dependence of the zero bias conductance of a quantum dot system can be calculated exactly within the FDM-NRG, for example via (5.86) for the 2LM. We have seen in section 5.4 a universal scaling form results for $G_C(T; V_{\rm sd} = 0, h = 0)$ vs. $T/\omega_K^{S=1}$, in the 2LM, that is not dissimilar from that of the single-particle spectrum as a function of frequency. We now undertake a brief survey of the field-dependent scaling conductance in both the single-level AIM and the 2LM. The main purpose of this section is to highlight how meaningful comparison with experimental results and exact theoretical results can be made.

We begin in fig. 6.12 with results for the zero-bias conductance of the AIM, as functions of h/ω_K and T/ω_K. We consider specifically the case of particle-hole symmetry for $\tilde{U} = 30$ (red), 20 (blue), and 15 (green). These values of $\tilde{U}$ give $\omega_K/\Gamma = 4.81 \times 10^{-5}$, 2.1×10^{-3}, and 1.3×10^{-2} respectively. For fixed h/ω_K (the values 0, 0.1, 0.3, 1, and 10 are shown explicitely) the zero-bias conductance $G_C(T; V_{\rm sd} = 0, h)$ is seen to be universal in T/ω_K, as evident from the clear scaling collapse of the different $\tilde{U}$ curves. The scaling behaviour naturally breaks down at non-universal scales $T \sim \min(\Gamma, U)$, and for $T \sim U$ the curves show clear peaks associated with incoherent sequential tunneling (as seen previously for the 2LM in section 5.4).

We will discuss the zero-temperature limit of these curves shortly. First we note that at finite temperature, for $h/\omega_K \gtrsim 0.3$ there is a universal peak in the zero-bias conductance at a temperature $T \sim h$ [127]. This is analogous to the peak at finite frequency in the $T = 0$ equilibrium spectrum, discussed in the section 6.2.1. Of further interest is that here the peak exists in a quantity that is directly measurable by experiment — measuring the zero-bias conductance of a quantum dot device at the centre of a Coulomb blockade valley (such that particle-hole symmetry results), as a function of temperature and magnetic field, should yield results similar to those of fig. 6.12.

The inset to fig. 6.12 shows an alternative way of viewing the universal conductance curves. We now fix T/ω_K (at the same values of h/ω_K used above) and vary the magnetic field over many orders of magnitude. Notice there is no incoherent peak at large h, in contrast to the T-dependence for fixed h. This is to be expected: for large fields the impurity is completely spin polarized — addition of a $\downarrow$-spin electron to the impurity (which contains already an $\uparrow$-spin electron) does not occur due

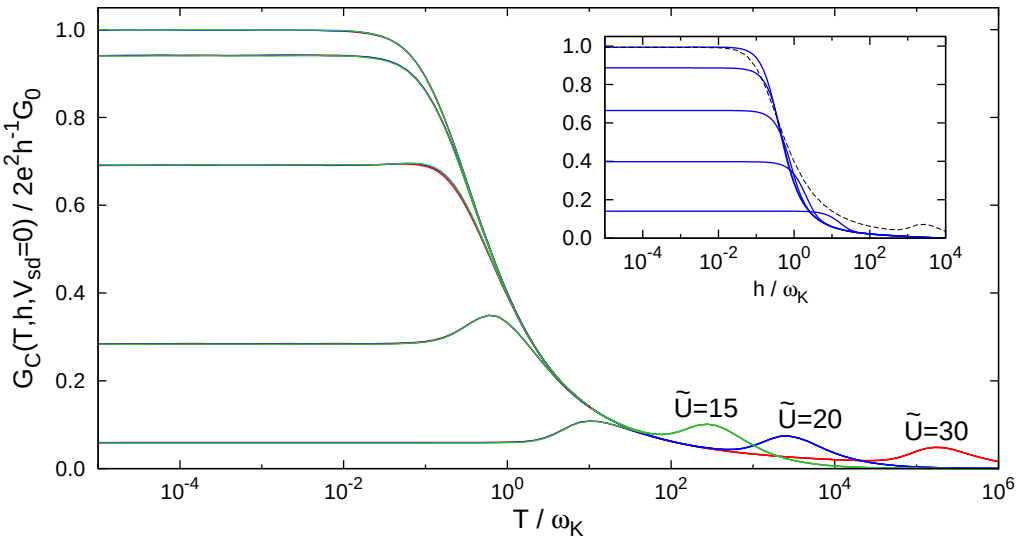

Figure 6.12: Scaling of the zero-bias conductance for the particle-hole symmetric AIM at finite temperature and field shown for $h/\omega_K = 0$, 0.1, 0.3, 1, and 10 (top to bottom) with $\tilde{U} = 30$ (red), 20 (blue), and 15 (green); the zero-field Kondo scale for these parameters being $\omega_K/\Gamma = 4.81 \times 10^{-5}$, 2.06×10^{-3}, and 1.32×10^{-2}. A peak occurs on a scale $T \sim \mathcal{O}(h)$ for $h \gtrsim 0.3\omega_K$. *Inset*: The zero-bias conductance now as a function of h/ω_K for $\tilde{U} = 20$ and $T/\omega_K = 0$, 0.1, 0.3, 1, and 10. The zero-field result as a function of T/ω_K (dashed) is shown for comparison.

to the prohibitively high energy $\epsilon_{i\downarrow}$. The conductance is therefore weak.

Figure 6.13 shows analogous results for the 2LM, again at particle-hole symmetry and for three sets of the impurity interactions $\tilde{U} = 2\tilde{U}' = 4\tilde{J}_H$. Universal finite-temperature peaks are seen in this case for $h \sim \omega_K^{S=1}$, and should be seen in experiments displaying an underscreened Kondo effect. However, the peaks appear less pronouced than in the case of the AIM, indicating that they may be more difficult to detect in spin-1 quantum dots than spin-$\frac{1}{2}$ dots. The inset to fig. 6.13 shows that in parallel to the AIM, again no incoherent tunneling peak is seen when the field dependence of the zero-bias conductance is examined.

Zero-bias, zero-temperature conductance

Before moving to examine experimental results, we consider now the zero-temperature limit of the conductance as shown in figs. 6.12 and 6.13. At zero temperature the zero-bias conductance is, from (5.86), entirely equivalent to the zero-frequency value of the appropriate single particle density: $\pi\Gamma D_{11}(\omega = 0)$ for the AIM and $2\pi\Gamma D_{ee}(\omega = 0)$ for the 2LM. We now generalize the analysis of section 5.2 to the case of broken spin symmetry in the 2LM.

To start we define the spin-dependent static impurity phase shift [113] via

$$2\pi\Gamma D_{ee;\sigma}(0;h) = \sin^2 \delta_\sigma \tag{6.3}$$

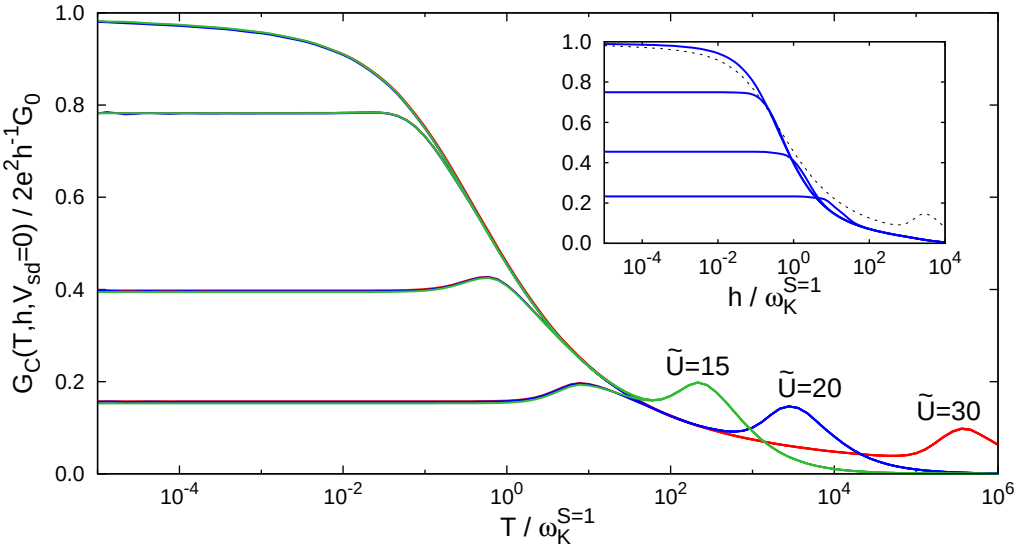

Figure 6.13: Analogous to fig. 6.12, zero-bias conductance scaling in the 2LM at particle-hole symmetry for $h/\omega_K = 0$, 0.1, 1, and 10 (top to bottom) with $U = 2U' = 4J_H$ and $\tilde{U} = 30$ (red), 20 (blue), and 15 (green) corresponding to $\omega_K^{S=1}/\Gamma = 2.06 \times 10^{-5}$, 1.64×10^{-3}, and 1.47×10^{-2}. *Inset*: The zero-bias conductance now as a function of $h/\omega_K^{S=1}$ for the $\tilde{U} = 20$ case and $T/\omega_K^{S=1} = 0$, 0.1, 1, and 10; the zero-field result as a function of T/ω_K (dashed) again shown for comparison.

with separate phase shifts for $\sigma =\uparrow,\downarrow$ of the form [*cf.* (5.38)]:

$$\delta_\sigma(0) = \pi n_{\mathrm{imp},\sigma} + I_{L\sigma}, \tag{6.4}$$

where

$$I_{L\sigma} = \mathrm{Im\,Tr} \int_{-\infty}^{0} \frac{\partial \mathbf{\Sigma}_\sigma(\omega)}{\partial \omega} \mathbf{G}_\sigma(\omega)\, \mathrm{d}\omega \tag{6.5}$$

is the now spin-dependent Luttinger integral. Now, the result of (5.26) holds in each spin channel separately and so we can write [via (5.86)]:

$$\begin{aligned} \frac{G_C(T=0;V_{\mathrm{sd}}=0)}{(2e^2/h)G_0} &= 2\pi\Gamma D_{ee}(\omega=0;h) \\ &= \frac{1}{2}\Big[\sin^2\delta_\uparrow(0) + \sin^2\delta_\downarrow(0)\Big] \end{aligned} \tag{6.6}$$

As mentioned in section 6.1 the USC fixed point is unstable for any finite field, $h \neq 0$, such that all renormalization group flows terminate at the Fermi liquid, strong coupling fixed point. Since the strong coupling fixed point is characteristic of adiabatic continuity to the non-interacting limit, for any finite h one would expect the two Luttinger integrals $I_{L\sigma}$ to vanish. We have confirmed this by direct calculation via (6.5), with FDM-NRG results for the self-energies and Green functions.

The Luttinger integrals thus change discontinuously (from $|I_{L\sigma}| = \frac{\pi}{2}$ to $I_{L\sigma} = 0$,

section 5.2) on introducing an arbitrarily small magnetic field at any point within the zero-field USC phase. The natural question is what effect does this have on the zero-bias conductance? To answer this we write the phase shifts in terms of the excess impurity charge and the magnetization [56] defined by

$$n_{\rm imp} = n_{{\rm imp},\uparrow} + n_{{\rm imp},\downarrow} \tag{6.7a}$$

$$m_{\rm imp} = n_{{\rm imp},\uparrow} - n_{{\rm imp},\downarrow} \tag{6.7b}$$

(with $n_{\rm imp} \equiv \langle \hat{n}_1 + \hat{n}_2 \rangle$ and $m_{\rm imp} \equiv m_1 + m_2$ in the infinite bandwidth limit). Equations (6.4) and (6.6) then give

$$\frac{G_C(T=0;V_{\rm sd}=0)}{(2e^2/h)G_0} = \frac{1}{2}\Big[\sin^2 \pi n_{{\rm imp},\uparrow} + \sin^2 \pi n_{{\rm imp},\downarrow}\Big] \tag{6.8a}$$

$$= \frac{1}{2}\Big[1 - \cos \pi n_{\rm imp} \cos \pi m_{\rm imp}\Big], \tag{6.8b}$$

for *any* point in the $x-y$ plane of the 2LM when $h > 0$. But from fig. 6.3 we know that the magnetization is finite for even an infintesimal field, $m(h = 0^+) = 1$, for all points in the $x-y$ plane corresponding to the zero-field USC phase. In common with the Luttinger integral, the magnetization therefore jumps discontinuously (from 0 to 1) on introducing even an infinitesimal field. Substituting this result into (6.8) therefore gives the conductance in this limit:

$$\frac{G_C(T=0;V_{\rm sd}=0)}{(2e^2/h)G_0} = \cos^2\left(\frac{\pi n_{\rm imp}}{2}\right) \qquad (h = 0^+). \tag{6.9}$$

This is precisely the result obtained in section 5.2 for the USC phase at zero field [(5.49)]. In other words, although both the Luttinger integrals and magnetization change discontinuously in the USC phase on applying a field — and hence the cases $h = 0$ and $h \to 0$ are very different — the conductance contains no signature of these abrupt changes. A verification of (6.8) is shown later in fig. 6.17.

6.3 Experimental results

In this final section we consider experimental results for the conductance of quantum dot devices at low temperatures and in the presence of a magnetic field. Experimental work has unfortunately not focused on the form of the *zero-bias* conductance as a function of both temperature and field, as in figs. 6.12 and 6.13.[5] Instead work has focused largely [46, 47, 120–123] on the position of field induced finite-bias Kondo peaks in the conductance, analogous to those arising in the single-particle spectra. With the current methods we cannot strictly say anything exact about these

[5] A very recent work, ref. [124], does attempt such a charaterisation of the zero-bias conductance.

features; in the following we are mindful that (5.87) is approximate, and examine the range of parameters for which the approximation appears valid. We begin by attempting quantitative analysis of an experiment performed with a spin-$\frac{1}{2}$ semiconductor device before looking qualitatively at a carbon nanotube device exhibiting both spin-$\frac{1}{2}$ and spin-1 Kondo effects.

6.3.1 Semiconductor quantum dots

The experiments of Liu *et al.* [123] measured the field dependence of the spin-$\frac{1}{2}$ Kondo effect in a GaAs device. The experiment compared two realizations of a quantum dot, referred to as configurations I and II, generated in a single device. The configurations differed only in the magnitude of the dot-lead tunnel couplings.

The simplest possible model able to describe the physics occurring in a quantum dot with spin $\frac{1}{2}$ is of course the AIM. At $T = 0$ the equilibrium model is characterised by the two dimensionless parameters U/Γ and ϵ_1/Γ, with the experimental $U = 1.4$ meV [123]. As in section 5.4.1 we take the level energy to depend linearly on the applied gate voltage and so write $\epsilon_1 + U/2 = \alpha e \delta V_g$, with δV_g the gate voltage measured relative to its value at the centre of the Coulomb blockade valley (the particle-hole symmetric point of the AIM). The parameter α is a dimensionless constant. Comparison of finite-bias features requires also the specification of the dimensionless parameter λ controlling the partitioning of the source-drain bias $V_{\rm sd}$ (section 5.4).

The values of U/Γ and α appropriate to experiment can in principle be obtained by comparing experimental curves for T_K as a function of δV_g, as plotted in fig. 6.14a), to results gathered from the NRG for different values of U/Γ. However, the range of experimental data available is insufficient to pin down the value of U/Γ with the required accuracy — the experimental data can be fit with various combinations of U/Γ and α. We have therefore used all the available experimental data to parameterize the model, choosing the best values of U/Γ, α, and λ to agree with the data set. The resultant parameters derived, from FDM-NRG calculations, are [with $T_K^0 \equiv T_K(\delta V_g = 0)$, the Kondo scale for $\epsilon_1 = -\frac{1}{2}U$ in the centre of the Coulomb blockade valley]:

Configuration	U/Γ	α	λ	T_K^0/K
I	8.0	0.020	0.7	0.2
II	7.2	0.017	0.65	0.3

To fit the data we have first found the values of U/Γ and λ by simple optimal fitting to the finite-field data at the centre of the Coulomb blockade valley [shown in fig. 6.14b)], using the approximation (5.87) for the finite-bias conductance [with $\pi\Gamma D_{11}(\omega;T)$ substituted for $2\pi\Gamma D_{ee}(\omega;T)$, as appropriate for the AIM]. To obtain α

we have then compared the experimental results for the Kondo scale T_K [fig. 6.14b)] to NRG results as described above. In order to perform this fit one can normalize both the experimental and theoretical data by the value of the Kondo scale at the centre of the valley, *i.e.* one fits the function T_K/T_K^0. The values so obtained are in line with the experimental estimate $\alpha \simeq 0.024$ [123]. The values of U/Γ quoted in ref. [123] are 5.3 and 4.0 for configurations I and II respectively.[6] The values we employ are larger than these experimentally estimated values, however there are at least two reasons why this is natural. In determining Γ from the widths of the charging peaks in a conductance map (*e.g.* a plot such as fig. 5.19) one must bear in mind that many-body broadening gives them a typical half-width at half-maximum of around $1.5 - 2\Gamma$ (as in section 5.4.1) [117, 118, 135], rather than simply Γ as arises in the non-interacting limit. Secondly the Haldane formula, used in ref. [123] to obtain U/Γ from the data in fig. 6.14a), applies asymptotically in the limit $U/\Gamma \gg 1$. Consequently U/Γ is underestimated somewhat when using this approach. Given the correct ratio U/Γ the experimental value $U = 1.4$ meV is then used to obtain Γ in these units, from which all other parameters of the model can be converted into units of meV. The resulting Kondo scales T_K^0, defined by $G_C(T_K^0; V_{\rm sd} = 0; h = 0)/G_0 = e^2/h$, in the table above are in good agreement with the experimental values [123], 0.3 K and 0.6 K, given the sensitivity of absolute Kondo scales to the bare parameters.

A second, independent, determination of λ can be obtained from the experimental conductance map, fig. 1a) of ref. [123]. The slopes of the sequential tunneling peaks, when plotted with $V_{\rm sd}$ as the horizontal axis, are readily shown [136] to be proportional to $1/\lambda$ and $1/(1-\lambda)$ such that their ratio yields $\lambda/(1-\lambda)$. From the experimental data [123] the value $\lambda \approx 0.7$ can be readily extracted and is in good agreement with the value derived above from fitting to the finite-field data.

With the parameters thus chosen, fig. 6.14b) compares the size of the peak splitting Δ_G (defined as half the peak-to-peak splitting in the finite-bias conductance) from theory (lines) and experiment (points). We have plotted the data in the form of ref. [123], subtracting the Zeeman level splitting $g\mu_B B = 2h$ from Δ_G to emphasize the deviation of the two. The open squares and filled circles are the experimental data for dots I and II respectively (as in fig. 4 of ref. [123]), while the blue (solid) and red (dot-dashed) lines are the corresponding theoretical predictions. The theoretical results have been gathered for $T = 0$; the experimental splittings are generally somewhat in excess of T [shown as a dotted line in fig. 6.14b)], and hence temperature does not play an important role in the analysis for points above this line. For fields close to the coalescence point where Δ_G vanishes [*i.e.* when the splittings approach the dashed curve in fig. 6.14b)] it is difficult to extract the precise value of the split-

[6] The quantity denoted Γ in ref. [123] is 2Γ here.

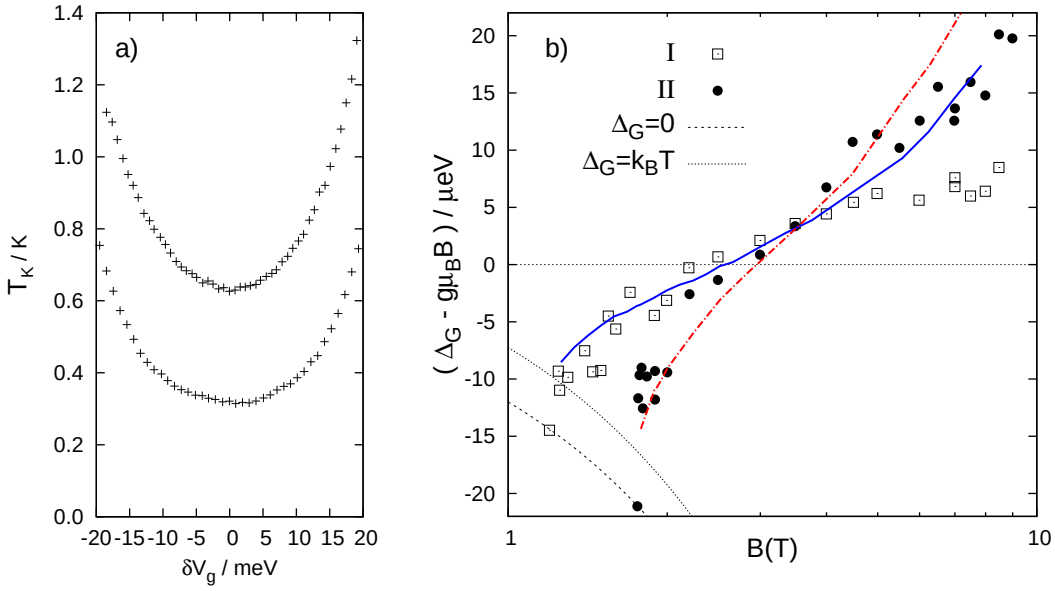

Figure 6.14: a) Experimental results [123] for the variation of the Kondo scale within a Coulomb blockade valley as the gate voltage V_g (equivalently the dot level energy) is varied. The two dot configurations, I (bottom) and II (top), show marginally different behaviours. b) Splitting of the Kondo conductance peak on application of a magnetic field, at the centre of the Coulomb blockade valley. Points represent the experimental results [123] for the two device configurations I and II, whilst lines give the FDM-NRG results for $U/\Gamma = 8$ and $\lambda = 0.7$ (blue solid), and for $U/\Gamma = 7.2$ and $\lambda = 0.65$ (red dot-dash). Lines corresponding to zero splitting (dash) and the experimental temperature ($T = 55$ mK, dot) are shown for reference.

tings, and hence we show only the sections of the curves for which the splitting can be determined reliably.

The agreement between theory and experiment is very good. In both cases theory reproduces well the experimental results up to fields of around 5 T, corresponding to Kondo peak splittings of around $\Delta_G = 1 - 2T_K^0$. At higher fields the theoretical curves certainly deviate from experiment, which we take to be a sign of the breakdown of the equilibrium approximation in (5.87), as known to occur from renormalized perturbation theory results for the AIM in a magnetic field [96]. Recently non-equilibrium and scattering states NRG methods [93, 95] have been developed with the latter being applied to the AIM in a magnetic field [137]. These approaches offer a promising means of determining peak splittings out of equilibrium, and further work comparing its predictions with those of (5.87) should help to establish the regimes of the model where non-equilibrium effects play a large role.

The final point to note here is that the FDM-NRG results reproduce the crossing of the two curves identified in the experiment. We find this to be entirely a consequence of the slightly different values of the parameters U/Γ and λ, as fig. 6.15 illustrates. If λ is maintained constant, results for different values of U/Γ do not

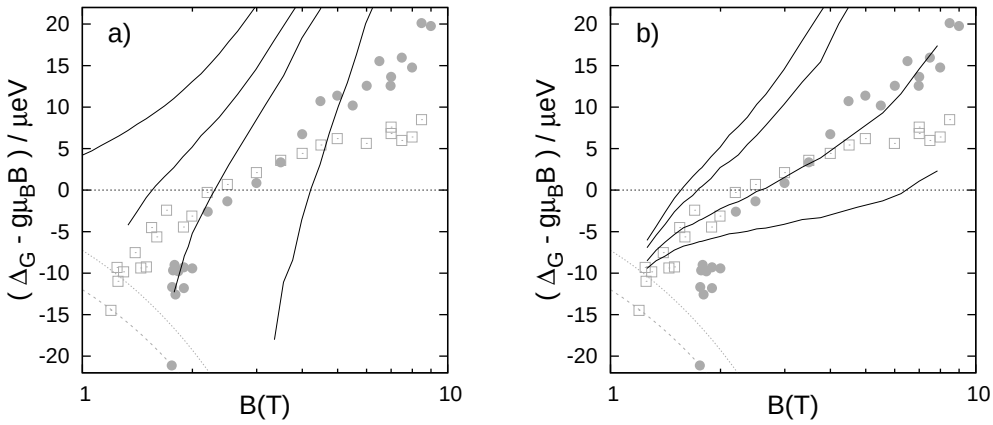

Figure 6.15: Conductance splittings obtained for a) fixed $\lambda = 0.5$ with $U/\Gamma = 10$, 8, 7.2, and 6 (top to bottom), and b) fixed $U/\Gamma = 8$ with $\lambda = 0.5$, 0.6, 0.7, and 0.8 (top to bottom). In each case the lines do not cross.

show a similar crossing: the lines of fig. 6.15a) maintaining a finite separation for all values of the field. Similarly, holding U/Γ fixed and increasing λ above 0.5 has the effect of reducing the splitting for all values of the field, with a larger reduction at high field strengths, fig. 6.15b). The crossing observed in the experimental data should not therefore be taken [123] to indicate a breakdown of universal scaling in one or other (or both) of the two configurations *per se*. Therefore, whilst the authors of ref. [123] go out of their way somewhat to point out this apparent breakdown of universality, we do not believe this to be the correct explanation of the crossing of the data sets in fig. 6.14.

This section has attempted a quantitative comparison with finite-bias conductance features by using the equilibrium approximation. As expected, the approximation appears to break down progressively as a system moves away from the equilibrium situation. The next section therefore focuses on more qualitative comparison with illustration of the basic physical phenomena occurring in a carbon nanotube quantum dot.

6.3.2 Carbon nanotube quantum dots

The experiments of Quay *et al.* [46] measured the conductance in two Coulomb blockade valleys of a carbon nanotube quantum dot. In the first valley a spin-$\frac{1}{2}$ Kondo effect was observed whilst in the second a spin-1 effect. We examine both set of results in turn.

Spin-$\frac{1}{2}$ Kondo Valley

In the spin-$\frac{1}{2}$ valley, conductance maps were obtained at zero and finite fields as a function of gate and source-drain biases [46]. The evolution of the finite-bias

conductance was also measured as a function of field. The splitting of the Kondo conductance at finite bias was compared to various theoretical predictions in the literature (refs. [127, 129, 130]). The level of agreement was rather poor. We now explain why the experiment did not recover the expected behaviour.

As in the previous section, the spin-$\frac{1}{2}$ Kondo effect in experiment is captured well by the AIM. By comparing with the available experimental data in ref. [46] we find $U/\Gamma = 8.5$ gives optimal agreement between theory and experiment. The coupling asymmetry can be found as described in the previous section (from the slopes of the sequential tunneling peaks [136]) to have a value $\lambda \simeq 0.58$. Finally the experimental Coulomb repulsion U can be determined from the Coulomb peak in fig. 2d) of ref. [46]. It is readily seen to take a value $U \simeq 2$ meV such that we obtain $\Gamma \simeq 0.24$ meV. From FDM-NRG calculations at $T = 0$ we then find $T_K^0 = 0.094\Gamma \sim 0.25$ K. This value is lower than the experimental estimate of 2 K. This means that the temperature of the device ($T = 352$ mK) is then on the order of the Kondo scale, rather than begin somewhat less than it. However we believe this to be more consistent with the measured conductance, as now explained.

The magnitude of the experimental Kondo scale can be gauged by inspection of fig. 2d) of ref. [46] [see also fig. 6.16d) for the FDM-NRG results]. If these results were obtained at a temperature somewhat below T_K^0, the Kondo peak would hardly be eroded by temperature, and instead one would naturally attribute the diminution of the zero-bias conductance from the unitary limit of $2e^2/h$ to the asymmetry of the couplings to the source and drain leads, *i.e.* the factor G_0. This was done in ref. [46]. But it is then difficult to explain the height of the Kondo peak relative to that of the Coulomb peaks as we expect the latter to be roughly a quarter of the height of the former for $T \ll T_K^0$ [117]. A much more likely explanation is that the Kondo scale is close to the temperature of the device, eroding the Kondo peak (but not the Coulomb peaks) and thus reducing its relative height.

Figure 6.16 shows theoretical results obtained via the FDM-NRG to be compared with that of fig. 2 of ref. [46]. The general agreement is good; the theory reproduces the intense sequential tunneling peaks in the conductance maps when the dot level is resonant with one of the lead chemical potentials, the somewhat weaker Coulomb diamond, and the narrower Kondo peak at zero-bias at the centre of the Coulomb blockade valley. The effect of switching on a field $h/\Gamma = 0.5$, shown in Figure 6.16b), is to transform the Kondo ridge into an ellipsoidal ring, resulting from the splitting of the Kondo conductance into two peaks symmetrically disposed about $V_{\rm sd} = 0$. Again, the overall agreement with experiment [46] is qualitatively very good.

The field dependence of the conductance is shown in more detail in fig. 6.16c) and d), which both show the conductance at the centre of the Coulomb blockade valley. We again recover the key features of the experiment (figs. 2c) and 2d) of ref. [46]). For fields sufficiently small compared to the zero-field Kondo scale ($h/\Gamma \lesssim 0.2$)

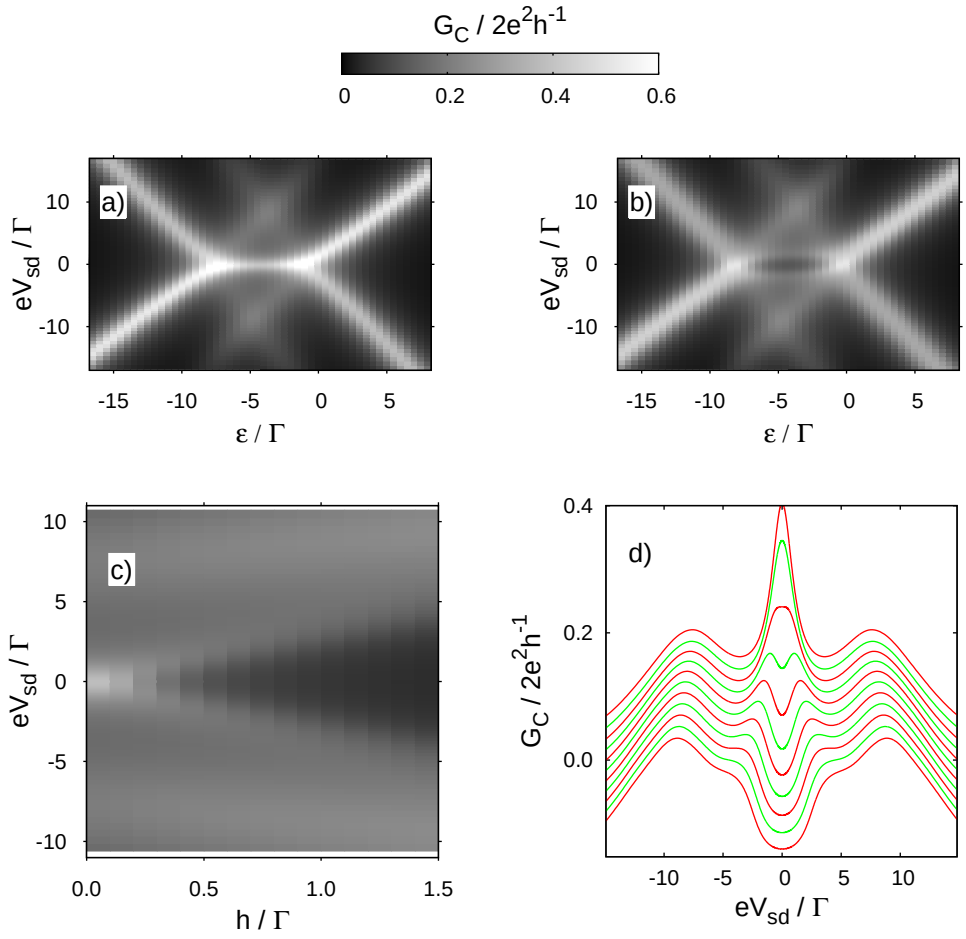

Figure 6.16: Spin-$\frac{1}{2}$ conductance maps at zero and finite magnetic field: to compare with fig. 2 of ref. [46]. An AIM is used with $\tilde{U} = 8.5$ (giving $\omega_K/\Gamma \simeq 0.15$), $T = \omega_K$ and $G_0 = 1$. a) Zero field conductance: a clear Kondo ridge is seen at zero-bias, $V_{\rm sd} = 0$. b) A finite field, $\tilde{h} = h/\Gamma = 0.5$, splits this ridge into twin peaks away from zero bias. c) Evolution of the Kondo peaks with field at the middle of the Coulomb valley (particle-hole symmetry). d) Vertical slices through c) with at $\tilde{h} = 0, 0.1, 0.2, ..., 0.9$ (top to bottom), offset by 0.02 $2e^2/h$ per slice.

the Kondo peak remains intact, while for larger fields it is progressively split and ultimately destroyed with increasing h, eventually leading to a region of almost zero conductance around $V_{\rm sd} = 0$. Comparing slices of fig. 6.16c) along lines of constant h, fig. 6.16d), we again observe good qualitative agreement with the experimental results.

We should point out at this stage that the value of $h/\Gamma = 0.5$ chosen in fig. 6.16b) corresponds, in physical units, to a field of about 2 T, around half the experimental field. This discrepancy can be attributed primarily to the breakdown of the equilibrium approximation (5.87) at fields larger than a couple of T_K. As seen earlier in fig. 6.14b) the approximation tends to overestimate the splitting at these high fields,

and hence a smaller h/Γ must be used in the calculation to obtain the same absolute splitting as the experiment. Based on the comparison of the previous section, noting the theoretical value here of $T_K^0 = 0.094\Gamma$, we can estimate that the equilibrium approximation begins to break down for this experiment at fields $B \gtrsim 1\mathrm{T}$.

While the above means we cannot compare quantitatively our NRG predictions at finite field to those of the experiment over the whole range of fields measured, we nonetheless believe the parameterization of the experiment to be reliable at low magnetic fields. This allows us to make order-of-magnitude predictions that explain the significance of the experimental results and the reason for the apparent disagreement with theory [46], as now explained.

The analysis of ref. [46] can be summarised as follows: first the splitting of the Kondo peak with field was extracted from the experimental data and plotted versus B. It was found that half the splitting tends to the form $\Delta_G = g\mu_B B$ at high field (with the experimentally measured g-factor being $g \simeq 2.07$). Direct comparison was then made between the full field-dependence of the conductance splitting obtained from several theories and experiment.

We point out that there are two basic problems with making this comparison. First and foremost, if one is interested in the *universal* form of the Kondo splitting, the experimental parameters need to satisfy both $U/\Gamma \gg 1$ and $h \ll \min(\Gamma, U)$. The former condition is necessary to ensure that the experiment is well-described by an effective Kondo model at low energies, and arises because the Schrieffer-Wolff transformation that maps the full Anderson model onto the Kondo model is formally valid only in the asymptotic limit $U/\Gamma \gg 1$. The latter condition defines what is meant here by 'low energies': even if U/Γ is large, the effective Kondo description will always break down at energies of the order of the non-universal scale Γ, and the results on such an energy scale will simply not show universal Kondo form.

One could argue that the $U/\Gamma \simeq 8.5$ here is sufficiently large for the experiment to be well described by a Kondo model at zero field, although we believe this to be a somewhat more borderline case. The main problem however is that the experimental U and Γ are too small for the high-field results to be universal. This can in fact be seen directly from fig. 2d) of ref. [46] [see also fig. 6.16d)]: even for moderate fields of $2-3$ T the Kondo peaks overlap significantly the non-universal Coulomb peaks. More formally, for some given h/T_K universality requires $h/\Gamma \ll 1$. In terms of the experimental parameters this implies the condition $g\mu_B B \ll \Gamma$ which in turn means universality can only arise for $B \ll 2\mathrm{T}$.

The second problem is that the predictions for the theoretical conductance [127, 129, 130] have all been made using (either explicitly or implicitly) the approximation of (5.87), rather than from a full-blown non-equilibrium approach. Even when we use the appropriate non-universal parameters in our NRG calculations, the comparison to both the present experiment and that of the previous section suggests

that (5.87) is quantitatively reliable only for fields smaller than a few multiples of the Kondo scale [128], and even then is strongly dependent on the value of λ. Until non-equilibrium approaches such as the scattering-states NRG [137] become more feasible, the quantitative, universal form of the conductance splitting for $h \gg T_K^0$ is an open question; one should certainly not expect *a priori* to obtain quantitative agreement between experiment and (5.87).

Spin-1 Kondo valley

Finally we consider the effect of magnetic field on the conductance of the 2LM, to make comparison with the spin-1 Kondo valley experiments of ref. [46]. Since there are more interactions in the 2LM than the AIM, it is obviously harder to parameterize the model from the available data in a fully systematic manner. We have thus used parameters similar to those found for the zero-field experiments analysed in section 5.4.1. We use the values $\tilde{U} = 12$, $\tilde{U}' = 6$, $\tilde{J}_H = -0.5$ and $(\tilde{\epsilon}_2 - \tilde{\epsilon}_1) \equiv \Delta\tilde{\epsilon} = 4.5$. For simplicity we take $T = 0$, $\lambda = \frac{1}{2}$ and $G_0 = 1$. Choosing a reasonable value of $\Gamma \sim 0.25$ meV [1, 45, 119] gives *e.g.* a charging energy $U \sim 3$ meV and level spacing $\Delta\epsilon \sim 1$ meV, both typical of experimental estimates [45, 119].

Figure 6.17a) shows the resultant splitting of the 'USC Kondo' conductance peak at a point in the USC phase near the zero-field phase transition [as indicated by the tail of the arrow in the phase diagram fig. 6.17c)]. The figure is qualitatively similar to that for the spin-$\frac{1}{2}$ Kondo peak in a magnetic field [fig. 6.17c)] but, as noted in the case of a stretched spin-1 molecule [7], the field at which the zero-bias peak is destroyed is a somewhat smaller fraction of the Kondo scale. This naturally reflects the sharper USC Kondo resonance [see fig. 6.9b)] compared to the spin-$\frac{1}{2}$ Kondo case.

The Kondo scale for the chosen parameters is $\omega_K^{S=1} \simeq 0.66\Gamma \simeq 2$ K, which again appears roughly in line with the widths of the Kondo peaks in the experimental conductance maps [46]. This means it is perhaps misleading to refer to the basic phenomenology here as 'underscreened Kondo' physics, since resonance widths on the order of Γ imply the model is far from being well described by a effective spin-1 Kondo model *per se*. As for the semiconducting quantum dot analyzed previously [64] it also appears that the experimental trajectory as a function of gate voltage ($\epsilon_1 \propto V_{\rm gate}$) passes through the USC phase quite some distance away from particle-hole symmetry where $\omega_K^{S=1}$ is relatively high (see *e.g.* fig. 5.20).

Just across the phase boundary into the FL phase, we obtain the conductance map shown in fig. 6.17b). Here we have kept the interactions and $\Delta\epsilon$ fixed, but increased ϵ_1 by 3.5Γ from its value in fig. 6.17a) [the head of the arrow in fig. 6.17c) gives the precise location relative to the phase boundary]. The qualitative agreement between theory and experiment, fig. 5b) of ref. [46], is again very good. We recover all basic features seen in experiment: at zero field the conductance peaks at around

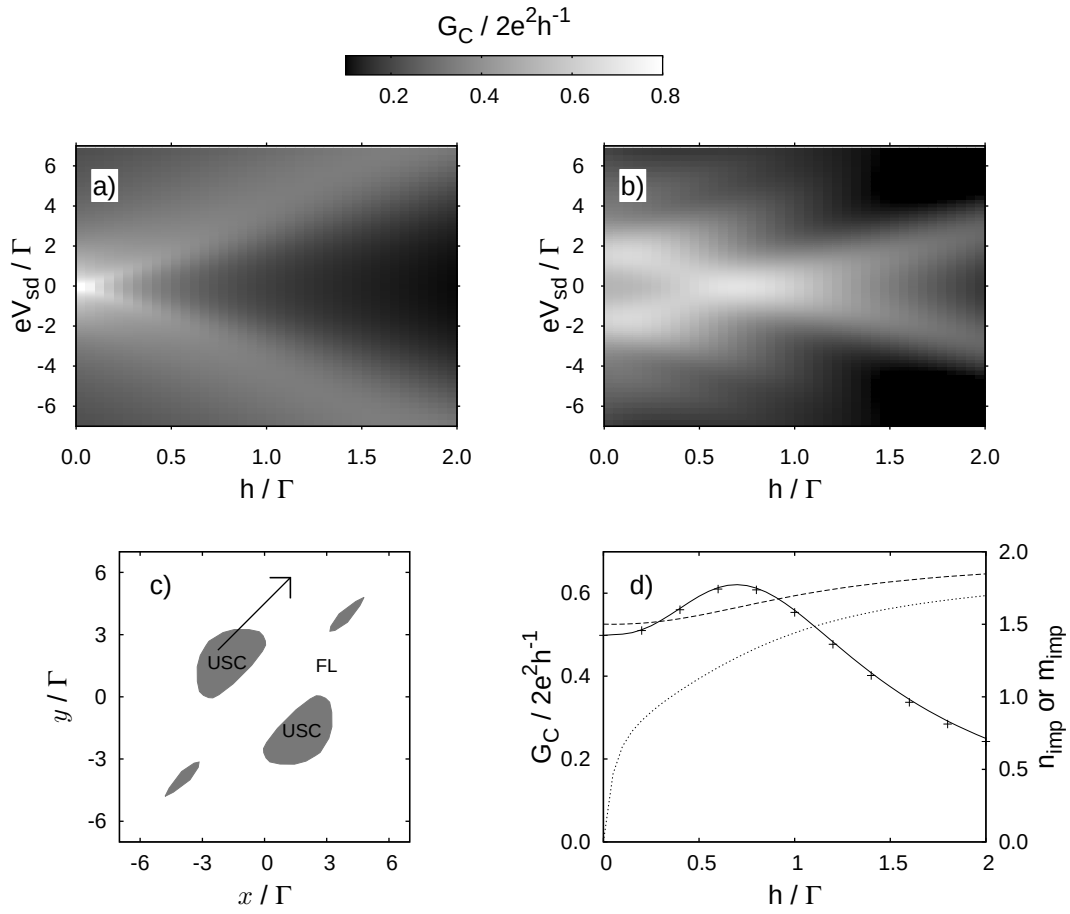

Figure 6.17: Conductance maps for the 2LM close to the $h = 0$ phase transition; for $\tilde{U} = 12$, $\tilde{U}' = 6$, $\tilde{J}_H = -0.5$ and $\Delta\tilde{\epsilon} = 4.5$, to be compared with figs. 5a) and b) of ref. [46]. a) USC phase for $y = -x = 2.25\Gamma$ ($x = \epsilon_1 + \frac{1}{2}U + U'$ and $y = x + \Delta\epsilon$, with $\epsilon_1 \propto V_g$). The conductance peak splits on applying a field. b) FL phase for $(x, y) = (1.25\Gamma, 5.75\Gamma)$. The $h = 0$ Kondo anti-resonance is 'filled-in' for $h > 0$; full discussion in text. c) $h = 0$ phase diagram for the above parameters as a function of x/Γ and y/Γ (equivalent to fig. 5.20), with the arrow showing the 'trajectory' taken in going from a) to b). d) Zero-bias cut through b) (crosses), along with the excess dot charge $n_{\rm imp}$ (dashed), excess magnetization $m_{\rm imp}$ (dotted) and conductance as given by (6.8b) (solid).

$\pm 2\Gamma \simeq \pm 0.5$ meV, reflecting the zero-bias *antiresonance* in the equilibrium spectrum just inside the FL phase as found in section 5.3. These peaks move toward each other, cross and ultimately move apart with increasing field, which can be loosely associated with a crossing of the isolated dot singlet and lowest triplet states, with a finite-field Kondo effect taking place at the crossing point. Again, the 'Kondo' scale here is rather large and as such one cannot describe the low-energy behavior in terms of a pure spin-$\frac{1}{2}$ Kondo model. We note that in our calculations the crossing takes place at $h \sim 0.7\Gamma \simeq 0.2$ meV and hence $B \sim 3$ T, again in good agreement with experiment. One can also make out various weaker features in the conductance, parallel to the main features and again seen experimentally, which mirror transitions

from the isolated dot singlet to the higher energy triplet states [46].

The zero-bias conductance is analyzed further in fig. 6.17d), which is a cut through fig. 6.17b) at $V_{\rm sd} = 0$. With increasing field, the conductance increases from its zero-field value of $\sim \frac{1}{2}$, passes through a maximum at $h/\Gamma \sim 0.7$ [as evident from fig. 6.17b)], and decreases monotonically thereafter. Also shown are the total excess dot charge $n_{\rm imp}$ and magnetization $m_{\rm imp}$ [defined in (6.7)], both of which increase smoothly and monotonically as the ground state evolves with increasing field. At zero field the dot is in a mixed-valent regime, with $n_{\rm imp} \simeq 1.5$ [and $m_{\rm imp} = 0$ by symmetry]. But with increasing field the dot ground state becomes progressively more like the simple $S_z = 1$ component of the isolated-dot triplet, with both total charge and magnetization tending to 2 for $h/\Gamma \gg 1$ (i.e. $n_{{\rm imp},\uparrow} = 2$ and $n_{{\rm imp},\downarrow} = 0$).

While the zero-bias conductance shown above is calculated using (5.86), and as such probes single-particle spectra, its field-dependence shown in fig. 6.17d) should equally be explicable from (6.8b), expressed solely in terms of the dot charge and magnetization. That this is indeed so is shown directly in fig. 6.17d): the solid line is calculated from (6.8b), and seen to be in very good agreement with the direct FDM-NRG calculations.

We have shown in this chapter that recent developments in NRG techniques have enabled quantitative analysis of the effect of a magnetic field in quantum impurity systems. With regards to the dynamic properties of the AIM we have elucidated the full universal scaling form of the position of the spectral maximum as a function of the field strength, recovering the known exact result at low field. Our analysis is limited only by the logarithmic broadening inherent in the NRG. For the 2LM our results suggest a constant spectral shift $\Delta_\sigma = 2h$.

We have also made direct comparison between NRG calculations and two recent sets of conductance experiments on quantum dots in a magnetic field. Agreement between theory and experiment is found to be very good qualitatively for both spin-$\frac{1}{2}$ [46, 123] and spin-1 [46] quantum dots. Further quantitative agreement can be found provided the system is not too far from equilibrium. The equilibrium approximation of (5.87) appears to give good results for fields up to a few multiples of the zero-field Kondo scale.

We have argued that neither experiment considered has measured the true universal conductance splitting of the spin-$\frac{1}{2}$ Kondo effect and have emphasised the sensitivity of the field-dependence of the conductance peak to the bias voltage asymmetry. In view of this we have suggested that more experimental attention should be given to the equilibrium, zero-bias conductance. Given exactly by (5.86) and independent of λ, its field dependence shows interesting features (figs. 6.12 and 6.13) that can be calculated exactly by theory. We believe also that it presents a better prospect for ascertaining the universality in the magnetic field dependence of spin-$\frac{1}{2}$ and spin-1 Kondo effects in real quantum dots.

CHAPTER 7

Summary

In this thesis we have studied systems of interacting two-level quantum dots. We have formed a model appropriate to the study of both molecular and semiconductor quantum dots displaying underscreened Kondo physics. In particular we have outlined the hierarchy of interactions present in these systems, and studied the effect of an applied gate voltage.

Quantum dots with multiple 'active' levels display fascinating physics including the competition between orbital and spin degrees of freedom: the formation of high spin states occurring only when it is energetically favourable to do so. The classic spin-$\frac{1}{2}$ Kondo effect, with its attendant Fermi liquid ground state, was until recently the rule in experimental systems.

On coupling to a single metallic conduction band channel, a quantum dot with a local spin $S > \frac{1}{2}$ is only partially screened giving rise to interesting non-trivial low-energy excitations. Specifically whilst scattering of conduction band electrons off of the impurity occurs elastically at the Fermi level (as for a regular Fermi liquid), the scattering matrix is non-analytic around ϵ_f. Systems have now been observed with properties which indicate the formation of such novel singular Fermi liquid ground states.

In chapter 2 we gave a brief introduction to the field of quantum impurity models focussing on the universal physics of the Kondo effect. We also motivated the model studied throughout this thesis, the two-level model (2LM), from the starting point of a molecule attached at two points to separate 'left' and 'right' metallic leads. We showed that in the case of proportional couplings to the left and right leads, an effective one-channel model can be derived. We have no doubt that such channel isotropy is not generally present in experiments, but the rich array of physics displayed in the current case more that justified this study.

To a large extent our work can be partitioned into two sections. In chapters 4 and 5 we studied the 2LM in the absence of an external magnetic field. We have made

use of perturbative techniques to obtain analytical results and low-energy effective models, which have in turn allowed simple interpretations of the physical behaviour of the full model to be made. We have used numerical renormalization group (NRG) techniques, which we introduced in chapter 3, to obtain accurate results for both the thermodynamic and dynamic properties of the 2LM. The dynamic results have been used to interpret experimental results for the conductance of real devices and guide future experiments. In chapter 6 we have focused on the effect an applied magnetic field in systems displaying the spin-1 Kondo effect and also in systems displaying the spin-$\frac{1}{2}$ effect. In the latter case we have attempted to clarify the current theoretical literature whilst also attempting a better understanding of experimental results.

We now summarise our key results. We started our study of the 2LM in section 4.1 by considering the atomic limit, the case of an isolated impurity. The shape of the phase boundary in the $\epsilon_1 - \epsilon_2$ plane was examined as a function of the impurity interactions U, U', and J_H (the intra- and interlevel Coulomb repulsions and the ferromagnetic interlevel spin exchange coupling). Increasing the exchange coupling favours the $(n_1, n_2) = (1, 1)$ state of the impurity. Conversely, an increase in U' destabilises the $(1, 1)$ state with respect to the $(2, 0)$ and $(0, 2)$ states.

Following an examination of the atomic limit we have moved to consider the renormalization group fixed points of the Anderson model (AIM) and the 2LM. We have illustrated the importance of the strong coupling fixed point $\hat{H}^*_{\mathrm{SC}}$ in the AIM and the flow to it from the spin-$\frac{1}{2}$ local moment fixed point $\hat{H}^*_{\mathrm{LM}}$. The strong coupling fixed point is the only stable fixed point in the AIM and so ultimately all RG flows terminate at it regardless of the bare parameters of the initial Hamiltonian. In the 2LM by contrast a second stable fixed point arises: the underscreened spin-1 fixed point associated with partial screening of a local impurity spin. Following the arguments of Nozières we have illustrated why the impurity spin is not fully screened.

Section 4.3 has examined the phase transition occurring in the 2LM which arises as a natural consequence of there being two stable renormalization group fixed points (more precisely, two lines of related fixed points). In the vicinity of particle-hole symmetry the underscreened spin-1 (USC) fixed point is found to occur; the system possessing a degenerate spin-$\frac{1}{2}$ ground state. On moving away from particle-hole symmetry the system eventually switches to a Fermi liquid (FL) groundstate. The transition is generically of the Kosterlitz-Thouless type with the Kondo scale on the FL side vanishing in an exponential fashion as the transition is approached. Exceptions to this are made along special lines of symmetry. At these points separability of the Hilbert space of the Hamiltonian leads to first-order level crossing transitions. The low-energy model derived in section 4.2.1 can be used to identify the location of these special points. We have concluded by very briefly examining the crossover from equally coupled impurity levels to a so-called side coupled dot in which one

impurity level is completely detached from the conduction band. The salient point here is that the physics in these cases precisely parallels the symmetric coupling case (the underlying fixed point structure is identical) although one's physical description of the ground state may alter.

In chapter 5 we have surveyed the dynamic properties of the 2LM largely through examining the single-particle spectrum in the even channel $D_{ee}(\omega)$. As an illustration of the singular nature of the USC fixed point we have shown the asymptotic form of the impurity self-energy $\Sigma_{ee}(\omega)$. We have defined and used the impurity phase shift to relate the impurity excess charge to the Luttinger integral I_L in our so-called Friedel-Luttinger sum rule. Through direct calculation we have demonstrated that Luttinger's theorem, $I_L = 0$, holds in the FL phase of the 2LM. We have shown further that $|I_L| = \pi/2$ in the USC phase. These results had an immediate consequence for the zero-frequency spectral density $D_{ee}(\omega = 0)$ in both of the phases: as the excess impurity charge varies continuously on crossing the Kosterlitz-Thouless transitions, $D_{ee}(0)$ must vary discontinuously as a result of the Luttinger integral changing.

We have systematically studied also the finite frequency features of $D_{ee}(\omega)$; it contains not only features which can be interpreted in terms of the isolated impurity states but also features relating to the Kondo effect. In the USC phase a sharp cusp-like Kondo resonance occurs. We have illustrated the universal scaling form of this resonance — it changes little with the system asymmetry η, measuring the departure from the particle-hole symmetric point. The Kondo resonance in the FL phase displays universal scaling also as a function of the system parameters. Along the special line $y = -x$ ($\epsilon_2 + \epsilon_2 = -U - 2U'$) a pristine Kondo *anti*resonance is seen in the FL phase, which also has a universal form.

In section 5.3.1 we studied in detail the case of $y = x$ ($\epsilon_1 = \epsilon_2$). Here is it useful to examine the odd impurity channel. We have derived analytic results for the even and odd renormalized impurity levels in terms of phase shifts and Luttinger integrals separate to each channel. Results from the NRG conform to these predictions. Interesting features corresponding to the odd renormalized level develop in the spectral density $D_{oo}(\omega)$ as the first-order transition is crossed. A sharp resonance above the Fermi level appears in the FL phase and moves closer to the Fermi level as the transition is approached; precisely at the transition a pole occurs at $\omega = 0$. The even spectral density by contrast changes discontinuously on crossing the transition and shows no sign of the odd renormalized level.

We examined both the zero and finite bias conductance of quantum dot systems, and its relation to the spectral density $D_{ee}(\omega)$, in section 5.4. The temperature dependence of the zero-bias conductance shows similar features to the frequency dependent form of the spectral. A Kondo conductance peak is observed which shows universal scaling in terms of the Kondo scale. We have shown how thermal broad-

ening of the finite-bias conductance has two components: first direct broadening occurs via the inclusion of higher frequency spectral components by the smooth Fermi functions of the leads whilst secondly, the spectral density is itself smeared. The overall effect can be to either increase *or* decrease the zero-bias conductance. We have illustrated also the complicating effect of the bias voltage asymmetry which can play an important role in interpreting experimental results.

Finally in chapter 5 we have analysed conductance experiments performed on a GaAs quantum dot displaying signs of Kondo effects in neighbouring Coulomb blockade diamonds. We have shown that features in the conductance profile originally explained in terms of the isolated dot states, can in fact be attributed to a many-body Kondo antiresonance. Theoretical results have been presented for two trajectories through the parameter space of the 2LM, giving favourable agreement with the experimental results.

Chapter 6 has examined the effect that a local magnetic field has on both single and two-level quantum dots. We started by showing that NRG results for the impurity magnetization as a function of the field are consistent with exact results known from the Bethe ansatz. We illustrated the dramatic effect that even an infinitesimal field has on high frequency components of the single particle density $D_{ee}(\omega)$ in the 2LM. This is in marked contrast to the AIM and is due to the 2LM possessing a polarizable local moment ground state. The zero frequency value of the spectra, and so the $T = 0$ zero-bias conductance, does not similarly show a sudden change when the field is turned on due to the cancelling effects of the magnetization and Luttinger integral in the Friedel-Luttinger sum rule.

Following this we focused almost exclusively on the splitting of the Kondo resonance on application of a field. We reviewed the case of the AIM where in the limit of low field strength, the magnitude of the splitting is known analytically to be $\Delta_\sigma = 4h/3$. Results from the FDM-NRG have been shown to be in agreement with this prediction. Numerical results for the high-field limit are less definitive and we cannot be entirely certain of our suppositions. We have however calculated a universal scaling form for the Kondo peak splitting over a large range of field strengths. In the underscreened spin-1 case our results are even less precise, although it seems that our results converge to the result that $\Delta_\sigma = 2h$ for all field strengths. Whilst we cannot give a firm analytic proof of this result, it seems plausible. Care should be taken however: it is the same intuition that might lead one to believe the splitting in the AIM is a simple linear Zeeman-like phenomenon.

In relation to experimental results we have shown that with currently feasible numerical methods, experimentalists and theorists should seek to make contact by comparing results for the temperature dependence of the zero-bias conductance. The approximation used currently to calculate the bias dependence of the conductance can be unreliable and is not suitable for the task of making quantitative comparison.

With the approximation we have nevertheless attempted some form of experimental rationalisation. We have concluded that the bias asymmetry plays an important role in determining whether experiments are performed in the universal Kondo scaling regime. In particular, the suggested breakdown of universality in one experiment can in fact be attributed to changes in the bias asymmetry between devices. We have finished by examining experiments carried out with a carbon nanotube quantum dot. Again this experiment was not performed in a strict scaling regime in which one would expect adherence to universal scaling forms for the Kondo conductance peak splitting. As in the case of the zero-field experiments analysed in chapter 5, we have shown that when one applies a magnetic field one should not attempt an explanation of conductance features solely in terms of the isolated impurity states.

In this thesis we have therefore studied the experimentally relevant physics of quantum dot devices containing one or two active levels. The formation of a singular, underscreened state has been examined along with the transition to a more usual Fermi liquid state. Further work remains, not least a full analytical understanding of the effect a magnetic field has on the single particle spectral density in the underscreened phase.

APPENDIX A

Symmetries of $\mathbf{G}(\omega)$ and $\mathbf{\Sigma}(\omega)$

In this appendix we explore the symmetries of the retarded Green functions under the particle-hole transformation of the 2LM. We start however by examining the symmetries of the time ordered impurity Green functions:

$$\tilde{G}_{ij}(t) = -i\langle \hat{T}[d_{i\sigma}(t)d^{\dagger}_{j\sigma}(t=0)]\rangle \tag{A.1a}$$
$$\tilde{G}_{ij}(\omega) = G^{R}_{ij}(\omega) - i\,\mathrm{sgn}(\omega)\pi D_{ij}(\omega), \tag{A.1b}$$

where $\hat{T}$ is the Wick time ordering operator. From time reversal symmetry we can write also that:

$$\tilde{G}_{ij}(t) = -i\langle \hat{T}[d_{i\sigma}(0)d^{\dagger}_{j\sigma}(-t)]\rangle \tag{A.2a}$$
$$= +i\langle \hat{T}[d^{\dagger}_{j\sigma}(-t)d_{i\sigma}(0)]\rangle \tag{A.2b}$$

In section 4.1 we discussed how the particle-hole transformation, $d^{\dagger}_{i\sigma} \leftrightarrow d_{i\sigma}$, achieves the relabelling of operators with $(x, y) \leftrightarrow (-x, -y)$, *i.e.* it corresponds to inversion through the origin. The Green function $\tilde{G}_{ij}(t)$ is equal to its particle-hole counterpart and so we can write:

$$\tilde{G}_{ij}(t; x, y) = -i\langle \hat{T}[d_{i\sigma}(0)d^{\dagger}_{j\sigma}(t)]\rangle_{(x,y)} \tag{A.3a}$$
$$= \left[-i\langle \hat{T}[d_{i\sigma}(0)d^{\dagger}_{j\sigma}(t)]\rangle_{(x,y)}\right]_{\text{p-ht}} \tag{A.3b}$$
$$= -i\langle \hat{T}[d^{\dagger}_{i\sigma}(0)d_{j\sigma}(t)]\rangle_{(-x,-y)} \tag{A.3c}$$
$$= -\tilde{G}_{ji}(-t; -x, -y) \tag{A.3d}$$

The Fourier transform of $\tilde{G}_{ij}(t)$ and the spectral density then obey:

$$\tilde{G}_{ij}(\omega; x, y) = -\tilde{G}_{ji}(-\omega; -x, -y) \tag{A.4a}$$
$$D_{ij}(\omega; x, y) = D_{ji}(-\omega; -x, -y). \tag{A.4b}$$

Using the results above that $\tilde{\mathbf{G}}(\omega; x, y) = -\tilde{\mathbf{G}}^{\mathrm{T}}(-\omega; -x, -y)$, where T denotes transpose, and $\tilde{\mathbf{G}} = \tilde{\mathbf{G}}^{T}$ it follows straight forwardly that the retarded propagators $G_{ij}(\omega) = G^{R}_{ij}(\omega) - i\pi D_{ij}(\omega)$ have the following symmetry under the particle-hole transform:

$$\mathbf{G}(\omega; x, y) = -\mathbf{G}^{\dagger}(-\omega; -x, -y) \tag{A.5}$$

We now find a similar result for the retarded self-energy defined by

$$\mathbf{\Sigma}(\omega; x, y) = [\mathbf{G}^{0}(\omega; x, y)]^{-1} - [\mathbf{G}(\omega; x, y)]^{-1} \tag{A.6}$$

in terms of the non-interacting propagators [see (3.31)], with $\mathbf{\Gamma}(\omega) = -i\Gamma$,

$$[\mathbf{G}^{0}(\omega; x, y)]^{-1} = \begin{pmatrix} \omega^{+} - x + \frac{1}{2}U + U' + i\Gamma & +i\Gamma \\ +i\Gamma & \omega^{+} - y + \frac{1}{2}U + U' + i\Gamma \end{pmatrix}. \tag{A.7}$$

On application of the particle-hole transform we find:

$$[\mathbf{G}^{0}(-\omega; -x, -y)]^{-1} = \begin{pmatrix} -\omega + i\eta + x + \frac{1}{2}U + U' + i\Gamma & +i\Gamma \\ +i\Gamma & -\omega + i\eta + y + \frac{1}{2}U + U' + i\Gamma \end{pmatrix} \tag{A.8a}$$

$$= (U + 2U')\mathbf{1} - \left\{[\mathbf{G}^{0}(\omega; x, y)]^{-1}\right\}^{\dagger}. \tag{A.8b}$$

Finally by inserting (A.8b) and (A.8b) into (A.6) the required result for the self-energy is found:

$$\mathbf{\Sigma}(-\omega; -x, -y) = (U + 2U')\mathbf{1} - \mathbf{\Sigma}^{\dagger}(-\omega; -x, -y). \tag{A.9}$$

Bibliography

[1] D. Goldhaber-Gordon *et al.*, Nature **391**, 156 (1998).

[2] L. Kouwenhoven and L. Glazman, Physics World, 2001.

[3] T. Jamneala, V. Madhavan, and M. F. Crommie, Phys. Rev. Lett. **87**, 256804 (2001).

[4] T. Uchihashi, J. Zhang, J. Kröger, and R. Berndt, Phys. Rev. B **78**, 033402 (2008).

[5] N. Roch *et al.*, Nature **453**, 633 (2008).

[6] N. Roch *et al.*, Journal of Low Temperature Physics **153**, 350 (2008).

[7] N. Roch *et al.*, Phys. Rev. Lett. **103**, 197202 (2009).

[8] S. Schnez *et al.*, Appl. Phys. Lett. **94**, 012107 (2009).

[9] C. Stampfer *et al.*, Appl. Phys. Lett. **92**, 012102 (2008).

[10] J. Singleton, *Band theory and electronic properties of solids*, *Oxford master series in condensed matter physics* (Oxford University Press, Oxford, 2001).

[11] L. P. Kouwenhoven and C. M. Marcus, Physics World **11**, 35 (1998).

[12] R. C. Ashoori *et al.*, Phys. Rev. Lett. **71**, 613 (1993).

[13] C. W. J. Beenakker, Phys. Rev. B **44**, 1646 (1991).

[14] T. A. Fulton and G. J. Dolan, Phys. Rev. Lett. **59**, 109 (1987).

[15] U. Meirav, M. A. Kastner, and S. J. Wind, Phys. Rev. Lett. **65**, 771 (1990).

[16] M. A. Reed *et al.*, Phys. Rev. Lett. **60**, 535 (1988).

[17] J. H. F. Scott-Thomas *et al.*, Phys. Rev. Lett. **62**, 583 (1989).

[18] B. Su, V. J. Goldman, and J. E. Cunningham, Science **255**, 313 (1992).

[19] J. Güttinger *et al.*, Phys. Rev. Lett. **103**, 046810 (2009).

[20] A. C. Hewson, *The Kondo Problem to Heavy Fermions* (Cambridge University Press, Cambridge, 1993).

[21] P. W. Anderson, Phys. Rev. **124**, 41 (1961).

[22] K. G. Wilson, Rev. Mod. Phys. **47**, 773 (1975).

[23] H. R. Krishna-murthy, J. W. Wilkins, and K. G. Wilson, Phys. Rev. B **21**, 1003 (1980).

[24] H. R. Krishna-murthy, J. W. Wilkins, and K. G. Wilson, Phys. Rev. B **21**, 1044 (1980).

[25] K. Yosida and K. Yamada, Progress of Theoretical Physics Supplement **46**, 244 (1970).

[26] K. Yosida and K. Yamada, Prog. Theor. Phys. **53**, 1286 (1975).

[27] K. Yamada, Prog. Theor. Phys. **53**, 970 (1975).

[28] J. Kondo, Prog. Theor. Phys. **32**, 37 (1964).

[29] P. W. Anderson, J. Phys. C **3**, 2436 (1970).

[30] P. Nozières, J. Low Temp. Phys. **17**, 31 (1974).

[31] N. Andrei, K. Furuya, and J. H. Lowenstein, Rev. Mod. Phys. **55**, 331 (1983).

[32] P. B. Wiegmann and A. M. Tsvelick, J. Phys. C **16**, 2281 (1983).

[33] N. Kawakami and A. Okiji, Progress of Theoretical Physics Supplement **101**, 429 (1990).

[34] K. Chen and C. Jayaprakash, Phys. Rev. B **57**, 5225 (1998).

[35] C. Gonzalez-Buxton and K. Ingersent, Phys. Rev. B **57**, 14254 (1998).

[36] D. M. Cragg and P. Lloyd, J. Phys. C **12**, 3301 (1979).

[37] H. B. Pang and D. L. Cox, Phys. Rev. B **44**, 9454 (1991).

[38] S. N. Evangelou and A. C. Hewson, J. Phys. C **15**, 7073 (1982).

[39] R. Bulla, H.-J. Lee, N.-H. Tong, and M. Vojta, Phys. Rev. B **71**, 045122 (2005).

[40] D. M. Cragg and P. Lloyd, J. Phys. C **12**, L215 (1979).

[41] P. W. Brouwer, Y. Oreg, and B. I. Halperin, Phys. Rev. B **60**, R13977 (1999).

[42] H. U. Baranger, D. Ullmo, and L. I. Glazman, Phys. Rev. B **61**, R2425 (2000).

[43] J. Schmid, J. Weis, K. Eberl, and K. v. Klitzing, Phys. Rev. Lett. **84**, 5824 (2000).

[44] W. G. van der Wiel *et al.*, Phys. Rev. Lett. **88**, 126803 (2002).

[45] A. Kogan *et al.*, Phys. Rev. B **67**, 113309 (2003).

[46] C. H. L. Quay *et al.*, Phys. Rev. B **76**, 245311 (2007).

[47] S. Sasaki *et al.*, Nature **405**, 764 (2000).

[48] J. J. Parks *et al.*, Science **328**, 1370 (2010).

[49] A. Posazhennikova, B. Bayani, and P. Coleman, Phys. Rev. B **75**, 245329 (2007).

[50] M. Pustilnik and L. I. Glazman, Phys. Rev. Lett. **87**, 216601 (2001).

[51] K. Kikoin and Y. Avishai, Phys. Rev. Lett. **86**, 2090 (2001).

[52] W. Hofstetter and H. Schoeller, Phys. Rev. Lett. **88**, 016803 (2001).

[53] M. Vojta, R. Bulla, and W. Hofstetter, Phys. Rev. B **65**, 140405 (2002).

[54] W. Koller, A. C. Hewson, and D. Meyer, Phys. Rev. B **72**, 045117 (2005).

[55] A. Posazhennikova and P. Coleman, Phys. Rev. Lett. **94**, 036802 (2005).

[56] M. Pustilnik and L. Borda, Phys. Rev. B **73**, 201301 (2006).

[57] P. Roura Bas and A. A. Aligia, Phys. Rev. B **80**, 035308 (2009).

[58] P. S. Cornaglia, P. R. Bas, A. A. Aligia, and C. A. Balseiro, Europhys. Lett. **93**, 47005 (2011).

[59] M. Pustilnik and L. I. Glazman, Phys. Rev. Lett. **85**, 2993 (2000).

[60] M. Pustilnik, L. I. Glazman, and W. Hofstetter, Phys. Rev. B **68**, 161303 (2003).

[61] O. Sakai and W. Izumida, Physica B: Condensed Matter **328**, 125 (2003).

[62] W. Hofstetter and G. Zarand, Phys. Rev. B **69**, 235301 (2004).

[63] R. Žitko and J. Bonča, Phys. Rev. B **76**, 241305 (2007).

[64] D. E. Logan, C. J. Wright, and M. R. Galpin, Phys. Rev. B **80**, 125117 (2009).

[65] C. J. Wright, M. R. Galpin, and D. E. Logan, Phys. Rev. B **84**, 115308 (2011).

[66] D. Pines and P. Nozières, *Theory of Quantum Liquids: Normal fermi liquids*, *Theory of Quantum Liquids, Volume I* (Addison-Wesley Pub. Co., Advanced Book Program, Boston, 1994).

[67] J. Friedel, Phil. Mag. **43**, 153 (1952).

[68] J. R. Schrieffer and P. A. Wolff, Phys. Rev. **149**, 491 (1966).

[69] C. Cohen-Tannoudji, J. Dupont-Roc, and G. Grynberg, *Atom-Photon interactions: basic processes and applications* (Wiley, New York, 1992).

[70] S. Andergassen *et al.*, Nanotechnology **21**, 272001 (2010).

[71] S. Florens *et al.*, J. Phys.: Condens. Matter **23**, 243202 (2011).

[72] S. Ilani and P. L. McEuen, Annual Review of Condensed Matter Physics **1**, 1 (2010).

[73] R. Bulla, T. A. Costi, and T. Pruschke, Rev. Mod. Phys. **80**, 395 (2008).

[74] P. W. Anderson and G. Yuval, Phys. Rev. Lett. **23**, 89 (1969).

[75] P. W. Anderson, G. Yuval, and D. R. Hamann, Phys. Rev. B **1**, 4464 (1970).

[76] V. L. Campo and L. N. Oliveira, Phys. Rev. B **72**, 104432 (2005).

[77] J. J. Binney, N. J. Dowrick, A. J. Fisher, and M. E. J. Newmann, *The Theory of Critical Phenomena* (Oxford University Press, Oxford, 1992).

[78] A. K. Mitchell, Ph.D. thesis, University of Oxford, 2009.

[79] R. Bulla, T. A. Costi, and D. Vollhardt, Phys. Rev. B **64**, 045103 (2001).

[80] T. A. Costi, A. C. Hewson, and V. Zlatic, J. Phys.: Condens. Matter **6**, 2519 (1994).

[81] R. Bulla, A. C. Hewson, and T. Pruschke, J. Phys.: Condens. Matter **10**, 8365 (1998).

[82] A. Weichselbaum and J. von Delft, Phys. Rev. Lett. **99**, 076402 (2007).

[83] H. O. Frota and L. N. Oliveira, Phys. Rev. B **33**, 7871 (1986).

[84] W. C. Oliveira and L. N. Oliveira, Phys. Rev. B **49**, 11986 (1994).

[85] M. Yoshida, M. A. Whitaker, and L. N. Oliveira, Phys. Rev. B **41**, 9403 (1990).

[86] D. N. Zubarev, Sov. Phys. Usp. **3**, 320 (1960).

[87] A. A. Abrikosov, L. P. Gorkov, and I. E. Dzyaloshinski, *Methods of Quantum Field Theory in Statistical Physics* (Pergamon Press Ltd., Oxford, 1965).

[88] T. A. Costi and A. C. Hewson, Philosophical Magazine Part B **65**, 1165 (1992).

[89] R. Peters, T. Pruschke, and F. B. Anders, Phys. Rev. B **74**, 245114 (2006).

[90] F. B. Anders and A. Schiller, Phys. Rev. B **74**, 245113 (2006).

[91] F. B. Anders and A. Schiller, Phys. Rev. Lett. **95**, 196801 (2005).

[92] Y. Meir and N. S. Wingreen, Phys. Rev. Lett. **68**, 2512 (1992).

[93] F. B. Anders, Phys. Rev. Lett. **101**, 066804 (2008).

[94] F. B. Anders and S. Schmitt, J. Phys.: Conf. Ser. **220**, 012021 (2010).

[95] F. B. Anders, J. Phys.: Condens. Matter **20**, 195216 (2008).

[96] A. C. Hewson, J. Bauer, and A. Oguri, J. Phys.: Condens. Matter **17**, 5413 (2005).

[97] P. Nozières and A. Blandin, J. Phys. France **41**, 193 (1980).

[98] P. Coleman and C. Pépin, Phys. Rev. B **68**, 220405 (2003).

[99] P. Mehta *et al.*, Phys. Rev. B **72**, 014430 (2005).

[100] A. K. Mitchell, T. F. Jarrold, and D. E. Logan, Phys. Rev. B **79**, 085124 (2009).

[101] R. Žitko and J. Bonča, Phys. Rev. B **74**, 045312 (2006).

[102] T. Kasuya, Prog. Theor. Phys. **16**, 58 (1956).

[103] M. A. Ruderman and C. Kittel, Phys. Rev. **96**, 99 (1954).

[104] K. Yosida, Phys. Rev. **106**, 893 (1957).

[105] R. M. Konik, Phys. Rev. Lett. **99**, 076602 (2007).

[106] R. M. Konik, New J. Phys. **9**, 257 (2007).

[107] M. Kulkarni and R. M. Konik, arXiv:0706.1234 (unpublished) (2010).

[108] C.-H. Chung, G. Zarand, and P. Wölfle, Phys. Rev. B **77**, 035120 (2008).

[109] R. Žitko and J. Bonča, Phys. Rev. B **73**, 035332 (2006).

[110] R. Žitko and J. Bonča, J. Phys.: Condens. Matter **19**, 255205 (2007).

[111] R. Žitko, Phys. Rev. B **81**, 115316 (2010).

[112] S. Sasaki, H. Tamura, T. Akazaki, and T. Fujisawa, Phys. Rev. Lett. **103**, 266806 (2009).

[113] D. C. Langreth, Phys. Rev. **150**, 516 (1966).

[114] J. M. Luttinger, Phys. Rev. **119**, 1153 (1960).

[115] W. Hofstetter, Phys. Rev. Lett. **85**, 1508 (2000).

[116] M. Pustilnik and L. Glazman, J. Phys.: Condens. Matter **16**, R513 (2004).

[117] D. E. Logan, M. P. Eastwood, and M. A. Tusch, J. Phys.: Condens. Matter **10**, 2673 (1998).

[118] F. B. Anders, D. E. Logan, M. R. Galpin, and G. Finkelstein, Phys. Rev. Lett. **100**, 086809 (2008).

[119] D. Goldhaber-Gordon *et al.*, Phys. Rev. Lett. **81**, 5225 (1998).

[120] S. M. Cronenwett, T. H. Oosterkamp, and L. P. Kouwenhoven, Science **281**, 540 (1998).

[121] D. H. Cobden *et al.*, Phys. Rev. Lett. **81**, 681 (1998).

[122] A. Kogan *et al.*, Phys. Rev. Lett. **93**, 166602 (2004).

[123] T.-M. Liu *et al.*, Phys. Rev. Lett. **103**, 026803 (2009).

[124] A. V. Kretinin *et al.*, arXiv:1108.1773v1 (unpublished) (2011).

[125] J. Bauer, A. Hewson, and A. Oguri, J. Magn. Magn. Mater. **310**, 1133 (2007).

[126] J. Bauer and A. C. Hewson, Phys. Rev. B **76**, 035119 (2007).

[127] T. A. Costi, Phys. Rev. Lett. **85**, 1504 (2000).

[128] A. C. Hewson, J. Bauer, and W. Koller, Phys. Rev. B **73**, 045117 (2006).

[129] D. E. Logan and N. L. Dickens, J. Phys.: Condens. Matter **13**, 9713 (2001).

[130] J. E. Moore and X.-G. Wen, Phys. Rev. Lett. **85**, 1722 (2000).

[131] R. Žitko, R. Peters, and T. Pruschke, New J. Phys. **11**, 053003 (2009).

[132] K. Furuya and J. H. Lowenstein, Phys. Rev. B **25**, 5935 (1982).

[133] H. Zhang, X. C. Xie, and Q.-f. Sun, Phys. Rev. B **82**, 075111 (2010).

[134] R. Žitko, Comput. Phys. Commun. **180**, 1271 (2009).

[135] N. E. Bickers, Rev. Mod. Phys. **59**, 845 (1987).

[136] D. E. Logan and M. R. Galpin, J. Chem. Phys. **130**, 224503 (2009).

[137] S. Schmitt and F. B. Anders, Phys. Rev. Lett. **107**, 056801 (2011).